Department of Exploration Geophysics

Effect of capillarity on the acoustics of partially saturated porous rocks

Qiaomu Qi

This thesis is presented for the Degree of
Doctor of Philosophy
of
Curtin University

August 2015

To the best of my knowledge and belief this thesis contains no material previously published by any other person except where due acknowledgement has been made. This thesis contains no material which has been accepted for the award of any other degree or diploma in any university.

"I think and think for months and years. Ninety-nine times, the conclusion is false. The hundredth time I am right."

- Albert Einstein

Acknowledgements

I would like to express my sincere gratitude to my supervisors, Professor. Boris Gurevich and Dr. Tobias Müller. Without their guidance and input, this journey would be much more difficult. Thank you Boris for providing me scholarship and funds from your consortium. I feel extraordinary lucky for being able to work with you and nourished by your vast experience. I am much obliged to Tobias, for being a tremendous mentor to me. I am grateful for your years of training which helps me grow as a research scientist.

A big thank you to Dr. Sofia Lopes and Dr. Maxim Lebedev, for sharing me your state-of-the-art laboratory data at the beginning of my PhD. It greatly helps me form my research motivation.

I would like to express my appreciation to Dr. Germán Rubino and Dr. Pratap Sahay for multiple simulating discussions which greatly improve my understanding of poroelasticity.

I want to say thank you to our reservoir geophysicists, Eva, Mateus and Hosni, for sharing me your practical insights of rock physics and commenting on my work.

A special shout-out to my Curtin friends and colleagues, Shahadat, Javad, Andrew, Sinem, Olivia, Felix, Michael, Stephanie and Tongcheng for years of companion which allows me to fulfil my dream without being so lonely. Also thank Deirdre and Robert for administrative and technical support, I have been taken good care of because of your hard work.

My final acknowledgement goes to my parents, to whom I owe so much in life. Thank you for being visionary and putting so much effort on my education since I was a teenager. This thesis is dedicated to you.

Abstract

It is well known that capillary forces control the fluid distribution in partially saturated rocks. However, the role of capillarity on acoustic signatures such as attenuation remains poorly understood. This thesis is dedicated to investigate the effect of capillarity on acoustic signatures within the framework of Biot's theory of wave propagation in a poroelastic medium and to explore its implications for rock physics modelling. The macroscopic manifestation of capillarity can be captured by replacing the pressure continuity boundary condition in Biot's theory by a pressure jump boundary condition with a non-vanishing interfacial impedance and involving the concept of membrane stiffness.

This interfacial impedance is incorporated into the classical White's model for seismic attenuation and dispersion due to wave-induced fluid flow in layered sedimentary structures by solving a boundary value problem for Biot's quasi-static poroelasticity equations. The membrane stiffness is also incorporated into models for 1D and 3D random patchy saturation. These generalized models predict that the P-wave velocity at low frequency limit increases, thereby decreasing the amount of dispersion and attenuation and change the velocity- and attenuation-saturation relations accordingly. The 3D capillarity-extended random patchy saturation model is applied to interpret ultrasonic data acquired during a forced imbibition experiment where capillarity is thought to be of importance. Furthermore, the poroelastic P-wave reflectivity is generalized to take into account the interfacial impedance. Two scenarios where interfacial impedance can arise in seismic investigations are analyzed, namely the P-wave reflection from a gas-water contact and from a fluid/gas-saturated-rock contact. For the fluid/gas-saturated-rock scenario the presence of capillarity substantially influences the frequency- and angle-dependence of the reflected P-wave amplitude.

Patchy saturation is inherently associated with a characteristic length scale of the fluid patches. Due to the interplay of capillary and viscous forces during the course of fluid injection into a reservoir this saturation scale varies and thus further complicates the interpretation of time-lapse seismic data. The developed patchy saturation model is used to study the influence of variable saturation scales on velocity (time-shifts) and seismic amplitude (time-lapse attenuation). For a brine-saturated reservoir undergoing gas injection it is found that an assessment of the saturation scale variation can be important for reliable discrimination between saturation and pressure changes.

Contents

Chapter 1

Introduction

The seismic method, as one of the most important geophysical prospecting methods, is powerful in delineating subsurface geological structures of interest. Beyond the conventional usage of seismic reflection data for imaging stratigraphic patterns, quantitative seismic interpretation (QSI) reduces the exploration risk by characterizing and forecasting hydrocarbon reservoir properties (Avseth et al., 2005; Bacon et al., 2007; Bjørlykke, 2010). QSI heavily relies on seismic rock physics models, that is idealized descriptions of seismic responses from reservoir rocks. These rock physics models aim at providing a link between geological and petrophysical parameters with (an-)elastic properties relevant for wave propagation. Wave measurements such as ultrasonic, sonic-log, crosswell, VSP (Vertical Seismic Profile) and surface seismic entail characteristic frequencies and consequently encode geological information of various scales, i.e., from a fraction of core sample at 1 MHz ultrasonic frequency up to geological facies scale at 100 Hz seismic frequency. Maximizing the value of these data for successful QSI requires to integrate the measured or modelled results from one frequency band to another. Thus, in order to achieve this up- or down-scaling a rock physics model has to take both frequency and scale effects into account. This requires a good understanding of the relation between frequency-dependent wave velocity and attenuation with petrophysical quantities, such as saturation and transport properties.

It is believed that a major source of fluid-related velocity dispersion and attenuation is due to wave-induced fluid flow (WIFF), i.e., that is the oscillatory fluid

motion relative to the porous rock frame (Pride et al., 2004; Müller et al., 2010; Liner, 2012). Particularly, in a partially saturated reservoir WIFF is thought to be prominent, as it can occur not only across fluid patches at the millimetre- and centimetre-scale (Lee and Collet, 2009; Morgan et al., 2012) but also at gas-water, gas-oil contacts at the metre-scale (Rutherford and Williams, 1989; Zhao et al., 2015). This shows that WIFF in partially saturated rocks is inherently associated with a characteristic length scale. In the following we refer to this length scale as the saturation scale. An intriguing feature of this saturation scale is that it can change with time. This saturation scale variation is more prevalent during the course of dynamic fluid injection as evidenced in laboratory experiments (Lebedev et al., 2009). It is very likely that dynamic fluid injection in reservoir stimulation operations also leads to a variation of the saturation scale. Then, the saturation scale might affect time-lapse seismic data interpretation which, in turn, requires time-lapse QSI methods to be developed. For example, it is not fully understood how a change of the saturation scale complicates the discrimination between saturation and pressure effects from time-lapse seismic data.

WIFF in partially saturated rocks is inherently connected with two- or multiphase flow phenomena at the pore scale. One phenomenon is capillarity. It is important since there always exist pore spaces in form of thin capillarities. Capillarity is an old subject in petroleum engineering and is known as an important control of two-phase flow (Homsy, 1987; Leonormand, 1990). Despite the ubiquitous nature of capillarity in porous rocks saturated with immiscible fluids, its effect is neglected in the classical treatments of wave-induced fluid flow (White et al, 1975; Dutta and Odé, 1979; Dutta and Odé, 1983). More recently, studies on the basis of modified Biot theories point out the potential impact of capillarity on acoustic properties and attenuation (Tserkovnyak and Johnson, 2003; Lo and Sposito, 2005; Markov and Levin, 2007). However, these predictions have never been tested against laboratory data and therefore lack validation. Given the potential importance of WIFF in partially saturated rocks for QSI, it is the main objective of this thesis to establish a rock physics model that accounts for the combined effects of wave-induced fluid flow and capillarity. This model will be applied to better understand the acoustic signatures observed in a dynamic fluid injection experiment at the core sample scale. Finally, this rock physics model is also at the core of a workflow devised to interpret time-lapse changes in a simplified reservoir production scenario.

1.1 Background and Motivation

Why partially saturated rocks?

A rock whose pore space is occupied by two or more types of immiscible fluids is referred as partially saturated rock. There are plenty of geological settings where partially saturated rocks occur. To name a few, underground aquifers infiltrated by contaminating fluids, salt-water intrusions induced by earthquakes and oil and gas reservoirs. In the hydrocarbon reservoir environment, partially saturated rocks are likely to be encountered in following scenarios (White, 1975):

- at the gas-oil or gas-water contact in a homogeneous reservoir rock, capillary pressure is responsible for a transition zone in which the gas saturation varies through a wide range;
- when the reservoir rock is spatially heterogeneous, it seems plausible that gas saturation may vary accordingly;
- shale stringers may seal off local pockets of gas creating a multitude of gas-liquid contacts;
- during production of a field, gas exsolution can create distributed pockets of free gas.

Moreover, during hydrocarbon production there will be changes in saturation. This time-dependency renders the study of partially saturated rocks particularly challenging and important from a reservoir surveillance point of view.

This explains why partially saturated rocks are of primary interest in petrophysical investigations and petroleum engineering. Saturation and its time evolution provides vital information for petroleum engineers to plan the field production. This also explains why the effective seismic properties of partially saturated rocks is a topic of continued interest. From a rock physics perspective, it means that there is a need for models that provide the link between the static and dynamic properties of partially saturated rocks. This motivates further study of the relation between wave velocities and saturation, velocity dispersion and attenuation in partially saturated rocks.

Wave-induced fluid flow (WIFF)

For an elastic wave travelling through a permeable porous rock, a wavelength scale pressure gradient always exists regardless of rock and fluid heterogeneities. WIFF occurring at wavelength scale, or macroscopic scale is the so-called Biot global flow (Biot, 1956; Geertsma and Smit, 1961; Dutta and Odé, 1983). The relative fluid-solid movement induced by wavelength scale pressure gradient is generally small at seismic frequencies so that resulting attenuation and dispersion are negligible for rocks with porosities less than 35%. However, recent numerical calculation of Dennemean et al. (2002), Gurevich et al. (2004) show that, in case of P-wave reflection at contact between liquid and gas-saturated rocks, Biot global flow can result in significant deviation of reflection coefficient from its elastic value at low frequencies. Therefore, it is motivated to investigate the joint role of capillarity and Biot global flow on seismic reflection coefficient.

At the pore scale, a wave can induce pressure gradients between regions of differing compliances, for instance, between compliant grain contacts and stiff surrounding pores in a granular sandstone (Murphy et al., 1986; Gurevich et al., 2009) or between clay or hydrate cements and grains in a shaly sandstone (Best et al., 2013) or gas-hydrate bearing rock (Priest et al., 2006). WIFF associated with pore scale is sometimes referred to as squirt flow. Squirt flow is generally considered to be significant at ultrasonic frequencies plus when the effective stress is low (Gurevich et al., 2009). Squirt flow may be enhanced by other attenuation mechanism and play a role in seismic and logging frequencies (Johnston et al., 1979; Rubino and Holliger, 2013).

In between wavelength- and pore-scale, there exists an intermediate scale, named mesoscopic scale and it is associated with mesoscopic flow (Pride et al., 2004; Müller et al., 2010). For elastic waves propagating through a partially saturated rock the mechanism of WIFF can be qualitatively described as follows. Due to the compressibility contrast of the two fluid phases the wave generates oscillating pressure gradients. These pressure gradients tend to equilibrate through pressure diffusion and therefore cause internal friction. This gives rise to attenuation and velocity dispersion. This process of wave-induced pressure diffusion is loosely called WIFF. It is, however, important to note that WIFF does not imply any net flow through the porous medium. WIFF can take place across various scales as illustrated in Figure 1.1. In typical sedimentary rocks, mesoscopic WIFF

can occur within a wide range of scales, from the largest pore size to the smallest wavelength, and therefore can cause attenuation for a broad range of frequencies. Particular in partially saturated rocks, centimeter to meter saturation scale give rise to significant velocity dispersion and attenuation at seismic frequencies (Kirstetter et al., 2006; Rubino et al., 2011).

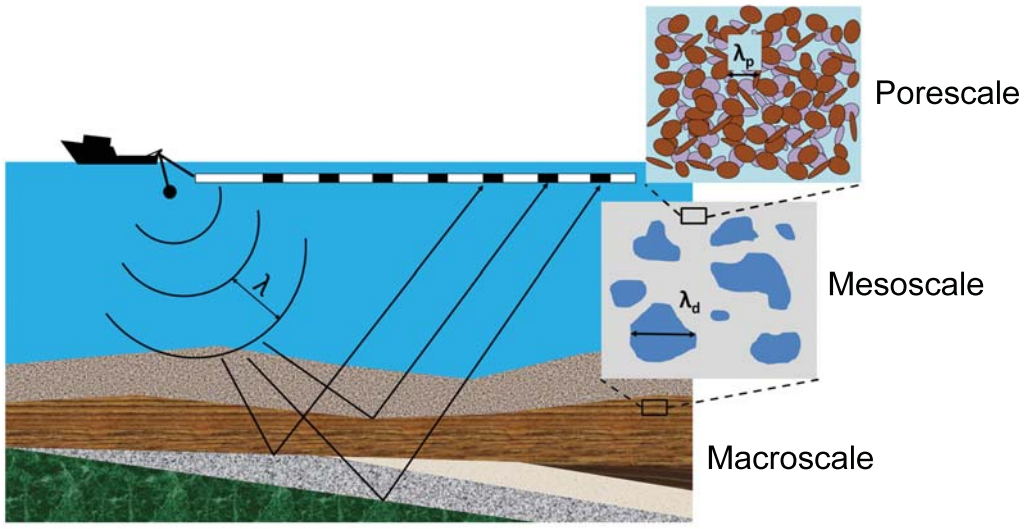

Figure 1.1: Scales of heterogeneities which are relevant for wave-induced fluid flow.

Reported examples of WIFF in partially saturated reservoir

A free gas zone beneath gas-hydrate charged marine sediments is believed to cause seismic attenuation through WIFF (Carcione and Picotti, 2006; Gerner et al., 2007). Morgan et al. (2012) estimate attenuation from seismic reflection data of a gas-saturated zone under methane hydrates at Blake Ridge (Figure 1.2a). They use a mesoscopic P-wave attenuation model (White et al., 1975) to invert for the gas saturation and that also matches with the observed attenuation. The inferred gas saturation agrees with log data estimates collected from the same site. Lee and Collett (2009) also report P-wave velocity dispersion between surface seismic and logging frequencies on the order of 25% in gas-hydrate-bearing sediments containing free gas. They find that the dispersion can be explained by patchy saturation model (White, 1975) assuming centimetre scale gas-pocket size.

Another field observation that could be explained by mesoscopic WIFF is the presence of gas chimneys that is often recorded in offshore seismic sections.

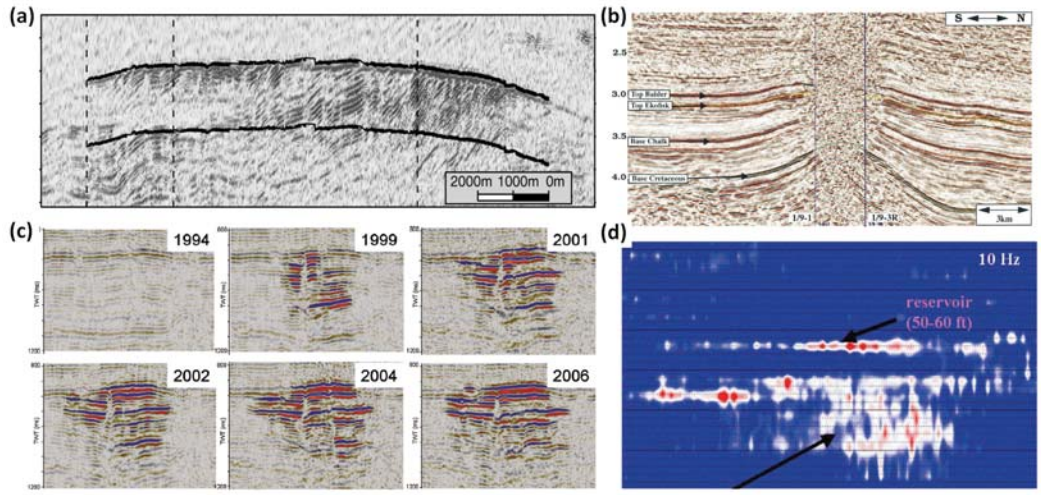

Figure 1.2: (a) Seismic section showing attenuation in a gas-saturated zone beneath hydrate-bearing sediments. After Morgan et al. (2012). (b) Gas chimney with strong distortion of seismic amplitudes. After Granli et al. (1999). (c) Seismic monitoring of CO_2 storage. After Arts et al. (2008). (d) Low frequency anomalies below gas reservoir. After Castagna et al. (2003).

The presence of gas, leaked from poorly sealed reservoir to its overburden, has the effect of lowering seismic velocities and increasing seismic attenuation. Gas chimney causes low signal-to-noise ratio P-wave sections. An example of data from Tommeliten chalk fields Alpha, North Sea is shown in Figure 1.2b (Granli et al., 1999), strong distortion of seismic amplitudes can be seen. A typical case involving a gas chimney is related to the CO_2 injection in a saline aquifer of Utsira formation, Sleipner field (Arts et al., 2008). Interpretation of repeated seismic surveys indicates that the thin intra-reservoir shale layers allow vertical migration of CO_2 towards top of the reservoir. This forms a gas chimney at depths above the injection point. In next section, it will be shown that those amplitude distortion (Figure 1.2c) can be explained by attenuation due to mesoscopic WIFF.

Seismic low-frequency effects with reference to reflections from hydrocarbon reservoir may reveal the high attenuation nature and be used as direct hydrocarbon indicator (Castagna et al., 2003; Goloshubin et al., 2006; Chapman et al., 2006). Using spectral decomposition technique, Castagna et al. (2003) observe high amplitude anomalies beneath gas reservoir appear in low frequency section only (Figure 1.2d). Goloshubin et al. (2006) also show that low-frequency shadows are likely to be associated with fluid saturated reservoirs. Analyses of laboratory and field data (Korneev et al., 2004) indicate that increased ampli-

tude and travel time at low frequency can be associated with wave propagating in a fluid-saturated thin-layer exhibiting high attenuation. Attenuation causing low-frequency shadow can be attributed to WIFF resulting from partial gas saturations at mesoscopic scale (Quintal et al., 2009).

WIFF in time-lapse seismic monitoring

4D seismic, that is based on analysis of repeated 3D seismic data, opens new horizons for monitoring changes of reservoir properties such as temperature, saturation and fluid pressure during the productive life of a field (Aronsen et al., 2004). The detection of areas with significant changes helps reservoir engineers to determine new drilling sites (Johnston, 2013). Quantitative estimation of saturation and pressure changes can be obtained using time-lapse P- and S- wave information derived from elastic inversion or from AVO analysis (Tura and Lumley, 1999; Cole et al., 2002; Davolio et al., 2011).

Figure 1.3: Estimated fluid saturation changes (left) and pore pressure changes (right) based on 4D AVO analysis for the top Cook interface at Gullfaks. Yellow color represents significant change, red line shows original oil-water contact. After Landrø (2001).

Landrø (2001) presents a rock-physics-based inversion scheme that directly solves for pressure and saturation changes from AVO intercept and gradient attributes. Landrø's approach assumes that the elastic properties associated with saturation change is given by Gassmann equation whereas pressure changes is governed by effective stress law obtained from ultrasonic core measurement. The validity of Gassmann equation restricts to homogeneous fluid distribution (Mavko

and Mukerji, 1998). Thus, employing Gassmann's equation as saturation law excludes the possible attenuation effect arising from a patchy fluid distribution. On top of that, the change of reservoir forces during dynamic fluid injection can give rise to time-dependent saturation scale. This means that there is yet another variable controlling the time-lapse seismic signal on top of the saturation and fluid pressure change. Therefore, it seems to be prudent to understand the effect of saturation scale changes on WIFF.

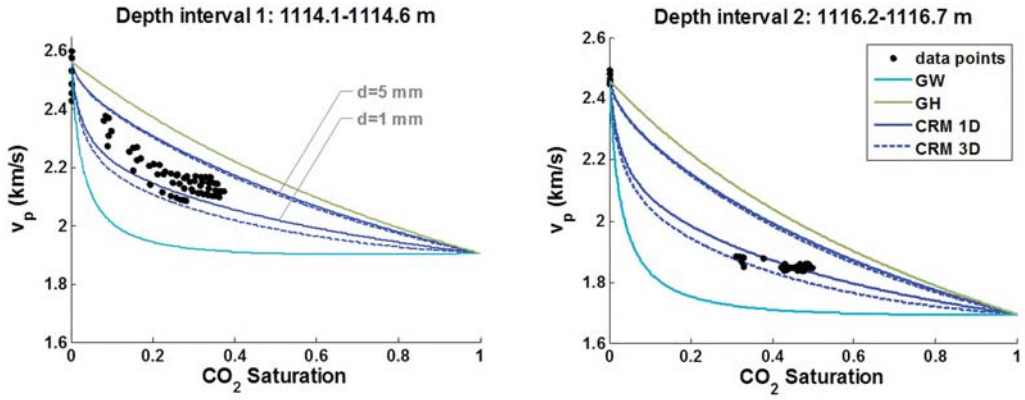

Figure 1.4: Comparison between modeled velocity-saturation relation and time-lapse log data for the (a) shallower and (b) deeper depth interval at sonic frequencies. 'GW', 'GH' and 'CRM' are the Gassmann-Wood lower bound, Gassmann-Hill upper bound and patchy saturation model, respectively. The model employs a patch size 'd' of 1 and 5 mm. Modified after Caspari et al. (2011).

There are field studies that point to mesoscopic WIFF as a probable mechanism controlling the time-lapse seismic signatures. Konishi et al. (2009) study time-lapse sonic and neutron logs obtained from a CO_2 sequestration test site in Japan. They find that P-wave velocity gradually (almost linearly) decreases with increasing CO2 saturation and concluded that this behaviour could indicate the presence of mesoscopic CO_2 patches. Ajo-Franklin et al. (2013) present results of a high-resolution time-lapse crosswell seismic survey for a pilot CO_2 injection experiment. Therein, the observed variations in P-wave velocity may be explained with a patchy saturation model. Caspari et al. (2011) analyse the sonic-log velocities of two thin reservoir sections from Nagaoka CO_2 site (Konishi et al., 2009). A comparison of P-wave velocities to the theoretical patchy saturation bounds (Müller et al., 2010) is shown in Figure 1.4. It can be observed that the data points for the two depth intervals fall between the bounds of uniform (denoted by GW) and patchy saturation (denoted by GH) indicating that mesoscopic flow

might play a role. To test this assumption, Caspari et al. (2011) model the velocity-saturation relation using the random patchy saturation model (denoted by CRM 1D, 3D) with varying patch sizes. The velocity-saturation trend of the smoothed data can be explained by the patchy saturation model for a range of patch sizes.

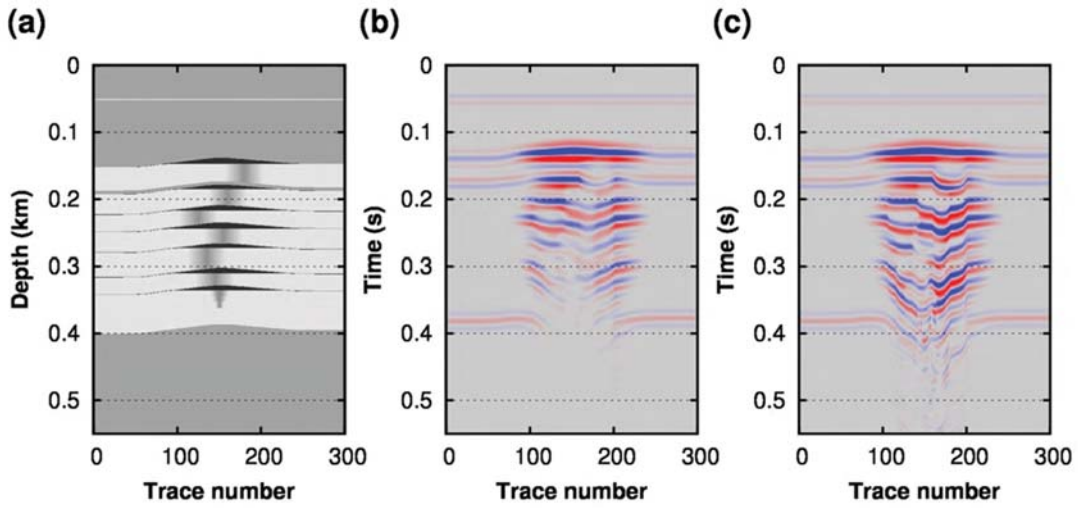

Figure 1.5: (a) Scheme of the geological model for the Sleipner field. The black thin areas indicate the main CO2 component. The narrow gray shaded areas indicate the presence of a diffuse CO2 component. (b) Seismic response considering WIFF effects due to the presence of CO2 patches. (c) Seismic response for an equivalent elastic model with P-wave velocity given by Gassmanns formula. Modified after Rubino et al. (2011).

Rubino et al. (2011) explore the potential implications for mesoscopic flow on surface seismic data. Their study is inspired by the Sleipner field CO_2 storage project (Arts et al., 2008). Rubino et al. (2011) simulate the propagation of seismic waves through a Utsira like reservoir containing centimetre-scale CO_2 patches (Figure 1.5a). Two modelling methods are employed, one is elastic modeling with velocity calculated from Gassmann equation (which implies homogeneous saturation) and the other one is viscoelastic modelling which accounts the effect of WIFF (in this case due to patchy saturation). By comparing the resulting zero-offset synthetic seismic sections they observe that when velocity dispersion is considered, velocity push-down caused by the presence of CO_2 becomes less pronounced whereas amplitudes around CO_2 plumes diminish (Figure 1.5b,c,) Their

results indicate that WIFF due to the presence of centimetre-scale fluid patches may produce noticeable changes in the observed surface seismic data.

Core-flooding combined with ultrasound and CT-imaging

The most detailed insights into the fluid distribution and accompanying evolutions of velocity- and attenuation- saturation relations can be gained from laboratory core-flooding monitored by both ultrasonic transducers and X-ray CT imaging (Lei and Xue, 2009; Alemu et al., 2013; Lopes et al., 2014). As an exam-

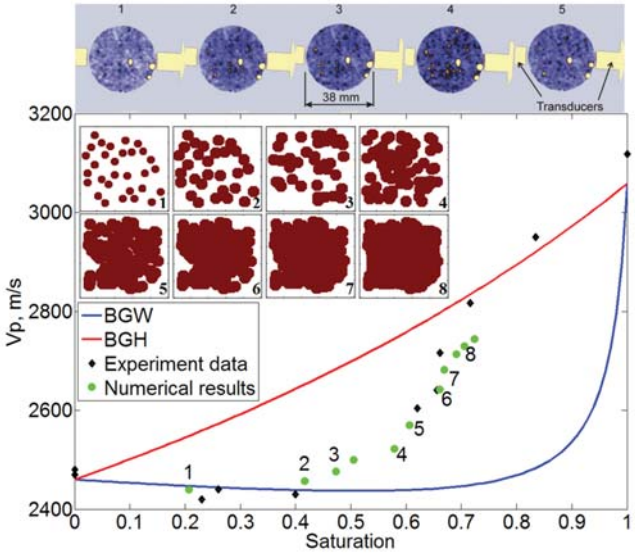

Figure 1.6: Velocity-saturation relation determined from numerical simulations of wave propagation in a poroelastic solid with randomly distributed patches that cluster for larger saturation values (see inset). Experimentally determined velocities for the quasi-static injection experiment are also shown. After Lebedev et al. (2009).

ple, in the experiment of Lebedev et al. (2009), the P-wave velocity-saturation relation resulting from an imbibition exhibits a transition between Gassmann-Wood and Gassmann-Hill predictions as shown in Figure 1.6. They model the data by performing numerical simulation, that is based on Biot's wave equations. The varying degree of saturation is characterized by increasing the size of the randomly distributed fluid clusters. Despite the simplified numerical set-up, the simulation results reproduce the overall behavior of the measured VSR as seen in Figure 1.6. The modelling indicates that the behaviour of velocity-saturation relation can be attributed to mesoscopic WIFF. Moreover, from a modelling view-

point, it is important to know that the saturation scale, i.e., water patch size, increases with increasing water saturation during imbibition.

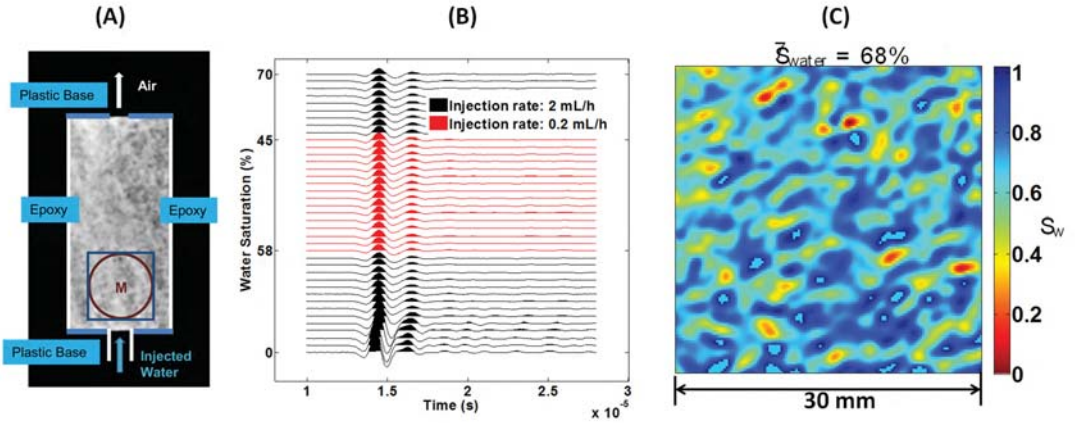

Figure 1.7: (a) Measurement set up and raw CT scan of the sample: the red circle indicates the acoustic monitoring field; (b) The ultrasonic waveforms at various saturations. The black waveforms correspond to an injection rate of 2 mL/h while the red waveforms correspond to a reduced injection rate of 0.2 mL/h.(c) Water saturation map (average S_{w}=68%) derived from the CT images. Mesoscopic fluid patches appear.

The fluid distribution information inferred from the measurement of Lebedev et al. (2009) however remains qualitative. More recently, Lopes et al. (2014) perform simultaneous acquisition of high-resolution CT scans and ultrasonic waveforms during forced water imbibition on a Savonnières limestone sample (Figure 1.7a). The CT image reveals minimum one-tenth millimetre feature of the sample that is a good candidate for studying wave-induced fluid flow due to partial saturations at mesoscopic scale. Let us take a closer look at the data by modelling the measured P-wave velocities and attenuation. First, consecutive CT imaging during core-flooding (Lopes et al., 2014) allows for obtaining statistical information, such as autocorrelation function, from the saturation maps (Figure 1.7c). Toms et al. (2007a) propose a so-called continuous random patchy saturation model (CRM) which quantifies the fluid distribution by statistical measures. Therefore, this model is employed here to give estimates of the velocity and attenuation. Mechanical properties of the rock and fluids as well as the frequency in the modelling are set to be consistent with the measurement. The results are presented in Figure 1.8. The measured velocities fall in between patchy saturation bounds which confirms mesoscopic flow to be the driving mechanism. However, the modelled velocity underestimates the overall measured velocities whereas the modelled attenuation overestimates the overall measured attenuation. It appears that there is a discrepancy that cannot be satisfactorily explained by CRM model and hence

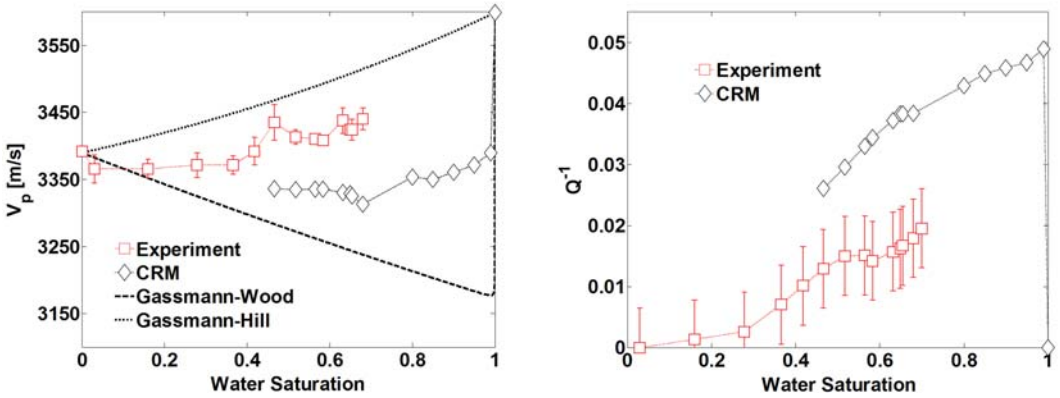

Figure 1.8: Modeling ultrasonic data obtained during a capillary-force-dominated imbibition: (a) velocity- and (b) attenuation- saturation relations.

by the mechanism of WIFF alone. A possible explanation for this mismatch is related to the capillary effect.

Capillarity effects on the acoustics of partially saturated rocks

Theoretical and experimental works of two-phase flow associated with imbibition suggest that the fluid distribution for immiscible flows is controlled by the interplay between viscous and capillary forces. Specifically, in petrophysical experiments the relative importance of the capillary effect is quantified by the capillary number (e.g., Riaz et al., 2007):

$$\mathrm{Ca} = \frac{\mu_{\mathrm{f}} U}{\gamma}, \quad U = \frac{4q}{\pi D^2} \tag{1.1}$$

where μ_{f} is the shear viscosity of the injected fluid and γ is the interfacial tension between the two fluids. U is the injection velocity which depends on the injection rate q and the diameter of the sample D. In the experiments of Lopes et al. (2014), the capillary number is on the order of 10^{-9}. In the context of reservoir flow simulations, the ratio of viscous force to capillary force is expressed as (Sengupta and Mavko, 2003)

$$R_{\mathrm{cv}} = \mathrm{Ca}\,\frac{lr}{\kappa}, \tag{1.2}$$

where l is the length of the core sample and r is a representative pore-throat radius. The flow permeability is denoted as κ. R_{cv} in the Lopes et al. (2014)

experiment is on the order of 10^{-3}. Therefore, both the capillary number Ca and the critical flow ratio R_{cv} indicate that the flow regime is dominated by capillary forces.

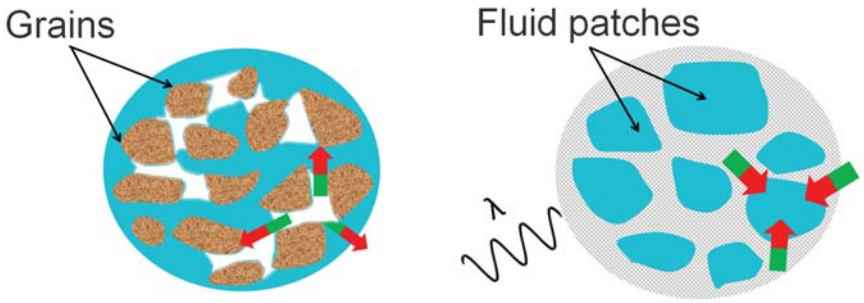

Figure 1.9: Microscopic capillary forces (left) produce a net effect at macroscopic scale (right). The macroscopic capillary pressure may change the overall stiffness of the saturated rock and consequently affects the wave responses. Arrows denote micro- and macro- capillary pressure gradients.

It is, however, not clear how this capillarity affects the acoustics of partially saturated rocks. There is experimental evidence that capillarity can lead to changes in elastic stiffnesses and hence to changes in wave velocities and attenuation (Moerig et al., 1996; Averbakh et al., 2010). This also involves the questions how capillary forces affect the velocity-saturation relation and WIFF. This becomes a particular important problem in the presence of mesoscopic fluid patches. While capillary forces only exist at fluid-fluid interfaces at the pore-scale, one can expect that they produce a net effect up in scale (De la Cruz et al., 1995; Tserkovnyak and Johnson, 2003), thereby creating a new attribute across mesoscopic patches, or between macroscopic gas-water, gas-oil contacts. Given that the mesoscopic WIFF is often applied to interpret seismic attenuation (Morgan et al., 2012; Blanchard and Delommot, 2015), any significant changes induced by capillarity may possibly entail important implications. This is one of the primary motivations for including the capillarity effect into models for mesoscopic WIFF.

It is the aim of this thesis to incorporate the mesoscopic manifestation of capillarity in the framework of Biot's poroelasticity theory. This, in turn, enables us to extend existing models for patchy-saturation that are based on Biot's poroelasticity theory. It further allows us to study how capillarity affects WIFF and what implications for the interpretation of seismic (time-lapse) signatures arise.

1.2 Thesis outline

Chapter 2: A mathematical review of relevant theories for acoustics in partially saturated porous media is given.

Chapter 3: Capillarity effect is incorporated in White's layered model for studying acoustic responses, i.e., velocity, attenuation and poroelastic fields resulting from mesoscopic fluid flow.

Related publication: *Qiaomu Qi, Tobias M. Müller, Germán Rubino, 2014. Seismic attenuation: Effect of interfacial impedance on wave-induced pressure diffusion: Geophysical Journal International, 199, 1677-1681. doi: 10.1093/gji/ggu327*

Chapter 4: Random patchy saturation theory is generalized to include capillarity effect. The theory is validated by comparing with laboratory data.

Related publication: *Qiaomu Qi, Tobias M. Müller, Boris Gurevich, Sofia C. Lopes, Maxim Lebedev, Eva Caspari, 2014. Quantifying the effect of capillarity on dispersion and attenuation in patchy-saturated rocks: Geophysics, 79(5), WB35-WB50. doi: 10.1190/geo2013-0425.1*

Chapter 5: Reflection coefficients for contact between saturated porous media and liquid/porous-medium contact are generalized to include capillarity.

Related publication: *Qiaomu Qi, Tobias M. Müller, Boris Gurevich, 2015. The role of interfacial impedance on poroelastic reflection coefficient. EAGE Technical Program Expanded Abstract. doi:10.3997/2214-4609.201412626*

Chapter 6: A workflow on application of developed theory for quantitative analysis of time-lapse seismic signatures is established.

Related publication: *Qiaomu Qi, Tobias M. Müller, Boris Gurevich, 2015. Saturation scale effect on time-lapse seismic signatures: submitted to Geophysical Prospecting.*

Chapter 7: The thesis is finalized by concluding remarks and future recommendations.

Chapter 2

Theoretical background

2.1 Acoustics in saturated porous media — Biot's theory of poroelasticity

The theory of wave propagation in a poroelastic solid containing a viscous compressible fluid has been established by Biot (Biot, 1956a, b; Biot, 1962). It not only forms the theoretical foundation of seismic wave propagation in fluid-saturated rocks but also is used in many other disciplines related with porous media. Biot's equations of poroelasticity will be frequently referred in this thesis. Therefore, it is of primary importance here to review its basic concepts. As with any physical theories, the work of Biot (1956) is based on certain assumptions:

- Porous medium is elastic and statistically isotropic.
- Pore fluid is continuous and does not support shear stress.
- Wave motion induces small deformations only and no thermal variation.
- Seismic wavelength is substantially larger than the pore sizes.

In subsequent sections, the definitions of potential, kinetic and dissipated energies in Biot's theory will be introduced. The physical meaning of Biot's elastic coefficients will be elaborated. These are followed by the derivation of wave equation from solving the corresponding Lagrange equation.

2.1.1 Potential energy and stress strain relation

Consider a unit cubic aggregate of fluid and solid, the stress tensor of such elementary volume is given by

$$\underbrace{\begin{Bmatrix} \sigma_{xx}+\sigma & \sigma_{xy} & \sigma_{xz} \\ \sigma_{yx} & \sigma_{yy}+\sigma & \sigma_{yz} \\ \sigma_{zx} & \sigma_{zy} & \sigma_{zz}+\sigma \end{Bmatrix}}_{Total\ \tau_{ij}} = \underbrace{\begin{Bmatrix} \sigma_{xx} & \sigma_{xy} & \sigma_{xz} \\ \sigma_{yx} & \sigma_{yy} & \sigma_{yz} \\ \sigma_{zx} & \sigma_{zy} & \sigma_{zz} \end{Bmatrix}}_{Solid\ \sigma_{ij}} + \underbrace{\begin{Bmatrix} \sigma & 0 & 0 \\ 0 & \sigma & 0 \\ 0 & 0 & \sigma \end{Bmatrix}}_{Fluid\ \delta_{ij}\sigma}. \tag{2.1}$$

The total stress components τ_{ij} equal the sum of solid and fluid force acting on each face of the two-phase cube. σ_{ij} represent the force components acting on the solid portion of the cube face. On the other hand, σ represents the total normal tension force applied to the fluid portion of the cube face. The fluid stress relates the hydrostatic fluid pressure in the pores via

$$-\sigma = \phi p_f. \tag{2.2}$$

σ is taken negative when the force acting on the fluid is pressure whereas σ_{ij} is positive if the force in the solid is tension. The porosity ϕ of the skeleton is defined as

$$\phi = \frac{V_p}{V_b}, \tag{2.3}$$

where V_p is the volume of the pores contained in the bulk volume V_b. The average displacement components of the solid are designated by u_x, u_y, u_z whereas for the fluid they are U_x, U_y, U_z. The strain tensor of the solid is represented by

$$e_{ij} = \begin{Bmatrix} e_{xx} & e_{xy} & e_{xz} \\ e_{yx} & e_{yy} & e_{yz} \\ e_{zx} & e_{zy} & e_{zz} \end{Bmatrix} \tag{2.4}$$

with

$$e_{xx} = \frac{\partial u_x}{\partial x},\ e_{xy} = \frac{1}{2}\left(\frac{\partial u_x}{\partial y} + \frac{\partial u_y}{\partial x}\right),\ \text{etc.} \tag{2.5}$$

The strain tensor in the fluid is given by

$$\epsilon = \frac{\partial U_x}{\partial x} + \frac{\partial U_y}{\partial y} + \frac{\partial U_z}{\partial z}. \tag{2.6}$$

It is sometimes more convenient to define the relative average displacement of fluid relative to the solid frame as

$$\mathbf{w} = \phi(\mathbf{U} - \mathbf{u}). \tag{2.7}$$

The associated strain for the relative displacement is the incremental fluid content which is defined as

$$\xi = -\nabla \cdot \mathbf{w} = \phi(e - \epsilon), \tag{2.8}$$

where $e = e_{xx} + e_{yy} + e_{zz}$ is the compressive strain. With a generalization of elasticity theory (Love, 1944), the potential (strain) energy of the poroelastic elementary volume is expressed as (Biot, 1962)

$$V = \tau_{xx}e_{xx} + \tau_{yy}e_{yy} + \tau_{zz}e_{zz} + \tau_{xy}e_{xy} + \tau_{yz}e_{yz} + \tau_{xz}e_{xz} + p_f\xi. \tag{2.9}$$

The stress components are given by the partial derivatives of the potential energy

$$\tau_{xx} = \frac{\partial V}{\partial e_{xx}},\ \tau_{xy} = \frac{\partial V}{\partial e_{xy}}, \ldots, p_f = \frac{\partial V}{\partial \xi}. \tag{2.10}$$

According to equations 2.10, the stress-strain relation in a general anisotropic poroelastic medium is characterized by 7 independent equations

$$\begin{pmatrix} \tau_{xx} \\ \tau_{yy} \\ \tau_{zz} \\ \tau_{xy} \\ \tau_{yz} \\ \tau_{xz} \\ p_f \end{pmatrix} = \begin{pmatrix} c_{11} & c_{12} & c_{13} & c_{14} & c_{15} & c_{16} & c_{17} \\ & c_{22} & c_{23} & c_{24} & c_{25} & c_{26} & c_{27} \\ & & c_{33} & c_{34} & c_{35} & c_{36} & c_{37} \\ & & & c_{44} & c_{45} & c_{46} & c_{47} \\ & & & & c_{55} & c_{56} & c_{57} \\ & & & & & c_{66} & c_{67} \\ & & & & & & c_{77} \end{pmatrix} \begin{pmatrix} e_{xx} \\ e_{yy} \\ e_{zz} \\ e_{xy} \\ e_{yz} \\ e_{xz} \\ \xi \end{pmatrix} \tag{2.11}$$

The requirement of the symmetry of the stress and strain tensors lead to 28 independent poroelastic coefficients in equations 2.11. For an isotropic material, the potential energy 2.9 takes the simplified form as

$$2V = (\lambda + 2\mu)e^2 - \mu I - 2\alpha M e\xi + M\xi^2, \tag{2.12}$$

where the invariant I is given by

$$I = e_{xy}^2 + e_{yz}^2 + e_{xz}^2 - 4e_{xx}e_{yy} - 4e_{yy}e_{zz} - 4e_{xx}e_{zz}. \tag{2.13}$$

From equations 2.2, 2.10 and 2.12, we obtain the stress strain relation for an isotropic poroelastic medium

$$\tau_{ij} = (\lambda e - \alpha M \xi)\delta_{ij} + 2\mu e_{ij} \ , \tag{2.14}$$

$$p_f = -\alpha M e + M\xi \ , \tag{2.15}$$

where δ_{ij} denotes the Kronecker Delta. In either case of $\phi = 0$ or $\mathbf{w} = 0$, the potential energy 2.12 reduces to the case analogous to isotropic elasticity. Accordingly, the stress strain relations 2.14, 2.15 become analogous to elastic Hooke's law.

2.1.2 Poroelastic constants

Four poroelastic coefficients, namely $\lambda,\ \alpha,\ M,\ \mu$ appeared in the stress strain relations 2.14, 2.15 of Biot's theory. They incorporate the solid, fluid properties as well as micro-structural information of the porous medium. The determination of the meaning and internal relation of these poroelastic coefficients require four Gedanken experiments (Biot and Willis, 1957; Gassmann, 1951).

Pure shear deformation

First, assuming the porous medium is subjected to a pure shear deformation such that

$$e = \xi = 0 \quad \rightarrow \ \tau^s_{ij} = \tau_{ij} - \frac{1}{3}\tau_{ll}\delta_{ij} = \mu\left(\frac{\partial u_i}{\partial x_j} + \frac{\partial u_j}{\partial x_i}\right), \tag{2.16}$$

where Einstein summation with repeated indices is applied. Since the fluid does not sustain shear force, it is clear that the parameter μ which relates the shear stress and strain is the shear modulus of the dry matrix.

Jacketed compressibility test

In this experiment, the porous medium is enclosed in a thin impermeable jacket and then subjected to an external hydrostatic pressure P_{e}. To ensure constant internal fluid pressure, the interior of the jacket is made to communicate with the

atmosphere through a tube, therefore

$$p_f = 0 \ \rightarrow \ \xi = \alpha e \ . \tag{2.17}$$

With the dilation of the sample e being measured, the jacketed bulk modulus can be given by

$$K_0 = -\frac{P_\mathrm{e}}{e} = \frac{1}{3}\frac{\tau_{ll}}{e} \ . \tag{2.18}$$

Because the entire external pressure is transmitted to the frame, K_0 is identical to the bulk modulus of the dry matrix. Equations 2.14, 2.15, 2.17, 2.18 together yields the following relation

$$\lambda = K_0 - \frac{2}{3}\mu + \alpha^2 M \ . \tag{2.19}$$

This also indicates that a new parameter $\lambda_c = \lambda - \alpha^2 M$ is equivalent to Lamé coefficient of the dry matrix.

Unjacketed compressibility test

In this experiment, the sample remains unjacketed and is immersed in the fluid where a pressure $-P_\mathrm{e}$ is applied. Since the fluid will completely penetrate the sample, one has

$$p_f = P_\mathrm{e} \ . \tag{2.20}$$

With the dilatation of the sample e being measured, the unjacketed bulk modulus is given by

$$K_s = -\frac{P_\mathrm{e}}{e} = \frac{1}{3}\frac{\tau_{ll}}{e} \ . \tag{2.21}$$

Because the applied pressure is transmitted to the solid skeleton, K_s is equivalent to the bulk modulus of the solid grain. Equations 2.14, 2.15, 2.20,2.21 together yields another Biot's parameter

$$\alpha = 1 - \frac{\lambda - \alpha^2 M + \frac{2}{3}\mu}{K_s} \ . \tag{2.22}$$

Using obtained result 2.19, parameter α can be expressed in terms of two measured quantities, namely the jacked and unjacketed bulk modulus

$$\alpha = 1 - \frac{K_0}{K_s} \ . \tag{2.23}$$

Assuming that the fluid strain ϵ has also been measured during the unjacketed test, the bulk modulus of the pore fluid can be expressed as

$$K_f = -\frac{P_\mathrm{e}}{\epsilon} \ . \tag{2.24}$$

The incremental fluid content under unjacketed test can be now written as

$$\xi = \phi P_\mathrm{e} \left(\frac{1}{K_f} - \frac{1}{K_s} \right) \tag{2.25}$$

Equations 2.15, 2.20 and 2.25 together gives the expression of the last Biot's parameter

$$M = \left(\frac{\alpha - \phi}{K_s} + \frac{\phi}{K_f} \right)^{-1} \ . \tag{2.26}$$

The first parameter α (2.23) derived from unjacketed test is the so-called Biot-Willis coefficient (Biot and Willis, 1957), also known as Biot's effective stress coefficient (Nur and Byerlee, 1971). It dominates the proportion of fluid pressure which produces the same strains as the total stress. The second parameter M (2.26) is fluid storage modulus which is a measure of constrained storage capacity (Wang, 2000).

Undrained compressibility test

Let us now explore the physical meaning of Biot's parameter λ, though it has already been expressed in terms of other defined quantities (eq. 2.19). This requires one more so-called undrained compressibility test (Gassmann, 1951). In this experiment, a saturated sample is jacketed and no fluid is allowed to escape from the medium. This implies zero incremental fluid content

$$\xi = 0 \ . \tag{2.27}$$

The sample is subjected to static compression P_e such that the induced pore

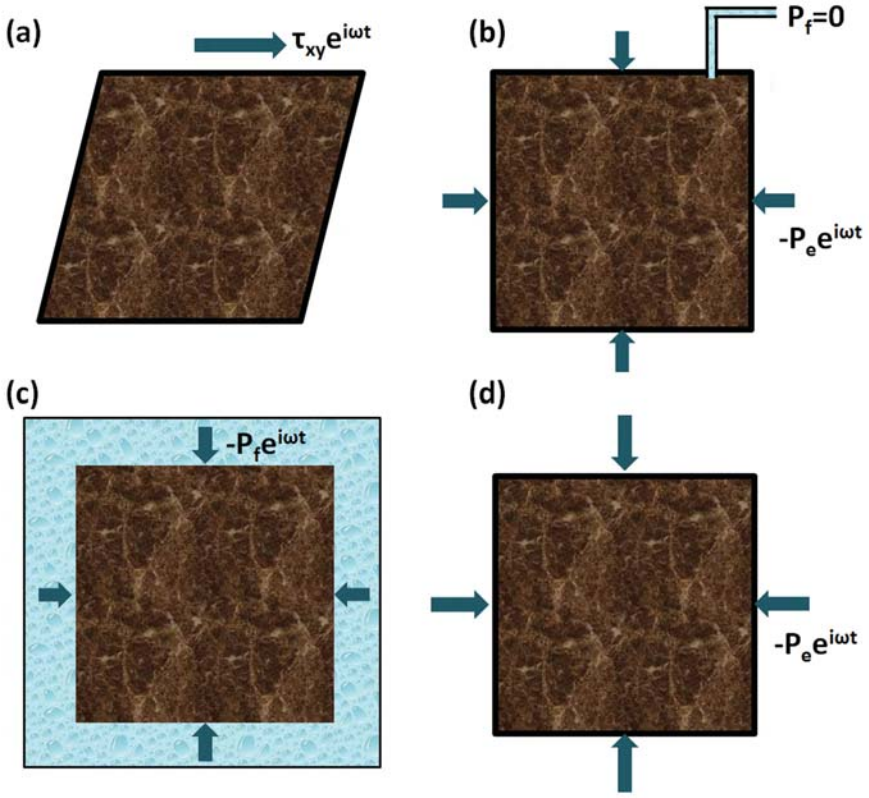

Figure 2.1: Gedanken experiments for determining 4 Biot's poroelastic constants and Gassmann equation: (a) pure shear test; (b) jacketed compressibility test; (c) unjacketed compressibility test; (c) undrained compressibility test.

pressure is equilibrated within a compression cycle. With the dilatation being measured, the undrained bulk modulus of the closed system can be obtained

$$K_{\mathrm{ud}} = -\frac{P_{\mathrm{e}}}{e} = \frac{1}{3}\frac{\tau_{ll}}{e} \ . \tag{2.28}$$

Because the fluid does not contribute to the shear modulus, it leads to

$$\mu_{\mathrm{ud}} = \mu \ . \tag{2.29}$$

Applying equations 2.27, 2.28, 2.29 to equation 2.14, one immediately find

$$\lambda = K_{\mathrm{ud}} - \frac{2}{3}\mu_{\mathrm{ud}} \ . \tag{2.30}$$

It is clear now that parameter λ is identical to the undrained Lamé coefficient. Lastly, equations 2.19 and 2.30 together yields the Gassmann's equation

$$K_{\text{ud}} = K_0 + \alpha^2 M \ , \tag{2.31}$$

which is expressed in terms of Biot's parameters. Gassmann obtained his results directly by considering elementary elasticity without employing α and M. Alternative forms and extensions of Gassmann's equation can be found in Mavko et al., (2009). Now with all Biot's parameters being defined and expressed in terms of measurable rock physics quantities, namely

$$\begin{cases} \lambda = K_0 + \alpha^2 M - \frac{2}{3}\mu \ , & \text{Undrained Lamé coefficient} \\ \alpha = 1 - \frac{K_0}{K_s} \ , & \text{Biot-Willis coefficient} \\ M = \left(\frac{\alpha - \phi}{K_s} + \frac{\phi}{K_f} \right)^{-1} . & \text{Fluid storage modulus} \end{cases} \tag{2.32}$$

one can proceed with the derivation of Biot's dynamic equations.

2.1.3 Kinetic energy

The assumption of isotropy implies that all directions are equivalent and dynamically uncoupled. Then, the kinetic energy per unit volume is expressed as

$$2E = \rho_{11} \dot{u}_i \dot{u}_i + 2\rho_{12} \dot{u}_i \dot{U}_i + \rho_{22} \dot{U}_i \dot{U}_i \ , \tag{2.33}$$

where $\rho_{11},\ \rho_{12},\ \rho_{22}$ are the mass coefficients. They render the fact that the relative fluid flow can be non-uniform and satisfy the following relations

$$\begin{aligned} &\rho_{11} + \rho_{12} = (1 - \phi)\rho_s \ , \\ &\rho_{12} + \rho_{22} = \phi \rho_f \ , \\ &\rho_{12} = -(S^\infty - 1)\phi \rho_f \ , \end{aligned} \tag{2.34}$$

where ρ_s is the grain density and S^∞ the tortuosity. The mass coefficients must obey the following inequalities to give a positive kinetic energy

$$\rho_{11} > 0,\ \rho_{22} > 0 \ ,\ \rho_{11}\rho_{22} - \rho_{12}^2 > 0 \ . \tag{2.35}$$

2.1.4 Dissipation function

Steady-state permeability

When the viscous fluid flow under an oscillatory pressure gradient $\nabla P e^{i\omega t}$ is of Poiseuille type (i.e. the Reynolds number of the flow which equals the ratio of inertial force to viscous force is less than a critical Reynolds number), the dissipation function D is defined by

$$D = \frac{1}{2}\frac{\eta}{\kappa_0}(\dot{w}_x^2 + \dot{w}_y^2 + \dot{w}_z^2) \ , \tag{2.36}$$

where the dot operator denotes the time derivative and $\eta,\ \kappa_0$ are the fluid shear viscosity and steady-state permeability. Equation 2.36 assumes that the dissipation due to relative fluid-solid motion is governed by Darcy's law. The fluid force is obtained by taking the derivative of the dissipation function with respect to the relative fluid-solid displacement

$$-\nabla p_f = \frac{\partial D}{\partial \dot{w}} = \frac{\eta}{\kappa_0}(\dot{w}_x + \dot{w}_y + \dot{w}_z) \ . \tag{2.37}$$

The result is equivalent to the steady-state Darcy's law.

Dynamic permeability

The assumption of Poiseuille flow breaks down when frequency of the oscillatory fluid flow exceed the characteristic frequency

$$\omega_d = \frac{2\eta}{\delta^2 \rho_f} \ , \tag{2.38}$$

where ρ_f is the fluid density, δ is the viscous skin depth. In this regime, the viscous skin depth δ is small compared to the characteristic pore size and the flow follows a potential flow pattern (Johnson et al., 1987). This fluid transport phenomenon can be captured by postulating a dynamic-equivalent Darcy's law which renders the permeability a frequency-dependent quantity. To account for this effect, the dynamic permeability model has been suggested by Johnson et al.

(1987)

$$\kappa(\omega) = \kappa_0 \left(\sqrt{1 + i\frac{J}{2}\frac{\omega}{\omega_c}} + i\frac{\omega}{\omega_c} \right)^{-1} , \tag{2.39}$$

where J is a shape factor which is often set to unity. The crossover frequency ω_c which separates the viscosity and inertia-dominated regimes is

$$\omega_c = \frac{\phi\eta}{\kappa_0 \rho_f S^\infty} , \tag{2.40}$$

where ρ_f is the fluid density. The replacement of the steady-state permeability κ_0 in equations 2.36 and 2.37 with formula 2.39 yield respectively the high-frequency-corrected dissipation function

$$\hat{D} = \frac{1}{2}\frac{\eta}{\kappa(\omega)}\dot{\mathbf{w}}^2 , \tag{2.41}$$

and dynamic-equivalent Darcy's law

$$-\nabla p_f = \frac{\eta}{\kappa(\omega)}\dot{\mathbf{w}} . \tag{2.42}$$

Alternatively, equation 2.42 can be represented by

$$-\nabla p_f = S(\omega)\frac{\rho_f}{\phi}\ddot{\mathbf{w}} , \tag{2.43}$$

where $S(\omega)$ is the so-called dynamic tortuosity. The relation between dynamic permeability and dynamic tortuosity is clear from equations 2.42, 2.44 that

$$S(\omega) = -\frac{i\eta\phi}{\kappa(\omega)\omega\rho_f} . \tag{2.44}$$

Depending on the circumstances, it is convenient to describe the linear responses of the system in terms of either $\kappa(\omega)$ or $S(\omega)$ (Johnston et al., 1994). More details of dynamic permeability and its application can be found in Appendix E. The inertial effect when the viscous skin depth decreases is also considered by Biot (1956b) who modelled porous media as an ensemble of cylindrical ducts.

2.1.5 Equations of motion

Upon the establishment of potential energy 2.12, kinetic energy 2.33 and dissipated energy 2.41, the equations of motion can now be obtained from the Euler-

Lagrange equation which is derived from Hamilton's principle of least action (Achenbach, 1984)

$$\frac{\partial}{\partial t}\left(\frac{\partial L}{\partial \dot{q}}\right) + \frac{\partial \hat{D}}{\partial \dot{q}} = \frac{\partial L}{\partial q} \ , \tag{2.45}$$

where the volumetric Lagrangian density is defined as

$$L \equiv E - V. \tag{2.46}$$

The generalized coordinate q is characterized by the displacements associated with solid u and fluid U. Treating the solid and fluid on an equal footing by executing equation 2.45 with respect to $q = u$ and $q = U$ lead

$$\begin{aligned} \hat{\rho}_{11}\ddot{\mathbf{u}} + \hat{\rho}_{12}\ddot{\mathbf{U}} &= P\nabla(\nabla \cdot \mathbf{u}) + Q\nabla(\nabla \cdot \mathbf{U}) - \mu\nabla \times \nabla \times \mathbf{u} \ , \\ \hat{\rho}_{12}\ddot{\mathbf{u}} + \hat{\rho}_{22}\ddot{\mathbf{U}} &= Q\nabla(\nabla \cdot \mathbf{u}) + R\nabla(\nabla \cdot \mathbf{U}) \ , \end{aligned} \tag{2.47}$$

which are coupled equations of motion. The definition of the notations are as follows

$$\begin{aligned} P &= \lambda + 2\mu + (\phi^2 - 2\alpha\phi)M \ , \\ Q &= (\alpha - \phi)\phi M \ , \\ R &= \phi^2 M \ . \end{aligned} \tag{2.48}$$

Dynamic mass coefficients are introduced in equations 2.47. They incorporate the dissipation terms and satisfy the following relations

$$\begin{aligned} \hat{\rho}_{11} + \hat{\rho}_{12} &= (1 - \phi)\rho_s \ , \\ \hat{\rho}_{12} + \hat{\rho}_{22} &= \phi\rho_f \ , \\ \hat{\rho}_{12} &= -(S(\omega) - 1)\phi\rho_f \ , \end{aligned} \tag{2.49}$$

Applying the dynamic tortuosity 2.44 in conjunction with dynamic permeability 2.39 in above mass coefficients results in their explicit forms

$$\begin{aligned} \hat{\rho}_{11} &= \rho_{11} - \frac{i\beta F}{\omega} \ , \\ \hat{\rho}_{12} &= \rho_{12} + \frac{i\beta F}{\omega} \ , \\ \hat{\rho}_{22} &= \rho_{22} - \frac{i\beta F}{\omega} \ . \end{aligned} \tag{2.50}$$

The steady-state Darcy's coefficient β and frequency correction factor F are defined as

$$\beta = \frac{\eta\phi^2}{\kappa_0} \ , \quad F = \sqrt{1 + i\frac{J}{2}\frac{\omega}{\omega_c}} \ . \tag{2.51}$$

2.1.6 Solutions of wave equations

In the case of isotropy, dilatational waves are uncoupled from the rotational waves. In order to obtain the independent wave equations, scalar and vector valued displacement potentials are introduced in following fashion

$$\begin{pmatrix} \mathbf{u} \\ \mathbf{U} \end{pmatrix} = \begin{pmatrix} \nabla\Phi_1 \\ \nabla\Phi_2 \end{pmatrix} + \begin{pmatrix} \nabla \times \Psi_1 \\ \nabla \times \Psi_2 \end{pmatrix} \ . \tag{2.52}$$

Decomposition of dilatational wave and shear wave can be carried out by introducing the irrotational $\nabla\mathbf{\Phi}$ and isovolumetric $\nabla \times \mathbf{\Psi}$ fields into the coupled wave equations 2.47, respectively.

Dilatational waves

Introducing the scalar potential $\mathbf{\Phi} = (\Phi_1, \Phi_2)^T$ in the motion equation 2.47 yields a set of differential equations as the following

$$\begin{pmatrix} P & Q \\ Q & R \end{pmatrix} \nabla^2\mathbf{\Phi} = \begin{pmatrix} \hat{\rho}_{11} & \hat{\rho}_{12} \\ \hat{\rho}_{12} & \hat{\rho}_{22} \end{pmatrix} \ddot{\mathbf{\Phi}}. \tag{2.53}$$

Considering plane wave solutions for P-wave propagating along x direction

$$\Phi_j = \hat{\Phi}_j \exp(i(\omega t - kx)) \ , \ j = 1, 2 \ , \tag{2.54}$$

where $\hat{\Phi}_j$ are the amplitudes, k is the complex wavenumber and ω is the angular frequency. Substituting 2.54 into 2.53 lead

$$\begin{pmatrix} Pk^2 - \hat{\rho}_{11}\omega^2 & Qk^2 - \hat{\rho}_{12}\omega^2 \\ Qk^2 - \hat{\rho}_{12}\omega^2 & Rk^2 - \hat{\rho}_{22}\omega^2 \end{pmatrix} \begin{pmatrix} \Phi_1 \\ \Phi_2 \end{pmatrix} = 0. \tag{2.55}$$

For the above homogeneous linear system having non-trivial solution, the determinant of the coefficient matrix must be zero. This results in a dispersion relation

which is a quadratic equation of $\zeta = \omega^2/k^2$

$$(\hat{\rho}_{11}\hat{\rho}_{22} - \hat{\rho}_{11}^2)\zeta^2 - (P\hat{\rho}_{22} + R\hat{\rho}_{11} - 2Q\hat{\rho}_{12})\zeta + (PR - Q^2). \tag{2.56}$$

Two physical solutions can be obtained for the complex velocity square

$$\hat{V}^2 = \zeta = \frac{\Delta \pm \sqrt{\Delta^2 - 4(\hat{\rho}_{11}\hat{\rho}_{22} - \hat{\rho}_{11}^2)(PR - Q^2)}}{2(\hat{\rho}_{11}\hat{\rho}_{22} - \hat{\rho}_{11}^2)}\ , \tag{2.57}$$

where $\Delta = P\hat{\rho}_{22} + R\hat{\rho}_{11} - 2Q\hat{\rho}_{12}$. In accordance with the plane wave ansatz 2.54, a positive attenuation coefficient requires $\mathrm{Im}\{\mathrm{k}\} < 0$. This further shows that only two solutions for the complex wavenumber exist. They correspond to two dilatational wave modes in saturated porous media. It is easy to show from 2.55 that the amplitudes of the solid and fluid are coupled in following fashion

$$\frac{\hat{\Phi}_2}{\hat{\Phi}_1} = \frac{\hat{\rho}_{11}\omega^2 - Pk^2}{Qk^2 - \hat{\rho}_{12}\omega^2} = \frac{\hat{\rho}_{12}\omega^2 - Qk^2}{Rk^2 - \hat{\rho}_{22}\omega^2}. \tag{2.58}$$

The orthogonality relation (Biot, 1956a) for the wave amplitudes shows that the amplitudes for one wave mode is in phase whereas for another is out of phase. The former corresponds to the fast P-wave mode and the latter is the slow P-wave mode. The terminology fast/slow derives from their corresponding phase velocities. The phase velocities and attenuation coefficients for the two P-wave modes can be calculated via

$$V_{\mathrm{fast,slow}} = \frac{\omega}{\mathrm{Re}\{\mathrm{k}_{\mathrm{fast,slow}}\}}\ ,\ \gamma = \mathrm{Im}\{\mathrm{k}_{\mathrm{fast,slow}}\}. \tag{2.59}$$

An numerical example is given in Figure 2.2 for a unconsolidated sandstone, the fast wave exhibits little dispersion and attenuation over several decades of frequency. On the other hand, the slow wave is highly dispersive at low frequency and only becomes propagatory at high frequency. The phase velocity of the latter is much slower than the former. Beyond theoretical prediction of Biot (1956a,b, 1962), Plona (1980) experimentally confirmed the existence of the two P-wave modes in saturated porous solids.

Rotational wave

Introducing the vector potential $\mathbf{\Psi} = (\Psi_1, \Psi_2)^T$ in the motion equations 2.47 yields a set of differential equations of the form

$$\begin{pmatrix} \mu & 0 \\ 0 & 0 \end{pmatrix} \nabla^2 \mathbf{\Psi} = \begin{pmatrix} \hat{\rho}_{11} & \hat{\rho}_{12} \\ \hat{\rho}_{12} & \hat{\rho}_{22} \end{pmatrix} \ddot{\mathbf{\Psi}} \tag{2.60}$$

A plane wave ansatz for the rotational wave mode leads

$$\begin{pmatrix} \mu k^2 - \hat{\rho}_{11}\omega^2 & -\hat{\rho}_{12}\omega^2 \\ -\hat{\rho}_{12}\omega^2 & -\hat{\rho}_{22}\omega^2 \end{pmatrix} \begin{pmatrix} \Psi_1 \\ \Psi_2 \end{pmatrix} = 0. \tag{2.61}$$

The dispersion relation for the rotational mode is therefore

$$(\hat{\rho}_{11}\hat{\rho}_{22} - \hat{\rho}_{11}^2)V_s^2 - \mu\hat{\rho}_{22} = 0. \tag{2.62}$$

Only one physical solution to the dispersion relation exists. It corresponds to the only rotational wave mode in Biot's theory. Appying the dynamic mass coefficients 2.49 in equation 2.62, the resulting shear velocity reads

$$V_{\text{shear}} = \left(\frac{\mu}{((1-\phi)\rho_s + (1 - \frac{1}{S(\omega)}))\phi\rho_f} \right)^{\frac{1}{2}}. \tag{2.63}$$

According to equation 2.61, the fluid to solid amplitude ratio for rotational mode is given by

$$\frac{\hat{\Psi}_2}{\hat{\Psi}_1} = -\frac{\hat{\rho}_{12}}{\hat{\rho}_{22}}. \tag{2.64}$$

Because the acceleration of the fluid must be opposed to that of solid (Biot, 1956a), the coupling mass coefficient $\hat{\rho}_{12}$ is always negative. Accordingly from equation 2.49, $\hat{\rho}_{22}$ is obvious positive. Therefore, the shear motion of the solid and fluid is in phase as pointed out from equation 2.64. Sahay (2008) showed that on top of the in-phase shear mode, there exists another out-of-phase shear mode in porous media saturated by a Newtonian fluid.

2.2 Viscosity-extended Biot framework

The viscosity-extended Biot (VEB) framework (Sahay, 2008) refers to a modification of Biot's original theory. The modification consists of incorporating the

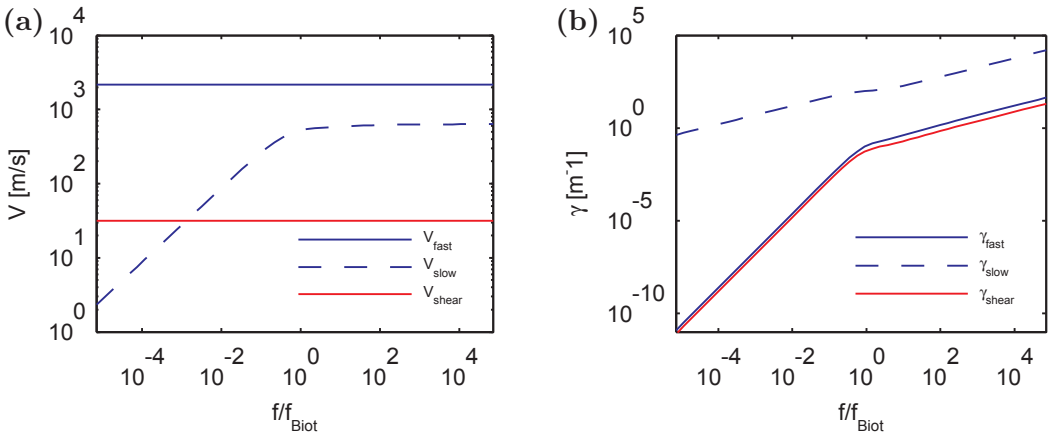

Figure 2.2: An example of (a) dispersion and (b) attenuation coefficient for three wave modes in a water-saturated unconsolidated sandstone.

viscous stress terms in the fluid stress tensor, i.e., equation 2.1. This means that the strain rate terms and thus the fluid bulk and shear viscosities enter the constitutive relations. A feature of VEB framework is that it renders the constitutive relation of a Newtonian fluid if the porosity is unity. A further consequence is that the VEB framework entails a slow shear wave in addition to the fast shear wave appearing in Biot's theory. This slow shear wave can be thought of as the out-of-phase shearing motion. It plays therefore a similar role as the Biot slow compressional wave that represents the out-of-phase compressional motion. The nature of the out-of-phase shear motion is characterized by the Biot's relaxation frequency 2.38. When $\omega \ll \omega_c$, the slow shear wave is governed by following diffusion operator with a damping term

$$\frac{\partial}{\partial t} + \frac{\omega_c}{d_\mathrm{f} S^\infty} = \frac{D_\nu}{S^\infty} \nabla^2 \tag{2.65}$$

where the kinematic viscosity is $D_\nu = \eta/\rho_\mathrm{f}$. The damping term is $\omega_c/(d_\mathrm{f} S^\infty)$ with $d_\mathrm{f} = (S^\infty - m_\mathrm{f})^{-1}$ and m_f the fluid mass fraction. In the regime $\omega \gg \omega_c$ the damping term vanishes and the slow shear wave is an ordinary diffusion wave with diffusivity D_ν/S^∞. Mode conversion into slow shear wave in certain case represents an efficient dissipation mechanism. For example, when shear wave propagating through an air-water interface, neglecting the slow shear mode (i.e., using the classical Biot's theory) can result in underestimation of the reflected S-wave amplitude (Sahay, 2008). Moreover, the dynamic permeability 2.39 can be modelled as conversion scattering process from Biot slow P-wave into slow shear wave (Müller and Sahay, 2011a,b). An application of VEB framework in

modelling dynamic permeability is given in Appendix E.

2.3 Alternative formulation of Biot's theory

In certain cases, it is more convenient to express the relative fluid-solid displacement **w** instead of the fluid displacement **U** in Biot's equations. To reformulate the equations of motion, we now redefine the kinetic energy as (Bourbié et al., 1987)

$$2C = \rho_b \dot{u}_i \dot{u}_i + 2\rho_f \dot{u}_i \dot{w}_i + \frac{\rho_f S^\infty}{\phi} \dot{w}_i \dot{w}_i \ , \tag{2.66}$$

where the bulk density ρ_b is given by

$$\rho_b = (1-\phi)\rho_s + \phi\rho_f. \tag{2.67}$$

Execution of the Lagrange equation 2.45 with the newly defined kinetic energy 2.66 lead to following equation of motion

$$\tau_{ij,j} = \rho_b \ddot{u}_i + \rho_f \ddot{w}_i \ , \tag{2.68}$$

$$-p_{f,i} = \rho_f \ddot{u}_i + \frac{\rho_f S^\infty}{\phi} \ddot{w}_i + \frac{\eta}{\kappa(\omega)} \dot{w}_i \ . \tag{2.69}$$

2.4 Quasi-static approximation of Biot's theory

Considering low frequency regime where

$$\omega \ll \omega_c = \frac{\phi\eta}{\kappa_0 \rho_f S^\infty} \ , \tag{2.70}$$

the acceleration terms $\ddot{u}$, $\ddot{w}$ are negligibly small in comparison with the velocity term $\dot{w}_i$. Meanwhile, the dynamic permeability is taken on a character of steady-state permeability. Dropping the acceleration terms and replacing $\kappa(\omega)$ with κ_0 in 2.68 yields the quasi-static formulation of Biot's poroelasticity

$$\tau_{ij,j} = 0 \ , \tag{2.71}$$

$$-p_{f,i} = \frac{\eta}{\kappa_0} \dot{w}_i \ . \tag{2.72}$$

Formulae 2.71, 2.72 represent the equation of equilibrium and Darcy's law, respectively. The combined sets are also known as the Biot's consolidation equations

(Biot, 1941). In conjunction with the stress strain relation 2.14, 2.15, one can derive a diffusion equation from the consolidation equations

$$D_p \nabla^2 p_f = \dot{p}_f \ , \tag{2.73}$$

where D_p is the hydraulic diffusivity (Chandler and Johnson, 1981)

$$D_p = \frac{k_0}{\eta \phi^2} \frac{PR - Q^2}{P + 2Q + R}. \tag{2.74}$$

The diffusion equation can also be formulated in terms of the relative fluid-solid displacement $\mathbf{w}$. This indicates that the out-of-phase movement ($\mathbf{w} \neq 0$) which is associated with Biot slow wave obeys diffusion (Chandler and Johnson, 1981; Bourbié et al., 1987).

2.5 Poroelastic boundary conditions

2.5.1 Open-pore boundary condition

Based on the assumption of the existence of perfect contact between the contiguous media, the standard boundary condition of Deresiewicz and Skalak (1963) or so-called open pore boundary condition can be established. Such boundary condition is derived based on conservation of total energy and proved by Bourbie et al (1987) using Hamilton's principle. In the space-frequency domain, the continuity of energy flux at the interface of two porous media requires

$$\langle i\omega(\sigma_{ij} u_i + \sigma \delta_{ij} U_i) n_j \rangle = 0, \tag{2.75}$$

where $\sigma \delta_{ij} = -\phi p_{\mathrm{f}} \delta_{ij}$ is the fluid stress, $\sigma_{ij} = \tau_{ij} - \sigma \delta_{ij}$ is the solid stress, n_j denotes the unit normal of the interface between the two dissimilar porous media, the angle bracket calculates the difference of the quantity between the two media. The individual continuity for each term in equation 2.75 is implicitly assumed (Sahay, 2012)

$$\langle T_i u_i \rangle = 0, \tag{2.76}$$

$$\langle \sigma U_n \rangle = 0, \tag{2.77}$$

where $T_i = \sigma_{ij} n_j$ is the traction of the solid phase, $U_n = U_i n_j \delta_{ij}$ is the normal component of the fluid displacement. Therefore, conditions 2.76, 2.77 correspond to the energy flux continuity of the solid phase and fluid phase respectively. Accordingly, each of the constituents in 2.76, 2.77 is required to be continuous across the interface

$$\langle T_i^{\mathrm{s}} \rangle = 0, \tag{2.78}$$

$$\langle u_i \rangle = 0, \tag{2.79}$$

$$\langle U_n \rangle = 0, \tag{2.80}$$

$$\langle \sigma \rangle = 0. \tag{2.81}$$

By considering conservation of fluid mass at the interface, the quantity of $i\omega w_n = i\omega\phi(U_n - u_n)$ is required to be continuous. In order to be compatible with 2.78, it demands the contintuity of porosity ϕ or no flow $(U_i - u_i)n_i = 0$ at the interface as subjoined condition. Therefore, by replacing the fluid component U_i with $\frac{w_i}{\phi} + u_i$, equation 2.75 can be rewritten as

$$\langle i\omega(T_i u_n - p_{\mathrm{f}} w_n) \rangle = 0, \tag{2.82}$$

where $T_i = \tau_{ij} n_j$ is the total traction. Similarly, the continuity of each quantity requires

$$\langle T_i \rangle = 0, \tag{2.83}$$

$$\langle u_i \rangle = 0, \tag{2.84}$$

$$\langle w_n \rangle = 0, \tag{2.85}$$

$$\langle p_{\mathrm{f}} \rangle = 0. \tag{2.86}$$

The last boundary condition is so-called open-pore boundary condition which indicates a perfect hydraulic contact across poroelastic interface.

2.5.2 Partially open boundary condition

The physical model depicted by the open pore boundary condition assumes that the pores of the two media are completely connected. However, this situation is by no means unique. Non-alignment of a portion of the pores can produce an interfacial flow area which is smaller than that in either medium adjacent to the interface. This effect might be accomplished physically by inserting a porous

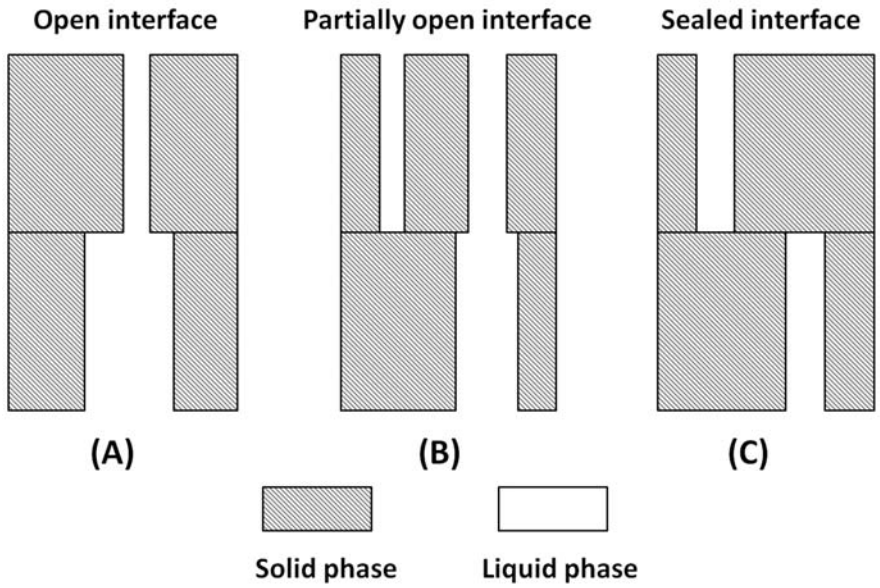

Figure 2.3: Simplified diagram of an interface between two porous media (after Bourbié et al, 1987).

membrane between the two media. Thus, flow through such an interface would result in a pressure drop across the interface (Deresiewicz and Skalak, 1963)

$$p_{\mathrm{fa}} - p_{\mathrm{fb}} = Z_I \dot{w}_{\mathrm{n}}, \tag{2.87}$$

where Z_I is interfacial impedance and $\dot{w}_{\mathrm{n}} = \dot{w}_i n_i$ is the normal component of relative velocity. For perfect hydraulic contact, β equals zero and the boundary condition 2.87 recovers the standard open-pore boundary condition 2.86. When Z_I goes to infinite large, it is equivalent of inserting an impermeable membrane between the two saturated media. This situation refers to the no-flow boundary, or closed pore boundary condition. In order to apply the partially open or closed interface condition in the context of Biot's theory, the physical meaning of the resistance coefficient should be determined. The initial interpretation of the resistance coefficient is given by Deresiewicz and Skalak (1963) as a proxy for pore mis-alignment. For example, the interfacial impedance can be applied in simulating mud-cake effect for acoustic wave travelling inside borehole (Rosenbaum, 1974). An end-member value of $Z_I = \infty$ indicates a total blockage of borehole surface whereas $Z_I = 0$ represents open-pore borehole condition.

2.6 Acoustics in partially saturated porous media

The velocity dispersion and attenuation in rock fully saturated with a single fluid can be satisfactorily described by Biot's theory. However, it is generally accepted that Biot's theory cannot adequately interpret observed magnitudes of attenuation and dispersion in the low frequency regime (Johnston et al., 1979; Winkler, 1985; Gist, 1994). On the other hand, for partially saturated rocks, depending on the compressibility contrast and distribution of the pore fluids, it can result in significant attenuation and velocity dispersion across a wide range of frequency. There are number of different approaches for modelling attenuation and dispersion due to presence of multiphase pore fluids. Each approach emphasizes a particular physical aspect and can be summarized into the following five categories (Johnston et al., 1979; Mavko et al.,2009; Müller et al., 2010):

1. **Mesoscale distribution of immiscible fluids**

   These models consider fluid heterogeneities scale greater than the pore scale but less than wavelength. An elastic wave induces pressure relaxation between mesoscopic fluid heterogeneities and gives rise to attenuation and dispersion. The fluid inhomogeneities are often modeled in fashion of periodic or random distribution (White et al., 1975; Johnson, 2001; Pride et al., 2004; Müller et al., 2004; Toms et al., 2007a). Mesoscopic fluid flow also known as patchy saturation provides explanation for acoustic signatures in exploration frequency band (Müller et al., 2010).

2. **Porescale distribution of immiscible fluids**

   These models are often referred as local or squirt flow models. Attenuation and velocity dispersion arise due to wave-induced pressure relaxation between liquid-filled compliant cracks and surrounding stiff pores which can be partially saturated (Murphy et al., 1986; Mavko and Nolen-Hoeksema, 1994; Gurevich et al., 2009). Squirt flow mechanism is often important for encountered attenuation at ultrasoinc frequencies (Mavko et al., 2009).

3. **Gas bubble oscillation**

   This class of models consider presence of gas bubbles at pore or larger scale. Attenuation rises when wave-induced bubble oscillations occur and result in viscous and thermal damping (Bedford and Stern, 1983; Lopatnikov and

Gorbachev, 1987; Smeulders and van Dongen, 1997). On the other hand, porescale gas bubble effectively reduce the fluid bulk modulus and further enhance other dissipation mechanisms (Johnston et al., 1979).

4. Multi-fluid-phase Biot models

There exists a class of models describing the acoustics in porous rocks saturated with two immiscible fluids wherein capillary pressure is incorporated using a three phase (two fluids and one solid phase) extension of the Biot's poroelasticity framework (Santos et al., 1990; Tuncay and Corapcioglu, 1997; Lo et al., 2005). Therein a second slow P-wave is reported and attenuation is caused by joint effects of capillary pressure and inertial coupling (Lo et al., 2005).

5. Models based on viscoelastic rheology

These models intend to capture the attenuation and dispersion resulting from wave-induced pressure relaxation phenomenon with relaxation behaviour of viscoelastic material (Mavko et al., 2009; Picotti et al., 2010). The fluid-related attenuation is thought to obey Standard linear solid (SLS) model and the dynamic undrained moduli is bounded by physics-based relaxed and unrelaxed moduli (Dvorkin and Mavko, 2009). These models are useful in applications of seismic modelling.

Beyond the listed mechanisms which focus on the fluid effects, there also exists a class of models which emphasize the effects of the fractures on velocity and attenuation (Hudson et al., 1996, 2001; Chapman, 2003). Among all the mechanisms, this thesis particularly focuses on mesoscopic flow with respect to partial saturation. Two types of patchy saturation models which are frequently applied for interpreting acoustic signatures in partially saturated rocks will be reviewed.

2.6.1 Periodic model

Four decades ago, J. E. White and co-authors published two important papers (White, 1975; White et al., 1975) on two theoretical models which provide predictions for the attenuation and dispersion of compressional seismic waves in brine saturated rocks containing mesoscopic gas heterogeneities. The first model of White (White, 1975) considers periodic, gas-filled regions in brine saturated porous rock. The second model (White et al., 1975) considers a stack of sedimentary layers alternatively saturated by water and gas. The representative

elementary volume (REV) of both models are considered larger than the pores but smaller than the wavelength. Therefore, the fluid heterogeneities are considered as mesoscopic. It is discovered that for certain sizes of the gas pocket and layering, the resulting P-wave attenuation and dispersion can be significant at seismic frequencies. Since then, wave-induced pressure diffusion at mesoscale is considered as one important candidate for seismic attenuation under the earth. A thorough review of White's layered model with my extension will be introduced in Chapter 3. Here, the review of the White's spherical patchy saturation model is given.

The original patchy saturation theory of White (White, 1975) includes a number of approximations such as ignoring the motion of the solid and assuming a frequency-independent pressure discontinuity across the liquid-gas interface (Dutta and Seriff, 1979). Dutta and Odé (1979) carried out a more systematic derivation based on Biot's equations and correct the approximated solutions of White (1975). However, the approach of Dutta and Odé can lead to significant loss of numerical accuracy due to the ill-conditioned nature of the coefficient matrix. Johnson (2001) showed that the boundary value problem of White (1975) and Dutta and Odé (1979) can be solved within the context of quasi-static Biot's poroelasticity (see eqs 2.71, 2.72) as long as the frequency of interest is below the Biot's relaxation frequency (see eq 2.40). More recently, Vogelaar et al. (2009) obtained the exact analytical solutions for the spherical White's model using quasi-static Biot's equations.

The set-up of the problem is essentially an upscaling procedure of Biot's dynamic equations with respect to a mesoscopic geometry configuration. Considering a partially saturated rock, the gas filled regions are spherical and all of the same radius a. The gas pockets are positioned periodically in an uniform cubic lattice. A unit cell of this configuration consists of a single sphere at the centre of a cube of half side-length b'. The cubic cell is further approximated by a sphere with radius b such that the new unit sphere has the same volume with the unit cube. This approximation ensures the unchanged gas saturation $S_g = (a/b)^3$ and further facilitates the mathematical treatment. Further assumptions are made as follows:

- Radius of gas pocket a is larger than typical pore sizes.

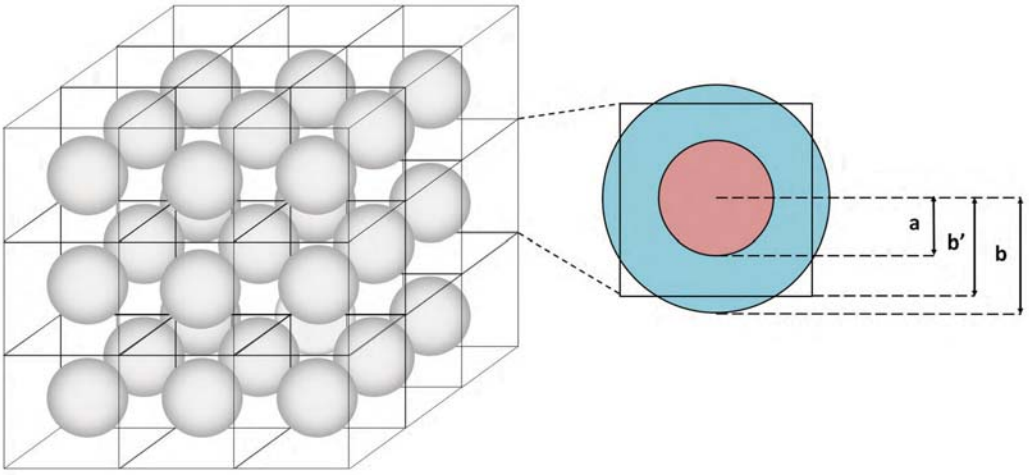

Figure 2.4: White's model of regularly distributed spherical gas pockets of uniform size. A spherical unit cell is equivalent in volume to a cubical unit cell containing a gas pocket.

- Unit cell is subjected to periodic or sealed boundary condition such that no exchange of fluid pressure between the cells.
- Wavelength is much longer than the dimension b' so that the partially saturated rock appears to be macroscopically isotropic and homogeneous.
- External pressure field $P_{\mathrm{e}} \exp(i\omega t)$ which applies on the unit cell is considered as spatially homogeneous.

Under all above assumptions, the resulting complex bulk modulus of the entire medium coincides with the effective bulk modulus of mesoscopic unit cell. The effective undrained bulk modulus is defined by the ratio between the applied stress and the fractional volume change $\Delta V/V$ of the unit cell, thereby

$$K_{\mathrm{ud}}(\omega) = -\frac{-P_{\mathrm{e}}}{\Delta V/V} = -\frac{1}{3}\frac{b}{u_b(b)}P_{\mathrm{e}}, \tag{2.88}$$

where $u_b(b)$ is the resulting solid displacement at the outer surface of the unit sphere. To highlight the fluid effect, the rock frame can be considered as homogeneous. Thus, the undrained shear modulus is the same with the drained shear modulus $\mu_{\mathrm{ud}} = \mu_0$. However, the assumption of a homogeneous rock frame is not essential in the mathematical formulation.

The starting equations for describing coupled motion of solid and fluid in the

unit cell follows quasi-static Biot's poroelasticity. In conjunction with a set of well-defined boundary conditions, solution of interest 2.88 can be obtained. The quasi-static Biot's equations under symmetrically spherical coordinate is given by (Johnson, 2001)

$$\frac{\partial}{\partial r}\left[(P+Q)\left(\frac{\partial u}{\partial r}+\frac{2u}{r}\right)+(Q+R)\left(\frac{\partial U}{\partial r}+\frac{2U}{r}\right)\right]=0\ ,$$
$$i\omega\phi(U-u)=\frac{\kappa_0}{\eta\phi}\frac{\partial}{\partial r}\left[Q\left(\frac{\partial u}{\partial r}+\frac{2u}{r}\right)+R\left(\frac{\partial U}{\partial r}+\frac{2U}{r}\right)\right]\ , \tag{2.89}$$

where r denotes the radial distance and $u,\ U$ are the radial displacements of the solid and fluid, respectively. The general solutions to equations 2.89 can be written as (Johnson, 2001)

$$u(r)=Ar+BR^{-2}+(Q+R)[Fj_1(k_2r)+Gn_1(k_2r)]\ , \tag{2.90}$$
$$U(r)=Ar+BR^{-2}-(P+Q)[Fj_1(k_2r)+Gn_1(k_2r)]\ , \tag{2.91}$$
$$p_f(r)=-\frac{3(Q+R)}{\phi}A+\frac{(PR-Q^2)}{\phi}k_2[Fj_0(k_2r)+Gn_0(k_2r)]\ , \tag{2.92}$$
$$\tau(r)=3K_{\mathrm{BG}}A-4\mu r^{-3}B-\frac{4\mu(Q+R)}{r}[Fj_1(k_2r)+Gn_1(k_2r)]\ , \tag{2.93}$$

where $j_i,\ n_i$ are the spherical Bessel functions of order i. The slow P-wavenumber is $k_2=\sqrt{i\omega/D_p}$, where the hydraulic diffusivity is shown in equation 2.74. $A,\ B,\ F,\ G$ are arbitrary constants yet to be determined from the following boundary conditions

$$u_a(a)=u_b(a)\ , \tag{2.94}$$
$$U_a(a)=U_b(a)\ , \tag{2.95}$$
$$p_{fa}(a)=p_{fb}(a)\ , \tag{2.96}$$
$$\tau_a(a)=\tau_b(a)\ , \tag{2.97}$$
$$u_b(b)=U_b(b)\ , \tag{2.98}$$
$$\tau_b(b)=-P_{\mathrm{e}}\ . \tag{2.99}$$

The first four boundary conditions (BC) designate the open-pore interface conditions of Deresiewicz and Skalak (1963), see section 2.5. The fifth and sixth BCs refer to the no-flow condition and continuity of stress at the outer surface of the unit cell, respectively. The requirement that the particular solution be finite at $r=0$ implies $B_a=G_a=0$. The remaining six unknown constants,

namely $A_a,\ A_b,\ B_b,\ F_a,\ F_b,\ G_b$ can be solved from the six boundary conditions analytically (Vogelaar et al., 2009). The resulting expression for the undrained P-wave modulus, after a lot of algebra, can be written as (Vogelaar et al., 2009)

$$
\begin{aligned}
H_{\mathrm{ud}}(\omega) &= \frac{K_{\mathrm{BG}b} + \frac{4}{3}\mu}{1-g} \ , \\
g &= s_a \left(1 - \frac{H_a}{H_b} + \frac{3X^2}{P_b R_b - Q_b^2} \frac{f_1}{f_0} \frac{1}{k_{2b} a} \frac{1}{1-h} \right) \ , \\
f_l &= j_l(k_{2b} a) - n_l(k_{2b} a) \frac{j_1(k_{2b} b)}{n_1(k_{2b} b)} \ , \ l = 1, 2., \\
X &= (R_b + Q_b) - (R_a + Q_a) \frac{H_b}{H_a} \ .
\end{aligned} \tag{2.100}
$$

The P-wave phase velocity and attenuation can be calculated by (Carcione et al., 2006)

$$
v_p = \left[\mathrm{Re} \left(\frac{1}{\hat{\mathrm{v}}} \right) \right]^{-1} \ , \tag{2.101}
$$

$$
Q = \frac{\mathrm{Im}(\hat{\mathrm{v}}^2)}{\mathrm{Re}(\hat{\mathrm{v}}^2)} \ . \tag{2.102}
$$

The complex velocity is defined by the relation $\bar{\rho} v^2 = H_{\mathrm{ud}}$. The averaged density is $\bar{\rho} = (1-\phi)\rho_s + \phi S_w \rho_{fw} + \phi S_g \rho_{fg}$, where $\rho_{fw},\ \rho_{fg}$ are the densities of liquid and gas, respectively. The White's spherical model given by equation 2.100 is based on effective medium theory 2.88 and quasi-static Biot's equations 2.89. Therefore, two assumptions must be made before its application:

- Angular frequency ω of propagating wave must be much smaller than resonant frequency of scattering $\omega_s = 2\pi \sqrt{H_{\mathrm{BG}} / \bar{\rho} b^2}$ such that the effective medium theory is applicable.

- Angular frequency ω of propagating wave must be much smaller than Biot's relaxation frequency $\omega_b = \frac{\eta \phi}{\kappa_0 \rho_f S^{\infty}}$ such that quasi-static assumption is valid.

The characteristic frequency of any mesoscopic attenuation model is defined as the frequency when the Biot slow wavelength equals the characteristic length of the inhomogeneity (Gurevich and Lopatnikov, 1995). In terms of White's spherical

model, this transition frequency is approximated by (Carcione et al., 2003)

$$f_c = \frac{D_p}{(b-a)^2}, \tag{2.103}$$

where D_p is the hydraulic diffusivity (eq 2.74). The characteristic length is consider as $b-a$ instead of b. This is because the resulting fluid pressure is different between the inner sphere and the outer shell. Hence, the relaxation distance should be the difference between the two radii (Gist, 1994; Carcione et al., 2003). There are two ways of increasing the gas saturation according to the concentric sphere configuration. The gas saturation can be either increased by increasing the radius of the inner sphere or by increasing the radius of the outer shell. Following the first approach by setting a constant radius b of the outer sphere, a critical water saturation S_{wc} corresponding to the maximum attenuation can be deduced from equation 2.103 (Carcione et al., 2003)

$$S_{wc} = 1 - \left(1 - \sqrt{\frac{D_p}{\pi f b^2}}\right)^3 . \tag{2.104}$$

On the other hand, for constant radius of inner sphere a, the critical water saturation is given by

$$S_{wc} = 1 - \left(1 - \sqrt{\frac{D_p}{\pi f a^2}}\right)^3 . \tag{2.105}$$

Within the consideration of White's model, there exists two scenarios associated with mesoscopic loss: first, presence of fluid heterogeneities at mesoscale, i.e., patchy saturation, which is the main focus. Secondly, presence of frame heterogeneities of different porosities and permeabilities. Though the numerical results of White et al. (1975) indicate that no significant attenuation and dispersion is associated with mesoscopic flow due to frame heterogeneities. It has later been pointed out that permeability fluctuation at mesoscale can indeed lead to appreciable attenuation for a wide range of frequency (Shapiro and Müller, 1999; Carcione and Picotti, 2006; Müller et al., 2007). White's spherical model has recently been extended to include Biot global flow with a so-called Biot equivalent medium approach (Kudarova et al., 2014).

2.6.2 Random model

In contrast to the patchy saturation model dealing with idealistic fluid distribution, i.e., periodic distribution, there exists a category of models considering arbitrary fluid inclusions (Johnson, 2001; Pride et al., 2004; Müller and Gurevich, 2004). Models of Johnson (2001) and Pride et al. (2004) rely on a branching function which ensures causality of the solution and convergence to low- and high-frequency limits. However, evaluation of these models for arbitrary fluid inclusions require numerical methods (Toms et al., 2007b; Masson and Pride, 2007). On the other hand, the model of Müller and Gurevich (2004) is based on statistical approach and provides explicit analytical results.

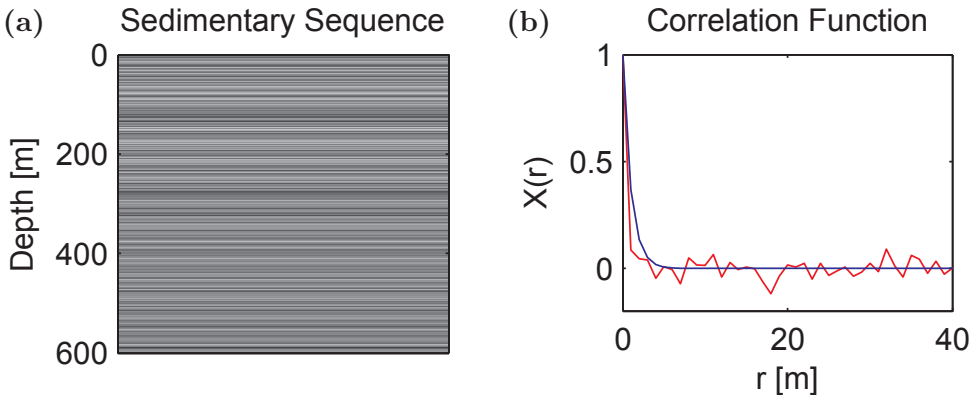

Figure 2.5: (a) An example of random sequence of partially saturated sedimentary layers. Spatial distribution of the saturation follows a exponential correlation function as shown in (b).

The patchy saturation model of Müller and Gurevich (2004) is based on the more general results of Gurevich and Lopatnikov (1995). The latter considers wave propagation in a randomly inhomogeneous porous medium whose material coefficients are random functions of position. The starting formulae of Gurevich and Lopatnikov (1995) model is low frequency Biot's equations with P-wave and 1D consideration

$$\begin{aligned} \frac{d}{dz}\left(H\frac{du}{dz}+C\frac{dw}{dz}\right)+\omega^2(\rho u+\rho_f w)=0\ , \\ \frac{d}{dz}\left(C\frac{du}{dz}+M\frac{dw}{dz}\right)+\omega^2(\rho_f u+q w)=0\ , \end{aligned} \tag{2.106}$$

where a time harmonic dependence $\mathrm{e}^{-\mathrm{i}\omega\mathrm{t}}$ is implicitly assumed and $q=i\eta/\kappa_0\omega$ is the friction coefficient. By introducing vector $\mathbf{V}=\{u,\ w,\ \tau_{zz},\ p_f\}$, where τ_{zz} is

the normal component of the total stress, the equations 2.106 can be reformulated as following first-order system

$$\frac{d\mathbf{V}}{dz} + \mathbf{P}\mathbf{V} = 0. \tag{2.107}$$

The matrix $\mathbf{P}$ is defined as

$$\mathbf{P} = \begin{pmatrix} 0 & \mathbf{E} \\ \mathbf{F} & 0 \end{pmatrix}, \tag{2.108}$$

where $\mathbf{E}$ and $\mathbf{F}$ are 2×2 matrices

$$\mathbf{E} = \begin{pmatrix} -L^{-1} & -\alpha L^{-1} \\ \alpha L^{-1} & N^{-1} \end{pmatrix}, \tag{2.109}$$

$$\mathbf{F} = \omega^2 \begin{pmatrix} \rho & \rho_f \\ -\rho_f & -q \end{pmatrix}, \tag{2.110}$$

$L = K_0 + 4/3\mu$ is the drained P-wave modulus and $N = ML/H$ where $H = L + 4/3\mu$ is the undrained P-wave modulus. Further assumptions are made that the parameters of the porous medium, namely each element in the matrix $\mathbf{P}$, fluctuate around their averaged value. If $\langle H(z) \rangle$ denotes an average value of $H(z)$ and $H'(z) = H(z) - \langle H(z) \rangle$, the coefficient matrix $\mathbf{P}$ can be decomposed as

$$\mathbf{P}(z) = \langle \mathbf{P}(z) \rangle + \mathbf{P}'(z). \tag{2.111}$$

Thus, the differential system 2.107 can be written as

$$\frac{d\mathbf{V}}{dz} + \langle \mathbf{P}(z) \rangle \mathbf{V} + \mathbf{P}'(z)\mathbf{V} = 0. \tag{2.112}$$

First, considering a homogeneous medium such that

$$\mathbf{P}'(z) \equiv 0, \ \langle \mathbf{P}(z) \rangle \equiv \mathbf{P}(z). \tag{2.113}$$

In this situation, the eigenvalues of the matrix $\mathbf{P}$ yields the wavenumbers of fast and slow P-waves for a saturated homogeneous rock. Secondly, considering a inhomogeneous medium and low frequency limit such that

$$\mathbf{P}'(z) \neq 0, \ \mathbf{P}(z) \equiv \langle \mathbf{P}(z) \rangle. \tag{2.114}$$

In this case, the eigenvalues of the matrix $\mathbf{P}$ yields wavenumbers for a effective

homogeneous medium. This is equivalent to the analysis of poroelastic Backus averaging (Gelinsky and Shapiro, 1997). Thirdly, for a inhomogeneous medium with variable coefficients under dynamic wave propagation, the corresponding wavenumbers must be solved from the ordinary differential equations 2.107. By considering the fluctuation term $\mathbf{P}'(z)$ is a stationary and ergodic random function of z, this can be achieved using so-called Bourret approximation (Karal and Keller, 1964). The latter method, which is based on perturbation theory, is an efficient tool for obtaining the effective wavenumber associated with a stochastic wave equation. Due to low frequency consideration, Gurevich and Lopatnikov (1995) further restricted their analysis to conversion scattering from fast P-wave to slow P-wave and neglected elastic scattering. The resulting effective P-wave modulus for wave travelling along z-direction of a inhomogeneous medium is given by (Gurevich and Lopatnikov, 1995; Müller and Gurevich, 2004)

$$H_{\mathrm{ud}}(\omega) = H_0 \left(1 - isk_2 \int_0^\infty \psi(\xi) \exp(ik_2\xi) d\xi\right), \tag{2.115}$$

where the effective slow P-wavenumber is given by

$$k_2 = \sqrt{i\omega} \frac{\left\langle \sqrt{\frac{\eta}{\kappa_0} N} \right\rangle}{\langle N \rangle}. \tag{2.116}$$

The normalized autocorrelation function $\psi(\xi)$ is

$$\psi(\xi) = \frac{\langle \varepsilon(z)\varepsilon(z-\xi) \rangle}{\langle \varepsilon^2(z) \rangle}, \tag{2.117}$$

The fluctuating parameter $\varepsilon(z)$ is

$$\varepsilon(z) = \frac{\alpha(z)M(z)}{H(z)} - \left\langle \frac{\alpha(z)M(z)}{H(z)} \right\rangle, \tag{2.118}$$

where the angle brackets denote ensemble averaging. The degree of inhomogeneity of the medium is characterized by

$$s = \left\langle \frac{1}{H} \right\rangle^{-1} \left(\left\langle \frac{\alpha^2 N}{L^2} \right\rangle - \left\langle \frac{\alpha}{L} \right\rangle^2 \left\langle \frac{1}{N} \right\rangle^{-1} \right). \tag{2.119}$$

Equations 2.115-2.119 provide the general results of Gurevich and Lopatnikov (1995). Müller and Gurevich (2004) further customized this model to specific

case of partial saturation. This is achieved by assuming a homogeneous rock frame and a heterogeneous fluid distribution. In this sense, the rock is alternatively saturated by water and gas layers with their presence and thicknesses being random function of depth z. Applying averaging operation on fluid related quantities in equations 2.116, 2.119 result in

$$k_2 = \frac{i\omega}{\kappa_0} \frac{\sqrt{\eta_w N_w} S_w + \sqrt{\eta_g N_g} S_g}{N_w S_w + N_g S_g}, \tag{2.120}$$

$$s = -\frac{\alpha^2 M_w M_g S_w S_g}{(N_g S_w + N_w S_g)(S_w H_g + S_g H_w)}, \tag{2.121}$$

which are the specialized slow P-wavenumber and inhomogeneity degree for partial saturation. H_0 appeared in equation 2.115 is effective modulus of the layered medium at low frequency limit. It can be calculated by Backus averaging (Gurevich and Lopatnikov, 1995). In case of patchy saturation, H_0 becomes the Gassmann modulus H_w with the effective fluid bulk modulus provided by Wood's mixing law (Müller and Gurevich, 2004). Assuming that the fluid distribution obeys certain type of correlation function, equation 2.115 can be evaluated analytically. For example, when an exponential correlation function $\psi(\xi) = \exp(-2|\xi|/d)$ describes the fluid distribution, resulting P-wave modulus is

$$H_{\mathrm{ud}}(\omega) = H_w \left(1 + s \left(1 + \frac{2i}{k_2 d} \right)^{-1} \right). \tag{2.122}$$

Gurevich and Lopatnikov (1995) and Müller and Gurevich (2004) further analysed the asymptotic behaviours of the attenuation in their models. In comparison with the periodic model (see previous section), they obtained two important results:

- In low frequency regime $\omega < \omega_c = D_p/d^2$, attenuation Q^{-1} is proportional to $\omega^{1/2}$ for random and to ω for periodic layering (fluid distribution).
- In high frequency regime $\omega > \omega_c = D_p/d^2$, attenuation Q^{-1} is proportional to $\omega^{-1/2}$ regardless of particular type of layering (fluid distribution).

Due to particular frequency scaling of the random model, it results in more gradual variation of velocity and width of attenuation over a much wider frequency range. A comparison of dispersion and attenuation predicted by periodic and random patchy saturation model is demonstrated in Figure 2.6. This fluid distribution in the random patchy saturation model is characterized by both the

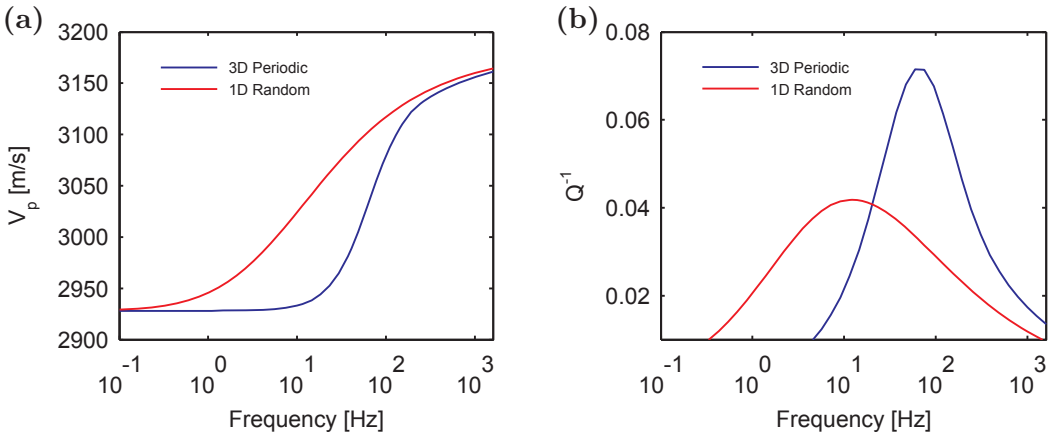

Figure 2.6: An example of (a) dispersion and (b) attenuation predicted by White's gas pocket model (3D periodic) and 1D random patchy saturation model for a partially saturated sandstone of 15% porosity.

correlation function and correlation d. The correlation length which measures the randomness and smoothness of the fluid heterogeneities (Müller et al., 2010) is analogous to the role of patch thickness $b - a$ in White's spherical model (see previous section). They both control the location of the peak attenuation and velocity inflection in frequency domain. The influence of these geometrical quantities, e.g., correlation function, correlation length, patch thickness on velocity and attenuation is known as fluid distribution effect. Its impact on interpretation of laboratory and seismic data will be discussed in chapter 4 and chapter 6, respectively.

2.7 Seismic reflection in porous media

In the previous section, wave propagation in homogeneous and heterogeneous saturated media has been reviewed. Wave-induced fluid flow at macroscopic and mesoscopic scales gives rise to velocity dispersion and attenuation, their relative significance depends on the employed wave frequency. In this section, let us consider seismic reflection between two unbounded saturated porous media. On top of wave-induced fluid flow, studying seismic amplitude loss due to reflection complements the understanding of wave attenuation at reservoir scale. More importantly, it will be shown that wave-induced fluid flow can affect seismic reflection via Biot slow P-wave. On the other hand, a solid understanding of amplitude-versus-angle (AVA) can help seismic interpreter to infer/distinguish the fluid and lithology information, delineate water-gas, oil-gas contacts from

pre-stack seismic data (Ostrander, 1984; Rutherford and Williams, 1989; Avseth et al., 2005).

2.7.1 Elastic reflection coefficient

At sufficiently low frequencies, the non-dispersive seismic velocity in saturated porous rock is given by Gassmann's equations (eqs. 2.29, 2.31). Further calculation of seismic amplitude is based on elastodynamic theory. The wave equation for an isotropic linear elastic medium with body force being neglected is given by

$$\lambda \nabla \nabla \cdot \mathbf{u} + \mu \nabla^2 \mathbf{u} = -\rho \omega^2 \mathbf{u}. \tag{2.123}$$

Here, a time dependence of $e^{i\omega t}$ is implied. $\lambda,\ \mu,\ \mathbf{u}$ are equivalent to pre-defined poroelastic quantities with zero porosity. Using the Helmholtz decomposition

$$\mathbf{u} = \nabla \Phi + \nabla \times \mathbf{\Psi}, \tag{2.124}$$

it is easy to show that the elastic wave equation results in two decoupled P- and S- wave equations. The corresponding wavenumbers are given by

$$k_p^2 = \frac{\rho \omega^2}{\lambda + 2\mu}, \tag{2.125}$$

$$k_s^2 = \frac{\rho \omega^2}{\mu}. \tag{2.126}$$

Assuming a plane interface Γ ($y = 0$) between two elastic solids Ω and $\Omega^{'}$ and a plane P/SV wave in Ω arriving at Γ with angle θ with respect to the normal of Γ. Such a perturbation generates a pair of reflected P- and S- waves and another pair of transmitted waves. The total compressional and shear displacement potentials in the two half-spaces can be expressed as

$$\begin{aligned}
\Phi &= A_I e^{i(\omega t - (kx + dy))} + A_R e^{i(\omega t - (kx - dy))}, \\
\Psi &= B_I e^{i(\omega t - (kx + hy))} + B_R e^{i(\omega t - (kx - hy))}, \\
\Phi^{'} &= A_T e^{i(\omega t - (k^{'} x + d^{'} y))}, \\
\Psi^{'} &= B_T e^{i(\omega t - (k^{'} x + h^{'} y))}.
\end{aligned} \tag{2.127}$$

The wavenumbers are related via

$$
\begin{aligned}
&k^2 + d^2 = k_p^2 \ , \ k^2 + h^2 = k_s^2 \ , \\
&k^{'2} + d^{'2} = k_p^{'2} \ , \ k^{'2} + h^{'2} = k_s^{'2} \ .
\end{aligned} \tag{2.128}
$$

The displacements and stresses are then given by

$$
\begin{aligned}
u_y &= \frac{\partial \Phi}{\partial z} + \frac{\partial \Psi}{\partial x}, \\
u_x &= \frac{\partial \Phi}{\partial x} - \frac{\partial \Psi}{\partial z}, \\
\tau_{yy} &= \lambda \frac{\partial^2 \Phi}{\partial x^2} + (\lambda + 2\mu) \frac{\partial^2 \Phi}{\partial z^2} + 2\mu \frac{\partial^2 \Psi}{\partial x \partial z}, \\
\tau_{xy} &= \mu \left(2 \frac{\partial^2 \Phi}{\partial x \partial z} - \frac{\partial^2 \Psi}{\partial z^2} + \frac{\partial^2 \Psi}{\partial x^2} \right) .
\end{aligned} \tag{2.129}
$$

Considering the plane boundary is in weld contact, the reflection coefficient between two elastic solids can be established on four boundary conditions (Aki and Richards, 2002):

$$
\begin{aligned}
&(1)\ u_x = u_x^{'} \quad \text{continuity of the x-component of solid displacement,} \\
&(2)\ u_y = u_y^{'} \quad \text{continuity of the y-component of solid displacement,} \\
&(3)\ \tau_{yy} = \tau_{yy}^{'} \quad \text{continuity of the normal stress in the solid,} \\
&(4)\ \tau_{xy} = \tau_{xy}^{'} \quad \text{continuity of the shear stress in the solid.}
\end{aligned} \tag{2.130}
$$

The resulting reflection coefficients for incident P-wave ($B_I = 0$) or SV-wave ($A_I = 0$) can be solved from following linear systems of equations

$$\mathcal{A}\mathcal{R}_P = \mathcal{B}_P \ , \tag{2.131}$$

$$\mathcal{A}\mathcal{R}_S = \mathcal{B}_S \ , \tag{2.132}$$

where

$$\mathcal{A} = \begin{pmatrix} k & h & -k & h^{'} \\ -d & k & -d^{'} & -k \\ -2kd\mu & -(h^2-k^2)\mu & -2kd^{'}\mu^{'} & (h^{'2}-k)\mu^{'} \\ (h^2-k^2)\mu & -2kh\mu & -\mu^{'}(h^{'2}-k^2) & -2kh^{'}\mu^{'} \end{pmatrix} \tag{2.133}$$

$$\mathcal{R}_P = \begin{pmatrix} R_{PP} \\ R_{PS} \\ T_{PP} \\ T_{PS} \end{pmatrix} \mathcal{B}_P = \begin{pmatrix} -k \\ -d \\ -2kd\mu \\ -\mu(h^2-k^2) \end{pmatrix} \mathcal{R}_S = \begin{pmatrix} R_{SP} \\ R_{SS} \\ T_{SP} \\ T_{SS} \end{pmatrix} \mathcal{B}_S = \begin{pmatrix} h \\ -k \\ \mu(h^2-k^2) \\ -2kh\mu \end{pmatrix} \tag{2.134}$$

A more compact form of the Zoeppritz equation can be found in Aki and Richards (2002), where P- ans SV- wave reflection coefficients are combined in one system. Approximations of Zoeppritz equation sometimes simplify the numerical calculation and provide more insights on rock and fluid quantities which affect the seismic amplitudes. An excellent summary of this topic is covered by Castagna et al. (1993). The formulation of above elastic reflection coefficient lays the foundation of the following derivation of viscoelastic reflectivity.

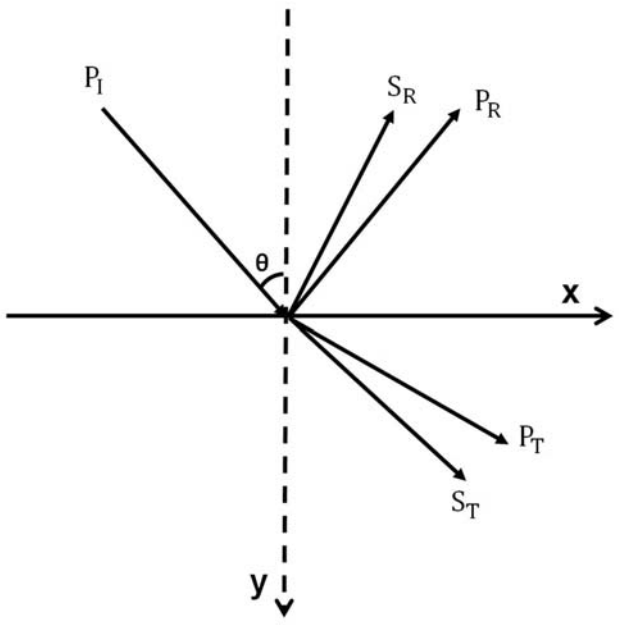

Figure 2.7: A diagram illustrating P-wave reflection and transmission between two elastic solids.

2.7.2 Viscoelastic reflection coefficient

When wave frequency no longer resides in the static regime, velocity of the saturated porous rock exhibits dispersion due to dissipation. In this case, the attenuating rock can be examined in the light of the viscoelastic solid (Bourbié et al., 1987; Carcione, 2007). Thus, viscoelastic theory enables us to study the fluid related frequency-dependent phenomena and their influences on seismic amplitudes. Due to correspondence principle of linear viscoelasticity, the wave equation for attenuating media can be obtained by replacing the real elastic moduli in elastodynamic equation (eq. 2.123) with complex elastic moduli (Cooper, 1967; Bourbié and Gonzalez-Serrano, 1983; Aki and Richards, 2002). This results in

$$\lambda(\omega)\nabla\nabla\cdot\mathbf{u}+\mu(\omega)\nabla^2\mathbf{u}=-\rho\omega^2\mathbf{u}. \tag{2.135}$$

With previously introduced decoupling technique, it is easy to find the corresponding wavenumbers of P- and S- waves are

$$\hat{k}_{p,s}^2=\frac{\rho\omega^2}{M(\omega)},\quad M(\omega)=\lambda(\omega)+2\mu(\omega),\ \mu(\omega). \tag{2.136}$$

Note the difference between modulus M here and previously fluid storage modulus. Introducing complex velocities and attenuation

$$\hat{V}_{p,s}=\sqrt{\frac{M(\omega)}{\rho}}\ ,\ Q_{p,s}^{-1}=\frac{\mathrm{Im}[M(\omega)]}{\mathrm{Re}[M(\omega)]}, \tag{2.137}$$

the corresponding phase velocities and attenuation coefficient are given by (Carcione, 2007)

$$V_{p,s}=\left[\mathrm{Re}\left(\frac{1}{\hat{V}_{p,s}}\right)\right]^{-1}\ ,\ A_{p,s}=\frac{\omega}{V_{p,s}}(\sqrt{Q_{p,s}^2+1}-Q_{p,s}). \tag{2.138}$$

The complex wavenumber can be reformulated as function of phase velocity and attenuation by

$$\hat{k}_{p,s}=P_{p,s}-iA_{p,s}=\frac{\omega}{V_{p,s}}-i\frac{\omega}{V_{p,s}}(\sqrt{Q_{p,s}^2+1}-Q_{p,s}). \tag{2.139}$$

The viscoelastic reflection coefficient can be evaluated analogously to the elastodynamic theory by replacing the real wavenumbers in the plane wave ansatz (eq.

2.127) with their complex counterparts (eqs. 2.139). Equation 2.139 facilitates the application of generalized Snell's law. However, it is only valid in sense of homogeneous plane wave, namely, the angle γ between propagation vector $\mathbf{P}_{p,s}$ and attenuation vector $\mathbf{A}_{p,s}$ is zero. Generally, the angle γ is not zero and results in inhomogeneous waves. Then, the true propagation angle associated with the reflection coefficient needs to be re-evaluated using (Aki and Richards, 2002)

$$\sin\theta_{true} = \frac{\mathrm{Re}(\omega\hat{\mathrm{k}}_{\mathrm{p,s}}\sin\theta)}{\mathrm{Re}(\sqrt{\hat{\mathrm{k}}_{\mathrm{p,s}}^2 - \omega^2\hat{\mathrm{k}}_{\mathrm{p,s}}^2\sin^2\theta})} \tag{2.140}$$

for individual plane wave. The formulation of viscoelasticity 2.139 allows one to

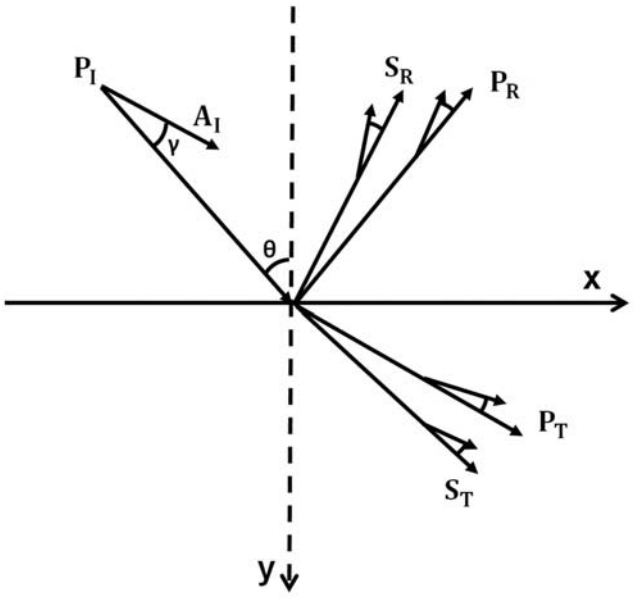

Figure 2.8: A diagram illustrating P-wave reflection and transmission between two viscoelastic solids.

customize the mechanical model for attenuation. Among others, the most popular candidates are constant Q model (Kjartansson, 1979), standard linear solid model (Zener, 1948; Mavko et al., 2009). In the specific seting of the constant Q model, Kjartansson (1979) shows that Kramers-Kronig relation (Aki and Richards, 2002)

leads to the exact result

$$V_{p,s} = V_{p,s}(\omega_0)\left(\frac{f}{f_0}\right)^{\vartheta_{p,s}}, \tag{2.141}$$

$$Q_{p,s}^{-1} = \tan(\pi\vartheta_{p,s}), \tag{2.142}$$

where $V_{p,s}(f_0)$ is phase velocity measured at reference frequency f_0 and $\vartheta_{p,s}$ is a constant which parameterizes the attenuation level. The constant Q results in frequency-independent attenuation and a linear relation between velocity and frequency under bi-logarithmic scale. There seems to be physical justification of constant Q in a partially saturated rocks. When the rock contains a distribution of fluid heterogeneity sizes, the resulting attenuation peaks may smooth out and remain constant over a broad frequency band (Spencer, 1981; Murphy, 1982). However, many field measurements (Sams et al., 1997; Gurevich and Pevzner, 2015) indicate that when the saturated sedimentary rocks are dominated by intrinsic attenuation, the resulting Q is frequency-dependent. To model the latter with viscoelasticity, it requires to employ the standard linear solid model (Zener, 1948; Mavko et al., 2009)

$$V_{p,s} = \left(\frac{M_0 M_\infty[1+(f/f_c)^2]}{\rho[M_\infty + (f/f_c)^2 M_0]}\right)^{-\frac{1}{2}}, \tag{2.143}$$

$$Q_{p,s}^{-1} = \frac{(M_\infty - M_0)(f/f_c)}{\sqrt{M_0 M_\infty}[1+(f/f_c)^2]}\ . \tag{2.144}$$

In the model, f_c is the characteristic frequency which controls the maximum attenuation; M_0 and M_∞ are the low- and high- frequency moduli, respectively. Dvorkin and Mavko (2006) customize standard linear solid (SLS) model to specific case of partial saturation. Picotti et al. (2010) approximate White's spherical model (see previous section) with SLS model and study its feasibility on viscoelastic modelling. A more general theory (Rubino et al., 2009; Rubino et al., 2011) indicates that the fast (effectve) P-wave modulus resulting from patchy saturation models (such as eqs. 2.100,2.122) is equivalent to the complex P-wave modulus of a viscoelastic solid. Thus, viscoelasticity formulation can be fed with the resulting velocity and attenuation from poroelastic models to study seismic signatures. Such an approach is computationally more feasible (Rubino et al., 2009). The application of this method for study of seismic amplitude will be discussed in detail in chapter 6. Viscoelasticity has its advantage on phenomenological modelling, however, it fails to describe the exact physics of wave propagation in saturated

porous media. This is because none of the viscoelastic models supporting the presence of Biot slow P-wave (Biot, 1962; Plona, 1980). The character of Biot slow P-wave in seismic reflectivity will be addressed in next section.

2.7.3 Poroelastic reflection coefficient

When P-wave arrives at the gas-water contact of a porous rock, the perturbation generates three converted body waves, namely fast and slow P-waves and one shear wave in each half space. At seismic frequencies, the slow P-waves are taken on a diffusion character which decay quickly away from the interface. Therefore, the slow P-wave will draw energy from the reflected P-wave and affect the seismic amplitude. To account the effect of slow P-wave on seismic reflectivity, the theoretical treatment of plane wave reflection problem needs to be based on Biot's equations of poroelasticity (Biot, 1962; Geertsma and Smit, 1961; Dutta and Odé, 1983). Previous plane wave analysis (see section 2.1.6) shows that corresponding

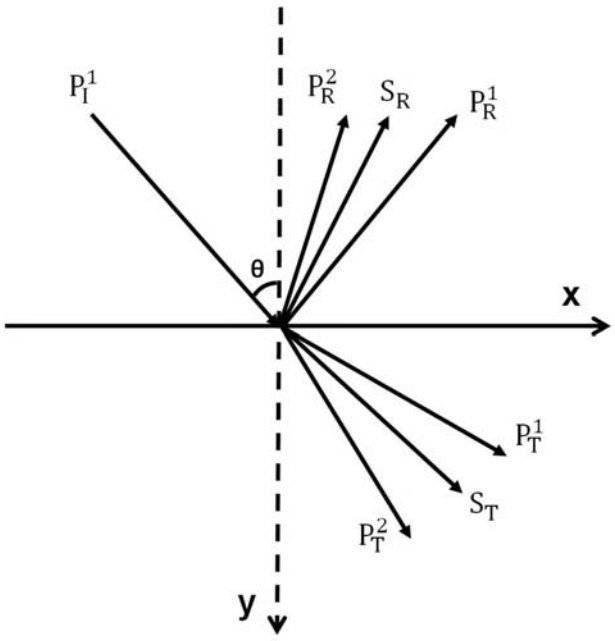

Figure 2.9: A diagram illustrating P-wave reflection and transmission between two poroelastic media.

P- and S- wavenumbers in saturated porous medium are

$$k_p^2 = \frac{2(\hat{\rho}_{11}\hat{\rho}_{22} - \hat{\rho}_{11}^2)\omega^2}{\Delta \pm \sqrt{\Delta^2 - 4(\hat{\rho}_{11}\hat{\rho}_{22} - \hat{\rho}_{11}^2)(PR - Q^2)}}\,, \tag{2.145}$$

$$k_s^2 = ((1-\phi)\rho_s + (1 - S(\omega)^{-1}))\phi\rho_f\mu^{-1}\omega^2. \tag{2.146}$$

The requirement of positive attenuation coefficient results in two P-wavenumbers and one shear wavenumber from above equations. The displacement potentials in elastodynamic theory can be extended to include Biot slow wave via

$$\Phi = A_I^1 e^{i(\omega t - (k^1 x + d^1 y))} + A_R^1 e^{i(\omega t - (k^1 x - d^1 y))} + A_R^2 e^{i(\omega t - (k^2 x - d^2 y))}, \tag{2.147}$$

$$\Psi = B_I e^{i(\omega t - (k^1 x + h y))} + B_R e^{i(\omega t - (k^1 x - h y))}, \tag{2.148}$$

$$\Phi^{'} = A_T^1 e^{i(\omega t - (k^{1'} x + d^{1'} y))} + A_T^2 e^{i(\omega t - (k^{2'} x + d^{2'} y))}, \tag{2.149}$$

$$\Psi^{'} = B_T e^{i(\omega t - (k^{1'} x + h^{'} y))}, \tag{2.150}$$

where superscripts $1, 2$ corresponds to fast and slow P-wave potentials, respectively. On top of interface conditions for the solid (eq. 2.130), two additional interface conditions are needed to account the existence of pore fluid

(5) $p_f = p_f^{'}$ continuity of the pressure in the fluid,,

(6) $w_y = w_y^{'}$ continuity of the y-component of the RFS displacement.

Assuming the amplitude of the incident waves are known (where A_I^1 corresponds to incident fast P-wave, B_I corresponds to incident SV-wave), the remaining six amplitudes of converted waves can be solved from six boundary conditions.

2.8 Effect of capillarity on acoustics

2.8.1 Concept of membrane stiffness

Following Nagy and Blaho (1994), the notion of a membrane stiffness is introduced for the simple pore geometry of a circular pipe (see Figure 2.10). The membrane stiffness is then defined as the ratio between the pressure discontinuity across the fluid-fluid boundary and fluid flow relative to the solid. Thus, at the pore-scale level we have

$$W_{\text{pore}} = \frac{p_{\text{c}}}{\phi_s(U_n - u_n)}\,, \tag{2.151}$$

where $p_c,\ \phi_s,\ U_n$ and u_n are the wave-induced capillary pressure, volume fraction, normal component of the pore-scale fluid and solid displacement.

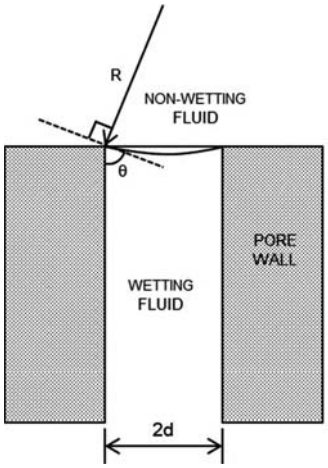

Figure 2.10: Schematic representation of the fluid boundary of a non-wetting and wetting fluid for a cylindrical pipe. The parameters $\theta,\ d,\ R$ are the contact angle, the radius of the tube and meniscus, respectively. Modified after Nagy and Blaho (1994).

Due to acoustic loading, there is a volume change dV of the wetting fluid relative to its at rest position. Figure 2.10 illustrates that dV is a function of the radius $R = \frac{d}{\cos\theta}$ of the bending meniscus. Following the chain rule of the differentiation, this volume change induced by p_c can be expressed as

$$\frac{dV}{dp_c} = \frac{\partial V}{\partial R}\frac{\partial R}{\partial p_c}. \tag{2.152}$$

The volume dV is approximated by the relative displacement multiplied by the area of the cross section of the tube

$$dV = (U_n - u_n)\pi d^2. \tag{2.153}$$

Hence we have the left hand side of equation 2.152 given by equations 2.151, 2.153

$$\frac{dV}{dp_c} = \frac{\pi d^2}{W_{\text{pore}}\phi_s}. \tag{2.154}$$

Assuming a moderate wettability condition that the contact angle θ is relatively large, we have $R \gg d$, then the first derivative on the right hand side of equation

2.152 can be approximated as

$$\frac{\partial V}{\partial R} = \frac{\pi d^4}{4R^2}\left[1 + \mathcal{O}\left(\frac{d^2}{R^2}\right)\right] \longrightarrow \frac{\pi d^4}{4R^2}. \tag{2.155}$$

According to the Young-Laplace equation, the pressure difference at the fluid-fluid interface is $p_0 - p_c = \frac{2\gamma}{R}$, where p_0 is the hydrostatic pressure. By considering p_0 to be negligible, the second derivative on the right hand side of equation 2.152 can be calculated as

$$\frac{\partial R}{\partial p_c} = \frac{R^2}{2\gamma}. \tag{2.156}$$

By substituting equations 2.154, 2.155 and 2.156 into equation 2.152 and rearrange, the membrane stiffness W_{pore} has the form (Nagy and Blaho, 1994)

$$W_{\text{pore}} = \frac{\gamma}{\left(\frac{\phi_s d^2}{8}\right)}. \tag{2.157}$$

Using the Kozeny-Carman relation, we replace the denominator of above equation by the flow permeability κ. Thus the macroscale analogue of the membrane stiffness becomes

$$W = \frac{\gamma}{\kappa}. \tag{2.158}$$

In most porous media the geometry of the void space is extremely irregular and complex and cannot be described analytically. To account for this complex pore geometry a shape factor s is introduced such that the membrane stiffness W becomes

$$W = s\frac{\gamma}{\kappa}. \tag{2.159}$$

W is the macroscopic analogue of W_{pore} and represents the ratio of a macroscopic pressure difference and the relative fluid solid displacement in a poroelastic solid.

2.8.2 Macroscopic capillarity in poroelasticity

Based on the work of Nagy and Blaho (1994), Tserkovnyak and Johnson (2003) analysed the effect of capillary forces for patchy-saturated porous rocks. Their analysis is based on an idea that capillary forces cause a discontinuity of pore fluid pressure at the boundary of neighbouring fluid patches. This pressure discontinuity is proportional to the average surface displacement of the fluid. The

poroelastic boundary condition is then

$$p - p' = W\phi(U_n - u_n), \tag{2.160}$$

where p and p' denote the fluid pressure in each patch, U_n and u_n represent the normal fluid and solid displacement components, ϕ is the porosity. W is a phenomenological parameter that can be interpreted as a membrane stiffness (Nagy and Blaho, 1994; Nagy and Neyfeh, 1995). It has a unit of Pa/m. In the absence of capillary forces this membrane has zero stiffness, $W = 0$. Then the fluid pressure continuity boundary condition of poroelasticity is recovered, $p = p'$ (Deresiewicz and Skalak, 1963; Bourbié et al., 1987; Gurevich and Schoenberg, 1999). If the right hand side of boundary condition 2.160 is parametrized in terms of relative fluid-solid velocity (similar to equation 2.87), the resulting interfacial impedance associated with capillarity is given by $Z_I^c = W/i\omega$.

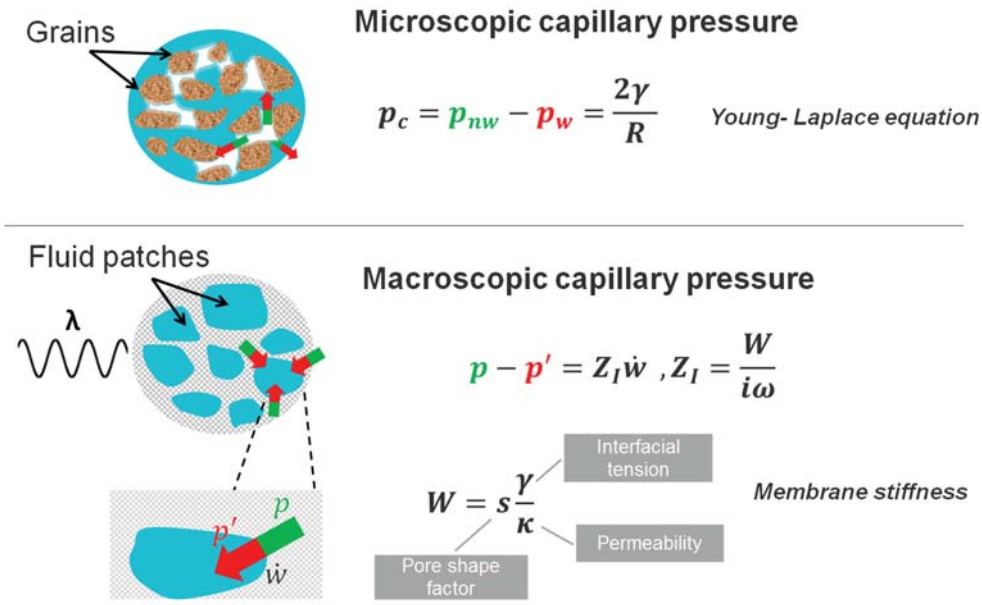

Figure 2.11: Cartoon illustration of macroscopic capillarity in poroelasticity

Based on the Young-Laplace equation (Bear, 1972), Nagy and Blaho (1994) prove that W, at macroscale, has the form of equation 2.159. Figure 2.11 illustrates the concept of macroscopic capillarity in poroelasticity. This definition of macroscopic capillarity has to be understood in a dynamic sense and is valid in presence of wave propagation. In the context of petrophysics, capillarity has different definition which refers to the entrance fluid pressure for injecting certain volume of fluid into a core sample (Purcell, 1949). It leads to a specific

capillary-pressure-saturation relation (Bear, 1972). However, one must note that both capillary pressures, namely the dynamic definition and the petrophysical definition, have the same origin, that is due to the surface tension. The effect of surface tension is characterized by Young-Laplace equation at microscopic scale, i.e., pore scale.

The validity of 2.160 is established on theoretical and experimental grounds. Nagy (1992) successfully use equation 2.160 to analyse his data on surface acoustic modes of fully saturated porous media. Tserkovnyak and Johnson (2003) find that the membrane tension effectively seals the patches into distinct regions so that fluid communication is impaired. This results in a fluid stiffening effect yielding higher P-wave velocities. At the same time, WIFF across the patches is diminished so that attenuation and dispersion become less pronounced. These results have been also found by Markov and Levin (2007) using equation (2.160) in a multiple scattering analysis for an assemblage of spherical poroelastic heterogeneities. However, none of these predictions has been verified by comparison with experimental data. It is the purpose of this thesis to investigate the effects of a non-zero membrane stiffness W on the acoustic properties of partially saturated rocks.

2.9 Other attenuation mechanisms

When the seismic waves travelling through the subsurface, it suffers the loss of amplitude due to attenuation. Attenuation accompanied with velocity dispersion occurs over a wide range of frequencies and scales from free oscillations of the entire earth to ultrasound in small rock samples (Aki and Richards, 2002). A classification of the attenuation mechanism is illustrated in Figure 2.12. The cause of attenuation and dispersion can be broadly divided into two categories: first, geometrical effects, where the wavefield energy is conserved (scattering attenuation, geometric spreading); second, absorption where wave energy is transformed into heat. Absorption also referred as intrinsic attenuation reveals the properties of rock and pore fluids, therefore, it is of particular interest in the fields of seismic interpretation and reservoir characterization. Besides wave-induced fluid flow, intrinsic attenuation in porous media can also be caused by intergranular friction, thermo-relaxation, change of chemical equilibrium, viscous shear relaxation, etc. Thorough reviews of these mechanisms can be found in the papers of Johnston et al. (1979) and Bourbié et al. (1987). The main focus of this thesis

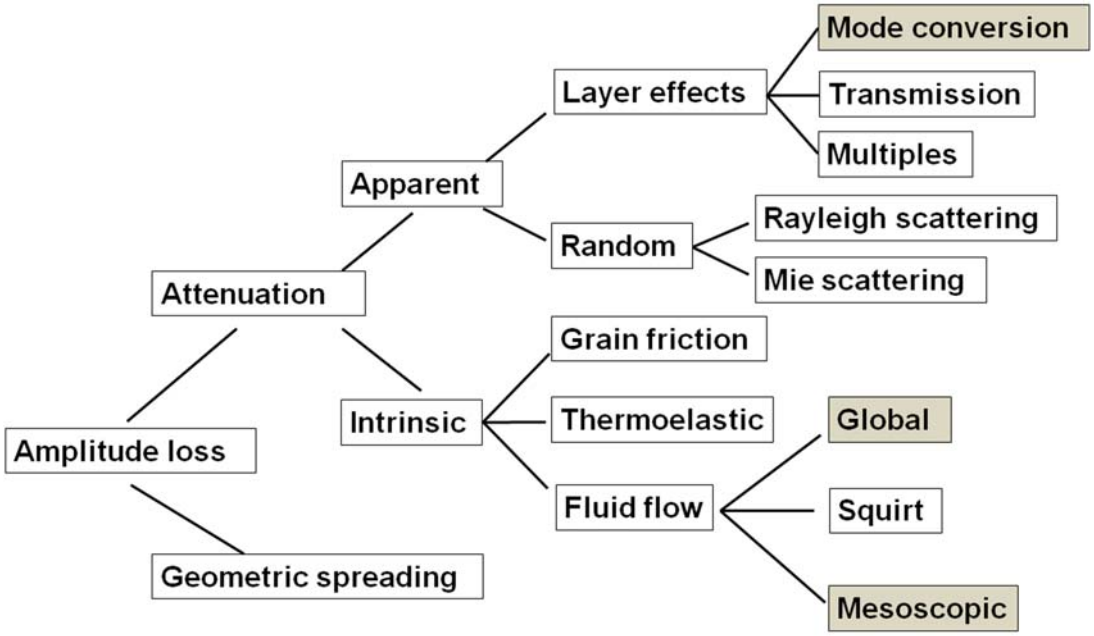

Figure 2.12: Classification of mechanisms responsible for loss of seismic amplitude. Coloured mechanisms are the main focus of this thesis.

is on how capillarity affects the attenuation mechanism due to *mesoscopic fluid flow* and how capillarity affects the *mode conversion*, i.e., seismic reflectivity via *Biot global flow*.

Chapter 3

Effects of interfacial impedance on wave-induced pressure diffusion

3.1 Summary

Seismic attenuation and dispersion in layered sedimentary structures are sometimes interpreted in terms of the classical White's model for wave-induced pressure diffusion across the layers. However, this inter-layer flow is severely dependent on the properties of the interface separating two layers. This interface behaviour can be described by a pressure jump boundary condition involving a non-vanishing interfacial impedance. In this work, we incorporate the interfacial impedance into the White's model by solving a boundary value problem in the framework of quasi-static poroelasticity. We show that White's predictions for attenuation and dispersion substantially change. These changes can be attributed to petrophysically plausible scenarios such as imperfect hydraulic contacts or the presence of capillarity.

3.2 Introduction

Nearly forty years ago White et al. (1975) presented a model for seismic P-wave attenuation and dispersion for a periodically stratified medium with alternating gas-water layers. The underlying attenuation mechanism is controlled by pressure diffusion as a consequence of wave-induced pressure gradients across the layers. Not only because of the relevance of partially saturated sediments for exploration seismology, but also because of the insightful physical arguments they used, their work continues to trigger research into wave propagation in porous media. The White's model has been reproduced within the framework of Biot's theory of poroelasticity (Biot, 1962) using different approaches (Markov and Yumatov, 1988; Norris, 1993). It has been subsequently specialized in order to analyze the effects of random layering (Gurevich and Lopatnikov, 1995; Müller and Gurevich, 2004), inhomogeneous rock properties (Carcione and Picotti, 2006), and embedded fractures with variable infill (Brajanovski et al., 2005; Kong et al., 2013). The White's model has been generalized to account for dissipation associated with the pressure diffusion at the wavelength scale (Vogelaar and Smeulders, 2007; Kudarova et al., 2013) and obliquely incident P- and SV-waves (Krzikalla and Müller, 2011).

Key to the White's model is the definition of a representative elementary volume (REV) encompassing the gas-water interface (Figure 3.1). At this interface the continuity of the fluid pressure is assumed to hold throughout the fluid pressure equilibration process, that is, from the onset of wave-induced fluid pressure gradients to the final constant pressure once equilibrium is reached. This interface condition is chosen in accordance with the open-pore boundary condition of Dereciewicz and Skalak (1963). The latter is, however, an end member of a more general, sometimes called natural boundary condition, wherein the pressure jump across the interface is proportional to the relative fluid solid velocity (Bourbié et al., 1987). This pressure jump boundary condition can be related to petrophysically plausible scenarios (Dutta and Odé, 1979; Feng and Johnson, 1983). One is associated with a perturbed hydraulic contact across the interface, as it may arise in the presence of non-load-bearing clay minerals clogging the pore throats (Figure 3.1). A second scenario is related to the presence of macroscopic capillarity, thereby creating a permanent pressure jump (Nagy and Blaho, 1994). Therefore, the question arises how this pressure jump boundary condition alters the predictions of the White's model. From analogous problems

in thermal diffusion it is known that this kind of jump boundary conditions can significantly alter the effective conductivity of heterogeneous structures (Cheng and Torquato, 1997). Given that the White's model is heavily used to interpret seismic attenuation estimates (e.g., Morgan et al., 2012), any significant changes may possibly entail important implications. Indeed, previous works indicate that the pressure jump boundary condition associated with capillary action reduces seismic attenuation (Tserkovnyak and Johnson, 2003; Markov and Levin, 2007).

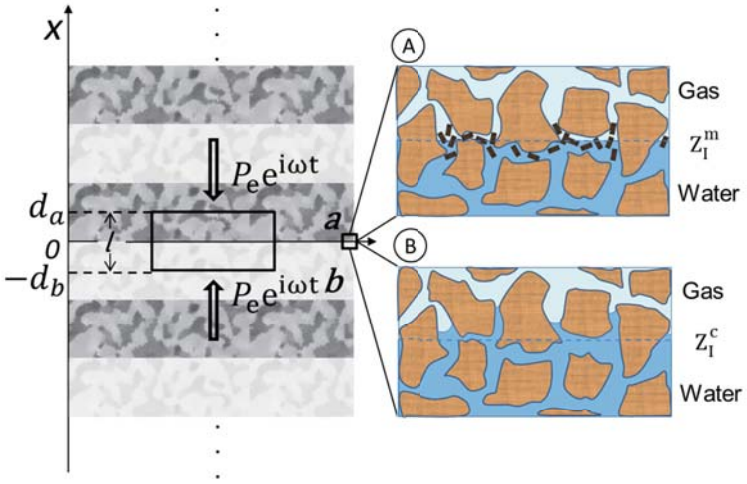

Figure 3.1: Schematic representation of a homogeneous sandstone alternatively saturated by water and gas layers. The sketch at pore scale shows two possible interface scenarios: A) clay minerals are clogging the hydraulic contact and B) meniscus unevenly distributed due to capillarity.

The aim of this chapter is to incorporate the pressure jump boundary condition into the White's model in a general fashion so that both aforementioned scenarios (and possibly other scenarios) can be modelled. To do so, we argue that the proportionality coefficient of the pressure jump boundary condition can be interpreted as an interfacial impedance. This interfacial impedance captures the particular interface properties that cannot be assigned to the gas- or water-saturated layer. We then solve the modified boundary value problem for the double layer geometry within the framework of quasi-static poroelasticity. The result is a generalized White's model wherein the interfacial impedance appears explicitly. Depending whether the interfacial impedance is a real- or complex-valued quantity, new modelling choices arise and the differences with respect to the original White's model predictions are worked out.

3.3 Theory

3.3.1 Background: White's model and interfacial impedance

White et al. (1975) determine the effective, frequency-dependent P-wave modulus $\tilde{H}(\omega)$ for a periodically layered system composed of porous layers alternately saturated with gas and water. Their approach consists in solving a boundary value problem for the REV with spatial semi-period $l = (d_a + d_b)$, as illustrated in Figure 3.1. Therein the action of the P-wave is simulated through a harmonically oscillating compression $P_e e^{i\omega t}$. The resulting ratio of vertical component of the average strain to stress is (White el al., 1975; their equation 14)

$$\frac{1}{\tilde{H}} = \frac{1}{H^{\mathrm{nf}}} + \frac{1}{\tilde{H}^{\mathrm{ff}}}. \tag{3.1}$$

Herein H^{nf} is the P-wave modulus when fluid exchange between consecutive layers is not permitted (hence the superscript "nf" for no-flow), as is the case when there is not enough time for the fluid pressure to equilibrate. Thus, H^{nf} can be interpreted as the high-frequency, or unrelaxed, limit. It is obtained from Backus averaging with the individual, undrained P-wave moduli calculated using Gassmann's equation (Gelinsky and Shapiro, 1997)

$$\frac{1}{H^{\mathrm{nf}}} = \left\langle \frac{1}{H} \right\rangle. \tag{3.2}$$

The angle brackets denote the volumetric, or saturation-weighted, average $\langle x \rangle = (d_a x_a + d_b x_b)/l$. According to the Biot-Gassmann theory the undrained P-wave modulus is given by $H = L + \alpha^2 M$, where $L = K_0 + 4\mu/3$ is the drained P-wave modulus, $\alpha = 1 - K_0/K_{\mathrm{s}}$ the Biot-Willis coefficient, and $M = ((\alpha - \phi)/K_{\mathrm{s}} + \phi/K_{\mathrm{f}})^{-1}$ the fluid storage modulus. K_{s} and K_0 denote the bulk moduli of the solid grains and of the dry frame. The porosity is ϕ and the frame shear modulus is μ.

The second term of the right-hand side (RHS) of equation 3.1 accounts for fluid pressure diffusion across the layers, thereby reducing the overall stiffness of the medium. As this is a transient process, $\tilde{H}^{\mathrm{ff}}$ turns out to be complex-valued

and frequency-dependent,

$$\frac{1}{\tilde{H}^{\mathrm{ff}}} = \frac{1}{i\omega l}\frac{(B_a - B_b)^2}{Z_a - Z_b} \equiv \frac{1}{i\omega l}\frac{(\Delta B)^2}{\Delta Z}\,. \tag{3.3}$$

This inter-layer flow term has a simple interpretation. The (uni-axial) Skempton coefficient B quantifies the fluid pressure built-up induced by the external loading P_{e} under undrained condition, that is, when the fluid increment ξ is zero

$$B = \frac{\partial p_{\mathrm{f}}^{\mathrm{nf}}}{\partial P_{\mathrm{e}}}\Big|_{\xi=0} = \frac{\alpha M}{H}. \tag{3.4}$$

Only if there is a contrast in the induced fluid pressures, or equivalently $\Delta B \neq 0$, fluid pressure diffusion can take place. This diffusion process is also controlled by the impedance contrast ΔZ. Herein, the diffusional impedance is defined as the ratio of the fluid pressure associated with Biot slow P-wave and the normal component of the relative fluid-solid velocity v_n at the interface

$$Z = \frac{p_{\mathrm{f}}^{\mathrm{ff}}}{v_{\mathrm{n}}}\Big|_{x=0} = \pm\frac{\coth(k_s d)}{\kappa k_s}\,. \tag{3.5}$$

We assume that the unit normal points from layer 'b' to layer 'a'. Thus, the sign of the diffusional impedance is positive for layer 'a' and negative for layer 'b'. The impedance entails the pressure diffusion wave number associated with Biot's slow P-wave number. In the quasi-static approximation this wave number is $k_s \equiv \sqrt{i\omega/D_{\mathrm{p}}}$ with the diffusivity $D_{\mathrm{p}} = \kappa N$. Herein κ is the hydraulic conductivity given by the ratio of permeability and fluid shear viscosity and $N = M(1-\alpha B)$. It is important to notice that equation 3.5 is independent of the properties of the interface, that is, the condition of fluid pressure continuity across the boundary is not used to obtain this expression.

From the above considerations it becomes clear that the induced fluid pressure difference across the interface is central to initiate inter-layer flow. It also means that interlayer flow is sensitive to the continuity of the pressure at the interface. In Biot 's theory of poroelasticity the pressure at the interface is generally described by (Dereciewicz and Skalak, 1963; Bourbié et al., 1987)

$$p_{\mathrm{fa}}|_{x=0} - p_{\mathrm{fb}}|_{x=0} = -Z_{\mathrm{I}} v_n|_{x=0}\,. \tag{3.6}$$

It relates the pressure jump across the interface with the relative fluid-solid veloc-

ity. The proportionality coefficient Z_{I} is called the resistance coefficient. If there is no resistance, $Z_{\mathrm{I}} = 0$, the layers are in perfect hydraulic contact. Then, the so-called "open-pore boundary condition" is satisfied and the pressure is continuous across the interface. Conversely, for any finite $Z_{\mathrm{I}} \neq 0$ there exists a pressure jump, whereas for $Z_{\mathrm{I}} \to \infty$ no pressure equilibration can take place. In general, Z_{I} can be interpreted as an interfacial impedance assigning a particular property to the interface. It may even have a reactance term ($\mathrm{Im}\{\mathrm{Z_I}\} \neq 0$), as discussed further below. In the next section we show how this interfacial impedance can be incorporated in the derivation of an effective P-wave modulus.

3.3.2 Effective strain for finite interfacial impedance

We base the derivation on the quasi-static poroelasticity equations (see section 2.4, eqs. 2.71, 2.72). In the space-frequency domain they are given by

$$\frac{\partial \tau_{xx}}{\partial x} = 0, \tag{3.7}$$

$$\frac{\partial p_{\mathrm{f}}}{\partial x} = -\frac{i\omega}{\kappa} w\,, \tag{3.8}$$

where τ_{xx} is the total stress, p_{f} the fluid pressure, and $w = v/i\omega$ the average relative fluid displacement per unit volume of bulk material. Equations 3.7 and 3.8 represent stress equilibrium and Darcy's law, respectively. They are coupled through the constitutive relations

$$\tau_{xx} = H\frac{\partial u}{\partial x} + BH\frac{\partial w}{\partial x}, \tag{3.9}$$

$$p_{\mathrm{f}} = -BH\frac{\partial u}{\partial x} - M\frac{\partial w}{\partial x}, \tag{3.10}$$

with u being the average displacement of the solid phase.

For a homogeneous medium, equations 3.7 to 3.10 can be combined such that the governing equation for w becomes

$$\frac{\partial^2 w}{\partial\, x^2} = \frac{i\omega}{D_{\mathrm{p}}} w. \tag{3.11}$$

This means that the out-of-phase movement between the fluid and solid phases, which is associated with the Biot slow P-wave, is governed by diffusion. The

solution for the considered REV can be written as

$$w_i = \sum_{\gamma=1}^{2} A_{i,\gamma} \exp\{(-1)^\gamma k_{si} x\}, \quad i = a, b, \tag{3.12}$$

with $A_{i,\gamma}$ being complex constants. Since the equation of equilibrium (3.7) implies that the stress is constant throughout the REV and equal to the applied compression, $\tau_{xx} = -P_{\mathrm{e}}$, we write the remaining poroelastic fields as

$$u_i = -B_i w_i - \frac{P_{\mathrm{e}}}{H_i} x + E_i, \tag{3.13}$$

$$p_{\mathrm{fi}} = B_i P_{\mathrm{e}} - N_i \frac{\partial w_i}{\partial x}, \quad i = a, b, \tag{3.14}$$

where E_i are two additional unknowns. For the REV under uni-axial deformation, the resulting overall strain and the effective plane wave modulus are defined by

$$\tilde{e}_{xx} = (u_a|_{x=d_a} - u_b|_{x=-d_b})/l\,, \tag{3.15}$$

$$\tilde{H}(\omega) = -P_{\mathrm{e}}/\tilde{e}_{xx}\,. \tag{3.16}$$

To uniquely determine the overall strain, another five equations are needed. These equations are obtained by choosing appropriate boundary conditions. Due to symmetry, we impose no-flow conditions at the boundaries of the REV

$$v_a|_{x=d_a} = v_b|_{x=-d_b} = 0\,. \tag{3.17}$$

In addition, we require continuity of solid displacement and relative fluid-solid velocity at the interface

$$u_a|_{x=0} = u_b|_{x=0}\,, \tag{3.18}$$

$$v_a|_{x=0} = v_b|_{x=0}\,. \tag{3.19}$$

The fifth boundary condition is provided by the partially open boundary condition 3.6. It can be written in decomposed form as

$$p^{\mathrm{nf}}_{\mathrm{fa}} + p^{\mathrm{ff}}_{\mathrm{fa}} = p^{\mathrm{nf}}_{\mathrm{fb}} + p^{\mathrm{ff}}_{\mathrm{fb}} - Z_{\mathrm{I}} v_n, \quad (x = 0) \tag{3.20}$$

where we interpret the pressure as $p_{\mathrm{f}} = p^{\mathrm{nf}}_{\mathrm{f}} + p^{\mathrm{ff}}_{\mathrm{f}}$.

The first term on the RHS of equation 3.14 quantifies the fluid pressure when fluid flow across the interface is not permitted, that is, $p_{\mathrm{fi}}^{\mathrm{nf}} = B_i P_{\mathrm{e}}$. The second term describes the fluid pressure in presence of pressure diffusion, that is, $p_{\mathrm{fi}}^{\mathrm{ff}} = -N_i \frac{\partial w_i}{\partial x}$. The associated diffusional impedance can be computed from the definition (3.5) by applying boundary condition (3.17).

Next, we compute the overall effective strain by substituting equation 3.13 into 3.15 and making use of boundary conditions 3.18 and 3.19. We obtain

$$\tilde{e}_{xx} = \underbrace{-\left(\frac{d_a}{H_a} + \frac{d_b}{H_b}\right)\frac{P_{\mathrm{e}}}{l}}_{e^{\mathrm{nf}}} + \underbrace{\frac{B_a - B_b}{i\omega l}\, v_n|_{x=0}}_{\tilde{e}^{\mathrm{ff}}} . \tag{3.21}$$

Equation (3.21) for the overall strain can be understood if, similarly to the pressure decomposition, the strain is represented as the sum of $\tilde{e} = e^{\mathrm{nf}} + \tilde{e}^{\mathrm{ff}}$. If solid and fluid phases move in-phase or, equivalently, $v = 0$, then the second term on the RHS of equation 3.21 vanishes, and thus the remaining term corresponds to the effective strain associated with no-flow condition, $e^{\mathrm{nf}} = -\langle H^{-1} \rangle P_{\mathrm{e}}$. If $v \neq 0$, the overall effective strain consists of two terms, wherein the second term corresponds to the additional strain in presence of pressure diffusion, $\tilde{e}^{\mathrm{ff}}$.

Employing equations 3.5, 3.19 in equation 3.20 yields the relative fluid-solid velocity at the interface

$$v_n|_{x=0} = -\frac{B_a - B_b}{Z_a - Z_b + Z_{\mathrm{I}}} P_{\mathrm{e}} \, . \tag{3.22}$$

This equality shows that the presence of resistance coefficient Z_{I} reduces the relative fluid-solid velocity. Making use of the extended relative fluid-solid velocity (3.22) in equation 3.21, we obtain the effective strain associated with the diffusion process

$$\tilde{e}^{\mathrm{ff}} = -\frac{(B_a - B_b)^2}{i\omega l (Z_a - Z_b + Z_{\mathrm{I}})} P_{\mathrm{e}}. \tag{3.23}$$

The overall effective strain can now be computed via summation of the component related to no flow across the interface, e^{nf}, and the contribution produced by fluid pressure diffusion between the layers, $\tilde{e}^{\mathrm{ff}}$.

3.3.3 Generalized White's model

The undrained P-wave modulus is obtained by substituting the overall effective strain into equation 3.16. Therefore,

$$\frac{1}{\tilde{H}} = \left\langle \frac{1}{H} \right\rangle + \frac{1}{i\omega l} \frac{(\Delta B)^2}{\Delta Z + Z_{\mathrm{I}}}. \tag{3.24}$$

This effective, undrained P-wave modulus is the main result of this chapter. The interfacial impedance appears in the denominator of the inter-layer flow term and adds to the impedance contrast ΔZ. If the interfacial impedance vanishes, $Z_{\mathrm{I}} = 0$, then equation 3.24 reduces to the P-wave modulus given by White et al. (1975; their equation 14). This shows that the fluid pressure continuity boundary condition is rooted in White's model.

This generalized White's model can be used to characterize P-wave dispersion and attenuation in partially saturated media wherein the interface separating the two fluid phases possesses specific properties. As originally envisaged by Deresiewicz and Skalak (1963) the partially open boundary condition (3.6) models a perturbed hydraulic contact. Then the interfacial impedance is real-valued, that is, it has the character of a resistance. It will be denoted as $Z_{\mathrm{I}}^{\mathrm{m}}$. Another scenario is related to the presence of capillary forces. The pressure jump boundary condition is then (Nagy and Blaho, 1994)

$$p_{\mathrm{fa}}|_{x=0} - p_{\mathrm{fb}}|_{x=0} = -\frac{W}{i\omega} v_{\mathrm{n}}|_{x=0}, \tag{3.25}$$

where W (Pa/m) is the so-called membrane stiffness, which controls the capillarity reinforcement. In this representation of the pressure jump condition, the interfacial impedance is an imaginary number, and is given by $Z_{\mathrm{I}}^{\mathrm{c}} = -i\frac{W}{\omega}$. That is, it has the character of a reactance. In the following we focus on the implications on seismic attenuation and dispersion for these two scenarios.

3.4 Attenuation and dispersion

Attenuation and dispersion can be obtained from equation 3.24 via $Q^{-1} = \mathrm{Im}(\tilde{\mathrm{H}})/\mathrm{Re}(\tilde{\mathrm{H}})$ and $V_{\mathrm{P}} = (\mathrm{Re}(1/\mathrm{V_{pc}}))^{-1}$, where the complex P-wave velocity is $V_{\mathrm{pc}} = \sqrt{\tilde{H}/\rho}$. The effective density ρ is given by the volumetric average of the grain and fluid densities. Depending on the physical interpretation of the

interfacial impedance new predictions for attenuation and dispersion emerge. We restrict the analysis of the results to the two scenarios mentioned above. In the first case the interfacial impedance has a resistance term only, while in the second case it is given by a reactance term. The mechanical properties of the rock and fluids for calculating the velocity and attenuation are given in Table 3.1. The corresponding attenuation and dispersion behaviours for a gas saturation of $S = 50\%$ are shown in Figure 3.2. Here the saturation is computed according to $S_i = d_i/l$ with $l = 0.2$ m.

Sand		Fluids	
K_0 (GPa)	7	K_{fa} (GPa)	2.25
μ_{m} (GPa)	9	ρ_{fa} (g/cm^3)	0.99
K_{s} (GPa)	35	η_{fa} (Pa s)	1e-3
ρ_{s} (g/cm^3)	2.65	K_{fb} (GPa)	0.1
ϕ	0.15	ρ_{fb} (g/cm^3)	0.1
κ_0 (m^2)	1e-13	η_{fb} (Pa s)	3e-5

Table 3.1: Mechanical properties of rock and fluids

The red and blue families of curves correspond to the resistance and reactance scenario, respectively, and the original White's prediction is indicated by the black curves. We note that in these numerical examples the White's model predictions lose their validity at very high frequencies, as then the wavelength becomes comparable to the layer thickness. However, to illustrate the asymptotic characteristics, we show velocity and attenuation up to a frequency of 0.1 MHz.

Two distinct behaviours can be observed. The resistance term causes the dispersion curve to shift towards lower frequencies with increasing resistance. The dispersion window remains unchanged and is bounded by the Gassmann-Wood (GW) and Gassmann-Hill (GH) predictions. Accordingly, the attenuation peak is shifted to lower frequencies. This shifting behavior can be understood as a consequence of the delay the imperfect hydraulic contact imposes on the pressure equilibration process. In other words, a real-valued interfacial impedance can be interpreted as the reciprocal of an interface permeability $Z_I^m = 1/\kappa_I$ (Gurevich and Schoenberg, 1999). Since the characteristic frequency of the White's model $\omega_c = \kappa_0 N/\eta l^2$ is proportional to the permeability κ_0 of the rock. An decreasing interface permeability κ_I (increasing interfacial impedance Z_I^m) results in a decreasing effective permeability κ_0 of the rock. Consequently, the characteristic frequency of the attenuation and dispersion shifts towards the lower frequen-

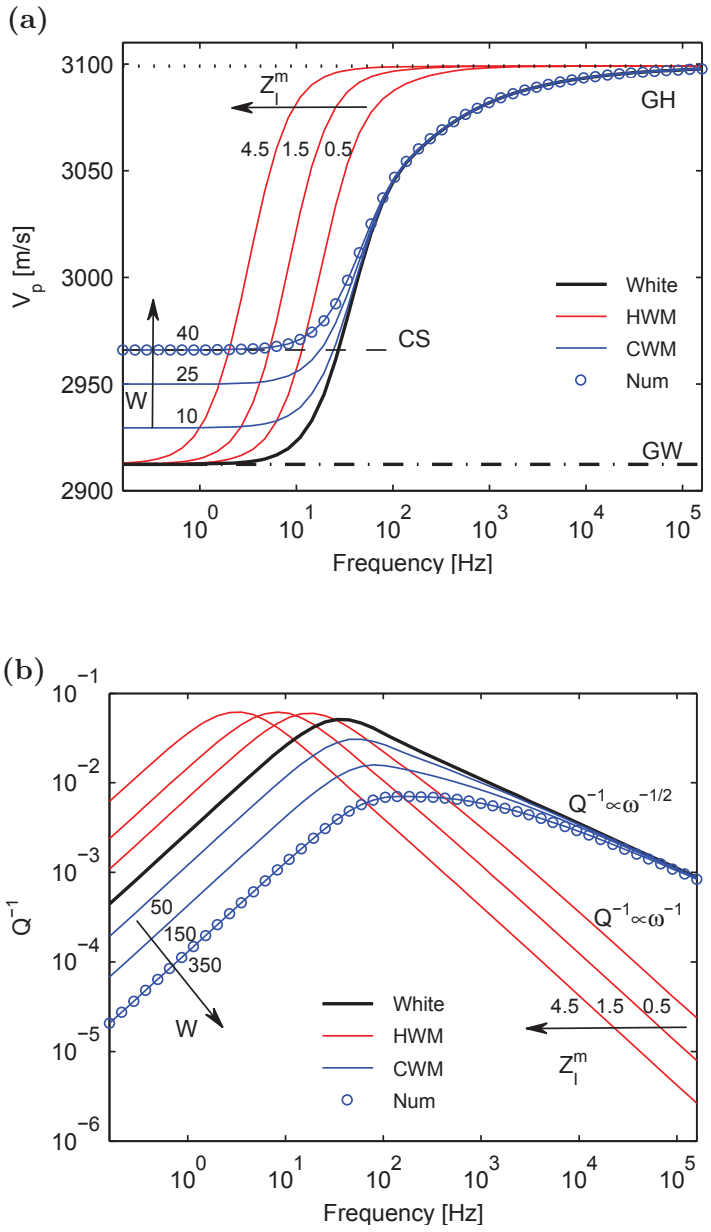

Figure 3.2: Phase velocity and inverse quality factor as functions of frequency for a homogeneous rock alternately saturated with gas and water. "HWM" refers to generalised White model with imperfect hydraulic contact, whereas "CWM" indicates the capillarity extended White model. The values of resistance $Z_{\mathrm{l}}^{\mathrm{m}}$ and membrane stiffness W are given in units of GPa $\cdot$ s/m and GPa/m, respectively.

cies. It is also interesting to note that the high-frequency attenuation asymptote changes from $Q^{-1} \propto \omega^{-1/2}$ for the White's prediction to $Q^{-1} \propto \omega^{-1}$. This change in asymptotic behaviour is attributed to the fact that, in the presence of imperfect hydraulic contacts, the distance over which the pressure gradients are

equilibrated has effectively increased (Müller et al., 2010).

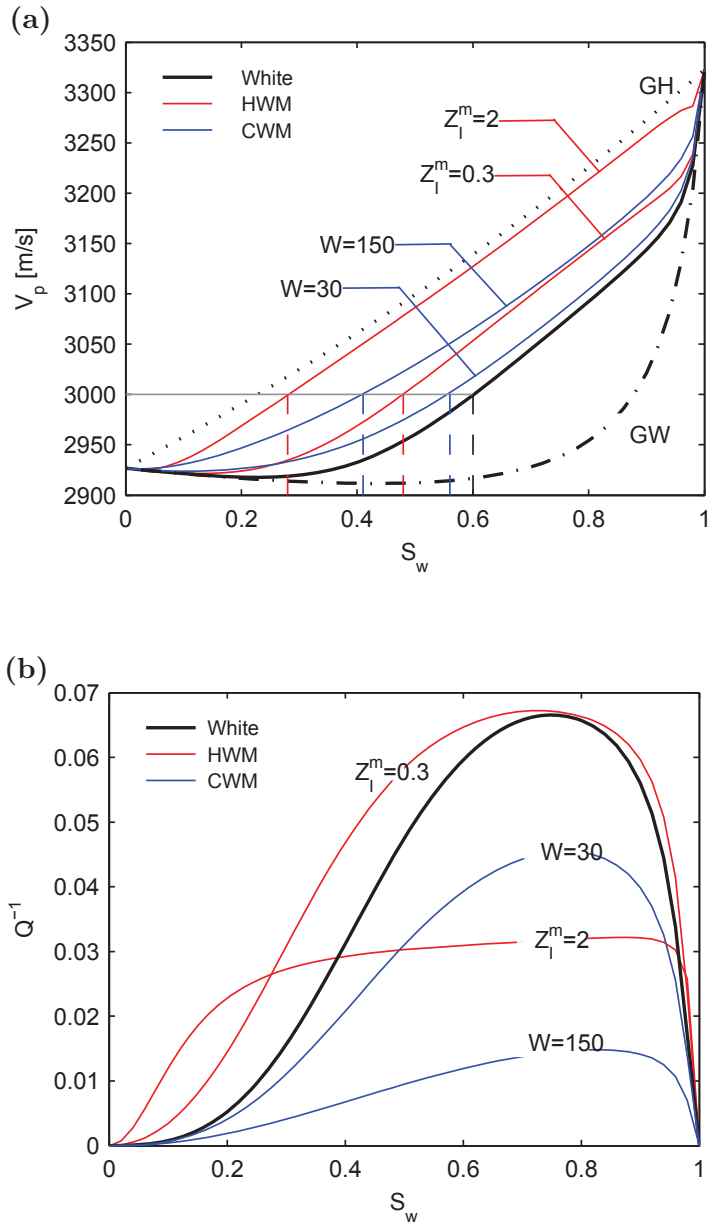

Figure 3.3: Velocity- and attenuation-saturation relations for a frequency of 25 Hz. The values of the resistance $Z_{\mathrm{I}}^{\mathrm{m}}$ and membrane stiffness W are given in units of GPa $\cdot$ s/m and GPa/m, respectively.

The reactance term manifests differently. In this case, the pressure jump at the interface effectively reduces the wave-induced pressure gradient across the layers. Accordingly, the effects of wave-induce pressure diffusion become less pronounced so that dispersion and attenuation are reduced. In essence, the sur-

face tension between two immiscible fluids perturbs the energy redistribution (or mode conversion process) across the interface (Markov, 2009), thereby creating a change of attenuation. In the capillarity interpretation of interface condition (3.25), an increasing membrane stiffness W increases the low-frequency limiting velocity above the GW prediction. The new capillarity-extended static (CS) limit is given by (this will be shown in the next chapter)

$$H^*_{\text{1D}} = \frac{z+T}{\dfrac{z}{H^{\text{GW}}}+\dfrac{T}{H^{\text{GH}}}},\; z = \left\langle \frac{N}{S^2} \right\rangle,\; T = Wl\,. \tag{3.26}$$

We also validate the capillarity-extended model by numerically solving a boundary value problem. The numerical results displayed by circles coincide with the model prediction.

As the present modelling refers to partially saturated layered media, it is also instructive to analyse the velocity- and attenuation-saturation relations. The velocity-saturation relations (VSRs) at fixed frequency (25 Hz) for both scenarios are shown in Figure 3.3a. It can be observed that both, the resistance and reactance terms, cause a deviation from the White's prediction towards the GH behaviour, thereby increasing the overall stiffness of the layered system. However, this is due to different reasons. In the resistance scenario, it is the shifting behaviour that is responsible for an increased velocity at fixed finite frequency. In the reactance scenario, the imposed pressure jump is permanent and adds to the overall stiffness. The attenuation-saturation relation (ASR) is shown in Figure 3.3b. Attenuation first increases with increasing resistance as the chosen frequency is below the characteristic frequency. For further increased resistance, the attenuation starts to decline significantly and a broadened peak can be observed.

3.5 Poroelastic fields

3.5.1 Full Biot's solution

Beyond attenuation and dispersion, it is also meaningful to analyse the resulting poroelastic fields associated with the pressure jump boundary conditions. In order to analyse the contributions from fast and slow P-wave on the poroelastic fields equivalently, we invoke low frequency Biot's dynamic equations for

compressional waves (see section 2.6.2, eq. 2.106)

$$\frac{d}{dz}\left(H\frac{du}{dz}+C\frac{dw}{dz}\right)+\omega^2(\rho u+\rho_f w)=0\ ,$$
$$\frac{d}{dz}\left(C\frac{du}{dz}+M\frac{dw}{dz}\right)+\omega^2(\rho_f u+q w)=0\ , \tag{3.27}$$

where the friction coefficient is

$$q=\frac{\rho_{\mathrm{f}}S^{\infty}}{\phi}-\frac{i\eta}{\omega\kappa_0}. \tag{3.28}$$

For a plane wave traveling along x-axis direction, the displacement fields have the following solutions

$$u_x=\Phi_1\exp\left[i(\omega t-kx)\right]\ , \tag{3.29}$$
$$w_x=\Phi_2\exp\left[i(\omega t-kx)\right]\ . \tag{3.30}$$

Introducing the ansatz 3.29 into the wave equations 3.27 and eliminating the amplitude constants $\Phi_1,\ \Phi_2$ we obtain the dispersion relation

$$V^2_{\mathrm{f,s}}=\frac{-\Delta\pm\sqrt{\Delta^2-4(\rho q-\rho_{\mathrm{f}}^2)(HM-C^2)}}{2(\rho q-\rho_{\mathrm{f}}^2)}, \tag{3.31}$$

where $\Delta=2\rho_{\mathrm{f}}C-\rho M-qH$. The fast and slow P-wavenumbers are calculated via $k_{\mathrm{f,s}}=\sqrt{\omega^2/V^2_{\mathrm{f,s}}}$. The amplitude ratio between the relative and solid displacement reads

$$\lambda_{\mathrm{f,s}}=\frac{\Phi_2}{\Phi_1}=\frac{H-\rho V^2_{\mathrm{f,s}}}{\rho_{\mathrm{f}}V^2_{\mathrm{f,s}}-C}. \tag{3.32}$$

Alternatively, solutions of solid and relative displacements written in terms of fast and slow P-wave components are

$$u_{xi}=A^{\pm}_{\mathrm{fi}}\exp\left(\mp ik_{\mathrm{fi}}x\right)+A^{\pm}_{\mathrm{si}}\exp\left(\mp ik_{\mathrm{si}}x\right), \tag{3.33}$$

$$w_{xi}=\lambda_{\mathrm{fi}}A^{\pm}_{\mathrm{fi}}\exp\left(\mp ik_{\mathrm{fi}}x\right)+\lambda_{\mathrm{si}}A^{\pm}_{\mathrm{si}}\exp\left(\mp ik_{\mathrm{si}}x\right). \tag{3.34}$$

The subscript i defines the associated property in the i-th layer of the REV. Substituting 3.33, 3.34 into the equations 3.13 and 3.14, we obtain the decomposed solutions for total stress and fluid pressure. The poroelastic fields consist of totally eight unknowns $A^{\pm}_{\mathrm{fi}},\ A^{\pm}_{\mathrm{si}}\ (i=1,2)$. On top of previously introduced five boundary conditions, i.e., equations 3.17-3.20, three addition boundary con-

ditions for the stress field are needed

$$\tau_a|_{x=0} = \tau_b|_{x=0} \ , \tag{3.35}$$

$$\tau_a|_{x=d_a} = -P_{\mathrm{e}} \ , \tag{3.36}$$

$$\tau_b|_{x=-d_b} = -P_{\mathrm{e}} \ . \tag{3.37}$$

Thus, a linear system of eight equations $\mathbf{I}_{8\times8} \times \mathbf{A}_{8\times1} = \mathbf{G}_{8\times1}$ can be solved numerically to yield the resulting dynamic fields under wave propagation. In the present context, an additional poroelastic field which is dynamic capillary pressure can be defined as

$$P_c(\omega) = p_{\mathrm{fa}}(\omega)|_{x=0} - p_{\mathrm{fb}}(\omega)|_{x=0} \ . \tag{3.38}$$

$P_c(\omega)$ can be interpreted as capillary pressure when it is associated with the capillary boundary condition 3.25. Otherwise, it can be understood as general pressure jump in the presence of discontinuity interface condition such as described by equation 3.20. To explore the contrasting attenuation behaviour resulting from different types of pressure jump boundary conditions, we also look into the dissipation. According to Johnson (2001), the dissipated power averaged over one wave cycle is given by

$$\bar{\mathcal{P}} = -\frac{1}{2}\int Re(\dot{w}^* \cdot \nabla p_{\mathrm{f}}) dV \ , \tag{3.39}$$

where * indicates the complex conjugate. If we define the average strain energy over one wave period T as

$$\bar{\mathcal{W}} = \frac{1}{2T}\int\int (\tau_{ij} e_{ij} - p_f \epsilon) dV dt \ . \tag{3.40}$$

Then, the attenuation (within low-loss media assumption) can be calculated via (Bourbié et al., 1987)

$$Q^{-1}(\omega) = \frac{1}{2\omega}\frac{F[\bar{\mathcal{P}}]}{F[\bar{\mathcal{W}}]}, \tag{3.41}$$

where operator F denotes the Fourier transform $F(\omega) = \int_{-\infty}^{+\infty} f(t)\exp(-i\omega t)dt$.

3.5.2 Numerical results

It is evident from Figure 3.4 that the existence of pressure jump across the fluid-fluid interface when capillarity is taken into account. On the other hand, open-pore interface condition presents a continuous fluid pressure across the interface. The contribution from fast P-wave to the fluid pressure is piecewisely constant within each fluid phase according to Figure 3.4a,b. Comparing Figure 3.4a,b and Figure 3.4c,d, the fluid pressure due to fast P-wave has no imaginary component but real component. This confirms that fast P-wave is non-diffusive at the two considered frequencies, namely 50 Hz and 300 Hz. The imaginary part of the pressure component is solely caused by slow P-wave. The liquid phase always supports higher pressure components because of the high Skempton's coefficient. At higher frequencies, the pressure amplitude (Figure 3.4e,f) transits more sharply from the liquid phase into the gas phase. The net pressure jump becomes smaller at higher frequency according to Figure 3.4f and the two scenarios (open-pore and capillarity) start to merge. The solid displacement field is plotted in Figure 3.5. Both fast and slow P-wave components are discontinuous across the interface regardless of the condition of fluid pressure (whether it is open-pore or capillarity). According to Figure 3.5e,f, the amplitude of displacement field is continuous across the interface. Also capillarity plays a negligible role on solid displacement regardless of frequency.

Figure 3.6 shows the profile of relative fluid-solid displacement. The fast P-wave does not contribute to this field at the two employed frequencies. This indirectly indicates that relative displacements at the two considered frequencies obey a diffusion equation. The diffusive character of slow P-wave is reflected by the net value of the relative displacement. Capillarity results in smaller relative displacement between fluid and solid comparing to the open-pore situation. However, this difference becomes smaller at higher frequency. The behaviour of relative displacement, to a certain degree, explains the attenuation behaviour in presence of capillarity shown in Figure 3.2.

The dynamic (or wave-induced) capillary pressure is plotted in Figure 3.7a as function of water saturation for difference frequencies. The capillary pressure according to our definition 3.38, depends on both frequency ω and amplitude $|P_{\mathrm{e}}|$ of the external loading $P_{\mathrm{e}}e^{i\omega t}$. The resulting capillary pressure saturation relation looks apparently different from what is being typically measured in the lab (see

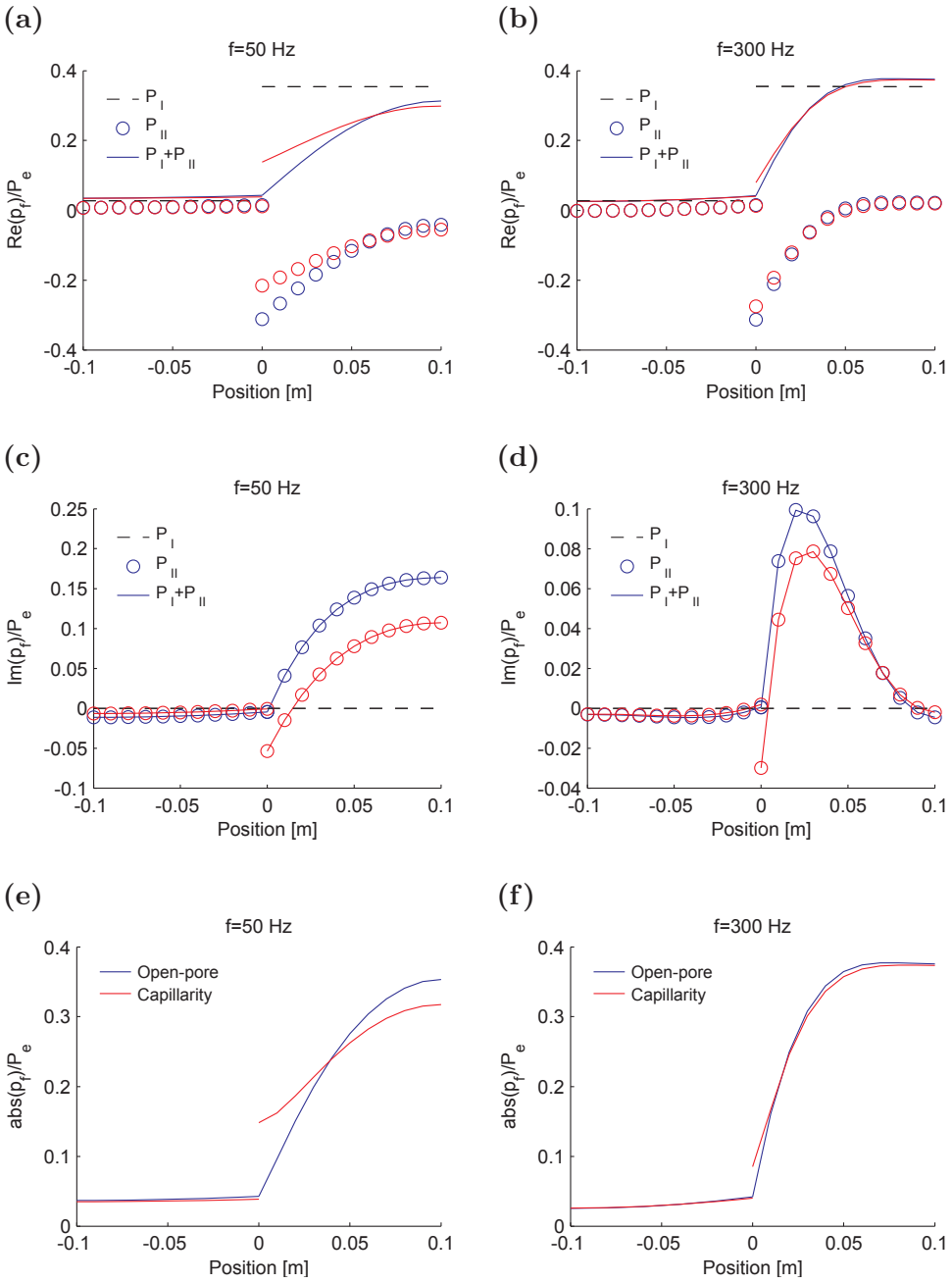

Figure 3.4: The real part (a), imaginary part (c) and amplitude (e) of fluid pressure at 50 Hz while (b),(d),(f) show their high frequency (300 Hz) counterpart. The blue colour refers to open-pore case whereas red colour refers to capillarity case. The dashed line refers to fast P-wave component whereas the circle corresponds to slow P-wave component. The total component is indicated by solid line.

Brooks and Corey (1964) for example). The latter takes on a petrophysical meaning and refers to the entrance fluid pressure for injecting certain volume of fluid into a core sample (Purcell, 1949). Nevertheless, one must note that both

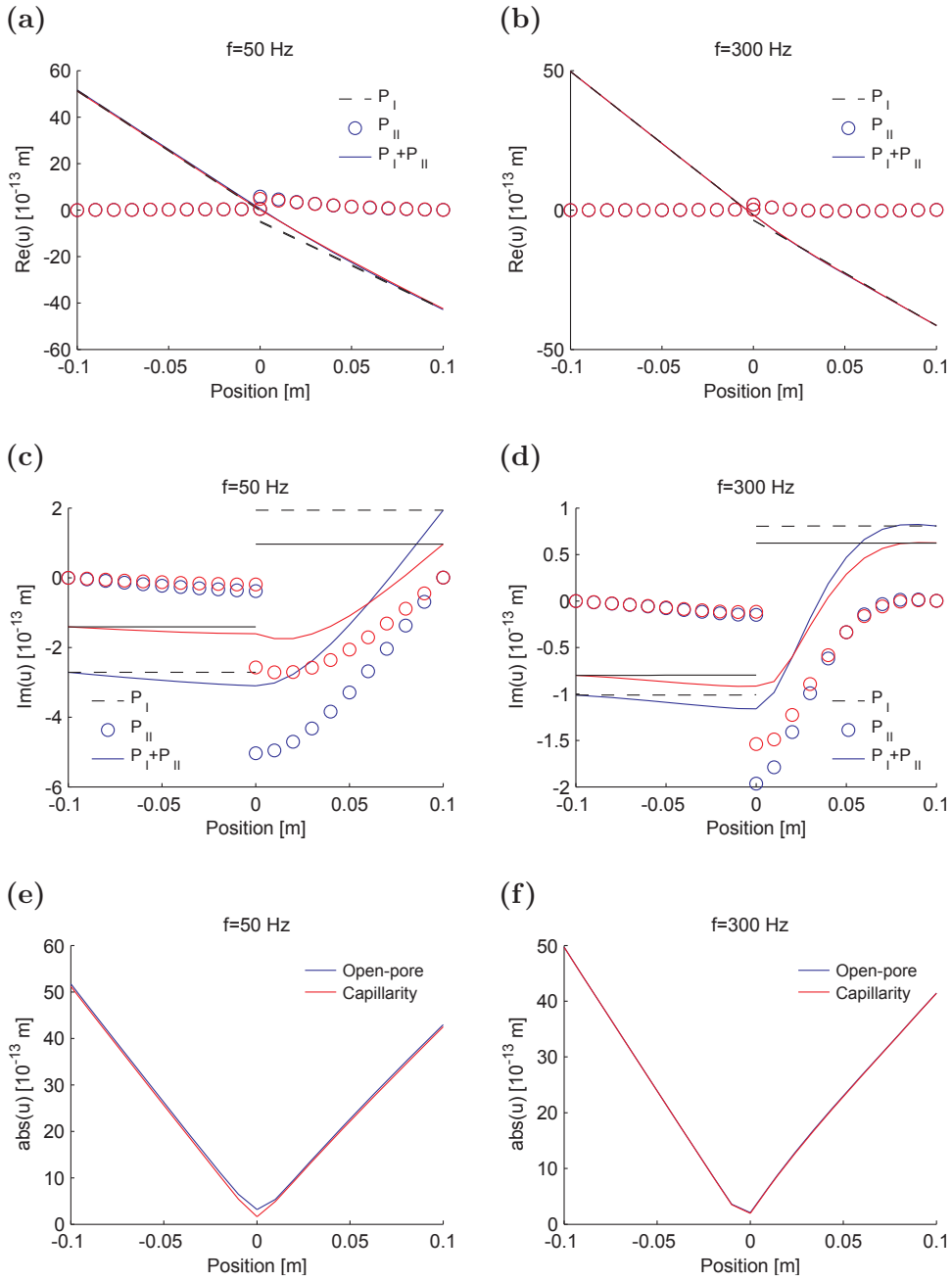

Figure 3.5: The real part (a), imaginary part (c) and amplitude (e) of solid displacement at 50 Hz while (b),(d),(f) show their high frequency (300 Hz) counterpart. The blue colour refers to open-pore case whereas red colour refers to capillarity case. The dashed line refers to fast P-wave component whereas the circle corresponds to slow P-wave component. The total component is indicated by solid line.

capillary pressure, namely the dynamic definition or the petrophysical definition, has the same origin which is due to the surface tension.

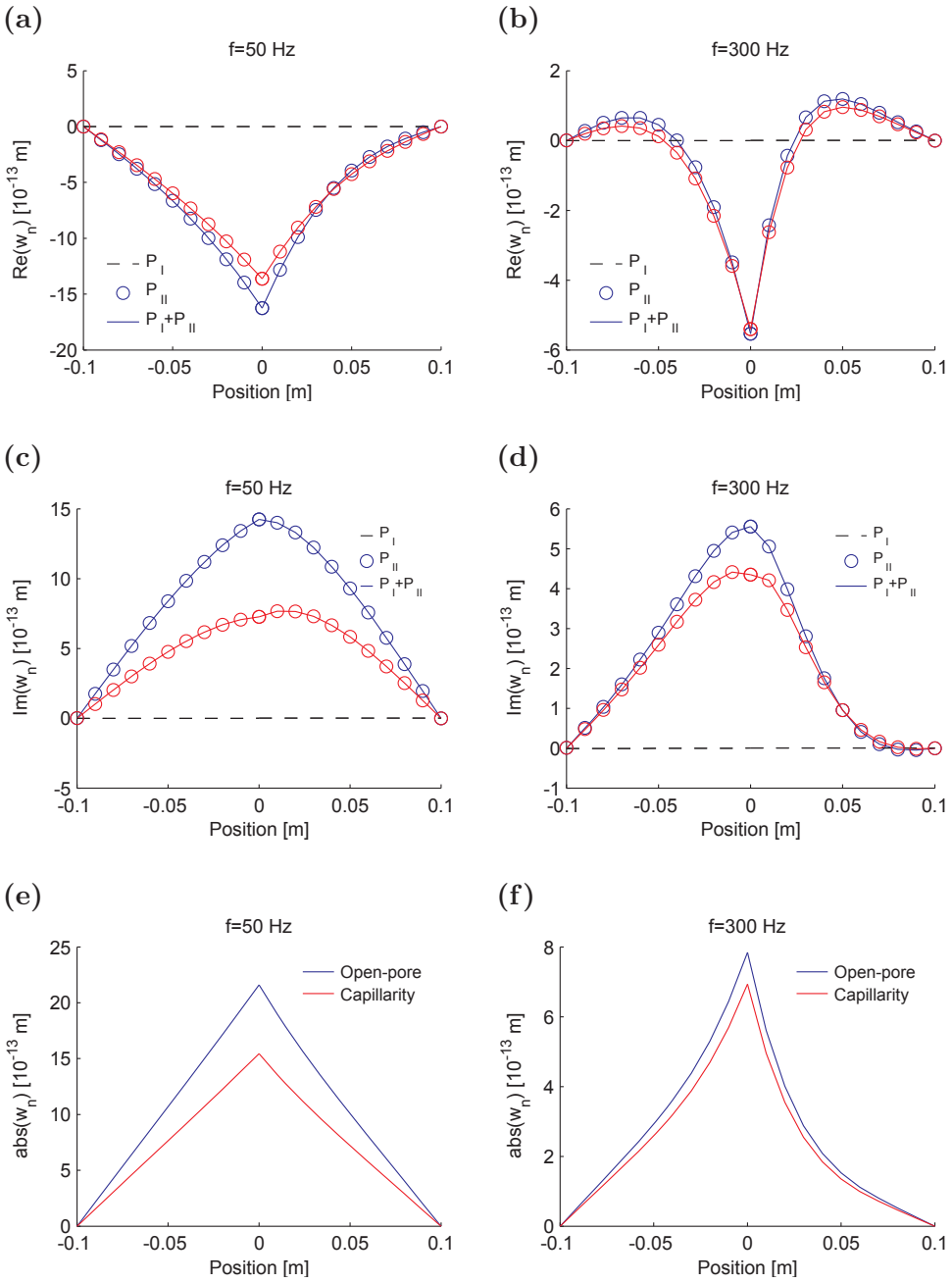

Figure 3.6: The real part (a), imaginary part (c) and amplitude (e) of relative displacement at 50 Hz while (b),(d),(f) show their high frequency (300 Hz) counterpart. The blue colour refers to open-pore case whereas red colour refers to capillarity case. The dashed line refers to fast P-wave component whereas the circle corresponds to slow P-wave component. The total component is indicated by solid line.

The pressure difference associated with capillarity and imperfect hydraulic contact (IHC) are plotted as function of frequency in Figure 3.7c. The capillary pressure decreases with increasing frequency whereas the pressure difference

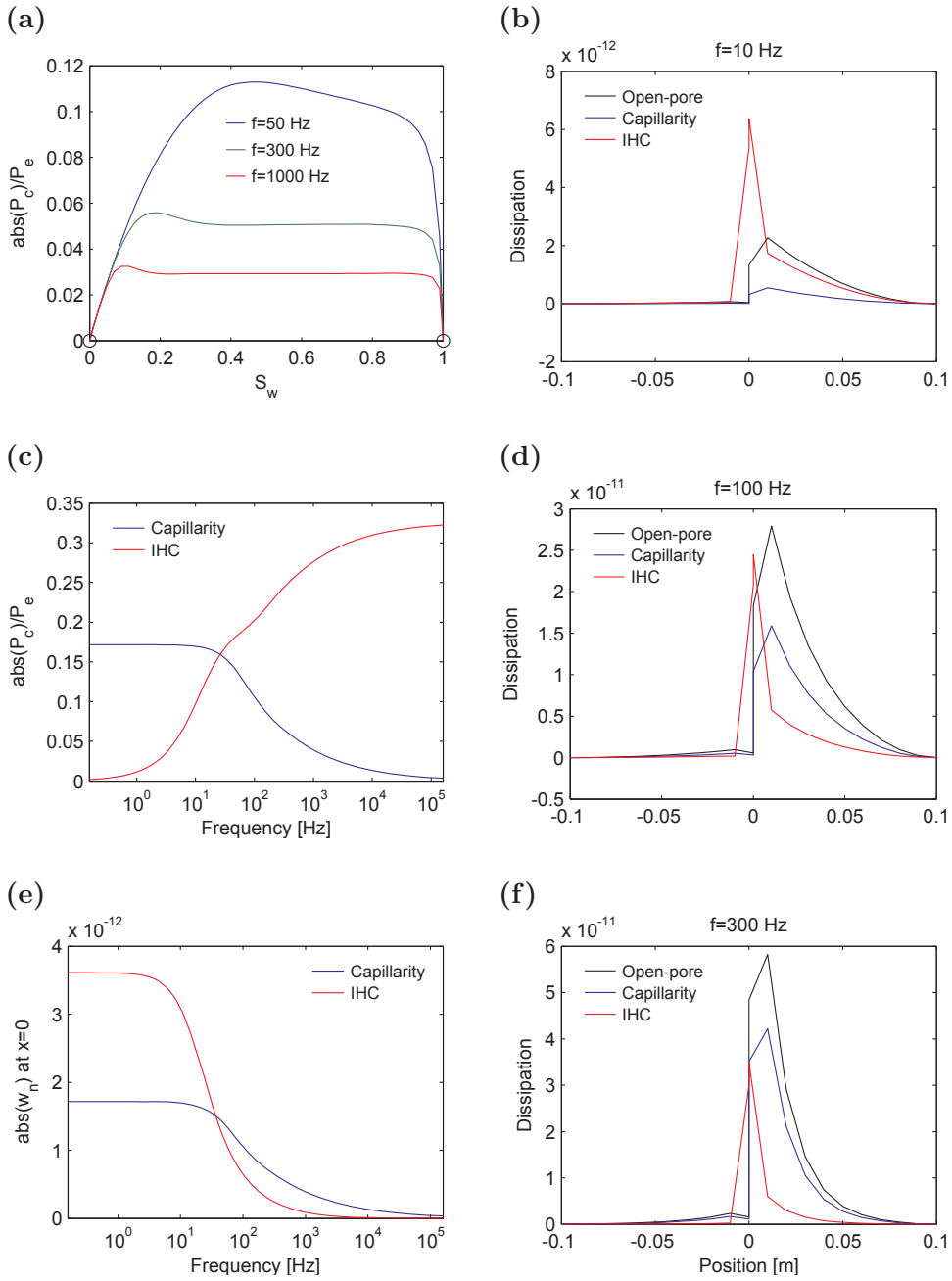

Figure 3.7: (a) Capillary pressure is plotted as function of water saturation for different frequencies. (c) Pressure difference and relative displacement at interface (e) are plotted as function of frequency. Dissipation at frequency of 10 Hz (a) 100 Hz (b) and 300 Hz.

due to IHC increases. Figure 3.7e shows the corresponding relative displacement at the interface. As can be seen, both capillarity and IHC result in decreasing relative displacement with increasing frequency. Last but not the least, the dissipation resulting from capillarity and IHC is examined in Figure 3.7b,d,f for three

different frequencies. The dissipation due to capillarity is always smaller than that for the open-pore scenario. On the other hand, dissipation due to IHC is highest at low frequency and it decreases with increasing frequency. The characteristics of the dissipation clearly explains the observed attenuation behaviours in Figure 3.2.

3.6 Chapter conclusions

A pressure jump boundary condition has been incorporated into the expression for the effective P-wave modulus of a partially saturated porous medium, which appears in form of an interfacial impedance (equation 3.24). This generalizes the original White's model wherein continuity of the fluid pressure at the gas-water interface is implicitly assumed.

Imperfect hydraulic contacts across fluid patches do not alter attenuation and dispersion in magnitude, but only decrease the characteristic frequency. It can be explained by that the imperfect hydraulic contacts give rise to an interface permeability which reduces the effective permeability of the rock, and consequently the characteristic frequency. Therefore, if one infers the size of fluid patches from attenuation estimates based on the original White's model, there will be a bias towards overestimating the patch size. Correspondingly, relating a measured wave velocity to saturation can result in substantial misinterpretation (e.g., in Figure 3.3a the proximity to the GH bound is unrelated to the fluid patch size). This might have important implications for understanding the role of interlayer flow in sand-shale sequences. Similarly, these results may have impact in estimations of permeability from seismic signatures.

The effect of capillarity on inter-layer flow can be modelled by an imaginary interfacial impedance. This membrane stiffness leads to an elevated low-frequency velocity and decrease in attenuation. The presence of interfacial impedance significantly changes the dynamic poroelastic fields, i.e., fluid pressure, relative fluid-solid displacement. Consequently, it affects the dissipation resulting from the oscillatory fluid flow and explains the attenuation behaviours.

Since capillary forces control the formation of fluid patches (Zhang et al., 2014), the generalized White's model can be useful in the assessment of the corresponding acoustic signatures in laboratory settings. The developed model

can be further extended to the study of inhomogeneous rock formations. This is of particular interest if, in addition to fluid saturation, aligned fractures complicate the analysis of attenuation (Amalokwu et al., 2014).

In conclusion, the generalized White's model for seismic attenuation and dispersion generates new modelling choices arising in the presence of an interfacial impedance. Though the underlying periodic double layer geometry may, in certain cases, be too simple to resemble real sedimentary records, the generalized model provides further insight into attenuation and dispersion due to inter-layer flow.

Chapter 4

Quantifying the effect of capillarity on attenuation and dispersion in patchy-saturated rocks

4.1 Summary

Waves in patchy-saturated rocks are attenuated through the mechanism of wave-induced pressure diffusion. We have shown in the last chapter that the characteristics of wave-induced pressure diffusion can be affected by the capillary pressure. On the other hand, previous studies revealed that attenuation and phase velocity dispersion can also depend on the fluid patch size and distribution. These patch characteristics in turn can be influenced by capillary forces. In this chapter, we investigate the combined effects of fluid distribution and capillarity on acoustic signatures. To do so we make use of the concept of patch membrane stiffness as a macroscopic expression of capillarity. We incorporate the membrane stiffness into the continuous random media model of patchy saturation. The membrane stiffness is associated with a pressure discontinuity at patch interfaces. This pressure discontinuity impedes wave-induced pressure diffusion and, therefore, reduces wave attenuation. Conversely, the phase velocity increases due to additional capillarity reinforcement. We apply this capillarity-

extended random media model to interpret velocity- and attenuation-saturation relations retrieved from an ultrasonically monitored core flooding experiment. As the fluid distribution is approximately known from accompanying computerized tomographic images, all but one required model input parameters can be inferred. The elusive input parameter is a shape factor quantifying the geometrical irregularity of the pore channels. We find, however, that the experimental data can be consistently modeled only if the capillarity effect is accounted for. The results suggest that wave-induced fluid pressure diffusion at mesoscopic patches in conjunction with capillary action can have important implication for interpreting ultrasonic velocity- and attenuation-saturation relations in patchy-saturated rocks.

4.2 Introduction

Quantification of seismic wave velocities in fluid-saturated, reservoir rocks and their variations due to production-induced saturation changes are of prime importance in seismic time-lapse studies (Calvert, 2005). However, seismic velocities do not only depend on the degree of saturation of each fluid phase but also on their spatial distribution. This observation is corroborated by laboratory experiments involving different measurement techniques (Murphy et al., 1984; Knight and Nolen-Hoeksema, 1990; Cadoret et al., 1995; Monsen and Johnstad, 2005; Alemu, 2012). Two end-member scenarios are typically employed to model the velocity-saturation relation (VSR). Uniform saturation refers to fluid mixing at the smallest scale, say pore-scale, whereas patchy saturation assumes the existence of sub-wavelength-scale fluid pockets. The P-wave velocity in the patchy-saturated case is larger than for the uniform saturation case (Mavko and Mukerji, 1998). Analysis of experimental data shows that the velocities often are between these uniform and patchy bounds (Shi et al., 2007; Caspari et al., 2011). One mechanism that explains the deviation from these bounds is broadly known as mesoscopic wave-induced fluid flow (WIFF, see Müller et al., 2010 for a review). It entails an oscillatory, relative fluid-solid movement induced by seismic waves and results in wave attenuation and dispersion due to dissipation. The magnitude of attenuation and dispersion in partially saturated rocks depends on the fluid compressibility contrast. So, one can expect significant attenuation if oil and gas is heterogeneously distributed, while little attenuation is expected for low compressibility contrast combination, e.g., oil and water. In turn, the characteristic frequency of WIFF attenuation and dispersion is controlled by the fluid mobility,

i.e., the ratio of permeability and fluid viscosity, and the characteristic length scale of the fluid patches. Modelling and interpretation of VSRs and associated WIFF attenuation and dispersion due to mesoscopic heterogeneities has been addressed in several studies (Tserkovnyak and Johnson, 2001; Pride et al., 2004; Toms et al., 2007a; Müller et al., 2008; Lei and Xue, 2009; Rubino and Holliger 2012; Tisato and Quintal, 2013).

A recent series of laboratory experiments allows us to gain further insights into the formation of fluid patches during forced water imbibition into air-dry rock samples and the accompanying evolution of ultrasonic P-wave velocity with saturation (Lebedev et al., 2009; Lopes and Lebedev, 2012; Lopes et al., 2014). X-ray computer tomography scans yield saturation images for the ultrasonically monitored rock volume during the course of water imbibition. These saturation images suggest that fluid patches are formed at the millimetre-scale. As these patches extend over the pore spaces in between several grains but are smaller than the dominant ultrasonic wavelength, we will refer to them as mesoscopic fluid patches. Theoretical and experimental works of two-phase flow associated with imbibition suggest that the fluid distribution for immiscible flows is controlled by the interplay between viscous and capillary forces. Specifically, the relative importance of the capillary effect can be quantified by either the capillary number (see equation 1.1) or the critical flow ratio (see equation 1.2). In the experiments of Lopes et al. (2014), the capillary number and the critical flow ratio are on the order of 10^{-9} and 10^{-3}, respectively. Therefore, both the numbers indicate that flow regime during the forced imbibition is dominated by capillary forces.

The capillary force underpinning saturation distribution has been implemented by Knight et al. (1998) and Rubino and Holliger (2012) to study the effect of fluid patches on seismic signatures of WIFF. The direct effect of capillarity on acoustic properties itself is neglected in these works. However, there is experimental evidence that capillarity can lead to changes in elastic stiffnesses and hence to changes in wave velocities and attenuation (Moerig et al., 1996; Averbakh et al., 2010). Then, the question arises how capillary forces affect the velocity-saturation relation. This is a particular interesting problem in the presence of mesoscopic fluid patches. While capillary forces only exist at fluid-fluid interfaces at the pore-scale, one might expect that they produce a net effect up in scale (De la Cruz et al., 1995), thereby creating a new attribute of the mesoscopic patches.

Based on the work of Nagy and Blaho (1994), Tserkovnyak and Johnson (2003) analysed the effect of capillary forces for patchy-saturated porous rocks. Their analysis is based on an idea that capillary forces cause a discontinuity of pore fluid pressure at the boundary of neighbouring fluid patches. This pressure discontinuity is proportional to the average surface displacement of the fluid. The poroelastic boundary condition is then

$$p - p' = W\phi(U_n - u_n), \tag{4.1}$$

where p and p' denote the fluid pressure in each patch, U_n and u_n represent the normal fluid and solid displacement components, ϕ is the porosity. W is a phenomenological parameter that can be interpreted as a membrane stiffness (Nagy and Blaho, 1994). It has a unit of Pa/m. In the absence of capillary forces this membrane has zero stiffness, $W = 0$. Then the fluid pressure continuity boundary condition of poroelasticity is recovered, $p = p'$ (Deresiewicz and Skalak, 1963; Bourbié et al., 1987; Gurevich and Schoenberg, 1999). Based on the Young-Laplace equation, Nagy and Blaho (1994) argue that W, at macroscale, has the form (see section 2.8 for details)

$$W = s\frac{\gamma}{\kappa}. \tag{4.2}$$

Here s is a shape factor accounting for the irregularity of pore spaces (see also Nagy and Neyfeh, 1995). In the presence of capillary forces, Tserkovnyak and Johnson (2003) find that the membrane tension effectively seals the patches into distinct regions so that fluid communication is impaired. This results in a fluid stiffening effect yielding higher P-wave velocities. At the same time, WIFF across the patches is diminished so that attenuation and dispersion become less pronounced. These results have been also found by Markov and Levin (2007) using equation (4.1) in a multiple scattering analysis for an assemblage of spherical poroelastic heterogeneities. None of these predictions has been verified by comparison with experimental data.

The aim of this chapter is two-fold. First, we extend the random patchy saturation model of Toms et al. (2007a) so that the effect of capillary forces is incorporated. In order to do so we draw from the result of Tserkovnyak and Johnson (2003) for the low-frequency approximation of the undrained P-wave modulus. The construction of this capillary-extended random patchy saturation model

is motivated by the fact that experimental evidence suggests that mesoscopic patches are not only randomly distributed but also of random shape (Toms et al., 2009). Moreover, in core flooding experiments these random patch shapes change over time and, therefore, with saturation. This dependency can be incorporated in the random patchy saturation model. Second, the imbibition experiments of Lopes and Lebedev (2012) and Lopes et al. (2014) provides the opportunity to apply this model to the experimentally derived velocity- and attenuation-saturation relations. It also serves as a validation of the above-mentioned predictions with respect to the fluid stiffening effect and reduction of WIFF attenuation. In fact, it will be shown that all but one parameter entering the capillarity-extended random patchy saturation model can be derived from the experimental data. The only unconstrained parameter is the shape factor appearing in equation (4.2). While previous estimations of this shape factor have been obtained for relatively simple porous media, here the possibility arises to invert for s in a carbonate rock with rather complicated pore structure.

4.3 Model for random patchy saturation including capillary pressure

4.3.1 Static limit

Gassmann-Wood theory

The immiscible fluids can be seen as homogeneously mixed at pore scale when the frequency of the incident wave is sufficiently low or the characteristic fluid patch size is much smaller than the diffusion length

$$\lambda_d = \sqrt{\frac{\kappa N}{\omega \mu_{\mathrm{f}}}}, \tag{4.3}$$

where κ is the flow permeability, μ_{f} the shear viscosity, ω the angular wave frequency, and N is a combination of poroelastic moduli specified below.

In absence of capillarity, the pore pressure continuity condition $p = p'$ holds valid at the fluid patch interfaces. In this case, the static P-wave modulus can be

predicted by the Gassmann-Wood equation (Johnson, 2001)

$$H^{\mathrm{GW}} = L + \alpha^2 M(K_{\mathrm{f}}^{\mathrm{W}}), \tag{4.4}$$

with the effective fluid bulk modulus $K_{\mathrm{f}}^{\mathrm{W}}$ given by Wood's equation

$$K_{\mathrm{f}}^{\mathrm{W}} = \left(\sum_{i=1}^{n} \frac{S_i}{K_{\mathrm{f}i}} \right)^{-1}. \tag{4.5}$$

The P-wave modulus of the drained frame is given by $L = K_0 + 4/3\mu$. The fluid storage modulus is $M = [\phi/K_{\mathrm{f}} + (\alpha - \phi)/K_{\mathrm{s}}]^{-1}$, and $\alpha = 1 - K_0/K_{\mathrm{s}}$ is the Biot-Willis coefficient. K_0 and μ denote the bulk and shear modulus of the drained frame. K_{s} and K_{f} are the bulk modulus of the solid and fluid phase, respectively. S_i denotes the saturation of the ith fluid.

Static limit including capillary action

When the assumption of vanishing capillary force is relaxed, the Gassmann-Wood prediction is not valid any more. Generally, capillary forces exist when the porous rock is saturated with two immiscible fluids. Due to joint action of adhesive and cohesive intermolecular forces, the edges of the wetting fluid in a pore space preferentially adhere to the pore wall. It forms a meniscus at the pore fluid interface. This results in a surface tension and a local pressure difference. At macroscopic scale, the upscaled effect of the capillary forces leads to a macroscopic pressure difference across the fluid patch boundary. This is captured by the boundary condition equation 4.1.

According to Tserkovnyak and Johnson (2003), the introduction of the pressure discontinuity boundary condition 4.1 into macroscopic poroelastictiy framework, results in a rescaled static undrained bulk modulus. Following their approach, we re-derive the static modulus using Biot constitutive relations for an isotropic and homogeneous saturated poroelastic solid (Biot, 1962)

$$\tau_{ij}^{(m)} = [(H^{(m)} - \phi C^{(m)} - 2\mu)e_{ii}^{(m)} + \phi C^{(m)} \epsilon^{(m)}]\delta_{ij} + 2\mu e_{ij}^{(m)}, \tag{4.6}$$

$$p_{\mathrm{f}}^{(m)} = (\phi - \alpha^{(m)}) M^{(m)} e_{ii}^{(m)} - \phi M^{(m)} \epsilon^{(m)}, \tag{4.7}$$

where τ_{ij} is the total stress, p_{f} is the fluid pressure. The undrained P-wave modulus is $H = K_{\mathrm{ud}} + \frac{4}{3}\mu$. The undraineded bulk modulus is $K_{\mathrm{ud}} = K_0 + \alpha^2 M$ and $C = \alpha M$. The strains of the solid phase e_{ij} and fluid phase ϵ relate to the displacement fields via $e_{ij} = (u_{i,j} + u_{j,i})/2$ and $\epsilon = \nabla \cdot \mathbf{U}$. The superscript m designates the mth phase. For composites consisting of isotropic and uniform phases, the overall undrained bulk modulus can be computed by (Hill, 1964)

$$K^*_{\mathrm{ud}} = \frac{1}{3}\frac{\langle \tau^{(m)}_{ii} \rangle}{\langle e^{(m)}_{ii} \rangle}. \tag{4.8}$$

The angle brackets $\langle \cdot \rangle$ denote volume average of the poroelastic fields within a representative elementary volume. Such a representative elementary volume is subjected to either sealed or periodic boundary condition. By extending the theory of Hill (1964) to account for the boundary condition 4.1, the static undrained bulk modulus K^*_{ud} involving capillarity can be derived analytically. The detailed derivation is given in Appendix A. Then, we can also compute the static undrained P-wave modulus $H^* = K^*_{\mathrm{ud}} + \frac{4}{3}\mu$. We find

$$H^* = \frac{z + T}{\dfrac{z}{H^{\mathrm{GW}}} + \dfrac{T}{H^{\mathrm{GH}}}}. \tag{4.9}$$

The parameter z is defined as

$$z = \frac{L}{H_1 S_1} + \frac{L}{H_2 S_2}\,. \tag{4.10}$$

The parameter T is

$$T = \frac{W}{s_{\mathrm{v}}}, \tag{4.11}$$

where s_{v} is the specific surface area (SSA) of the mesoscopic fluid patches. H^* is a monotonically increasing function of T (see Appendix A). A numerical example of $H^*(T)$ is given in Figure 4.1 for a limestone sample at 58% water saturation. The other properties of the limestone can be found in Table 4.1.

As shown Figure 4.1, if $T \to 0$, the static modulus reduces to the Gassmann-Wood modulus, H^{GW}. This suggests that the fluid pressure is fully equilibrated for vanishing T. For intermediate values of T ($0 < T \lessgtr \dfrac{H^{\mathrm{GH}}}{H^{\mathrm{GW}}} z$), H^* is proportional to the membrane stiffness W and inversely proportional to the specific surface area of the fluid patches. The capillary pressure now persists between the fluid patches

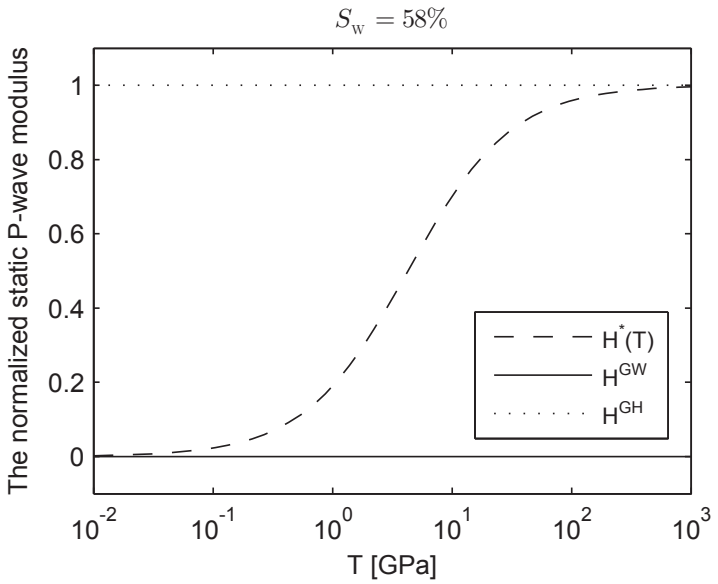

Figure 4.1: Normalised static undrained P-wave modulus is plotted as a function of capillarity stiffening T for 58% water saturation (the solid blue line); the black solid line denotes the Gassmann-Wood limit while the dotted line denotes the Gassmann-Hill limit.

and will affect the pressure diffusion process. As the parameter T controls the significance of capillarity on wave-induced pressure diffusion, we refer to it as the capillarity stiffening parameter. When the rock is saturated with a single fluid, the capillarity vanishes and the capillarity stiffening T becomes zero. Therefore, the static modulus 4.9 reduces to the Gassmann-Wood modulus (equation 4.4).

4.3.2 No-flow limit

The Gassmann-Hill (GH) theory applies when the frequencies of the passing wave are sufficiently high or patch size is much larger than the diffusion length. Then, there is insufficient time for the fluid pressure to equilibrate. Spatially variable pressure results in a spatially variable bulk modulus while the shear modulus is uniform. In this limit, Hill's theorem can be used to determine the P-wave modulus of the saturated rock via harmonic averaging of the P-wave moduli:

$$H^{\mathrm{GH}} = \left(\sum_{i=1}^{n} \frac{S_i}{H(K_{\mathrm{f}i})} \right)^{-1}, \tag{4.12}$$

where $H(K_{\mathrm{f}i})$ denotes the P-wave modulus of the rock saturated with ith fluid with bulk modulus $K_{\mathrm{f}i}$.

If the capillarity stiffening $T \gg \dfrac{H^{\mathrm{GH}}}{H^{\mathrm{GW}}} z$, the static modulus 4.9 results in the Gassmann-Hill modulus. This implies the fluid pressure becomes piecewisely constant throughout the porous medium. The undrained medium approaches the no flow condition as the membrane tension locks the fluid patch and therefore prevents pressure equilibration. Figure 4.1 illustrates this point by showing that the P-wave modulus approaches to GH limit when capillarity stiffening becomes strong. We refer to these conditions (either $\omega \to \infty$, or $T \to \infty$) as the no-flow limits.

4.3.3 Mesoscopic wave-induced pressure diffusion

For intermediate frequencies the uneven deformation of fluid patches caused by the passing wave results in mesoscopic WIFF. This leads to wave attenuation and velocity dispersion which can be modeled by the 3D continuous random model (also known as 3DCRM, Toms et al., 2007a). This model is developed on the basis of the generalized 3D poroelastic model of Müller and Gurevich (2005). The basic assumption of the model is that the fluid saturation is a statistically uniform random function of position. The behaviour of this random function is quantified by an autocorrelation function.

As discussed above, the presence of the membrane tension gives rise to a change in the static limit of the saturated bulk modulus. More specifically, the effect of capillary force rescales the static undrained bulk modulus from $K_{\mathrm{ud}}^{\mathrm{GW}}$ to K_{ud}^{*}. The capillarity-extended P-wave modulus H^* can be incorporated in the CRM model by renormalizing the effective P-wave modulus with the low-frequency limit. Then, the capillarity-extended CRM model (CCRM) can be written as

$$\widetilde{H}^*(\omega) = H^* \left[1 + \delta^* (\tau \tilde{\xi}^2 + (\tau - 1)\tilde{\xi})\right] , \tag{4.13}$$

where $\delta^* = \frac{H^{\mathrm{GH}} - H^*}{H^*}$ signifies the magnitude of dispersion and ensures that the model converges to the known low and high frequency limits. The frequency dependence is contained in the function

$$\tilde{\xi}(\omega) = \tilde{k}_{\mathrm{ps}}^2 \int_0^\infty r\chi(r) \exp(i\tilde{k}_{\mathrm{ps}} r) dr \, , \tag{4.14}$$

where $\tilde{k}_{\mathrm{ps}} = \sqrt{\frac{i\omega\mu_{\mathrm{f}}}{\kappa N}}$ is the Biot slow P-wavenumber. The factor τ in equation 4.13

Table 4.1: Petrophysical properties of rock and fluids

Rock	K_0 (GPa) [a]	K_s (GPa) [b]	μ (GPa) [a]
Limestone	10.04	70	9.26
	ρ_s (g/cm^3)	κ (mD)	ϕ
	2.65	91	26.5%
Fluids	K_f (GPa)	ρ_f (g/cm^3)	μ_f (Pa · s)
Water [c]	2.25	1.04	1e − 3
Gas (Air)	1e − 4	1e − 3	1e − 5
Supercritical CO_2 [d]	0.046	0.62	7e − 5

[a] K_0 and μ are computed using $K_0 = \rho_0 V_p^2 - (4/3)\mu$, $\mu = \rho_0 V_s^2$, the velocities V_p, V_s and density ρ_0 of the drained frame are experimentally acquired.

[b] Grain modulus of calcite (Mavko et al, 2009), as it constitutes 98% of Savonnières limestone.

[c] The surface tension for water and gas (air/supercritical CO_2) is 7.3e − 2 (N/m) at 25°C.

[d] Lei and Xue (2009).

is given by

$$\tau = \frac{\alpha^2 N}{4\bar{H}} \cdot \sigma_{_{MM}}^2, \tag{4.15}$$

where $N = \bar{M}L/\bar{H}$. The background P-wave modulus $\bar{H}$ is obtained from the background fluid storage modulus $\bar{M} = \langle M(K_{fi})\rangle$ via $\bar{H} = L + \alpha^2\bar{M}$. The normalized correlation function is $\chi(r)$ and the normalized variance (variance of the fluid storage moduli of the mesoscopic patches normalised by their mean value) is $\sigma_{_{MM}}^2$. The fluid patch geometry-related parameters $\chi_{_M}(r)$ and $\sigma_{_{MM}}^2$ can either be assumed or quantified through CT images. Equation 4.13 converges to the CRM prediction when the membrane tension is absent, $T = 0$. The characteristic frequency of CCRM model can be obtained by equalling the heterogeneity size a and the diffusion length λ_d. We have

$$f_c = \frac{\kappa N}{a^2 \mu_f}. \tag{4.16}$$

In order to show how the capillary action affects the acoustic properties, we study the frequency- and the saturation- dependence of velocity and attenuation predicted by CRM and CCRM models. Different correlation lengths are chosen to model various fluid distributions. The correlation function is of the form $\chi_{_M}(r) = \exp(-\frac{|r|}{a})$. The properties of the rock and pore fluids (water and supercritical CO_2) used for the numerical example are specified in Table 4.1.

For $T = 12$ GPa at 58% water saturation, we plot the P-wave velocity and reciprocal quality factor as a function of normalized frequency using both models. Figure 4.2a shows that the CCRM model predicts a higher P-wave velocity in the low frequency limit if compared with the CRM prediction, thereby causing a reduction of dispersion. This increase in velocity is caused by an increase of the effective fluid patch stiffness due to the capillarity effect. This results an overall stiffening of the rock frame. The membrane stiffness strengthens the patch interface and therefore weakens the relative flow between the fluids and solid. This results in lower attenuation (Figure 4.2b). Meanwhile, larger correlation lengths result in a shift of dispersion and attenuation towards lower frequencies.

The saturation-dependent acoustic properties at a frequency of 0.5 MHz with a constant correlation length $a = 1$ mm for different T values are presented in Figure 4.3a, 4.3b. Substantial deviation of the static limit from Gassmann-Wood limit is observed. The difference in velocity predictions by CRM and CCRM models reaches maximum at 80% water saturation. When T is increasing from 0 GPa to 7 GPa, the peak of the attenuation reduces by 45%. At full saturation, W vanishes as this corresponds to the case of a single fluid. Hence, the CRM and CCRM results coincide. Interestingly, the effect of capillarity on velocity is more pronounced below the characteristic frequency of mesoscopic flow, as the velocity difference between two models vanishes at high frequencies. On the other hand, the discrepancy in attenuation is insensitive to frequency.

Assuming that the fluid distribution is two-phase (e.g., water and gas) and exponentially-correlated. The specific surface area (SSA) of the fluid patches can be expressed as function of correlation length via (Blair et al., 1996; Toms et al., 2007a)

$$SSA = 4 \times \frac{S_w \cdot S_g}{a} \ . \tag{4.17}$$

Figure 4.4a shows the dependence of SSA on the correlation length for different water saturations. Rock and fluid properties from Table 3.1 is used to illustrate the relation here. Applying this relation in the capillarity stiffening 4.11 and further in the CCRM model, we are now able to study both velocity dispersion and capillarity-extended static velocity, their dependence on the fluid distribution (e.g., correlation length) in a joint fashion. Figure 4.4b shows the dependence of the capillarity-extended static velocity on the correlation length for various saturation. It is interesting to see that the static velocity, despite their dependence

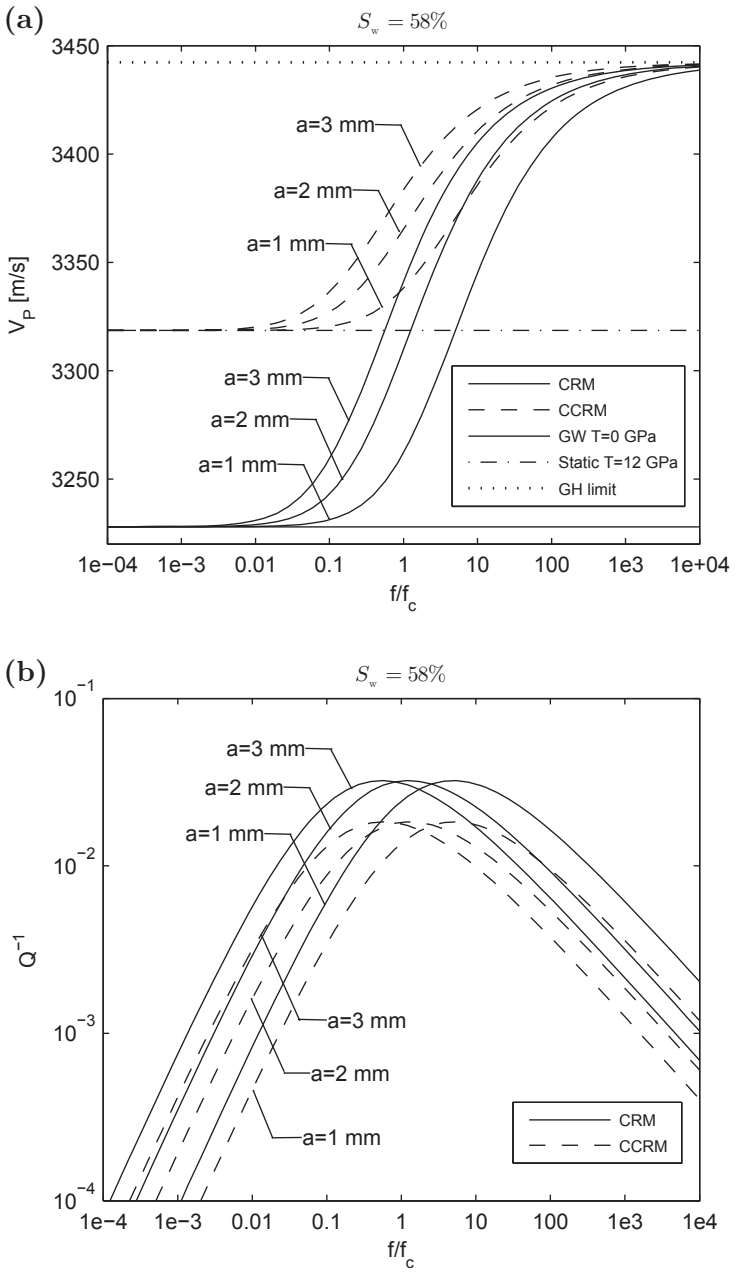

Figure 4.2: (a) Velocity dispersion and (b) attenuation of the CRM ($T = 0$ GPa) and CCRM ($T = 12$ GPa) modelled at 58% water saturation. The correlation lengths are $a = 1,\ 2,\ 3$ mm (the correlation function if of the form $\exp(-\frac{|r|}{a})$). The frequency f is normalized by critical frequency f_c which is defined by equation 4.16.

on saturation, increases with increasing correlation length. This is because, according to Figure 4.4a, the SSA decreases with increasing correlation length. A decreased SSA according to equation 4.11 corresponds to an increased capillarity stiffening effect. The velocity dispersion and attenuation after applying relation

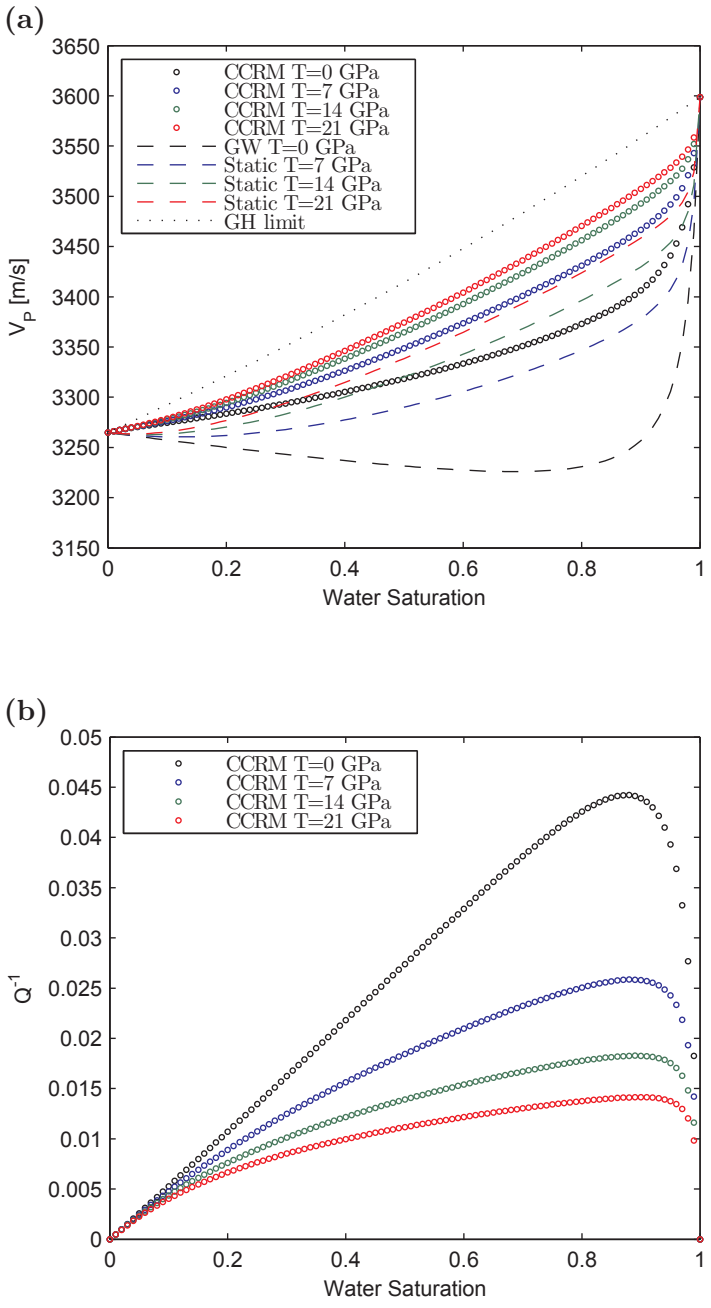

Figure 4.3: Velocity- (a) and attenuation- (b) saturation relations predicted by CRM ($T = 0$ GPa) and CCRM ($T = 7,\ 14,\ 21$ GPa) models at 0.5 MHz. The correlation length is assumed to be $a = 1$ mm.

4.17 is given in Figure 4.5. In Figure 4.5a, an increasing correlation length not only results in a shift of velocities towards lower frequency but also increases the static velocities. In other words, when the fluid distribution is described by larger correlation length, stiffening effects from both WIFF and capillarity jointly con-

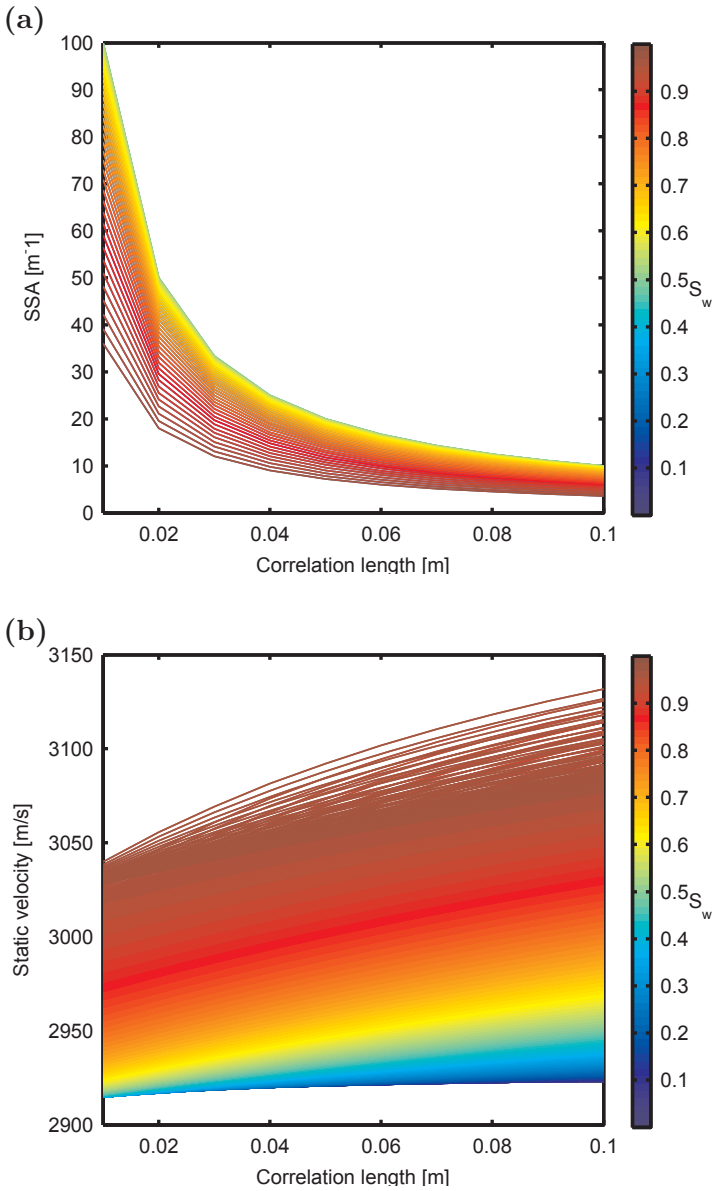

Figure 4.4: (a) Specific surface area (SSA) and (b) capillarity-extended static velocity are plotted as function of correlation length for different water saturations.

tribute to a larger velocity at low frequencies. On the other hand, for attenuation shown in Figure 4.5b, capillarity effect becomes less pronounced for decreasing correlation length.

4.3.4 Joint effect of capillarity and fluid distribution

In this section, capillarity-extended patchy saturation models with respect to different fluid distribution consideration are compared. The fluid distribution

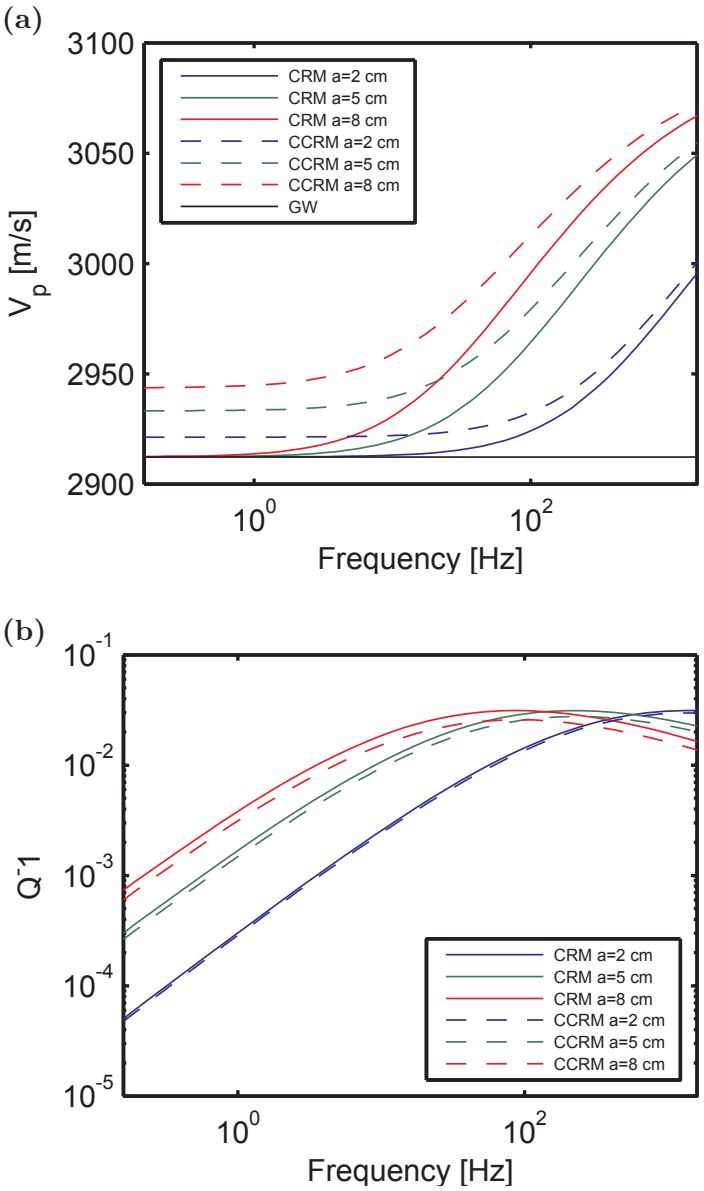

Figure 4.5: (a) Velocities and attenuation predicted by CRM and CCRM model for different correlation lengths. The stiffening effects due to capillarity and WIFF both depend on correlation length.

considered here are layered model (chapter 3), random model (this chapter) and spherical gas-pocket model (details of this model is not included). A membrane stiffness of $W = 300$ GPa/m, a gas saturation of 30% are employed in the calculation. The layering period d for layered model, outer radius R_b for gas-pocket model and correlation length for random model are set to be the same as 0.2 meter. The specific surface area for the layered model can be calculated as (Johnson,

2001)

$$SSA = \frac{2}{d} \ . \tag{4.18}$$

For the gas-porket model, the SSA is given by (Johnson, 2001)

$$SSA = \frac{3R_a^2}{R_b^3} \ , \tag{4.19}$$

where R_a is the inner radius of the gas pocket. The corresponding SSA for the random model is calculated using equation 4.17. Therefore, the resulting SSAs for 30% gas saturation consideration are 6.7 m^{-1} for the gas-pocket model, 5 m^{-1} for layered model and 4.2 m^{-1} for random model. The resulting velocity and attenuation predicted by these models are given in Figure 4.6. We can see clearly different levels of capillarity stiffening resulting from models with different fluid distribution consideration. At seismic frequencies, the attenuation predicted from capillarity-extended layer model and gas-pocket model are smaller comparing to the original White's model. However, the attenuation given by the capillarity-extended random model overtakes the attenuation given by the original White's model at lower frequencies. This observation points out that the dispersion and attenuation in partially saturated rocks can be jointly controlled by capillarity and fluid distribution. In addition to the patchy saturation models, there exists a class of models describing the acoustics in porous rocks saturated with two immiscible fluids wherein capillary pressure is incorporated using a three phase (two fluids and one solid phase) extension of the Biot poroelasticity framework (Santos et al., 1990; Tuncay and Corapcioglu, 1997; Lo et al., 2005; also see section 2.6). Therein a second slow P-wave is reported in presence of capillary pressure. In order to have a comprehensive comparison of the results between our models and the extended Biot models (EBM), we choose the model of Lo and Sposito (2013). They provide an explicit formula for calculating the undrained fast P-wave modulus. To model the various hysteresis processes of two phase flow, different capillary pressure saturation relations are employed in the modelling. The results are shown by black circles in Figure 4.6a. Interestingly, the fast-wave velocity predicted by the EBM model shows less sensitivity to the capillary pressure. Moreover, the numerical results coincide with Gassmann-Wood prediction. Therefore, it seems that the P-wave modulus given by Lo and Sposito (2013) is a static approximation. Direct comparison with our observation, if one assumes non-vanishing capillarity, then Gassmann-Wood result can only be achieved via a presence of large specific surface area. Therefore, it is meaningful to understand

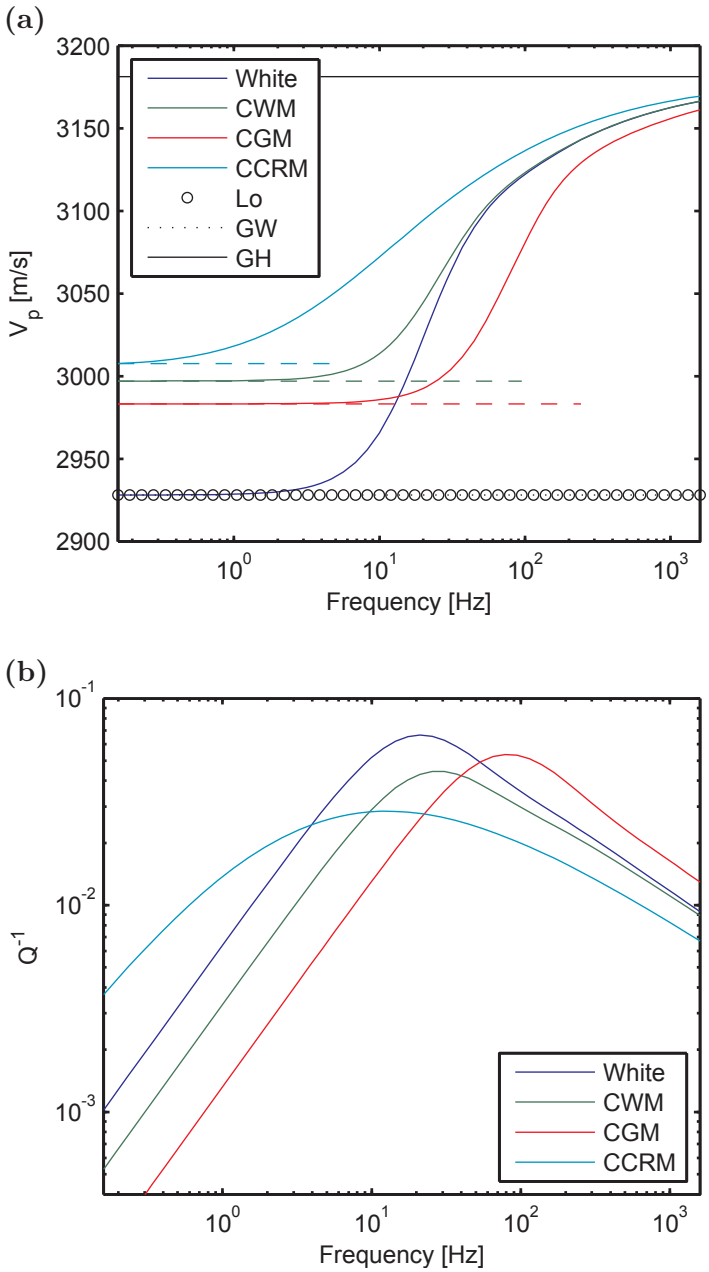

Figure 4.6: Comparison of (a) velocity and (b) attenuation predicted by models of different fluid distribution consideration. 'White' refers to White's original model; 'CWM' refers to capillarity-extended White's model; 'CGM' refers extended gas-pocket model; 'CCRM' refers to extended random model; 'Lo' refers to acoustic model of Lo and Sposito (2013).

the assumption of the fluid distribution behind EBM model.

In Figure 4.3a, 4.3b, the velocity- and attenuation- saturation relations are plotted using saturation-independent correlation length and specific surface area.

However, in a realistic case the specific surface area and the correlation length both depend on the saturation in a non-trivial manner. Thus T will also be a function of saturation. The merit of the capillarity-extended random model is that the fluid distribution and its related parameters, that is, the specific surface area (equation 4.11), correlation function (equation 4.14), normalized variance (equation 4.15) as well as degree of saturation can be estimated from CT images of the porous rock. In the following sections, we apply capillary-extended random model to interpret the velocity- and attenuation- saturation relations drawn from ultrasonic data.

4.4 Modelling the saturation-dependent velocity and attenuation

4.4.1 Simultaneous acquisition of X-ray CT and acoustics during water imbibition

Experimental set-up and ultrasonic waveforms

Lopes et al. (2014) perform an experimental study to understand the dependence of velocity-saturation relations on the injection rate. The main part of the laboratory set-up is illustrated in Figure 4.7a. It involves forced water imbibition into a Savonnières limestone cylinder via an injection pump. The mantle surface of the rock sample was wrapped up by epoxy allowing the flow direction to be vertical. Two plastic rings were glued to each end of the rock with a hole in the center. The injection pump was connected to the bottom hole, and distilled water was imbibed vertically through the hole, displacing air through the top hole. The direct contact of top hole with the atmospheric pressure minimizes the pressure build-up. Imbibition was performed at room temperature with an initial rate of 2 mL/h at the first 4 hours, followed by a decrease of injection rate to 0.2 mL/h for 15 hours, and then restored 2 mL/h for the rest 3 hours.

Ultrasonic measurements are conducted as the water saturation changes. By using ultrasonic transducers, P-wave and S-wave waveforms at 1 MHz propagating in the direction perpendicular to the core axis are recorded. The resulting waveforms are shown in Figure 4.7b. These waveforms reveal a reduction in am-

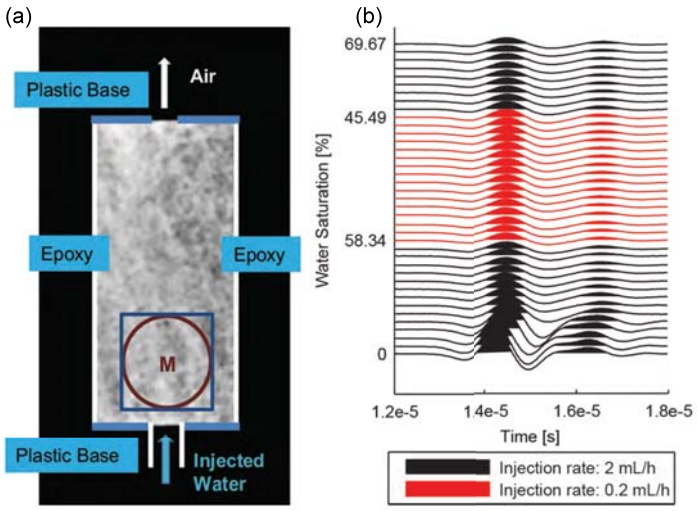

Figure 4.7: (a) Measurement set up and raw CT scan of the sample: the red circle indicates the acoustic monitoring field; (b) The ultrasonic waveforms at various saturations. The black waveforms correspond to an injection rate of 2 mL/h while the red waveforms correspond to a reduced injection rate of 0.2 mL/h.

plitude with increased water imbibition. Velocities are calculated by picking the first-break of the output waveforms. For more elaborated velcity extraction procedures we refer to Zhubayev and Ghose (2012). As we assume isotropic samples with low attenuation, the velocity estimated by this method should be close to the phase velocity (Cadoret et al, 1995). The central frequency of 0.5 MHz of the received waveforms, which can be identified from the spectral amplitudes as shown in Figure 4.8, are only half of the inputs. This is attributed to attenuation during wave propagation.

Simultaneously, the distribution of fluid phases during the imbibition process is captured by a medical X-ray scanner. CT images are taken along the axial cross section and contain information on fluid distribution. This time-space monitoring allows us to link P-wave velocities with its corresponding saturation level and saturation pattern. By assuming the limestone sample is macroscopically homogeneous and isotropic, the local saturation of the selected slice is statistically representative of the local saturation of the sample. For further details of the experimental set-up, we refer to Lopes et al. (2014).

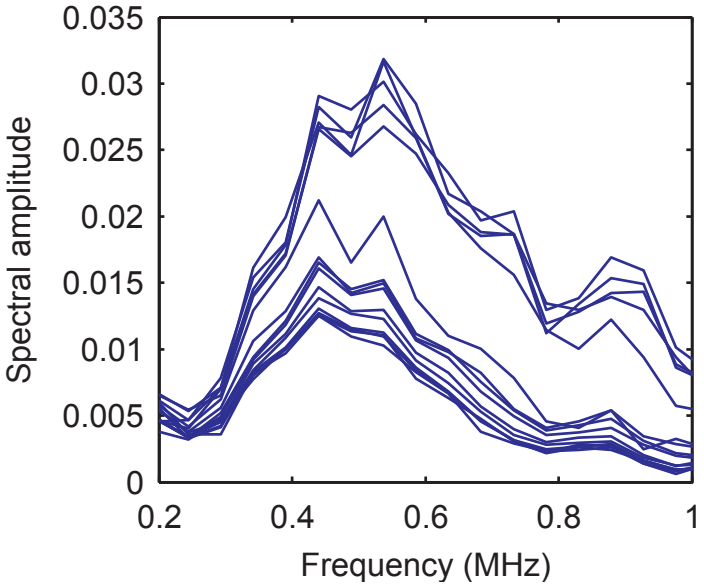

Figure 4.8: Spectral amplitudes of the ultrasonic waveforms.

CT images and resulting saturation maps

A square section M in Figure 4.7a of pixel size 128×128 (30 mm $\times$ 30 mm) is cut out from the original CT scan (512×512). This section represents the local saturation of the acoustically monitored volume. The voxel size of the medical X-ray scanner is 0.2mm $\times$ 0.2mm $\times$ 1mm, and we filter the image by convolving it with a 5×5 square matrix consisting of unity, as X-ray adsorption is five times stronger in z-dimension. Though the resolution is limited, the view area is relatively large and this allows us to quantify fluid patches at the mesoscopic scale.

Based on the raw CT scans, we create saturation maps. The CT value of each pixel is converted from intensity to the local saturation level. The details of saturation map constructing procedure is given in Appendix B. In Figure 4.9, it can be seen that mesoscopic fluid patches arise. Figure 4.9 illustrates that the characteristic patch size increases with saturation in the first four saturation maps when saturation is under 60%. At large saturations, there are no observable changes in the patch size. Each fluid patch spans a few millimetres.

For our analysis we choose four CT images consecutively scanned at injection rate $q = 2$ mL/h (before the rate change) and four at injection rate $q = 2$ mL/h (after rate change). The capillary number using equation 1.1 is 2.5×10^{-9}. The

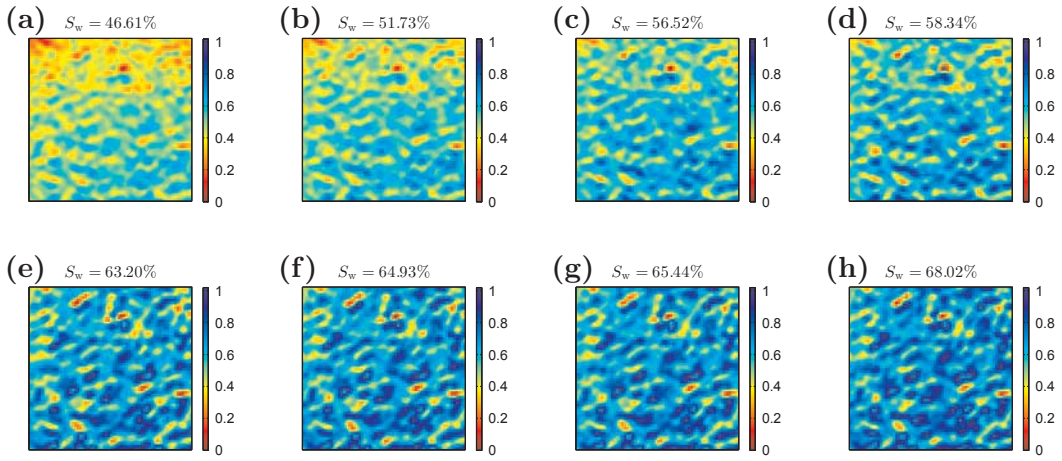

Figure 4.9: Water-saturation maps at different imbibition stages, where dark blue represents full water saturation and dark red represents full gas (air) saturation. The saturation maps are constructed from the raw CT scans for the monitoring area. The size of the maps is 3 cm × 3 cm. The colour-bar indicates water saturation.

Table 4.2: Spatial correlation information for water-saturation maps

S_w	a_D *	RMS_{single}	a_S *	a_L *	b_L	RMS_{double}	$s_v(m^{-1})$
46.61%	2.26	0.1088	0.5783	8.0632	0.3668	0.0316	665.25
51.73%	1.38	0.0944	0.6108	8.7186	0.2513	0.0319	744.84
56.52%	0.97	0.0652	0.6392	8.3566	0.1591	0.0302	803.61
58.34%	0.85	0.0572	0.6510	11.4104	0.1058	0.0308	820.16
63.20%	0.70	0.0310	0.6382	10.3231	0.0402	0.0255	837.72
64.93%	0.67	0.0253	0.6340	9.9458	0.0266	0.0226	852.83
65.44%	0.65	0.0258	0.6135	10.4476	0.0288	0.0223	842.84
68.02%	0.58	0.0198	0.5471	9.6817	0.0208	0.0176	840.75

* all correlation length is in unit of millimetre.

small capillary number indicates that the capillary forces contribute to the formation of the mesoscopic fluid distribution. The saturation map contains information about water saturation in the local pore space. Therefore local saturation of the acoustically monitored volume can be obtained by averaging value for all pixels $S_w = \frac{1}{n}\sum_{i=1}^{n} S_w^i$, where n is the total number of pixels. More importantly, the saturation map reflects the alteration of the fluid mixture pattern in 3D space. Hence, we can extract the fluid variation information quantitatively using statistical tools. More precisely, our CCRM model requires information on the correlation function and length, the specific surface area and the variance of the fluid storage modulus. Next, we introduce how to extract the morphological information from the CT images.

4.4.2 Extraction of correlation function, specific surface area and variance

To extract second order statistics from the saturation maps in Figure 4.9, these maps have to be converted into binary maps. To achieve this, we follow the statistical processing procedure of Toms et al (2009). Firstly, a global-threshold segmentation is applied, it segments the map into water and gas domains using the pixel mean distribution value, while preserving most morphological features of the water-saturation map. In Appendix C we explain the procedure to extract the two-point correlation function and autocovariance function. In Figure 4.10a, the solid blue curve represents the two-point correlation function $\mathcal{S}_2$ extracted from $S_{\mathrm{w}} = 58\%$ saturation map. For values of the correlation lag near 0, the slope of $\mathcal{S}_2$ is related to the specific surface area (SSA) s_{v} of the fluid patches (Blair et al., 1996)

$$\mathcal{S}_2'(0) = -\frac{s_{\mathrm{v}}}{4}. \tag{4.20}$$

The SSA is defined as the ratio of the total surface area of the water-gas interface to the total volume of the saturated material. The slope $\mathcal{S}_2'(0)$ is obtained by linear fitting (red line in Figure 4.10a. The SSA values computed from each saturation map are listed in Table 4.2.

Eight images with medium to large water saturation ($46\% \sim 68\%$) are chosen to be analysed (Figure 4.9). We exclude maps with low water saturation, because the water-air interface (saturation front) has not passed the acoustically monitored volume. The normalized autocovariance functions for saturations 46% to 68% are plotted in Figure 4.10b. It can be seen that when the water saturation is below 60%, the autocovariance functions change as the fluid distribution alters (Figure 4.9a-4.9d). However, the last four correlation functions for water saturations above 60% show only subtle changes. This observation coincides with the fluid pattern in Figure 4.9e, 4.9h which becomes stable regardless of increasing water saturation.

In a next step these autocovariance functions are approximated by a statistical model to obtain closed form expressions for the P-wave modulus in the CRM and CCRM model. Here we choose the Debye correlation function (Debye and Bueche,

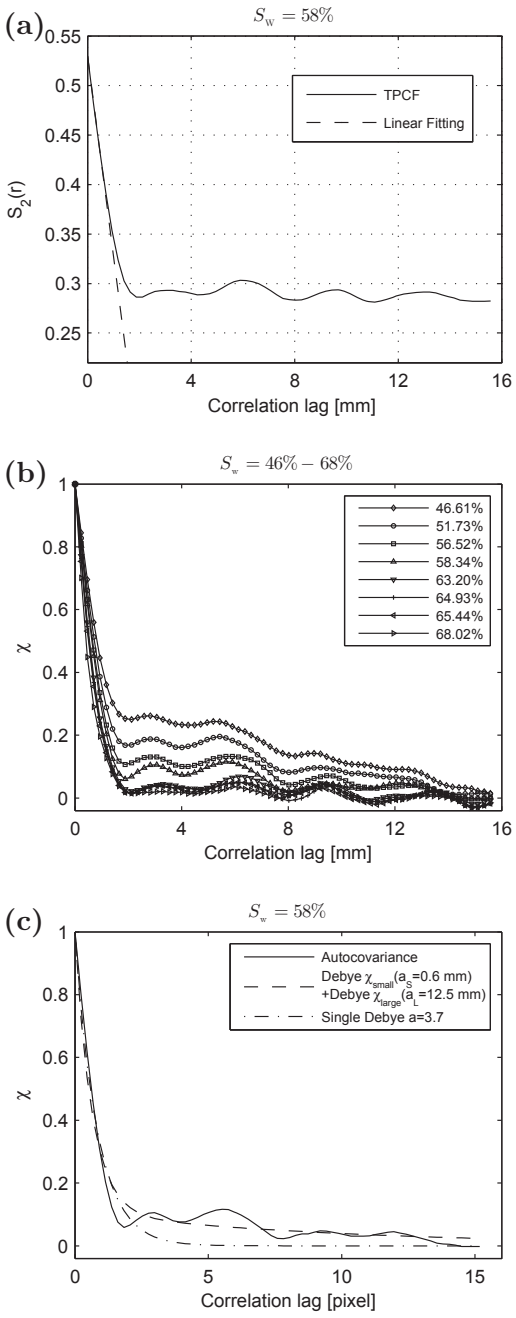

Figure 4.10: (a) Two-point correlation function (TPCF) of the binarized water-saturation map; (b) Normalised autocovariance functions extracted from the fluid storage modulus maps for different indicated water saturations; (c) Comparison between two approximation methods: single Debye model (black dashed line) and superposition Debye model (blue solid line). The red solid line is the autocovariance function at 58% water saturation.

1949) given by

$$\chi_N(r) = \sum_{i=1}^{N} b_i \exp\left(-\frac{|r|}{a_i}\right), \tag{4.21}$$

where a_i is the Debye correlation length and the weight coefficient b_i satisfies $\sum_{i=1}^{N} b_i = 1$, the subscript i gives the number of correlation length. However, a single Debye correlation function $\chi_1(r) = \mathrm{e}^{-|r|/a}$ approximates the autocovariance function only at small correlation lags (Figure 4.10c). Therefore, it is insufficient to use a single Debye correlation function to represent the fluid distribution statistically. To overcome this problem, a superimposed Debye function consisting of two exponential functions $\chi_2(r) = b_S \mathrm{e}^{-|r|/a_S} + b_L \mathrm{e}^{-|r|/a_L}$ is used. The RMS errors of the fitting is considerably reduced after employing the latter method (see Table 4.2). The correlation lengths $a_S = 0.6$ mm characterizes the size of the smallest patches while the other $a_L = 12.5$ mm indicates the presence of longer-range disorder, respectively. The correlation information is listed in Table 4.2. The superimposed correlation lengths are in effect equivalent to the average patch size 0.6 mm observed in Figure 4.9.

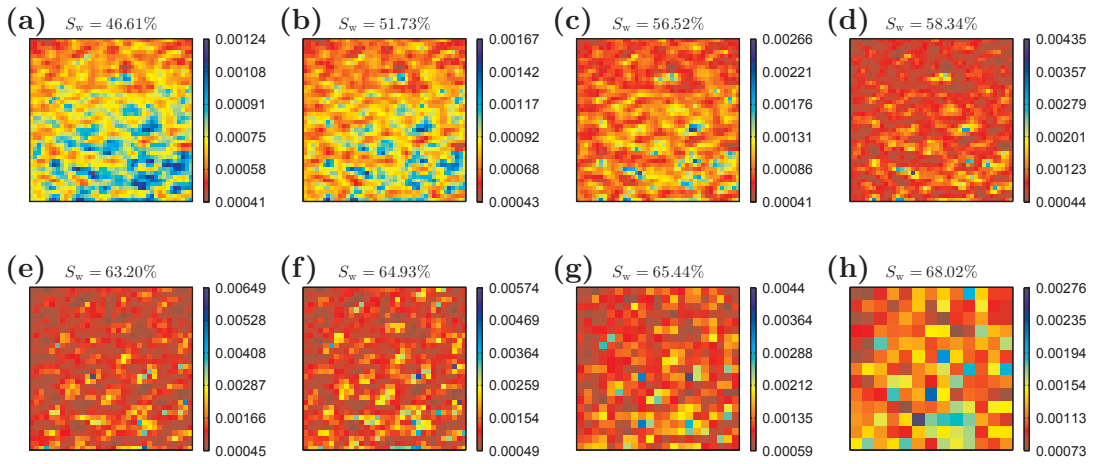

Figure 4.11: Partitioned fluid modulus maps for different water saturations. The colour-bar indicates the fluid storage modulus of the mesoscopic patch. Dark blue areas indicate a large fluid-modulus (GPa), while dark red areas indicate a small modulus. Note, that the colour-bars have different scalings to better represent the variability of the fluid moduli at each saturation.

The normalized variance of the fluid storage modulus σ^2_{MM} is a measure of the compressibility contrast of the mesoscopic fluid patches. This variance is computed at the patch-scale level instead of each unit cell in order to preserve the patch-to-patch contrast. The detailed procedure is given in Appendix C. Figure 4.11 shows the maps constructed at each saturation level. As water saturation grows from 46.6% to 64.9%, the normalized variance increases from 0.03 to 0.23. This can be explained by the fact that at higher water saturation, part of the fluid

patches reach almost full water saturation ($S_{\mathrm{w}} > 90\%$). The effective fluid bulk modulus of these particular patches can be $10^3 \sim 10^4$ times larger than for patches below 90% saturation. This water stiffening effect results in a drastic fluctuation of the fluid storage modulus between the patches. For water saturations over 64.9% the stiffening effect is dominated by the patch-size. As higher saturations form larger fluid patches, these larger patches average the exceptionally high-moduli of small patches out. This results in smoothed fluctuations and smaller normalized variances.

4.4.3 Modelling the experimental data

The saturation S_{w}, fluid distribution function $\chi_2(r)$ and fluctuation strength $\sigma^2_{_{MM}}$ are now estimated from the CT images. With incorporation of all other poroelastic parameters into equation 4.13, the frequency-dependent P-wave modulus $\widetilde{H}^*(\omega)$ is determined. The phase velocity and attenuation (inverse quality factor) are then given by

$$v(\omega) = \sqrt{\frac{\Re\{\widetilde{H}^*(\omega)\}}{\bar{\rho}}}, \quad Q(\omega)^{-1} = \frac{\Im\{\widetilde{H}^*(\omega)\}}{\Re\{\widetilde{H}^*(\omega)\}}. \tag{4.22}$$

Here, $\bar{\rho} = (1-\phi)\rho_{\mathrm{s}} + \phi(S_{\mathrm{w}}\rho_{\mathrm{w}} + S_{\mathrm{g}}\rho_{\mathrm{g}})$ is the average density with $\rho_{\mathrm{s}},\ \rho_{\mathrm{w}},\ \rho_{\mathrm{g}}$ the density of mineral grain, water and gas, respectively. The angular frequency $\omega = 2\pi f_{\mathrm{EXP}}$, where $f_{\mathrm{EXP}} = 0.5$ MHz is the central frequency of the ultrasonic waves. The petrophysical properties of Savonnières limestone and fluids are specified in Table 4.1.

CRM interpretation

Let us first compare the velocities-saturation relations (VSR) deduced from the experiment with the predictions of the CRM model. Figure 4.12 shows the experimental VSR (the red squares) and the VSR generated by the CRM model (the black diamonds). We also extrapolate the CRM prediction to higher saturations ($S_{\mathrm{w}} = 80\%, 85\%, 90\%, 95\%, 99\%$), where no experimental data is available. As discussed earlier, at high water saturations, the fluid compressibility contrast between mesoscopic patches is small. This makes the parameter τ given by equation 4.15 negligible. Thus, equation 4.13 reduces to $\widetilde{H}^*(\omega) = H^*(1 - \delta^*\tilde{\xi}(\omega))$. Given

that the autocovariance function can be well fitted by a single Debye correlation function when $S_w > 80\%$, we use a single correlation length inferred from gas saturation map ($S_g = 1\%, 5\%, 10\%, 15\%, 20\%$) of Toms et al (2009) for $\chi_M(r)$ approximation. The results are plotted in Figure 4.12 (black diamonds). Both experimental velocities and the CRM simulations show weak saturation dependence. Error bars for the experimentally derived velocities are used to account for errors in the travel time picking. The velocities at saturations over 80% start to increase, suggesting that the rock stiffening effect dominates over the density effect at this saturation. This can be explained as a result of larger fluid patches ($a \gg \lambda_d$) forming at higher water saturations. Then the proximity to the Gassmann-Hill bound is expected.

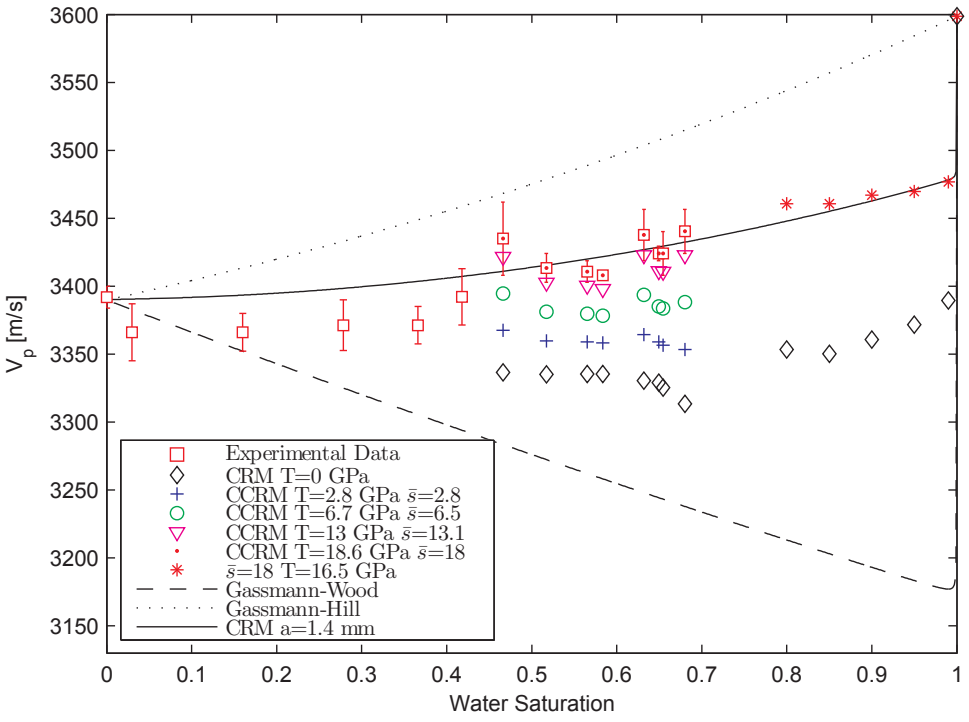

Figure 4.12: Comparison between experimentally observed and theoretically predicted VSRs at 0.5 MHz. Red squares denote the experimental velocities and black diamonds are the CRM predictions. Dots, triangles, circles and crosses are modelling results of the CCRM model for different values of the capillarity stiffening T. The values of T and the values of the shape factor $\bar{s}$ are averaged over saturations. The dashed line indicates the GW bound and the dotted line indicates the GH bound. The solid black line shows the CRM prediction for a correlation length of $a = 1.4$ mm. Red asterisks are forward modelled velocities at higher saturations based on an average shape factor $\bar{s}_{t=1}$.

We note that the CRM predictions are on average 80 m/s lower than the experimental values. The solid black line in Figure 4.12 shows for which characteristic patch size the CRM model would correctly approximate the velocities. Mesoscopic fluid distribution correlated by a single Debye function $\chi_1(r)$ with a constant correlation length of 1.4 mm could explain the experimental data. However, no evidence of such patch correlation has been found from CT images. As shown above, the fluid distribution is best described by a double Debye correlation function with parameters specified in Table 4.2.

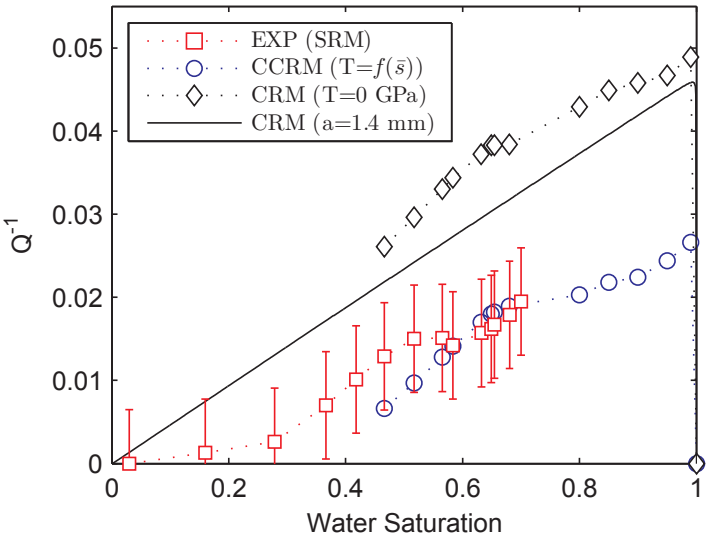

Figure 4.13: Comparison between experimentally observed and theoretically predicted ASRs at 0.5 MHz. Red squares show the inverse quality factor obtained from the measured waveforms (spectral ratio method (SRM)) and the error bars indicate the standard deviation; black diamonds are the modelling results of the CRM model; blue circles are the modelling results of the CCRM using the inversely modelled shape factor $\bar{s}_{t=1} = 18$ from velocity matching.

The experimentally determined attenuation-saturation relation (ASR) is plotted in Figure 4.13. The inverse quality factor Q^{-1}_{EXP} is obtained by applying the spectral ratio method (SRM) on the amplitude spectrum of the received waveforms. In order to avoid the additional attenuation caused by the initial water weakening effect (Lopes et al., 2014), we choose the spectral amplitude of the wetted rock of 3% water saturation as the reference amplitude. The error bars indicate the possible shifts of the attenuation due to different choice of the reference amplitude. There is a little 'plunge' of the ASR curve at 58% water saturation as we exclude the low injection rate period. After the saturation reaches 62% the injection rate is reduced from 2 mL/h to 0.2 mL/h, and it recovers 2

mL/h at 63% water saturation. During the low injection rate period, an increase in wave amplitude is observed (see Figure 4.7b, the red waveforms). Thus, a relative small attenuation associated with change of injection rate takes place. The available data over saturation $46\% \sim 68\%$ shows that the quality factor Q given by CRM model is $38 \sim 26$. This is lower than the experimental quality factor $78 \sim 51$. In other words, the CRM model overestimates the attenuation. Using the correlation length obtained by fitting the VSR with a single Debye correlation function with $a = 1.4$ mm, we also estimate the corresponding attenuation, indicated by solid line in Figure 4.13. Comparing with the attenuation predicted using image-extracted correlation lengths $a \approx 0.6$ mm (as discussed earlier, the superimposed correlation length is equivalent to the observed fluid patch size), the attenuation is slightly lower. This is due to the fact that the experimental frequency is slightly above the characteristic frequency of the mesoscopic flow. In this particular frequency range, a larger correlation length results in a lower attenuation, see also Figure 4.2b.

The discrepancy in phase velocities and attenuation reveals that wave-induced pressure diffusion at mesoscale as described by the CRM model is insufficient for proper interpretation of the observed ultrasonic signatures. This velocity underestimation is possibly due to the fact that CRM ignores the additional patch stiffening in the presence of capillary forces. Correspondingly, neglecting the presence of capillarity-induced membrane stiffness at fluid patch boundaries causes an overestimation in viscous dissipation. This could explain the discrepancy in Q.

CCRM interpretation

Using the CCRM model, we predict the superimposed rock stiffening effect due to membrane tension and mesoscopic flow on acoustic properties. However, to model velocity and attenuation using equation 4.13, a value for the shape factor contained in the static undrained P-wave modulus H^* has to be assigned to Savonnières limestone. Based on membrane stiffness measurements, Nagy and Blaho (1994) calculate the shape factors using equation 4.2 for cylindrical pipes, synthetic beads and Berea sandstone. We are not aware of any shape factor estimate for limestones. Due to the lack of data for this parameter, we apply an inverse modelling procedure to extract the static P-wave modulus. Namely, we

choose certain value of the shape factor to fill the discrepancy between CCRM prediction and the experimental data. The validity of these chosen shape factor values will be discussed below.

In the CCRM model, the dynamic P-wave modulus $\widetilde{H}^*$ is complex and frequency-dependent, except for the two end-member cases, namely the static limit H^* and Gassmann-Hill limit H^{GH}, which are real-valued. Therefore, the velocity term is contained in the real part of the modulus $\widetilde{H}^*$, while the imaginary part contains information on attenuation. To obtain the shape factor, we first match the CCRM velocity prediction term with the target modelling velocity term (subscript m)

$$\Re(\widetilde{H}^*) = \Re(\tilde{H}_{\mathrm{m}}) = \bar{\rho} V_{\mathrm{m}}^2, \tag{4.23}$$

where $\widetilde{H}^*$ is obtained from equation 4.13. The velocity prediction is given by

$$V_{\mathrm{m}} = t(V_{\mathrm{EXP}} - V_{\mathrm{CRM}}) + V_{\mathrm{CRM}}, \tag{4.24}$$

where V_{EXP}, V_{CRM} are the experimentally observed velocity and the CRM velocity prediction (the black diamonds in Figure 4.12) respectively. The factor $t = \frac{V_{\mathrm{m}} - V_{\mathrm{CRM}}}{V_{\mathrm{EXP}} - V_{\mathrm{CRM}}}$ which varies between 0 and 1 is the normalised velocity discrepancy and $(V_{\mathrm{EXP}} - V_{\mathrm{CRM}}) \times t$ denotes the absolute velocity discrepancy. The complex part in the CCRM model (equation 4.13) is only contained in $\tilde{\xi}$ (equation 4.14) function. Therefore, by setting $\xi_0 = \Re(\tilde{\xi})$, equation 4.23 can be expressed as

$$H^*(1 + \frac{H^{\mathrm{GH}} - H^*}{H^*} D) = \Re(\tilde{H}_{\mathrm{m}}), \tag{4.25}$$

where $D = \tau {\xi_0}^2 + (\tau - 1)\xi_0$. The static P-wave modulus can be inverted through rearranging the above equation,

$$H^* = \frac{\Re(\tilde{H}_{\mathrm{m}}) - D \cdot H^{\mathrm{GH}}}{1 - D}. \tag{4.26}$$

At each saturation level, t is set to be $4\%, 18\%, 32\%, 45\%, 59\%, 73\%, 86\%, 100\%$. For each t level, we perform H^* inversion using equation 4.24 and equation 4.26 for each of the eight CT images. Correspondingly, the capillarity stiffening T can be solved from H^* using equation 4.9. The computed T at each velocity and saturation level are plotted in Figure 4.14a. We can see from Figure 4.14a that the inversely modelled values of T are closely associated with the absolute

velocity discrepancy (Figure 4.12) at each water saturation. Figure 4.14) also demonstrates that, at lower saturations, relatively larger T values are required to model a certain velocity level.

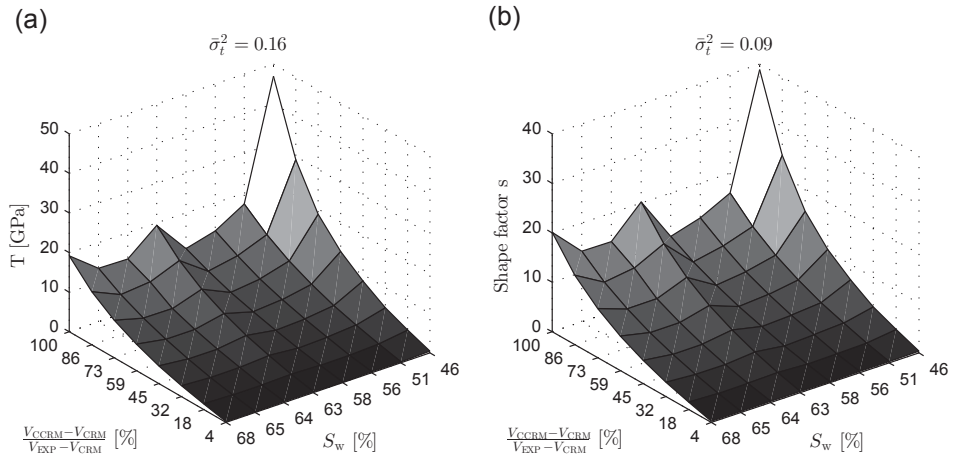

Figure 4.14: (a) Parameters of capillarity stiffening T plotted against normalised velocity discrepancy t and water saturation. (b) Shape factors plotted against normalised velocity discrepancy t and water saturation. The parameter $\bar{\sigma_t^2}$ is the average of the normalised variances of T (shape factor) for each t. The normalised variances are taken over all saturations at each t level.

The velocity prediction for $t = 32\%, 59\%, 86\%, 100\%$ are displayed in Figure 4.12. The influence of capillary force on VSR is examined by increasing T from zero (the CRM modeled velocities $T = 0,\ t = 0$) in Figure 4.12. For V_{m} accounts for $31\%, 58\%, 86\%, 100\%$ phase velocity discrepancy over $S_{\mathrm{w}} = 46\% \sim 68\%$, the mean T values are 2.8 GPa, 6.7 GPa, 13 GPa, 18.6 GPa respectively. The $\bar{T}$ denotes averaged T value deduced at each saturation. By substituting equation 4.2 into 4.11, we can invert for the shape factor s

$$s = \frac{s_{\mathrm{v}} \kappa T}{\gamma}. \tag{4.27}$$

Using of the SSA values extracted from the binary saturation maps, we obtain the associated shape factor at each level plotted in Figure 4.14b. The shape factors approximately share the characteristic of T in Figure 4.14a. However, the normalized variance of the shape factors of various saturations (averaged over the t levels) $\bar{\sigma_t^2} = 0.09$ is smaller than the normalized variance of T which is 0.16. This is due to fact that the shape factor is the intrinsic property of rock which

is a measure of the complexity of the pore structure (see section 2.8). Therefore, the shape factor tends to be constant at different saturations, and thus has a smaller normalized variance. The higher values of the shape factor at 46% water saturation are due to incorporation of a relatively small SSA into 4.27, as Figure 4.9a is not a strictly isotropic image, it results in a biased lower interfacial contact area after the segmentation (Table 4.2).

By making use of the mean shape factor $\bar{s} = \frac{1}{8}\sum s|_{t=1} = 18$ for which the CCRM model fully matches the experimental velocities, we predict the undrained P-wave velocities at higher saturations. The SSA values we used are inferred from the gas saturation maps ($S_{\mathrm{g}} = 1\%, 5\%, 10\%, 15\%, 20\%$) of a limestone (Toms, 2008) which can be regarded as a reasonable approximation for higher water saturations ($S_{\mathrm{w}} = 80\%, 85\%, 90\%, 95\%, 99\%$). In Figure 4.12 the modelling results are plotted by asterisks. Coincidentally, the data reside on the modelling results of WIFF arising between fluid distribution correlated by a single Debye function at 1.4 mm. This coincidence reveals that one must be careful when using CRM to do fluid distribution inversion, as neglecting capillarity can lead to a biased correlation relation. The larger SSAs value appeared at the end of the imbibition stages ($S_{\mathrm{w}} = 80\%, 85\%, 90\%, 95\%, 99\%$) result in decrease of the parameter T, see the legend of Figure 4.12. Due to lack of laboratory data at higher saturations, the modelling results cannot be corroborated.

To check the validity of the deduced shape factor, we compare the acoustic properties with respect to attenuation. We model the inverse quality factor using the mean shape factor $\bar{s} = 18$ (inverse modelled shape factors averaged over all saturations at 100% t level, Figure 4.14b). The results are plotted as ASRs against experimental Q^{-1}_{EXP} in Figure 4.13. The Q^{-1}_{CCRM} increases with water saturation from 0.006 to 0.026 and diminishes to zero at full saturation. Apart from a slight underestimation below 60% water saturation, the attenuation given by CCRM model overall matches with experimentally derived attenuation of the ultrasonic waves. The consistency confirms the reliability of the inversely modelled shape factor for Savonnières limestone. Therefore, we conclude that for the forced imbibition experiment where capillary forces are thought to be dominant, the combined effects of wave-induced pressure diffusion at mesoscopic patches and membrane stiffening in presence of capillary forces can consistently explain the velocity- and attenuation- saturation relations.

4.5 Discussion

Application of the CCRM model requires knowledge of the shape factor s appearing in equation 4.2. While all other parameters have been estimated from the available data set, we do not have a recipe to infer s. That is why s has been estimated by matching with the ultrasonic velocities (Figure 4.12) and then checking against the attenuation-saturation relation (Figure 4.13). Thus, s is only indirectly obtained by this consistency argument. It is interesting to note that our s estimate is larger than estimates that have been obtained from measurements on simple porous media (Nagy and Blaho, 1994). Even more, Nagy and Blaho (1994) argue that s is expected to be smaller than unity for complex porous media. Our choice of the shape factor can be also understood from the following consideration. The membrane stiffness for the simple pore geometry of a cylindrical tube can be written as (2.157)

$$W_s = \gamma/(\frac{\phi_s d^2}{8}), \tag{4.28}$$

where ϕ_s is the volume fraction of the tube, d is its radius. According to Kozeny-Carman relation, $\frac{\phi_s d^2}{8}$ equals the permeability of such a simple porous medium. The shape factor acts as a scaling parameter to account for irregularity of the pore space (Nagy and Blaho, 1994). By incorporating the shape factor s into equation 4.28, the membrane stiffness for a rock with complicated pore structure becomes

$$W = \gamma/\frac{\phi(\frac{d}{\sqrt{s}})^2}{8}. \tag{4.29}$$

If we assume that the form of Kozeny-Carman relation $\frac{\phi d_{\text{eff}}^2}{8}$ still holds for a porous medium with complex internal structure then an effective hydraulic radius will emerge, $d_{\text{eff}} = \frac{d}{\sqrt{s}}$. This is to say that the shape factor s simply expresses how an effective hydraulic radius emerges if pore channels are irregular and $s > 1$ means that the effective hydraulic radius is reduced. As much as capillary pressure increases for thin capillaries according to Young-Laplace equation, $s > 1$ only means that effect of capillary forces is boosted with respect to the hydraulic radius dependency. Therefore, if capillary action is significant, a s value larger than unity is perhaps expected.

The interpretation of the laboratory measurements based on the CCRM model only involves the mechanism of wave-induced pressure diffusion at mesoscopic fluid patches in conjunction with membrane stiffening. We briefly discuss other

mechanisms that could possibly affect the ultrasonic wave propagation in saturated porous rocks. Squirt flow between compliant pores (or micro-cracks) and stiff pores is a common mechanism of wave attenuation at ultrasonic frequencies (Müller et al., 2010). However, micro-CT images of Savonnières limestone show no such cracks. Furthermore, ultrasonic measurements show that pressure sensitivity of both P- and S-wave velocities is minimal. This indicates that compliant porosity is negligible and thus squirt flow attenuation can also be neglected. Attenuation due to elastic scattering is excluded as well. This is because the resonant frequency $f_{\text{scat}} = \frac{1}{2\pi a}\sqrt{\frac{\bar{H}}{\bar{\rho}}} = 0.6$ MHz at which the maximum elastic scattering takes place is slightly greater than the central frequency of the ultrasonic waves f_{EXP} (0.5 MHz). Apart from that, no evidence from the ultrasonic waveforms suggests the existence of scattering such as coda waves (Figure 4.7b).

The so-called Biot global flow dissipation mechanism is inherently coupled with the development of viscous boundary layer flow if the viscous skin depth becomes smaller than the pore throat thickness. Measurements in fluid saturated porous rocks with complex pore space structure and pore wall roughness indicate that dissipation in the viscous boundary layer due to vorticity diffusion results in an enhanced attenuation of ultrasound. Using the formalism of Müller and Sahay (2011), we compute the associated dispersion and attenuation with incorporation of pore-scale heterogeneity correlation information. The latter has been obtained by Müller et al. (2013) in the context of estimation the dynamic permeability. In order to quantify the proportion of viscous boundary layer flow effect in the partially saturated limestone, we firstly compare f_{EXP} with the Biot relaxation frequency given by

$$f_{\text{b}} = \frac{\mu_{\text{f}}\phi}{2\pi\kappa\rho_{\text{f}}S^{\infty}}, \tag{4.30}$$

where S^{∞} is the tortuosity of the pore space. It is the only unknown parameter. It can be estimated using the relation of Walsh and Brace (1984)

$$S^{\infty} = \sqrt{F\phi}, \tag{4.31}$$

where F is the formation factor. According to Archie's law,

$$F = \phi^{-m}, \tag{4.32}$$

where m is the cementation factor. For limestone of intergranular rock type we use $m = 2$ (Focke and Munn, 1987), so that $S^{\infty} = 1.9$. For gas saturated pore

space, f_{b} (2.6 MHz) is five times greater than f_{EXP}, and thus dispersion and attenuation is negligible. On the contrary, for the rock saturated with water, f_{b} (0.27 MHz) is comparable with f_{EXP}, dispersion due to vorticity diffusion is 17 m/s, whilst attenuation is still negligible. For a partially saturated rock, we take the saturation-weighted dispersion as the contribution to the rock stiffening effect. The result shows that 6% of velocity difference from the Gassmann-Wood bound can be attributed to Biot global flow dispersion.

As discussed above, the P-wave velocity difference predicted by CRM and CCRM models is expected to be significant below the characteristic frequency of mesoscopic pressure diffusion f_{c}. For the poroelastic parameters assigned to this Savonnières limestone sample, f_{c} is contiguous to the center frequency of the ultrasonic transducer. This explains why we observe that WIFF has a noticeable effect at ultrasonic frequencies. It is not clear if our findings can be extrapolated to the seismic frequency range. According to the CCRM model capillarity would affect seismic attenuation if the fluid patches become large enough, say a few centimetres. However, for such large fluid patches one can imagine that pore-scale heterogeneities in form of trapped fluid inclusions (say, air bubbles) affect the capillarity and possibly reduce the patch membrane stiffness. Moreover, Sengupta and Mavko (2003) argue that in typical reservoir flow simulations $R_{\mathrm{cv}} \gg 1$, i.e. capillary force is negligible as compared to viscous force. It requires further research to understand the effect of capillarity on large fluid patches.

In this study, the dispersion and attenuation are closely associated with fluid patch distribution, i.e. the experimentally-observed millimetre-scale fluid heterogeneities. Our data interpretation is sensitive to the results of the statistical analysis of the CT images. Therefore, the influence of fluid distribution rests on how much the mesoscopic fluid patch character has been preserved during image processing. The methodology we apply is based on the threshold value of the segmentation for correlation function extraction and on partitioning size for normalized variance calculation. The accuracy of the statistical characterization could be calibrated with improved image resolution.

4.6 Chapter conclusions

The random patchy saturation model is extended to include capillary action. The capillarity at the patch-scale involves two new parameters over the

random patchy saturation model: the interfacial tension between the two fluids and a shape factor accounting for irregular pore spaces. By construction, this capillarity-extended random patchy saturation (CCRM) model has a static limit which deviates from the Gassmann-Wood prediction. The capillary action leads to an additional stiffening thereby to higher phase velocities. It also implies a pressure discontinuity a patch interfaces so that wave-induced pressure diffusion process is weakened and attenuation is reduced. The joint stiffening effect from capillarity and wave-induced pressure diffusion becomes stronger when the fluid distribution is described by larger correlation length. To corroborate these CCRM predictions we model the experimentally-determined velocity- and attenuation-saturation relations for a forced imbibition experiment wherein the small capillary number suggests the presence of capillarity. The conclusions are as follows.

1. The experimentally-determined (ultrasonic) velocity-saturation relation cannot be modelled with either of the end-member models (theoretical bounds of the patchy saturation model), but results in velocities which fall in between the Gassmann-Wood and Gassmann-Hill bounds. Application of the spectral ratio method to the ultrasonic waveforms results in Q estimates on the order of 50-80 at 70% water saturation.

2. Saturation maps derived from CT scans indicate the presence of water patches at the millimetre-scale. The fluid patch distribution at consecutive imbibition stages is statistically described by autocovariance functions. The autocovariance function for medium water saturation 46%-68% can be well approximated by two superimposed Debye correlation functions.

3. The random patchy saturation model underestimates the ultrasonic velocities for all saturations while it over-estimates the attenuation. The CCRM model can provide a consistent prediction for the observed saturation relations for a certain choice of the shape factor. It is argued that the value of the shape factor $s > 1$ is expected if the capillarity effect is significant.

Our results suggest that the wave-induced fluid pressure diffusion between mesoscopic patches in conjunction with capillary action have implications for interpreting ultrasonic data in patchy-saturated rocks in flow regimes characterized by small capillary numbers. Further research is required in order to understand the applicability of the CCRM model to attenuation and dispersion obtained from

seismic low frequency measurements.

Chapter 5

The role of interfacial impedance on seismic reflectivity

5.1 Summary

The characteristics of the P-wave reflectivity can depend on the properties of the interface separating two dissimilar poroelastic half-spaces. This interface behaviour can be characterized by an interfacial impedance which is associated with petrophysical properties such as, imperfect hydraulic contact and capillarity effect due to presence of membrane stiffness. Using the quasi-static poroelasticity equations, we obtain a simple expression for the poroelastic P-wave reflectivity including interfacial impedance at normal incidence. The amplitude versus angle behaviour is obtained by solving the corresponding boundary value problem numerically. We analyze two seismic scenarios where interfacial impedance can arise, namely, P-wave reflection at gas-water contact and fluid/porous-medium contact. The interfacial impedance shows small influence on the P-wave reflectivity for the gas-water contact at seismic frequencies. For contact between fluid and gas-saturated rock, the reflectivity for different interface scenarios reveals distinct frequency and angle dependence. With increasing interfacial impedance, a critical angle starts to appear in the amplitude-versus-angle behaviour. Synthetic seismograms associated with each interface scenarios are compared. We find that weak hydraulic contact leads to annihilation of amplitudes at small incident angle, whereas strong capillarity causes a phase reversal at larger angles.

5.2 Introduction

The primary mission of amplitude interpretation among other things is to determine whether a water-saturated rock or a hydrocarbon-saturated rock generates the reflection of interest (Hilterman, 2001). The Zoeppritz equation in combination with Gassmann theory (Aki and Richards, 2002; Gassmann, 1951; also see section 2.7.1) provides the relationship between the seismic reflectivity and fluid content. However, this elastic-equivalent theory neglects oscillatory fluid flow across the contact and is only valid at low frequency limit. To account for the wave frequency-dependence, the calculation of reflectivity needs to be based on more general theory of Biot's poroelasticity (Biot, 1962). The core of the reflection theory based on Biot's poroelasticity is the generation of reflected/transmitted slow P-wave upon a body wave striking a poroelastic interface, i.e., gas-water contact. The frequency-dependence of slow P-wave controls the primary dynamic poroelastic effect on seismic reflectivity (Gurevich, 1996), as it draws energy from other wave modes, i.e., the reflected fast P-wave, and consequently reduces their amplitudes.

Dutta and Odé (1983) investigate the P-wave reflection at gas-water contact in a unconsolidated sandstone. Their numerical results indicate that energy loss due to converted slow P-waves is proportional to the square root of frequency. This renders a small difference between poroelastic and elastic P-wave reflectivity at seismic frequencies. Gurevich (1996) confirm the observation of Dutta and Odé (1983) by comparing elastic and poroelastic results for contacts between various types of pore fluids. Therefore, the application of Biot reflection theory is limited by the fact that the frequency-dependence of amplitude is hard to observe even with the best quality seismic data. Denneman et al. (2002) and Gurevich et al. (2004) study the seismic reflection for a completely different context where the porous rock is in contact with pure fluid. They observe that when the rock is saturated with gas, there exists a significant difference between poroelastic and elastic P-wave reflectivity.

The above studies of poroelastic reflectivity are based on so-called open-pore boundary condition (Deresiewicz and Skalak, 1963; Bourbié et al., 1987), wherein the fluid pressure across the interface is assumed to be continuous. That implies a perfect hydraulic connection between the two poroelastic half-spaces. However, this condition is not always valid (Geertsma and Smit, 1961; Deresiewicz and

Skalak, 1963). Especially in presence of capillarity between two immiscible fluids, the fluid pressure boundary condition needs to be modified to take account of membrane stiffness (Nagy and Blaho, 1994; Nagy and Nayfeh, 1995). On the other hand, in presence of imperfect hydraulic contact (i.e., pore mis-alignment; clay mineral clogging the pore space), the fluid pressure boundary condition needs to include an interface permeability for describing the proper mechanics of the interface (Bourbié et al., 1987; Gurevich and Schoenberg, 1999). As shown in previous chapters, the characteristics of slow P-wave, i.e., oscillatory fluid flow heavily rely on the poroelastic interface condition. Therefore, an alternative choice of the interface condition in solving the boundary value problem with respect to plane wave reflection may further influence the dynamic poroelastic effect on seismic amplitude.

The aim of this chapter is two-fold: first of all, using quasi-static poroelasticity, an analytical expression for the generalized P-wave reflectivity including an interfacial impedance is obtained. Depending on the explicit form of the interfacial impedance, it can be interpreted in terms of membrane stiffness due to capillarity or interface permeability due to imperfect hydraulic contact. Secondly, we consider two pertinent scenarios where interfacial impedance can play a role, namely, seismic reflection at gas-water contact (Dutta and Odé, 1983) and at fluid/porous-medium contact (Denneman et al., 2002; Gurevich et al., 2004). The resulting frequency- and angle- dependence of seismic reflectivity calculated via different approaches, i.e., Zoeppritz-Gassmann, poroelastic open-pore and current theory are compared. The synthetic seismograms for various interface scenarios are also compared.

5.3 Quasi-static Biot's theory

Following Biot's theory, we consider a isotropic and homogeneous rock saturated with a single Newtonian fluid. The grains of the solid are characterized by the grain bulk modulus K_s and grain density ρ_s. The rock frame is characterized by its bulk modulus K_0 and density ρ, shear modulus μ, porosity ϕ and steady-state permeability κ. The pore fluid is characterized by its bulk modulus K_f, density ρ_f and steady-state shear viscosity η. With $\mathbf{u}$ and $\mathbf{U}$ denoting the average solid and fluid displacements, the relative fluid-solid (RFS) displacement is defined as

$$\mathbf{w} = \phi(\mathbf{U} - \mathbf{u}). \tag{5.1}$$

Accordingly, the stress tensors in 2D space are defined as

$$\tau_{yy} = H\nabla \cdot \mathbf{u} + BH\nabla \cdot \mathbf{w} - 2\mu \frac{\partial u_x}{\partial x}, \tag{5.2}$$

$$\tau_{xy} = \mu \left(\frac{\partial u_x}{\partial y} + \frac{\partial u_y}{\partial x} \right), \tag{5.3}$$

whereas the fluid pressure is

$$p_f = -BH\nabla \cdot \mathbf{u} - M\nabla \cdot \mathbf{w}. \tag{5.4}$$

The definitions of the poroelastic constants H, L, B, M, α can be found in section 3.3.1. According to Biot's poroelasticity, there exists two types of compressional waves and one type of shear wave in saturated porous rock. In the low frequency regime, where the wave angular frequency ω is much smaller than the Biot's characteristic frequency

$$\omega \ll \omega_b = \frac{\eta\phi}{\kappa_0 \rho_f S^{\infty}}, \tag{5.5}$$

the wavenumbers of the fast, slow P-wave and the S-wave can be approximated as

$$k_\alpha = \frac{\omega}{v_\alpha}, \tag{5.6}$$

$$k_\beta = \sqrt{\frac{i\omega\eta}{\kappa N}}, \tag{5.7}$$

$$k_s = \frac{\omega}{v_s}. \tag{5.8}$$

The velocities of the fast and slow P-wave are $v_\alpha = \sqrt{H/\rho}$, $v_s = \sqrt{\mu/\rho}$, respectively. The parameter N is given by $N = ML/H$. Under the quasi-static assumption 5.5, the RFS displacements of the fast P-wave and shear wave are negligibly small, namely, $\mathbf{w} = 0$. For the slow P-wave, its solid and RFS displacements are coupled in following manner (Geertsma and Smit, 1961)

$$\mathbf{w} = \lambda \mathbf{u}, \ \lambda = -\left(\frac{H}{C} \right). \tag{5.9}$$

The above overview of Biot's theory provides the basis for deriving the poroelastic reflection coefficient at seismic frequencies.

5.4 Reflection between two saturated porous media

We consider an incident P-wave striking an interface between two saturated porous media. The incident wave will generate three reflected waves in the upper medium 1 and three transmitted waves in the lower medium 2. We assume I, α, β, s denote the incident, fast, slow and shear waves, respectively. We also denote the upper and lower medium by 1 and 2, respectively. The solid displacement potential of the plane wave can be described by

$$\Phi_l = A_l e^{i(\omega t - \mathbf{k}_l \cdot \mathbf{r})}, \quad l = I, 1\alpha, 1\beta, 1s, 2\alpha, 2\beta, 2s, \tag{5.10}$$

where A_l is the amplitude and

$$\mathbf{k}_l = (f_l, g_l) \ , \tag{5.11}$$

$$\mathbf{r} = (x, y) \ , \tag{5.12}$$

$$\mathbf{k}_l \cdot \mathbf{r} = f_l x + g_l y \ . \tag{5.13}$$

According to Snell's law, we can assign the x-component of the wave vector as

$$f_l = f_I = k_I \sin\theta_I. \tag{5.14}$$

The corresponding y-component of the wave vector can be obtained via

$$g_l = \begin{cases} \sqrt{k_l^2 - f_I^2}, & l = I, 2\alpha, 2\beta, 2s, \\ -\sqrt{k_l^2 - f_I^2}, & l = 1\alpha, 1\beta, 1s. \end{cases} \tag{5.15}$$

Under quasi-static assumption 5.5, for an incident fast P-wave, the solid and RFS displacements of the upper and lower media can be expressed as

$$\mathbf{u^{(1)}} = \nabla\Phi_I + \nabla\Phi_{1\alpha} + \nabla\Phi_{1\beta} + \nabla \times \Phi_{1s}, \tag{5.16}$$

$$\mathbf{w^{(1)}} = \lambda_1 \nabla\Phi_{1\beta}, \tag{5.17}$$

$$\mathbf{u^{(2)}} = \nabla\Phi_{2\alpha} + \nabla\Phi_{2\beta} + \nabla \times \Phi_{2s}, \tag{5.18}$$

$$\mathbf{w^{(2)}} = \lambda_2 \nabla\Phi_{2\beta}. \tag{5.19}$$

The gradient and curl operators are defined as $\nabla\Phi = \partial\Phi/\partial x\mathbf{i} + \partial\Phi/\partial y\mathbf{j}$, $\nabla \times \Phi = -\partial\Phi/\partial y\mathbf{i} + \partial\Phi/\partial x\mathbf{j}$, respectively. The amplitudes of different displacement

potentials relate each other via following six boundary conditions (BC)

$$u_y^{(1)} = u_y^{(2)}, \tag{5.20}$$
$$u_x^{(1)} = u_x^{(2)}, \tag{5.21}$$
$$w_y^{(1)} = w_y^{(2)}, \tag{5.22}$$
$$\tau_{yy}^{(1)} = \tau_{yy}^{(2)}, \tag{5.23}$$
$$\tau_{xy}^{(1)} = \tau_{xy}^{(2)}, \tag{5.24}$$
$$p_f^{(1)} - p_f^{(2)} = Z_I \dot{w}_y^{(2)}. \tag{5.25}$$

The first five BCs represent the continuity of normal displacement, shear displacement, normal RFS displacement, normal stress and shear stress. The last BC represent the natural boundary condition for fluid pressure. It incorporates an so-called interfacial impedance Z_I. Interpreting the interfacial impedance differently allows us to model different reflection scenarios, such as imperfect hydraulic contact, capillarity (see more details in chapter 3).

5.5 Reflection between fluid and porous medium

The seismic reflection at fluid/porous-medium contact can be regarded as a special case of reflection between two porous media with the porosity of one half-space equalling unity. By setting $\mathbf{u} = 0$ and $\phi = 1$ in equations 5.2, 5.4, we obtain the stress-strain relation for the fluid

$$\tau_{yy} = -p_f = K_f \nabla \cdot \mathbf{U}. \tag{5.26}$$

According to Biot's theory, only P-wave exists in the fluid and its wavenumber is given by

$$k_\alpha^f = \frac{\omega}{v_f},\ v_f = \sqrt{\frac{K_f}{\rho_f}}. \tag{5.27}$$

Considering incoming P-wave from the fluid, the displacement potential can be written as

$$U^1 = \nabla \cdot \Phi_I + \nabla \cdot \Phi_{1\alpha}. \tag{5.28}$$

The corresponding boundary conditions for fluid/porous-medium contact is

$$U^{(1)} = u_y^{(2)} + w_y^{(2)}, \tag{5.29}$$

$$\tau_{yy}^{(1)} = \tau_{yy}^{(2)}, \tag{5.30}$$

$$\tau_{xy}^{(2)} = 0, \tag{5.31}$$

$$p_f^{(1)} - p_f^{(2)} = Z_I \dot{w}_y^{(2)}. \tag{5.32}$$

The four BCs represent conservation of mass, continuity of normal stress, continuity of shear stress and natural boundary condition for fluid pressure, respectively.

5.6 Reflectivity at normal incidence

Solving the boundary value problem analytically yields simple expressions for fast P-wave reflection coefficients at normal incidence

$$R_{pp} = \frac{Z^{(1)} - (1 - X_a)Z^{(2)}}{Z^{(1)} + (1 + X_b)Z^{(2)}}, \tag{5.33}$$

where the static acoustic impedances are $Z^{(1)} = \rho_1 v_{1\alpha}$, $Z^{(2)} = \rho_2 v_{2\alpha}$. For reflection at contact between two saturated porous media

$$X_a = \underbrace{\frac{H_1 k_{1\alpha}(B_1 - B_2)^2}{k_{1\beta}N_1 + k_{2\beta}N_2}}_{\text{poroelastic}} + \underbrace{\frac{\omega Z_I}{k_{1\beta}N_1 + k_{2\beta}N_2}\left(\frac{H_1 k_{1\alpha}}{H_2 k_{2\alpha}} - 1\right)}_{\text{interfacial impedance}}, \tag{5.34}$$

$$X_b = \underbrace{\frac{H_1 k_{1\alpha}(B_1 - B_2)^2}{k_{1\beta}N_1 + k_{2\beta}N_2}}_{\text{poroelastic}} + \underbrace{\frac{\omega Z_I}{k_{1\beta}N_1 + k_{2\beta}N_2}\left(\frac{H_1 k_{1\alpha}}{H_2 k_{2\alpha}} + 1\right)}_{\text{interfacial impedance}}. \tag{5.35}$$

For reflection at fluid/porous-medium contact

$$X_a = \underbrace{\frac{H_1 k_{1\alpha}(1 - B_2)^2}{k_{2\beta}N_2}}_{\text{poroelastic}} + \underbrace{\frac{\omega Z_I}{k_{2\beta}N_2}\left(\frac{H_1 k_{1\alpha}}{H_2 k_{2\alpha}} - 1\right)}_{\text{interfacial impedance}}, \tag{5.36}$$

$$X_b = \underbrace{\frac{H_1 k_{1\alpha}(1 - B_2)^2}{k_{2\beta}N_2}}_{\text{poroelastic}} + \underbrace{\frac{\omega Z_I}{k_{2\beta}N_2}\left(\frac{H_1 k_{1\alpha}}{H_2 k_{2\alpha}} + 1\right)}_{\text{interfacial impedance}}. \tag{5.37}$$

Equations 5.33-5.37 are the generalized reflectivities for two often encountered poroelastic contacts. They can be used to assess the significance of contact-fluid-flow as well as interfacial impedance on seismic reflection. According to

the expressions, if $Z_I = 0$, the reflectivity 5.33 reduces to the open-pore case. Furthermore, if $X_a = X_b = 0$, the equation becomes the elastic reflectivity with velocity calculated via the Gassmann's equation (see section 2.7.1).

5.7 Numerical analysis

In order to analyse the reflectivity and study the effect of interfacial impedance, the following two scenarios are chosen: first, we consider seismic reflection at gas-water contact (Dutta and Odé, 1983); secondly, we consider reflection between free fluid and gas-saturated porous rock (Denneman et al., 2002; Gurevich et al., 2004). The mechanical properties of rocks and fluids are given in Table 5.1.

(a) Dutta and Odé (1983)

Sand 1		Fluids	
K_{m} (GPa)	1.7	K_{fa} (GPa)	2.4
μ_{m} (GPa)	1.86	ρ_{fa} (g/cm^3)	1
K_{s} (GPa)	35	η_{fa} (Pa s)	1e-3
ρ_{s} (g/cm^3)	2.65	K_{fb} (GPa)	0.022
ϕ	0.3	ρ_{fb} (g/cm^3)	0.1
κ_0 (m^2)	1e-12	η_{fb} (Pa s)	1.5e-5

(b) Gurevich et al. (2004)

Sand 2		Fluids	
K_{m} (GPa)	5.8	K_{fa} (GPa)	2.22
μ_{m} (GPa)	3.4	ρ_{fa} (g/cm^3)	1
K_{s} (GPa)	40	η_{fa} (Pa s)	1e-3
ρ_{s} (g/cm^3)	2.76	K_{fb} (GPa)	1e-4
ϕ	0.26	ρ_{fb} (g/cm^3)	1.2e-3
κ_0 (m^2)	9.5e-13	η_{fb} (Pa s)	1.82e-5

Table 5.1: Mechanical properties of rocks and fluids

In the first case, P-wave propagates from the upper gas-saturated poroelastic half-space through the lower brine-saturated half-space. The reflectivity at normal incidence is calculated using equations 5.33-5.35. We verify the analytical reflectivity by comparing with results obtained using Biot's dynamic equations of poroelasticity (section 2.1.5, eq. 2.47). Both reflectivities are calculated with open-pore assumption ($Z_I = 0$). In Figure 5.1a, the resulting amplitudes coincide up to 10^4 Hz. This confirms the validity of the expressions at seismic frequen-

cies. Next, we consider different interface scenarios by choosing different forms

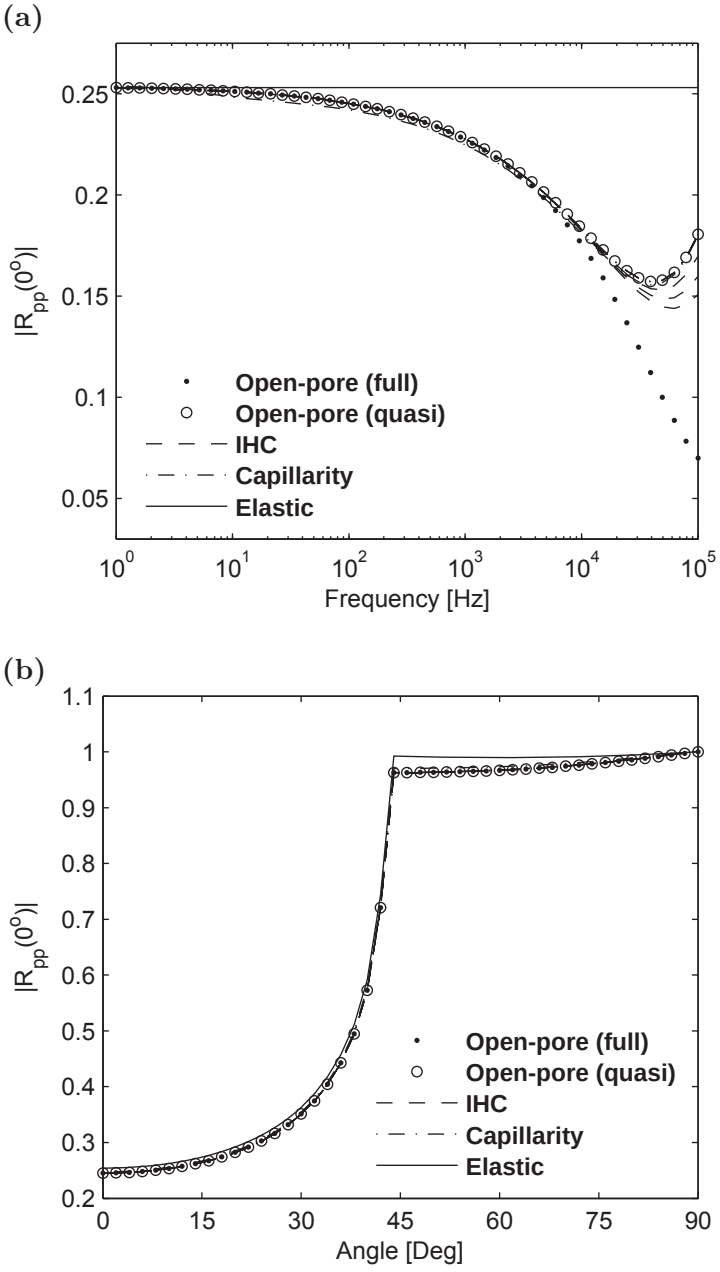

Figure 5.1: Seismic reflection between gas and water contact. Amplitude of reflected P-wave at normal incidence is plotted as function of frequency.

of interfacial impedances, i.e., $Z_I = \frac{1}{\kappa_I}$ for modelling the interface permeability and $Z_I = \frac{W}{i\omega}$ for modelling the membrane stiffness (capillarity). A range of interface permeabilities $\kappa_I = 0.3,\ ,0.5,\ 1$ $(10^{-6}\text{m/Pa}\cdot\text{s})$ and membrane stiffness $W = 0.1,\ 1,\ 10$ (GPa/m) are chosen for modelling the capillarity effect and

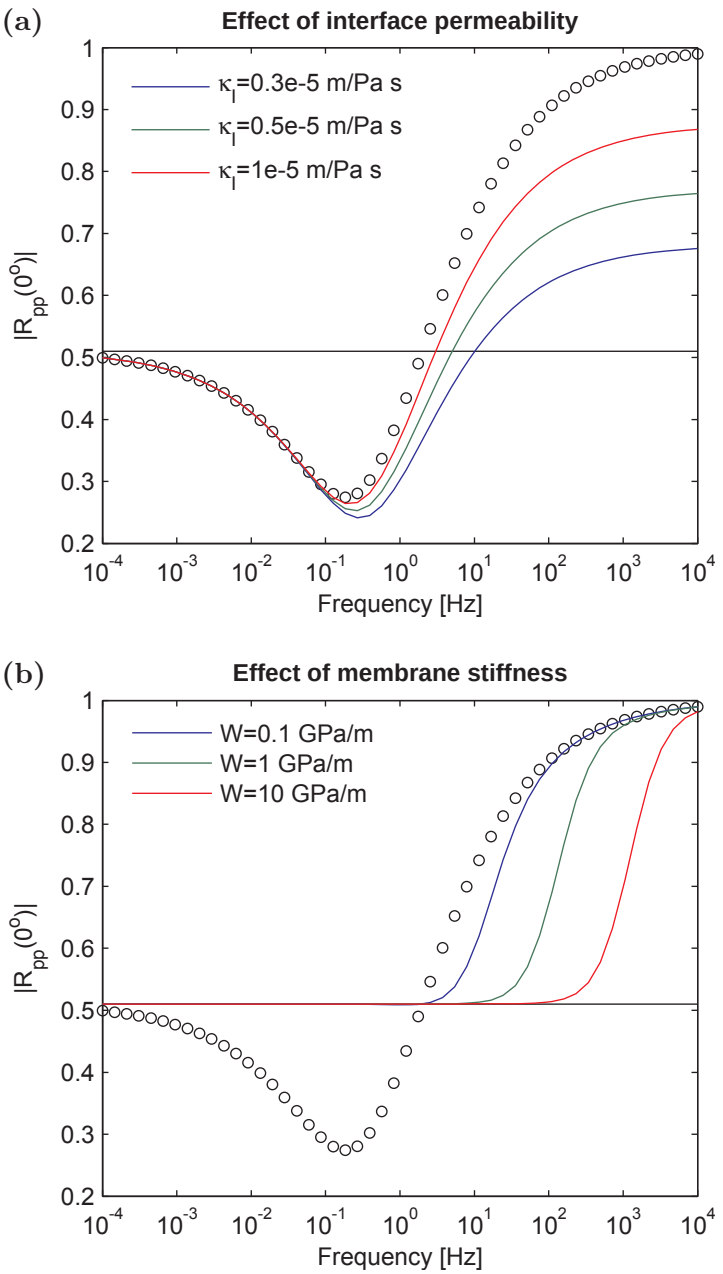

Figure 5.2: Seismic reflection between free fluid and gas saturated rock. Amplitude of reflected P-wave at normal incidence is plotted as function of frequency.

imperfect hydraulic contact (IHC), respectively. The amplitudes resulting from interface permeability and membrane stiffness are consistent with amplitude associated with open-pore condition at seismic frequencies. Solving the boundary value problem numerically, we also obtain reflectivities at different angles. The amplitude versus angle (AVA) at 100 Hz is shown in Figure 5.1b. Again, we find negligible effect of interfacial impedance on the amplitude. In Figure 5.1b,

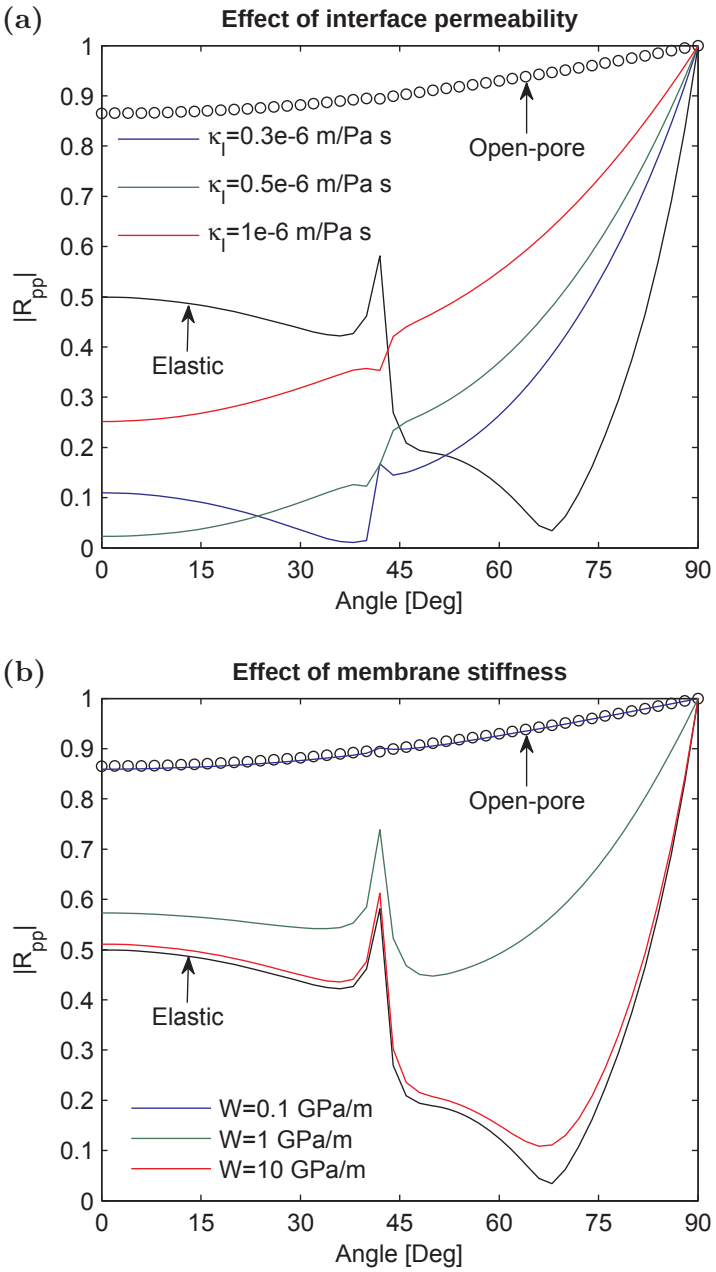

Figure 5.3: Seismic reflection between free fluid and gas saturated rock. Amplitude of reflected P-wave at 50 Hz is plotted as function of angle.

the poroelastic AVAs are compared with elastic AVA calculated using Zoeppritz-Gassmann theory. The comparison indicates that the seismic reflection between two saturated rocks can be described by elastic theory satisfactorily. This becomes more evident when we consider that Biot global flow is relatively significant for the employed unconsolidated rock at seismic frequencies.

For contact between free fluid and gas-saturated medium, the normal inci-

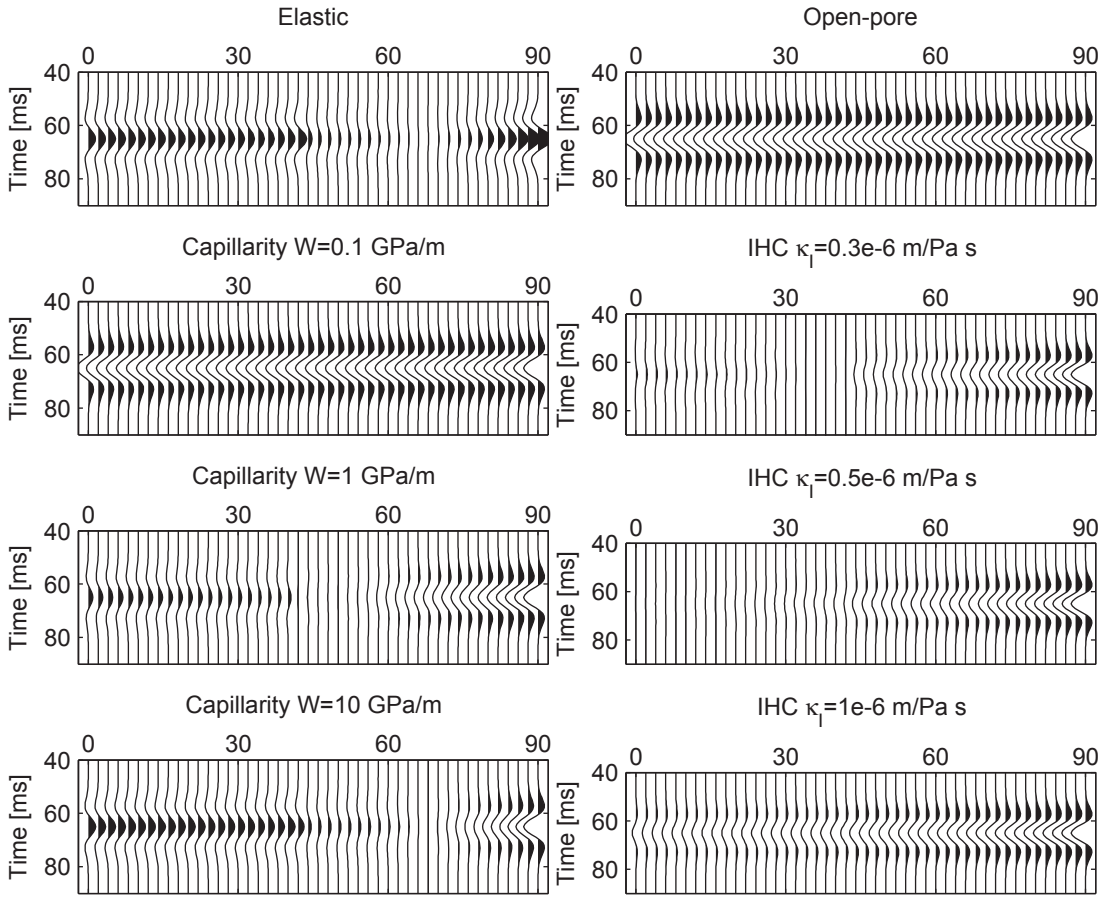

Figure 5.4: Seismic reflection between free fluid and gas-saturated rock, the resulting angle gathers for different interface conditions.

dence reflectivity considering different interface conditions show distinct frequency-dependence behaviour as shown in Figure 5.2. Considering the exploration frequency range 10 Hz - 10 kHz, there is a significant difference between poroelastic open-pore (circles) and elastic (solid line) reflection coefficients as originally observed by Denneman et al. (2002). The low frequency limit occurs as low as 10^{-3} Hz, where the poroelastic open-pore reflectivity reverts to the elastic value. The strong porolastic effect in this case may allow the effects of capillarity and interface permeability to be noticed. Indeed, as shown in Figure 5.2a, with increasing interface permeability, the reflection coefficient becomes similar to the open-pore poroelastic coefficient at seismic frequencies. On the other hand, in Figure 5.2b, for increasing membrane stiffness, the reflection coefficient becomes similar to the elastic reflection coefficient at seismic frequencies. The reflectivity associated with membrane stiffness is bounded by the elastic and poroelastic open-pore reflectivity. However, in presence of interface permeability, the reflectivity value

can even be lower than elastic and open-pore reflectivity from 10^{-1} Hz to 10 Hz.

The corresponding AVA signatures at 50 Hz are shown in Figure 5.3. Comparing with the poroleastic open-pore case, a critical angle appears due to the presence of membrane stiffness and interface permeability. The AVA behaviors in Figure 5.3a,b also confirm that in the case of interface permeability, the resulting reflectivities may not be bounded by elastic and open-pore reflectivities. The corresponding seismograms for Figure 5.3, which also integrate the phase information are presented in Figure 5.4. The seismograms are computed by convolving the resulting P-wave reflectivities with the Ricker wavelet. Interestingly, for strong capillarity, or large membrane stiffness, we observe phase reversal at larger incident angles. When the interface permeability is small, the amplitude can be very weak at small incident angles. The contrasting AVA behaviors reveals a potential application of this work. By comparing the theoretical reflectivity with lab measured reflectivity, we may be able to quantify the poroelastic boundary conditions, i.e., interface permeability, membrane stiffness.

5.8 Chapter conclusions

We study the influence of interfacial impedance on seismic reflection. Using quasi-static poroelasticity, we obtain analytical expression for P-wave reflectivity including interfacial impedance. The interfacial impedance shows negligible effect on seismic reflection at gas-water contact in the seismic frequency range. For contact between free fluid and gas-saturated rock, reflectivity considering different interface scenarios reveals distinct frequency and angle dependence. Critical angle starts to appear for increasing interface permeability and membrane stiffness. Comparing the corresponding seismograms, we find weak hydraulic contact leads to annihilation of amplitudes at small incident angle. Meanwhile, strong capillarity gives rise to phase reversal at larger incident angle. The results provide theoretical evidence for examining the poroelastic boundary conditions using lab measured reflectivity. Furthermore, for gas-saturated sea-floor whose surface is not perfectly sealed, incorporating interfacial impedance into AVO analysis may be important for extracting elastic properties from marine seismic data.

Chapter 6

The effects of saturation scale on time-lapse seismic signatures

6.1 Summary

Quantitative interpretation of time-lapse seismic signatures aims at assisting reservoir engineering and management operations. Relevant signatures include time shifts, reflection amplitude changes and time-lapse attenuation. Time-lapse signatures are thought to be primarily induced by saturation and pressure changes. However, core-scale laboratory measurements and reservoir-scale flow simulations indicate that a change of the driving forces during dynamic fluid injection gives rise to a varying saturation scale. This saturation scale is yet another variable controlling the time-lapse seismic signal. In this work, we investigate the saturation scale effect on time-lapse seismic signatures by analysing simple modelling scenarios. We consider three characteristic saturation scales – ranging from few millimetres to metres – which may form during gas injection in an unconsolidated reservoir. Using the random patchy saturation model, we compare the acoustic signatures associated with each saturation scale. We further investigate the scale effect on the reflection coefficient for a partially saturated reservoir encased by high-impedance shale layers. The results show that centimetre and metre saturation scales may cause significant attenuation and velocity dispersion at seismic frequencies. The magnitude of the reflection coefficient decreases with increasing saturation scale. The millimetre saturation scale produces the same

seismic signatures as obtained by elastic effective medium modelling, whereas the centimetre and metre saturation scales lead to highest amplitude decay and earliest arrival for the base reflection. The analysis of the time shift and amplitude change indicates that ignoring time-dependent saturation scale can result in biased estimations of saturation and fluid pressure. In the discussion we address the reservoir parameters which can influence the characteristic role of the saturation scale.

6.2 Introduction

Quantitative analysis of time-lapse (TL) seismic data is important for monitoring reservoir performance. The key to the time-lapse seismic interpretation is to understand the relation between the seismic properties such as velocity, attenuation and fluid information such as saturation, pressure. It is known that seismic velocity and attenuation do not only depend on the type of rock and fluids, amount of saturation but also the fluid distribution, namely the spatial scale how the fluids are mixed in the pore space. The reservoir fluid distribution is jointly controlled by multiple forces due to gravity, capillarity, viscosity and inertia (Johnston, 2013). The gravity force plays an important role in separating the reservoir fluids along the vertical dimension. It has a dominant role with fluids of large density contrast and in reservoir of shallow depth. The performance of capillary force and viscous force controls the efficiency of enhanced hydrocarbon recovery. Their characteristics are determined by the reservoir wettability condition, fluid mobility ratio and injection method. The inertial force reflects the reservoir flow capacity and is influenced by permeability and lithology variations. During the process of reservoir production and proceeding recovery, the balance of these reservoir forces is constantly changing and lead to time-dependent saturation scale. This makes the estimation of the fluid distribution and further quantifying its effect on 4D seismic exceptionally challenging.

Laboratory rock physicists endeavour to understand the relation between fluid distribution and elastic properties via core-flooding experiment combining with acoustic and X-ray computer tomography (CT) monitoring (Cadoret et al., 1995; Alemu et al., 2013; Nakagawa et al., 2013; Lopes et al., 2014). Cadoret et al (1995) shows that the fluid distribution induced by different saturation techniques can be different. They report the fluid distribution in a drying experiment (drainage) is more heterogeneous than during depressurization (imbibition) espe-

cially at high water saturation level. The difference in saturation scale leads to different measured P-wave velocity at the same saturation. Lopes et al. (2014) study the dependence of P-wave velocity on the injection rate during forced water imbibition. They observe that, for the same water saturation, P-wave velocity associated with high injection rate is larger than the velocity associated with smaller injection rate. This difference is attributed to the injection-rate dependent saturation scale. Alemu et al. (2013) and Nakagawa et al. (2013) conduct drainage core-flooding with CO_2 injection and subsequent imbibition with brine re-injection. They report the P-wave amplitude and attenuation can be sensitive to the fluid distribution, which is again strongly influenced by the sub-core frame heterogeneities. Toms et al. (2009) and chapter 4 apply statistical characterization on CT images acquired during core-flooding. They find the saturation scale, which can be quantified by a correlation length, varies with the saturation itself.

Studies on core-flooding reveal the dependence of fluid distribution on saturation method, injection rate, frame heterogeneities as well as the level of saturation. On the other hand, the reservoir-scale fluid distribution can be different from the core-flooding fluid distribution. This is because a change of the dominant forces of the two phase flow (Sengupta and Mavko, 2003) as well as the presence of complex geological heterogeneities at larger scale (MacBeth and Stephen, 2008). At field scale, the fluid distribution can be indirectly identified from the velocity -saturation relation (VSR). The establishment of field-scale VSR can be based on well log/VSP data (Caspari et al., 2012; Al Hosni et al., 2015) or saturation profile from flow simulation (Sengupta and Mavko, 2003). If the VSR follows prediction from Gassmann's equation, the fluid distribution is identified as uniform and otherwise patchy. Sengupta and Mavko (2003) perform fine-scale flow simulation and study the influence of petrophysical parameters (e.g., relative permeability, wettability, fluid mobility ratio and residual saturation) on the form of saturation scale. Their results indicate that patchy saturation is encountered in most gas injection scenarios. This is because the gravitational force induces subseismic-resolution gas cap, hence resulting patchy saturation at seismic scale. They also conclude that uniform saturation is commonly associated with water-flooding and primary production.

Integration of fluid distribution properly into flow simulation and seismic inversion is crucial for quantifying fluid saturation and pressure from time-lapse seismic data. This requires further understanding the physical mechanism behind the

velocity and attenuation -saturation relations in partially saturated rocks. When an elastic wave propagates in a saturated medium, it will induce local pressure gradient between rock regions of different compliances. The pressure gradient tends to equilibrate and gives rise to wave velocity dispersion and attenuation. Such process is referred as wave-induced fluid flow (Müller et al., 2010). The wave-induced fluid flow (WIFF) can take place over various scales. Particularly, for WIFF at mesoscopic scale, which is larger than the pore space but smaller than the wavelength, the resulting dispersion and attenuation is believed to be significant at seismic frequencies. When the reservoir fluids uniformly distribute in the pore space, the wave-induced fluid pressure has enough time to equilibrate at seismic frequencies. In this case, Gassmann theory can be invoked to predict the non-dispersive seismic velocity. On the other hand, each fluid phase can occupy a network of pores and forms as mesoscopic fluid patches. This scenario becomes more prevalent during dynamic fluid movement induced by injection. The scale of such fluid patches can differ by orders of magnitude depending on the reservoir forces.

The patchy saturation models are routinely applied for modeling the velocity and attenuation due to mesoscopic flow in the field (Morgan et al., 2012; Blanchard and Delommot, 2015). Two categories of models are frequently used. One assumes a periodic presence of gas layers (White et al., 1975; Carcione and Picotti, 2006; also see chapter 3). The other assumes a random fluid distribution, which can be quantified by different types of correlation functions (Gurevich et al., 1995; Gelinsky et al., 1998; Müller and Gurevich, 2004; Toms et al, 2007a). The saturation scale in the periodic model is given by the size of the representative elementary volume (REV) whereas in the random model, it is manifested as the correlation length. The applications of these models are commonly associated with an assumption of constant saturation scale over time. Namely, a constant REV size or correlation length is used during the course of fluid injection. Thus, the change of the velocity and attenuation are solely attributed to the change of saturation or fluid pressure. However, as evidenced from the studies of laboratory core-flooding and field-scale flow simulation, the saturation scale can differ over repeated seismic surveys due to the change of reservoir forces. Therefore, failing to include time-dependent saturation scale can result in biased saturation and

fluid pressure estimation. To overcome this, we propose a new modelling scheme:

$$K_{\text{sat}}^{\text{t}+\Delta\text{t}}(\omega) = \text{Patchy}[\quad \underbrace{S_{\text{gas}}^{\text{t}+\Delta\text{t}}}_{\text{Saturation change}} \quad , \quad \underbrace{K_{\text{dry}}(P_{\text{eff}}^{\text{t}+\Delta\text{t}}),\ \mu_{\text{dry}}(P_{\text{eff}}^{\text{t}+\Delta\text{t}})}_{\text{Pressure change}} \quad , \quad \underbrace{\text{b}^{\text{t}+\Delta\text{t}}}_{\text{Scale change}} \quad]. \tag{6.1}$$

Comparing with the conventional Gassmann modelling (Landrø, 2001):

$$K_{\text{sat}}^{\text{t}+\Delta\text{t}} = \text{Gassmann}[\quad \underbrace{S_{\text{gas}}^{\text{t}+\Delta\text{t}}}_{\text{Saturation change}} \quad , \quad \underbrace{K_{\text{dry}}(P_{\text{eff}}^{\text{t}+\Delta\text{t}}),\ \mu_{\text{dry}}(P_{\text{eff}}^{\text{t}+\Delta\text{t}})}_{\text{Pressure change}} \quad], \tag{6.2}$$

patchy saturation model (equation 6.1) operates on change of gas saturation S_{gas}, effective pressure P_{e} and an additional element — saturation scale b. The latter gives rise to attenuation and velocity dispersion. To illustrate the scale effect, we consider an initially water-saturated unconsolidated sandstone undergoes gas injection. Three contrastingly different saturation scales are independently assumed to be formed during the gas injection. They represent three typical attenuation characteristics at an employed seismic frequency. In the first part, we analyse the effect of the saturation scale on the acoustic impedance and attenuation using developed patchy saturation model. Further based on the model, we customize viscoelastic reflection coefficient for patchy-saturated reservoir and study scale effect on seismic amplitudes. Viscoelastic seismic modelling is applied to investigate the significance of saturation scale on seismic responses. In the second part, we illustrate how saturation scale variation affects the estimation of saturation and fluid pressure from time-lapse seismic signatures. We discuss reservoir parameters which can influence our analysis of saturation scale effect. Last but not the least, we address the importance of identifying time-lapse saturation scale for quantitative 4D study.

6.3 Scale effect in Partially Saturated Reservoir

6.3.1 Characteristic saturation scales

First, we assume a shallow and initially water-saturated reservoir which is made of unconsolidated sandstone. We further assume that the reservoir has undergone gas injection and therefore, becomes partially saturated. The scenario where injected gas stays immiscible with the reservoir fluids can be encountered in CO_2 sequestration, enhanced oil recovery using WAG (water alternating with

gas) and gas injection for secondary oil recovery as shown in Figure 6.1. We

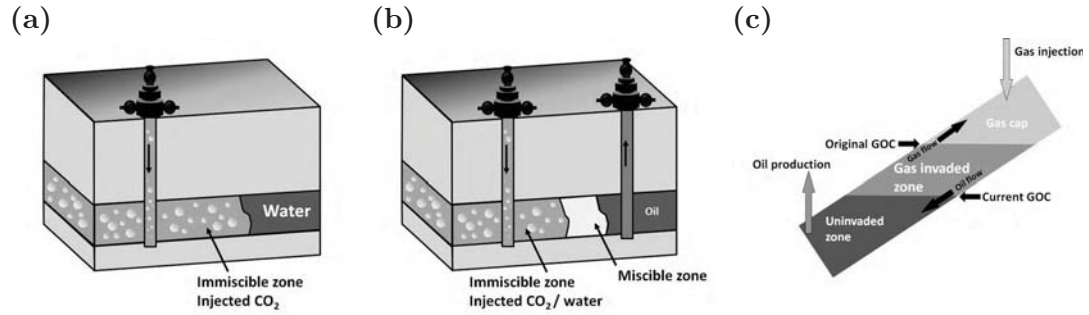

Figure 6.1: Three gas injection scenarios which are likely to induce patchy saturation. (a) CO_2 sequestration; (b) enhanced oil recovery using WAG (water alternating with gas); (c) gas injection in the gas cap for secondary oil recovery. Modified from Johnston (2013).

assume that one of the following three saturation scales forms during the gas injection: Patches on the order of 1) of millimetre, 2) centimetre and 3) metre. The saturation images of the rock containing these representative length scales are illustrated in Figure 6.2. The images are generated using an exponentially-correlated random fluid distribution with scales (correlation length) of 5 mm (left), 15 cm (middle), 2 m (right), respectively. Despite the difference in saturation scale, all images have the same gas saturation of 50%.

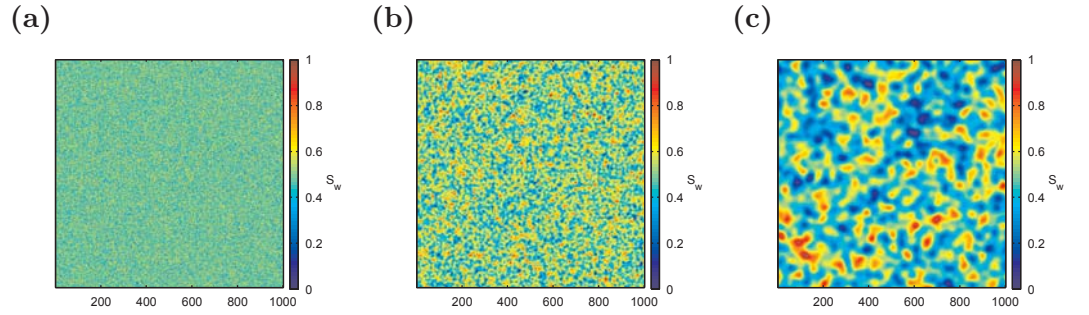

Figure 6.2: Synthetic saturation images of a rock with 50% gas saturation. The fluid distribution is exponentially-correlated with a correlation length of 5 mm for image (a), 15 cm for image (b) and 2 m for image (c).

Let us consider a seismic wave with certain frequency passing through rocks with such different saturation scales. The wave will instantaneously induce different fluid pressure within each fluid phase because of their different compress-

ibilities. This wave-induced pressure difference tends to equilibrate and the characteristic time for such equilibration is controlled by the ratio of the saturation scale b and the diffusion length l_d. Intuitively, for rock having small scale fluid heterogeneities ($b \ll l_d$) as shown in Figure 6.2a, the induced fluid pressure will have enough time to equilibrate during one wave cycle. Seismic wave now senses the rock as if it is saturated by a single, effective fluid. Hence, seismic velocity can be predicted by Gassmann's equation with the effective compressibility of the two-fluid mixture provided by Wood's mixing law. Meanwhile, in presence of strong capillarity, the Gassmann's equation needs to be modified to take the interfacial tension into account (see chapter 3 and 4). On the other hand, for large scale fluid heterogeneities ($b \gg l_d$) as shown in Figure 6.2c, the fluid pressure has no time to equilibrate and will remain piecewisely constant within each fluid phase. In this scenario, the unrelaxed fluid pressure adds to the overall stiffness of the rock and seismic velocity can be calculated by Hill's equation (see 4.3.2). Additionally, the Hill's equation can be modified to include the presence of residual saturation (Sengupta and Mavko, 2003). Lastly, for rocks having intermediate saturation scale ($b \approx l_d$) as shown in Figure 6.2b, wave-induced fluid pressure can only partially equilibrate during one wave cycle. Such diffusion process results in frequency-dependent velocity and attenuation.

6.3.2 Bounds-extended Patchy Saturation Model

Here, we extend random patchy saturation model of Toms et al. (2007a) to take capillarity (see chapter 3, 4) and irreducible saturation (Sengupta and Mavko, 2003) into account. The resulting effective P-wave modulus simply reads

$$\tilde{H}(\omega) = H_{\text{cap}} + (H_{\text{irr}} - H_{\text{cap}}) H_p(\omega) \ , \tag{6.3}$$

where $H_p(\omega)$ is normalized P-wave modulus and taken on a value between 0 and 1. That is, at low frequency limit, $H_p(\omega) = 0$ and the model converges to capillarity-extended static limit H_{cap}. At high frequency limit, $H_p(\omega) = 1$ and the model reaches irreducible-saturation-modified upper limit H_{cap}. Here, we give description for the extended bounds. The detailed expressions for calculating $H_p(\omega)$ can be found in chapter 4. First, the capillarity-extended lower bound is

written as (see section 4.3.1)

$$H_{\text{cap}} = \frac{z+T}{\frac{z}{H_{\text{GW}}} + \frac{T}{H_{\text{GH}}}},\ z = \frac{N_{\text{w}}}{S_{\text{w}}} + \frac{N_{\text{g}}}{S_{\text{g}}},\ T = \frac{bW}{4S_{\text{w}}S_{\text{g}}}, \tag{6.4}$$

where Gassmann-Wood (GW) H_{GW}, Gassmann-Hill H_{GH} moduli and parameter N can be found in chapter 4. In equation 6.4, T is a key parameter which controls the capillarity stiffening effect. It is a function of the saturation scale b and the membrane stiffness W. When either the saturation scale b or the membrane stiffness W is small, capillarity stiffening becomes negligible $T = 0$. In this case, the lower bound H_{cap} reduces to Gassmann-Wood modulus H_{GW}. The irreducible-saturation modified upper bound is given by (Sengupta and Mavko, 2003)

$$H_{\text{irr}} = \left(\frac{S_{\text{f1}}}{H_{\text{f1}}} + \frac{S_{\text{f2}}}{H_{\text{f2}}}\right)^{-1},\ S_{\text{f1}} = \frac{S_{\text{g}} - S_{\text{rg}}}{1 - S_{\text{irrw}} - S_{\text{rg}}},\ S_{\text{f2}} = \frac{S_{\text{w}} - S_{\text{irrw}}}{1 - S_{\text{irrw}} - S_{\text{rg}}}, \tag{6.5}$$

where H_{f1} is the GW modulus at the irreducible water saturation S_{rw}, H_{f2} is the GW modulus at the residual gas saturation S_{rg}. When there is no either irreducible water saturation or residual gas saturation $S_{\text{rw}} = S_{\text{rg}} = 0$, the upper bound H_{irr} reduces to Gassmann-Hill modulus H_{GH}.

To highlight the saturation scale effect, we first switch off the capillarity and irreducible saturation effects in our model, namely, we set $W = 0$, $S_{\text{irrw}} = S_{\text{rg}} = 0$. Their respective impact will be clearly shown at the end of the result section.

6.3.3 Characteristic frequency

To study the scale effect, it is essential to first look at the characteristic frequency of the model. When the diffusion length equals the saturation scale, maximum attenuation due to mesoscopic flow takes place. The frequency satisfying this condition is defined as the characteristic frequency which can be written as

$$f_c = \frac{1}{2\pi}\frac{D_p(S_{\text{g}}, P_{\text{e}})}{b^2(S_{\text{g}}, P_{\text{e}})}, \tag{6.6}$$

We see that the saturation scale b has an explicit role of controlling the frequency band where maximum attenuation happens. The diffusivity D_p incorporates the saturation and the bulk/shear modulus of the frame. Therefore, the characteristic frequency depends on the saturation and effective pressure. Assuming a given

porosity and clay content for the sandstone, the relation between its dry moduli and effective pressure can be written by the form (Eberhart-Phillips et al., 1989)

$$K_0, \mu_0 = A + BP_{\mathrm{e}} - Ce^{-DP_{\mathrm{e}}}. \tag{6.7}$$

The regression coefficients A, B, C, D can be derived by fitting the lab data. In light of work of Landrø (2001), we choose the coefficients directly from measurement of Eberhart-Phillips et al. (1989) for an unconsolidated sandstone ($A = 1.41$, $B = 0.435$, $C = 0.197$, $D = 14$ for the bulk modulus; $A = 0.64$, $B = 0.333$, $C = 0.107$, $D = 13$ for the shear modulus). The resulting pressure-dependent bulk and shear moduli are shown in Figure 6.3. The petrophysical

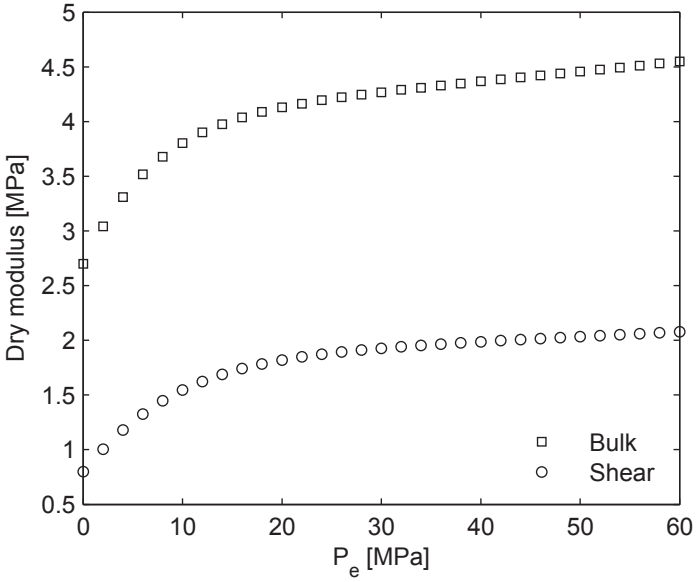

Figure 6.3: Relation between bulk and shear frame moduli and effective pressure for the unconsolidated sandstone.

properties of reservoir rock (at zero effective pressure) and fluids are given in Table 6.1.

Soft sand		Fluids		Shale	
K_0 (GPa)	2.7	K_{fa} (GPa)	2.4	V_p (m/s)	2400
μ_0 (GPa)	0.8	ρ_{fa} (g/cm^3)	1	V_s (m/s)	800
K_{s} (GPa)	35	η_{fa} (Pa s)	1e-3	ρ (kg/m^3)	2300
ρ_{s} (g/cm^3)	2.65	K_{fb} (GPa)	0.01		
ϕ	0.3	ρ_{fb} (g/cm^3)	0.14		
κ (m^2)	1e-12	η_{fb} (Pa s)	1e-5		

Table 6.1: Mechanical properties of rocks and fluids

Figure 6.4 shows the characteristic frequency as a function of saturation and effective pressure for different saturation scales . The common features of f_c revealed by Figures 6.4a, b, c are: 1. with increasing gas saturation, f_c is shifted towards higher frequency, then it maximizes at few percent of water saturation and drops drastically after this critical water saturation; 2. with increasing effective pressure, f_c is shifted towards higher frequency and the pressure dependence is stronger at lower gas saturation. Most importantly, by comparing Figures 6.4a, b, c, the saturation scales locate the characteristic frequencies (z-axis) in three rather separated frequency bands for all saturations and effective pressure. In other words, for the employed rock properties, the millimetre saturation scale will correspond to a dominant attenuation in kilohertz range; the centimetre saturation scale corresponds to a dominant attenuation in seismic frequencies whereas the metre-scale is associated with attenuation in millihertz band. These representative saturation scales will facilitate our discussion on their respect attenuation characteristics in the following sections.

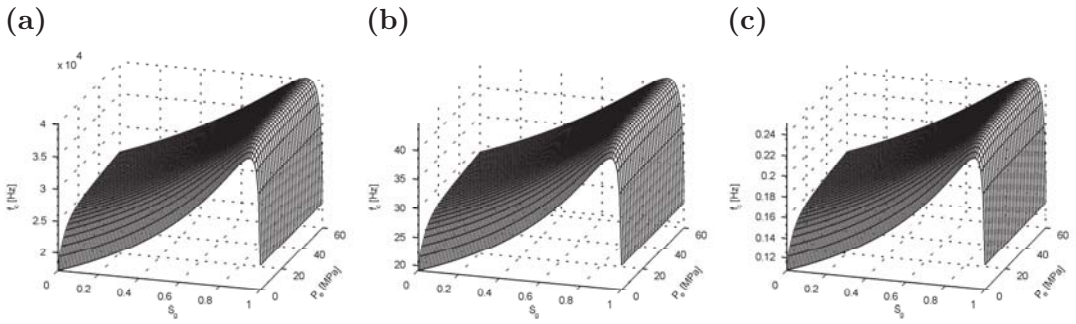

Figure 6.4: Characteristic frequency is plotted as function of saturation and effective pressure. The saturation scales are 5 mm for (a), 15 cm for (b) and 2m for (c).

6.3.4 Attenuation and Acoustic impedance

The attenuation and the acoustic impedance (AI) can be calculated via

$$Q^{-1} = \frac{\mathrm{Im}(\tilde{\mathrm{H}}(\omega))}{\mathrm{Re}(\tilde{\mathrm{H}}(\omega))} \quad , \quad Z = \sqrt{\rho_0 \mathrm{Re}(\tilde{\mathrm{H}}(\omega))} \; , \tag{6.8}$$

where the effective P-wave modulus $\tilde{H}(\omega)$ is given by equation 6.3. The effective density ρ_0 is calculated by taking the volumetric average of the grain and fluid densities. We discuss the acoustic impedance here instead of velocity, as it not only incorporates velocity information but also facilitate our further analysis on

seismic amplitude.

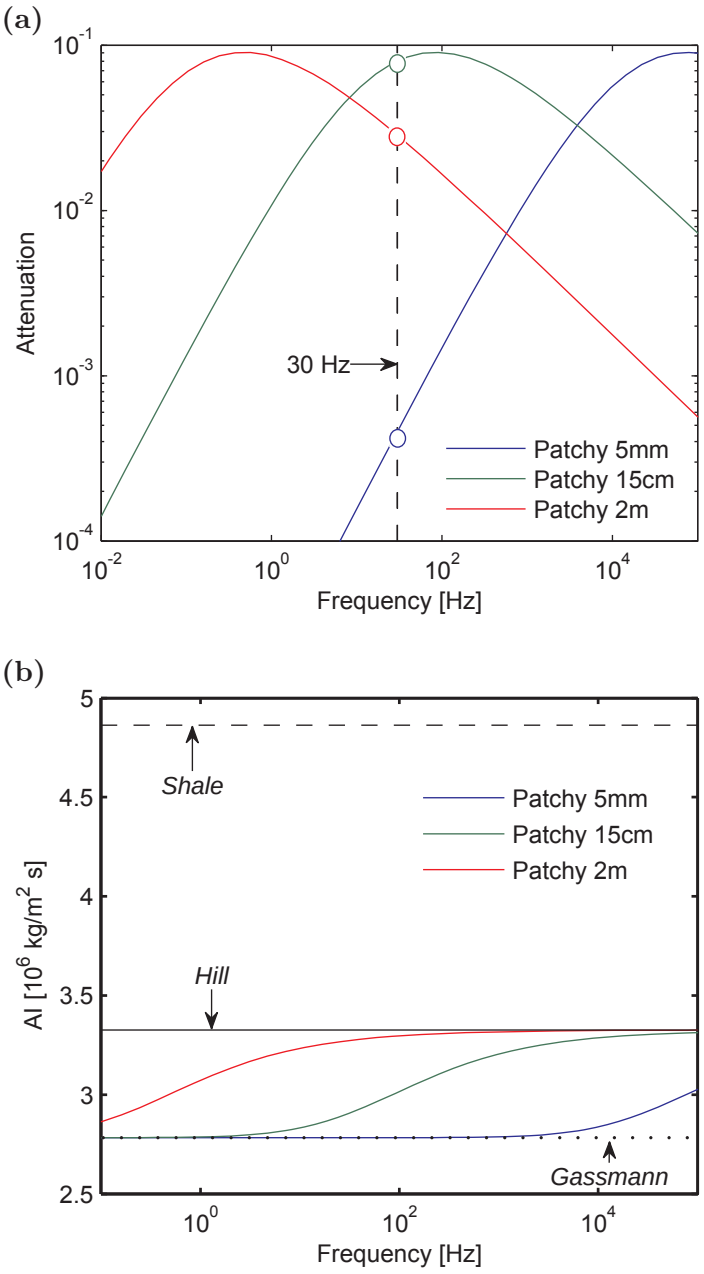

Figure 6.5: Attenuation and acoustic impedance are plotted as function of frequency. The saturation and effective pressure 50% and zero, respectively.

The attenuation and acoustic impedance are plotted as function of frequency in Figure 6.5. The water saturation is 50% whereas the effective pressure is zero. In Figure 6.5a, the three saturation scales reveals contrasting attenuation levels

within seismic frequency range (10 Hz $\sim$ 150 Hz). Let us consider 30 Hz as frequency of interest, for millimetre saturation scale, Q is over 1000 indicating negligible attenuation. For metre saturation scale, attenuation is appreciably larger with an inverse quality factor of 0.03, whereas for centimetre saturation scale, an inverse quality factor of 0.08 revealing highest attenuation. The acoustic impedances in Figure 6.5b are bounded by Gassmann and Hill limits. The metre saturation scale gives the largest dispersion at seismic frequencies whereas at centimetre scale, the dispersion is relatively small. The millimetre scale starts to cause noticeable dispersion above 10 KHz.

The attenuation- and impedance-saturation relations are shown in Figure 6.6. The frequency is 30 Hz and the effective pressure is zero in this case. The millimetre saturation scale produces minimum attenuation and its associated acoustic impedance is least sensitive with the water saturation. The centimetre saturation scale results in a maximum inverse quality factor of 0.2 ($Q = 5$) which is 5 times larger than the attenuation provided by the metre saturation scale. The associated acoustic impedances of both cases are sensitive with change of saturation.

The dependence of attenuation and AI on the effective pressure is presented in Figure 6.7. The frequency and saturation are 30 Hz and 50% respectively in this case. The centimetre saturation scale yields greatest attenuation and attenuation sensitivity with the effective pressure. For all cases, the attenuation and acoustic impedance level off when the effective pressure is above 30 GPa. The AI -pressure relation for partially saturation (Figure 6.7b) is controlled by the pressure-dependent dry moduli (Figure 6.3).

6.3.5 Seismic reflection amplitude

In this section, we study the effect of saturation scale on the seismic reflection. To do so, we employ a simple three-layer model where a low impedance sand layer is encased between two higher impedance shale layers. This type of reservoir model is categorized as Class III AVO anomaly (Rutherford and Williams, 1989). We assume the reservoir sand is partially saturated and attenuating as shown in previous sections whereas the overburden shale is fully saturated and non-dissipative at seismic frequencies.

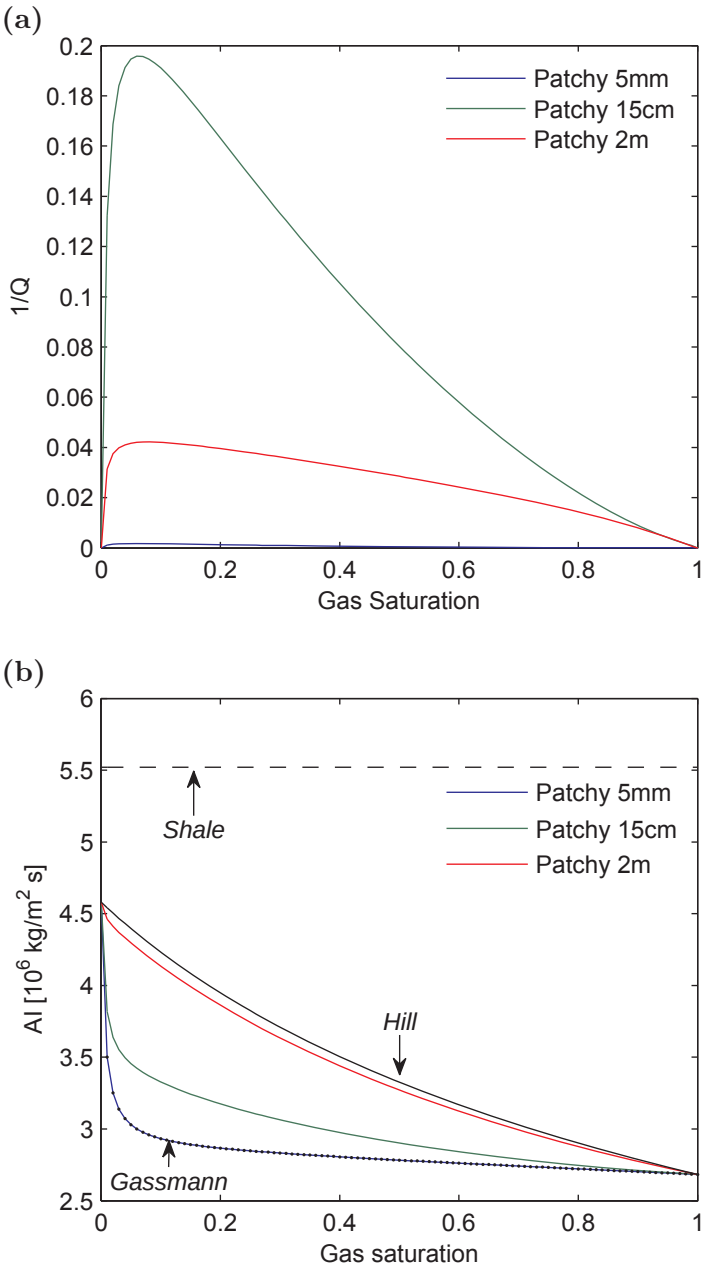

Figure 6.6: Attenuation and acoustic impedance are plotted as function of saturation. The frequency and effective pressure 30 Hz and zero, respectively.

We are dealing with seismic reflection between two porous media, in which case, the mode conversion across the interface will generate Biot slow wave. However, the energy carried away by the latter is negligible at seismic frequencies (Dutta and Odé, 1983). Therefore, we can simplify the problem to reflection between two viscoelastic half-spaces which can be solved by the extended Zoeppritz equation for attenuative media (Aki and Richards, 1980; Liu et al., 2011).

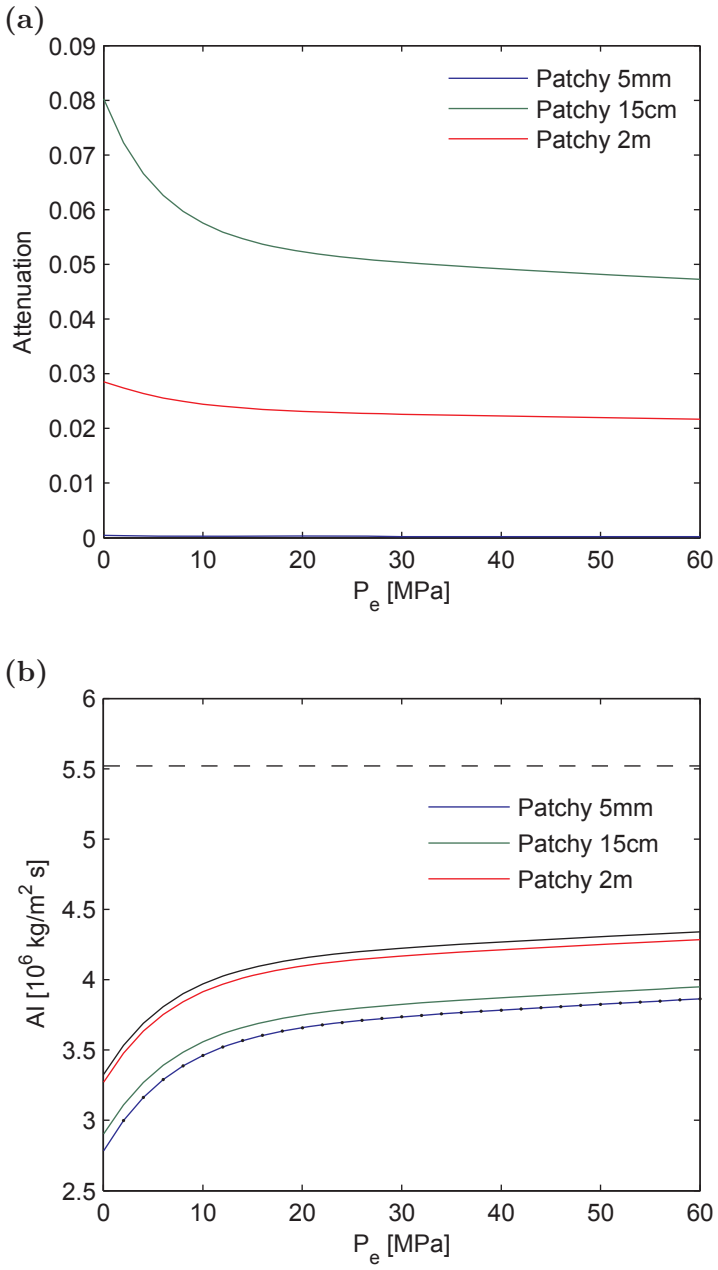

Figure 6.7: Attenuation and acoustic impedance are plotted as function of effective pressure. The frequency and saturation 30 Hz and 50%, respectively.

The resulting reflection coefficient incorporates the frequency-dependent phase velocities and attenuation of the rocks. The formula for the viscoelastic reflection coefficient is given in Appendix D.

We further assume the attenuation is negligible for the overburden shale and consequently constant velocity. We model the attenuation of the reservoir sand

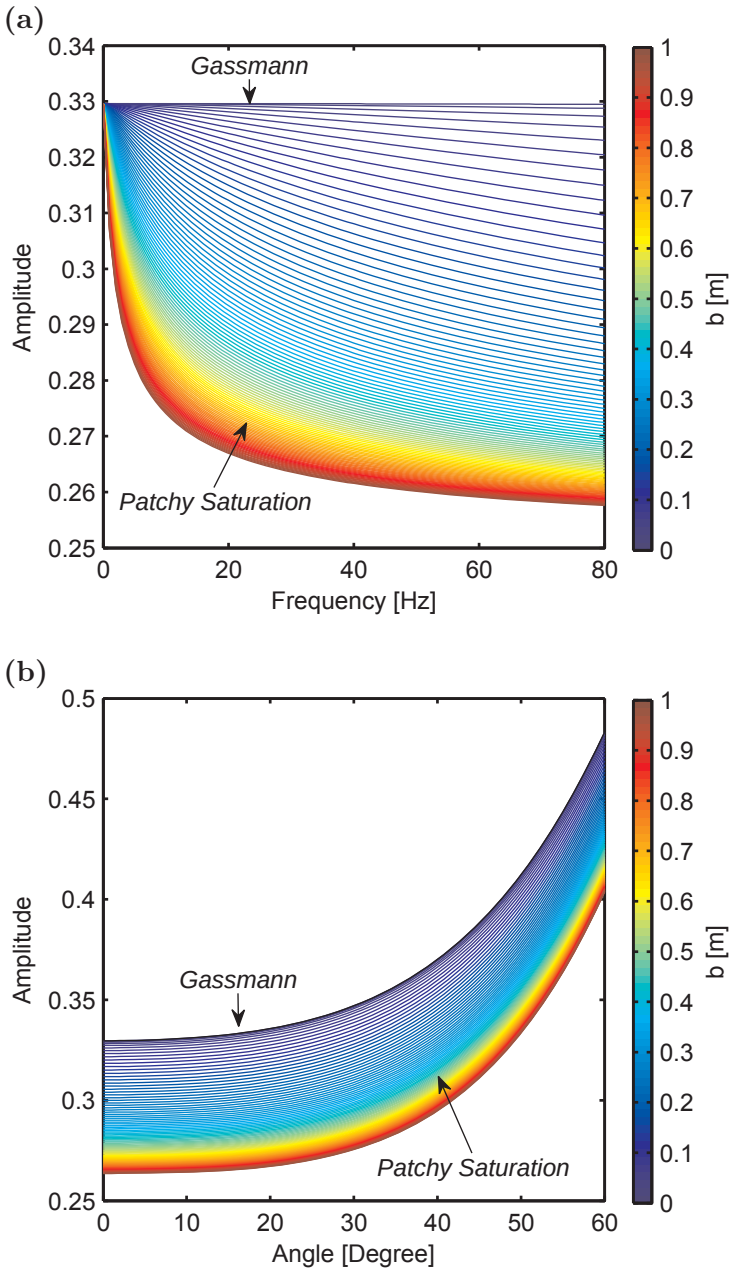

Figure 6.8: (a) Amplitude of reflection coefficient plotted as function of frequency. Incident angle is 0 degree. (b) Amplitude of reflection coefficient plotted as function of angle. Frequency is 50 Hz. In both plots, saturation is 50%. Colorbar denotes the saturation scale.

using the random patchy saturation model. Then, we investigate the amplitude variation resulting from P-wave reflection between the cap rock and the patchy-saturated reservoir rock having different characteristic saturation scale.

The velocities and density of the shale are given in Table 1. The resulting

acoustic impedance is shown in Figure 6.5b and Figure 6.6b. As can be seen, despite the dispersion, the impedance contrast between the shale and reservoir sand is constantly negative suggesting the AVO anomaly is Class III throughout the frequency and saturation ranges. The amplitude of the reflection coefficient for normal incident P-wave traveling from the upper shale to the lower sand is plotted in Figure 6.8a as a function of frequency. The saturation is 50% in this case. For uniform saturation, the amplitude is predicted by Zoeppritz equation in combination with Gassmann theory. This is the scenario of the largest impedance contrast as seen in Figure 6.5b, hence resulting in the highest amplitude-versus-frequency (AVF) as indicated by the top black line. While for patchy saturation AVF shows small variation for saturation scale between 0 and 10 centimetres. AVF decreases gradually with increasing saturation scale from 10 centimetres to 1 metre.

Figure 6.8b demonstrates the angle-dependence with 50% saturation and 30 Hz wave frequency. The amplitudes increase with increasing angle of incidence as expected from Class III AVO anomaly. Strong angle-dependence is observed above 20 degree. Larger saturation scale produce overall lower amplitudes. Figure 6.8a and Figure 6.8b show that, even at the same degree of saturation the amplitude can depend on the spatial fluid distribution. From uniform fluid mixture to saturation scale of 1m, the amplitude reveals maximum 20% reduction in both frequency and angle domains. Figure 6.8b also implies that, if we interpret the AVO signature with a linearised form, i.e, $R = R_0 + G\sin^2\theta$, it will result in a saturation scale -dependent AVO intercept R_0 and a scale-independent AVO gradient G. The amplitude of the reflected wave decreases with increasing saturation scale because of velocity dispersion. Thus, it should be noted that this will be opposite for Class I reservoir where the amplitude will increase with increasing saturation scale.

6.3.6 Seismic characteristics in an attenuative reservoir

Now let us investigate the significance of the saturation scale on seismic signatures. For P-wave propagating in a porous reservoir containing two fluids, the cause of attenuation consists of two parts, one is the mode converted Biot slow wave which diffuses away from the reservoir interface; the second is wave-induced pressure diffusion across the mesoscopic fluid inhomogeneities inside the reservoir. In the seismic frequency range, the former is often negligible whereas the

latter gives rise to major dispersion and attenuation (Müller et al., 2010). The poroelastic simulation at reservoir scale can be computationally expensive, especially for small saturation scale. Alternatively, the dispersive reservoir can be represented by a viscoelastic solid which incorporates the same attenuation and velocity curve (Rubino et al., 2011; Ba et al., 2014). Therefore, we can apply viscoelastic modelling, which captures the mesoscopic loss and meanwhile more efficient. We use the OASES code (Schmidt, 2011) for the viscoelastic reflectivity modelling with velocity dispersion provided by the random patchy saturation for each saturation and effective pressure. For homogeneous saturation with no attenuation, we apply elastic modelling with velocity provided by Gassmann's equation. The same geological model introduced in last section will be used here for the seismic modelling. We assume the gas sand reservoir is at 500 metre depth and of 100 metre thickness. Ten source-receiver pairs of different offsets are simulated. The burial depth of the sources is 10 metre and the receivers are placed at the surface. The impulse response from OASES is convolved with a Ricker wavelet of 30 Hz dominant frequency.

The geometrical-divergence corrected CMP gather for each saturation scale is shown in Figure 6.9. The saturation and effective pressure used for the modelling is 50% and zero, respectively. The resulting CMP gather covers an angle range from 0 to 30 degree. The AVO responses picked from the seismograms are normalized and compared with the amplitudes calculated by the viscoelastic reflection coefficient. The results show consistency between the modeling and theoretical prediction. By comparing Figure 6.9a and Figure 6.9b, we find that the seismic response of millimetre saturation scale is essentially the same with the result of the homogeneous saturation. This reveals the fact that millimetre saturation scale can be seen as 'homogeneous' at seismic frequencies. However, we have noted that this is no longer true at sonic log or ultrasonic frequency ranges as indicated by the characteristic frequency in Figure 6.4c. Under these high frequencies or short wavelengths, millimetre scale will play a role of 'patchy'. On top of frequency, the role transition from 'homogeneous' to 'patchy' can also be controlled by the lithology of the rock. This point is very important and will be addressed later.

As shown in Figure 6.9, with increasing saturation scale, the amplitude of the reflection at the top of the reservoir decreases progressively. This behaviour is consistent with the AVO signature shown in Figure 6.8b. The amplitude and

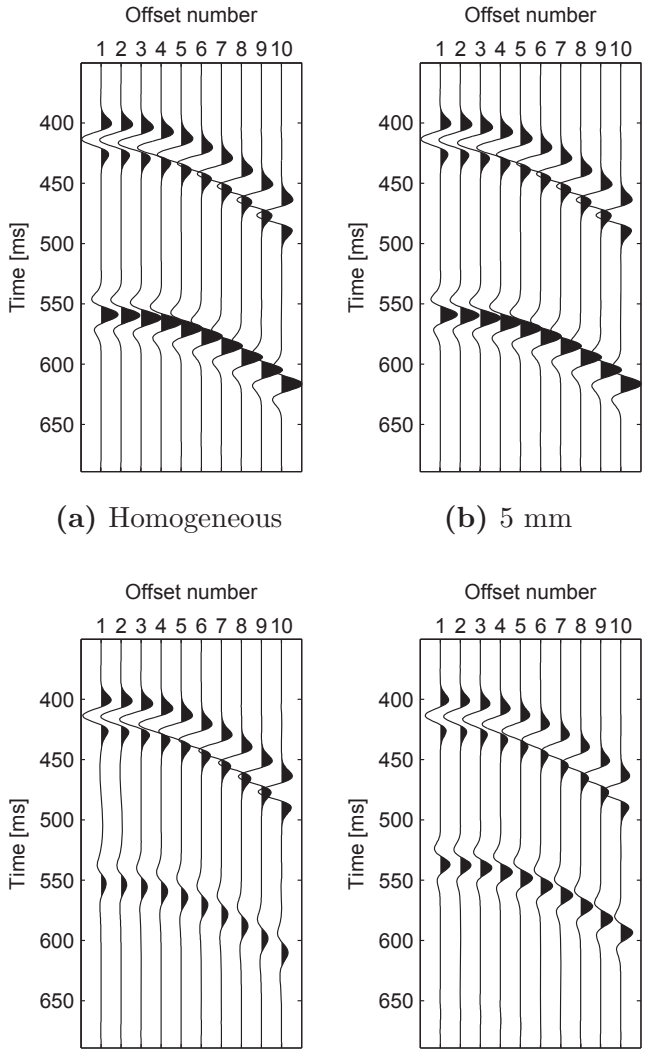

(a) Homogeneous **(b)** 5 mm

(c) 15 cm **(d)** 2 m

Figure 6.9: CMP gathers showing the reflections at top and bottom of the reservoir. Ricker wavelet of 30 Hz dominant frequency is used for the modelling. The reservoir is assumed to have 50% saturation and zero effective pressure. The saturation scales are (a) homogeneous; (b) 5 mm; (c) 15 cm; (d) 2m, respectively.

arrival time of the base reflection differs significantly for each saturation scale. Because the base reflection is not only affected by the reflection coefficient but also the attenuation due to wave propagation. This contrasting behaviour can be clearly identified by comparing the zero-offset traces in Figure 6.10a. The millimetre saturation scale possesses the largest base-reflection amplitude as the propagation loss is minimum. This is indicated by the negligible attenuation from Figure 6.5a. The arrival time of the reflected wave from the base is the latest for the millimetre saturation scale as its corresponding velocity is the lowest, which is also shown in Figure 6.5b. Then centimetre saturation scale has the smallest

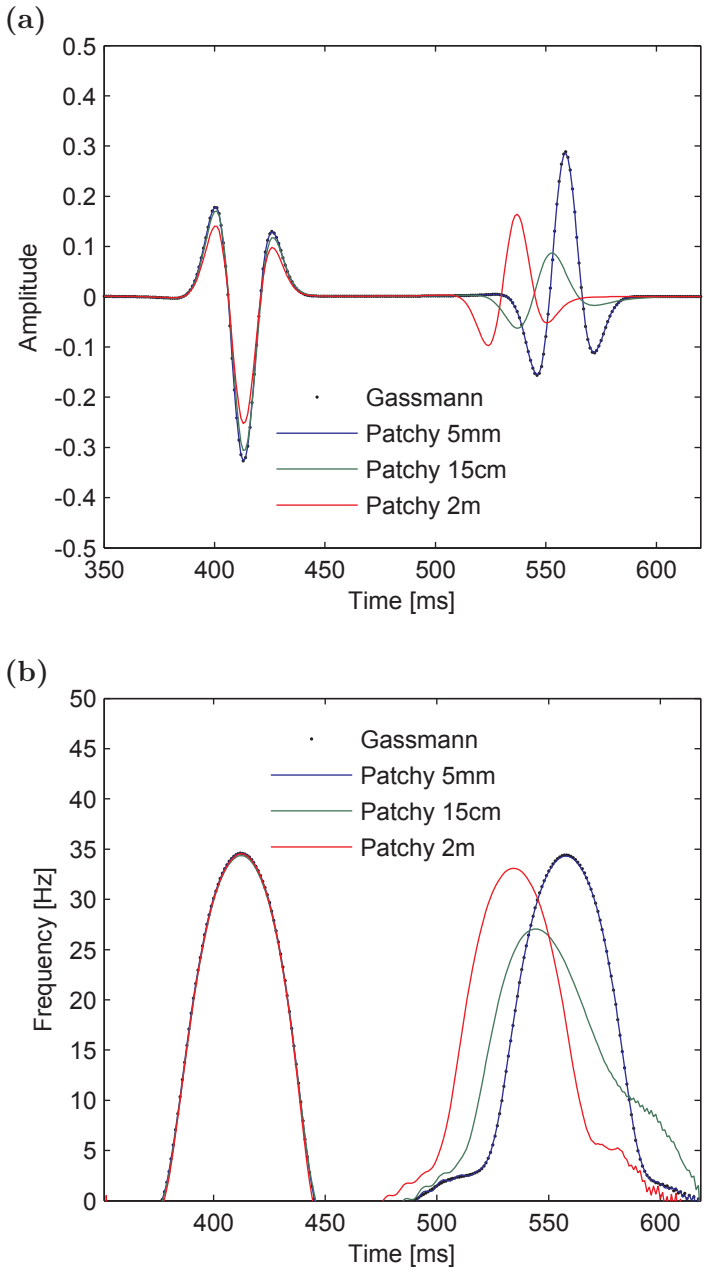

Figure 6.10: (a) Zero-offset trace extracted from the CMP gather in Figure 6.9; (b) Instantaneous frequency associated with the Zero-offset trace.

amplitude because of high attenuation due to wave-induced pressure diffusion. Meanwhile, it is associated with an early arrival time due to velocity dispersion. The biggest time-shift corresponds to the metre saturation scale whereas its amplitude resides in between the other two scales.

The instantaneous frequency can be a useful tool to illustrate the attenuation

behaviour of a reservoir (Castagna et al., 2003). In Figure 6.10b, we show the instantaneous frequency attribute of the zero-offset traces extracted from the CMP gathers. A loss of high frequency content after propagation can be observed for centimetre and metre saturation scale. Also accompanied with these two cases is a shifted time location of the dominant frequency. Most interestingly, two low frequency tails appears for the two attenuative saturation scales. The frequency content and width of the tails are proportional to the amount of attenuation. This behaviour is most likely associated with the low frequency shadow of hydrocarbon reservoir with high attenuation (Castagna et al., 2003).

Generally speaking, Figure 6.10a, 6.10b reveals the typical characteristics of a frequency-dependent attenuative reservoir. Let us envisage a reservoir dominated by a bell-shape attenuation curve with characteristic frequency f_c, the associated velocity is a monotonic increasing function of frequency. If the frequency of the incident wave is f, we have the following three cases

- $f \ll f_c \longrightarrow$ small V, small Q^{-1} ,
- $f \approx f_c \longrightarrow$ medium V, high Q^{-1} ,
- $f \gg f_c \longrightarrow$ high V, small Q^{-1} .

In the realm of patchy-saturation with Class III reservoir assumption, these three cases are associated with the presence of millimetre, centimetre and metre saturation scale, respectively. For a single 3D seismic survey, one can always use the patchy saturation model with a reasonable saturation scale or patch size to fit the observed velocity and attenuation. Accordingly, the saturation or fluid pressure are inverted. In a 4D seismic survey, the saturation, fluid pressure and saturation scale will all become a function of time. What commonly being used for 4D interpretation is to apply the patchy saturation model with a time-independent saturation scale and attribute the causes for time-lapse attenuation solely to the change of saturation or fluid pressure. This approach can be problematic, especially in presence of a drastic change of subsurface fluid distribution over time. As can be seen from Figures 6.6, 6.7, different scales with different saturation/pressure can result in the same attenuation and velocity, which creates an ambiguity for the interpretation. In the next section, we emphasize the importance of including the saturation scale into quantitative interpretation of 4D seismic signatures.

6.4 Implications for the interpretation of time-lapse data

The reservoir fluid distribution can differ over the repeated seismic surveys during the time-lapse monitoring. Therefore, integrating the time-dependent saturation scale is important for quantitative interpretation of time-lapse attenuation. Between two surveys, the time shift for the reflected P-wave from the reservoir base can be written as

$$\Delta t = 2\left(\frac{h}{V_2(S_{\mathrm{g}2}, P_{\mathrm{e}2}, b_2)} - \frac{h}{V_1(S_{\mathrm{g}1}, P_{\mathrm{e}1}, b_1))}\right) , \tag{6.9}$$

where h is the thickness of the reservoir. The change of the amplitude (or time-lapse amplitude) at the top of reservoir can be given by

$$\Delta A = |(A_2(S_{\mathrm{g}2}, P_{\mathrm{e}2}, b_2) - A_1(S_{\mathrm{g}1}, P_{\mathrm{e}1}, b_1))| , \tag{6.10}$$

In an attenuative reservoir, both the time shift and amplitude are frequency-dependent. For normal incidence, the amplitude between two dispersive half-spaces can be expressed as (Ren et al., 2009)

$$A(\omega) = \sqrt{\frac{\omega^2(V_{pl}\rho_2 - V_{pu}\rho_1)^2 + V_{pu}^2 V_{pl}^2(\rho_u a_l)^2}{\omega^2(V_{pl}\rho_l + V_{pu}\rho_u)^2 + V_{pu}^2 V_{pl}^2(\rho_u a_l)^2}} , \tag{6.11}$$

where the superscripts l, u denote the upper and lower half-spaces and a is the attenuation coefficient (see Appendix D). The amplitude given by equation 6.11 reduces to the elastic case when the attenuation coefficent a becomes zero. Equations 6.10 and 6.11 can be combined to calculate the time-lapse amplitude at normal incidence. Based on equations 6.9–6.11 and the reflection coefficient introduced in the previous section, we demonstrate how saturation scale affects the interpretation of time-lapse data by analysing the time shift, amplitude change and time-lapse AVA signature.

6.4.1 Scale effect on saturation estimation

The time-shift and amplitude change during gas injection is shown in Figure 6.11. The wave frequency is 30 Hz and the effective pressure here is assumed to be zero to highlight the saturation effect. In Figure 6.11a, the millimetre saturation

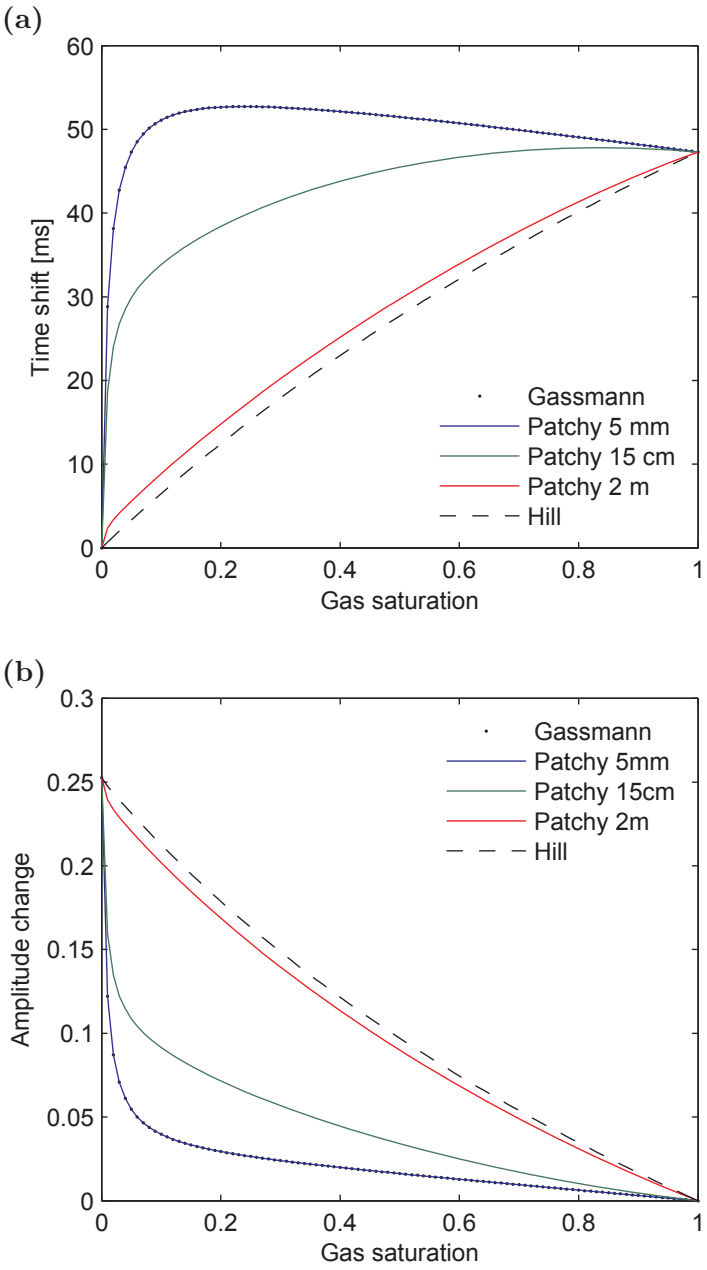

Figure 6.11: Time shift and amplitude change are plotted as function of saturation. The frequency and effective pressure are 30 Hz and zero, respectively.

scale presents an increasing time delay when the gas saturation increases from zero to few percent. When the gas saturation keeps increasing, the amount of time delay gradually decreases. The centimetre saturation scale presents a gradually increased time delay with increasing gas saturation. For the metre saturation scale, the time delay increases quickly and linearly with increasing gas saturation. In Figure 6.11b, the amplitude change decreases with increasing gas saturation for

all scales. In presence of millimetre saturation scale, the time shift and amplitude change shows less sensitivity with the change of gas saturation. In other words, with prior knowledge on the change of gas saturation (from well logging data), if the slopes of the time shift and amplitude change are small, we can deduce that there is neither larger fluid patches nor a jump in saturation scale during the repeated surveys. On the other hand, let us assume there is a change of fluid patch size or a jump in saturation scale (for example from the green curve to the red curve) with increasing gas saturation. In this case, interpreting an observed time shift and change in amplitude using Gassmann model or a constant scale patchy model can result in underestimation in the change of gas saturation.

Whether the reservoir fluids are distributed uniformly or in a patchy manner will have implications on AVO inversion. To illustrate this point, we compare time-lapse AVA signatures modelled by Gassmann theory and patchy model. A correlation length of 1 metre is assumed for the patchy case. In Figure 6.12, the AVA responses at the end-member saturations are the same for both models. The gas sand has appreciably stronger reflection than the wet sand. For uniform saturation, AVA responses for 0% to 95% gas saturations are localized near the gas bound. In contrast to in patchy saturation, AVAs are evenly distributed between the bounds. The difference can be explained by invoking the impedance-saturation relation, see Figure 6.12b. The random patchy saturation model entails a gradual change of the impedance with saturation which results in smoothed impedance contrast. Whereas the Gassmann-Wood model implies a strong 'gas effect', this causes a sudden drop of the impedance contrast near full water saturation. The comparison also indicates that, in presence of 'seismic scale' fluid patches, interpreting time-lapse AVA response with Gassmann model will overestimate the change in water saturation. Another interesting point we can draw from Figure 6.12 is that, for homogeneous saturation, the AVA responses can never reach below 0.2 (except for the wet sand). On the other hand, for patchy saturation, the minimum AVA response reaches 0.1. Hence, given the prior knowledge of the rock properties (from well logging data), one can use time-lapse AVA to deduce the information of fluid distribution.

6.4.2 Scale effect on pressure estimation

Figure 6.13 emphasize the effect of saturation scale on the estimation of pressure change. We consider here that the time-lapse signal variation is mainly

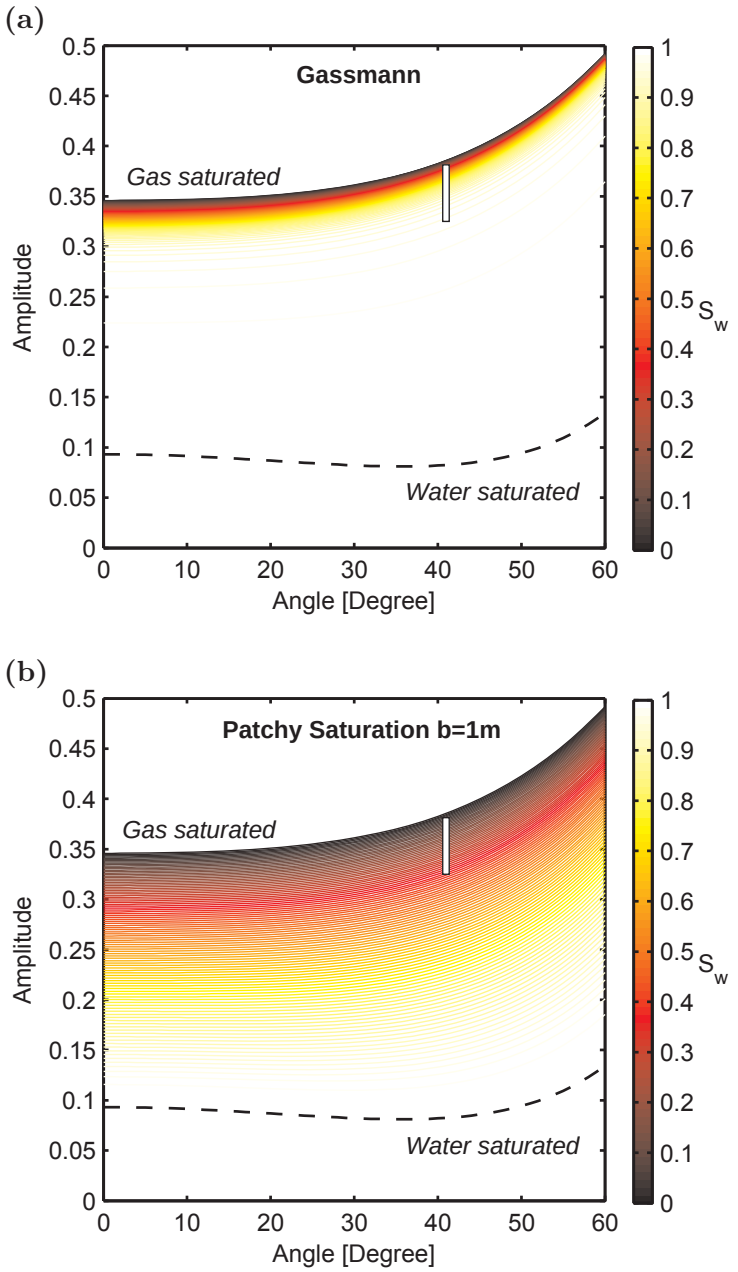

Figure 6.12: Time-lapse AVA signature for saturation change. Prediction is made using (a) Gassmann equation and (b) patchy saturation model with 1 m saturation scale. The frequency and effective pressure are 30 Hz and zero, respectively.

caused by change of pressure and consequently a constant saturation of 50%. The frequency is still 30 Hz. Let us also assume that the confining pressure remains constant and an average effective stress coefficient for the reservoir is 1. Thus, the increment of the effective pressure will be equivalent to the decrement of the fluid pressure. Here, we only focus on effective pressure varies from 0 to

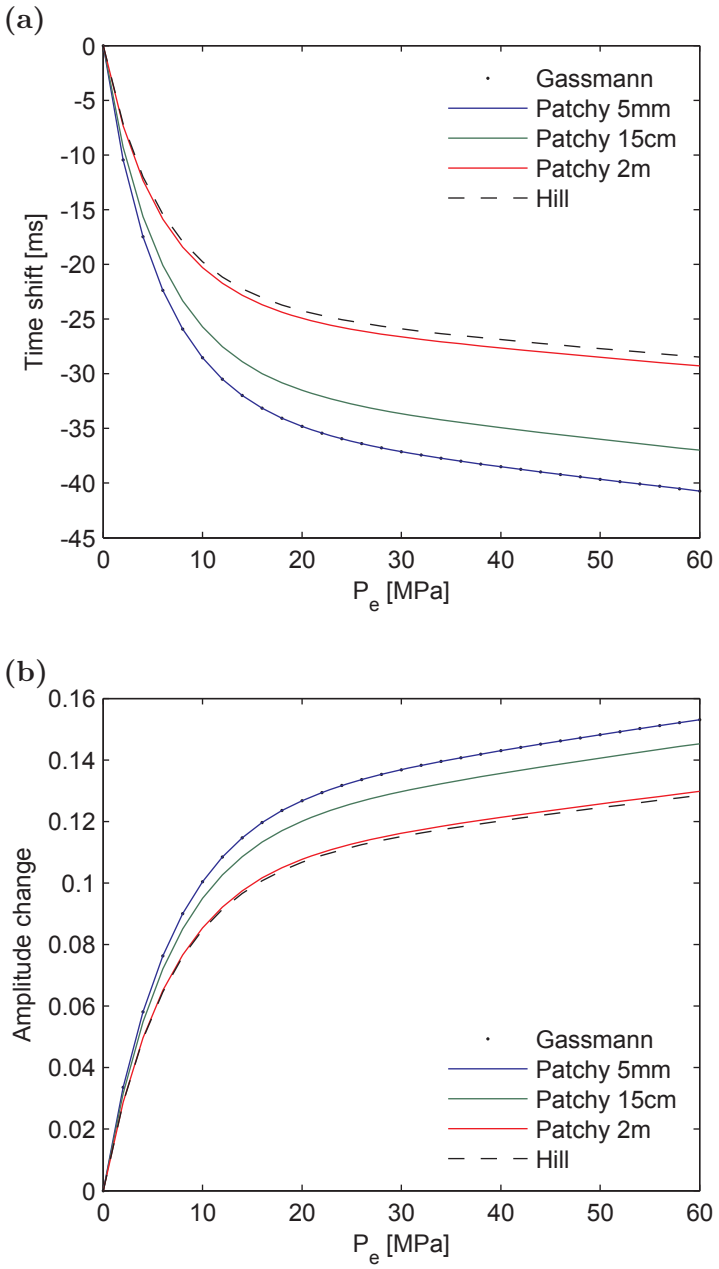

Figure 6.13: Time shift and amplitude change are plotted as function of effective pressure. The frequency and saturation are 30 Hz and 50%, respectively.

10 MPa as the maximum lithostatic pressure with 500 metre overburden shale is 10 MPa. As shown in Figure 6.13, the time pull-up and amplitude change increase with increasing effective pressure or decreasing fluid pressure. We see that saturation scale does not play a significant role on the signal for pressure changing from 0 to 5 MPa. When pressure change resides between 5 and 10 MPa, if we assume that the pressure change over repeated surveys is accompanied with

an increase in saturation scale (for example, from the blue curve to the green curve or from the green curve to the red curve). In this situation, interpreting an observed time shift or amplitude change with the Gassmann model or a constant scale patchy model will overestimate the decrement of fluid pressure. Also comparing with the saturation effect (on the net range of time shift and amplitude change) in Figure 6.12, we see that pressure effect has a relative small capability in influencing time-lapse signal.

We compare the time-lapse AVA signatures computed using Gassmann model and patchy model in Figure 6.14. The patchy model incorporates an correlation length of 1 metre. In Figure 6.14, from the zero effective pressure line (top blank line), every following line indicates an increase of 2 MPa effective pressure or decrease of 2 MPa fluid pressure. The amplitude decreases with increasing effective pressure (decreasing fluid pressure). On the contrary, the angle dependence is greater for larger effective pressure. Let us interpret a same time-lapse AVA decrease, denoted by the white rectangle in the plots, with the two different models. The patchy model with metre saturation scale predicts a decrease of fluid pressure from 1 MPa to 8 MPa whereas the Gassmann model predicts a decrease of fluid pressure from 8 MPa to 40 MPa. Here, we see that if the reservoir has a patchy fluid distribution, interpreting an observed time-lapse AVA response can result in both unreasonable change and value of the fluid pressure.

6.4.3 Effects of capillary pressure and residual saturation

Let us now analyse the influence of capillary pressure and irreducible water saturation on 4D interpretation. To this end, we assume a capillarity stiffening T of 1.5 GPa and a irreducible water saturation S_{irrw} of 20%. The modified lower and upper bounds for the P-wave modulus can be calculated using equation 6.4 and 6.5, accordingly. Then we calculate the corresponding time shift using equation 6.9 with the calculated velocities. The time shifts at low and high frequency limits for gas injection is shown in Figure 6.15. We compare the results associated with the modified bounds with the results associated with conventional Gassmann and Hill limits. In Figure 6.15, at low frequencies, the maximum time delay decreases upon consideration of capillarity (see the change from solid curve to squares). This is because the stiffening effect from capillarity compensates the softening effect from density. Time delay now gradually increases with increasing gas saturation. At high frequencies, due to presence of residual water satura-

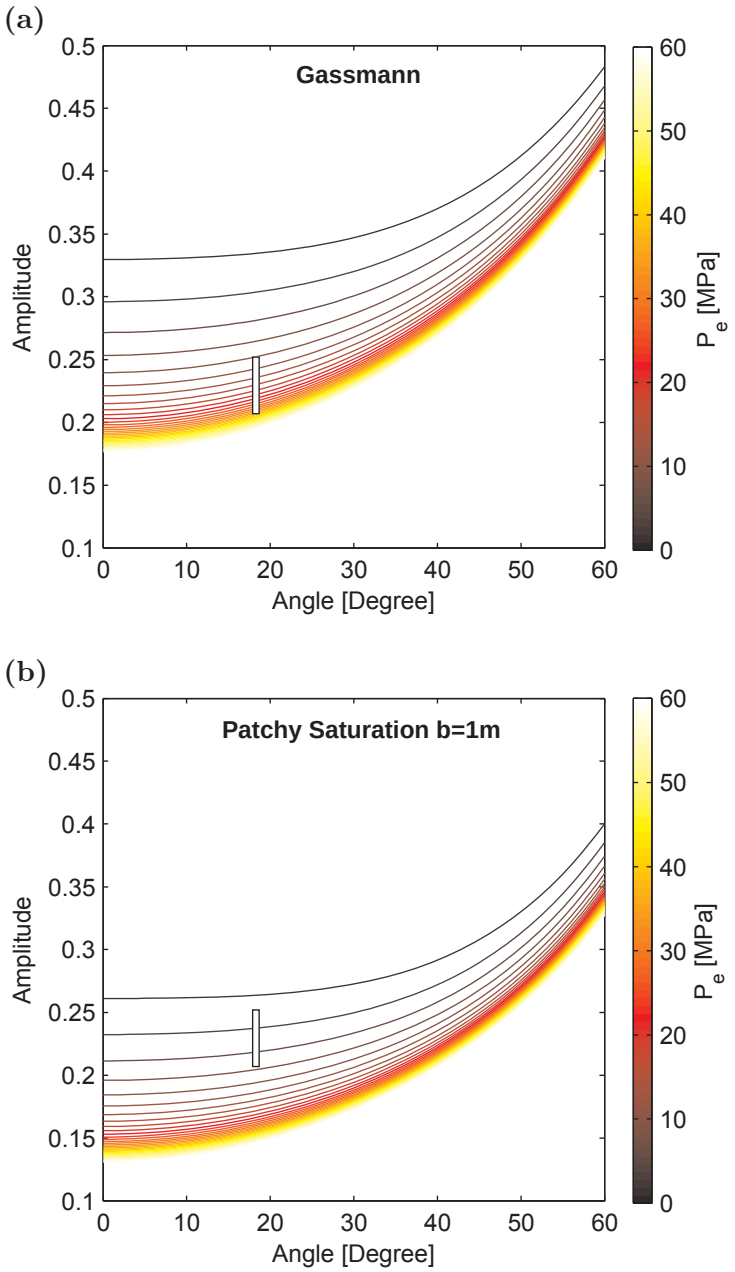

Figure 6.14: Time-lapse AVA signature for effective pressure change. Prediction is made using (a) Gassmann equation and (b) patchy saturation model with 1 m saturation scale. The frequency and saturation are 30 Hz and 50%, respectively.

tion, the time shift yields a stronger dependence on the change of gas saturation comparing with Hill prediction (see the change from dashed line to triangles). When both effects are considered, it results a narrower envelope of possible time shift between saturation limits of 0 and 80% gas saturation. Consequently, the uncertainty due to scale effect in predicting the saturation change becomes less.

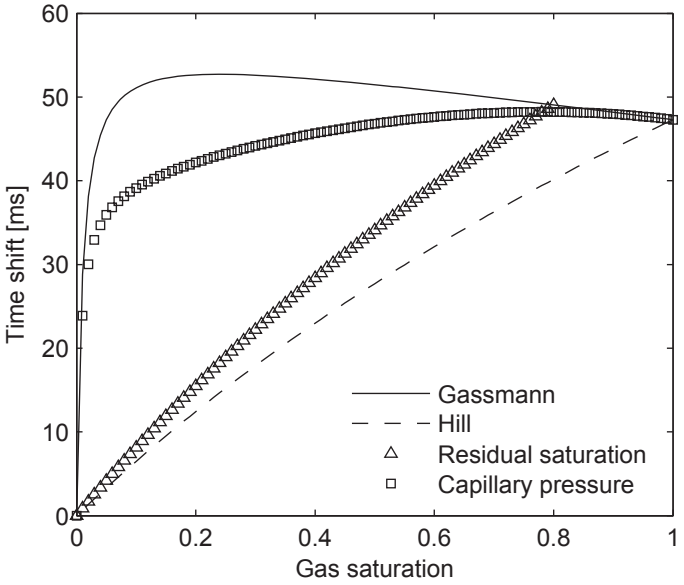

Figure 6.15: Comparison of time shift bounds calculated using two different methods. Methods based on Gassmann and Hill equation are given by solid and dashed line, whereas based on capillarity and residual saturation extended equations given by square and triangle.

Further petrophysical measurements and flow simulation are required to infer the capillarity and irreducible saturation before they being used as input for seismic interpretation.

6.4.4 Effect of lithology

The attenuation characteristics associated with the saturation scales in an unconsolidated rock may no longer be valid for other types of rock. As the lithology variation can result in different elastic moduli and consequently leads to different seismic velocities. Meanwhile, it can also result in different transport properties of the rocks and consequently different seismic attenuation. The elastic moduli and permeability can often be related with porosity using empirical equations. Therefore, a large number of the lithology effects on acoustics can be simplified and attributed to the porosity variation. The consolidation effect associated with small porosity variation can be classified into previously discussed pressure dependence of the frame moduli. Here, we explore the lithology effect by studying the dependence of the characteristic frequency on porosity. To this end, we express the frame moduli as a function of porosity using Krief model with quartz moduli (Carcione and Picotti, 2006). We relate the permeability with porosity using Kozeny-Carman (KC) relation (Carcione and Picotti, 2006). Then equa-

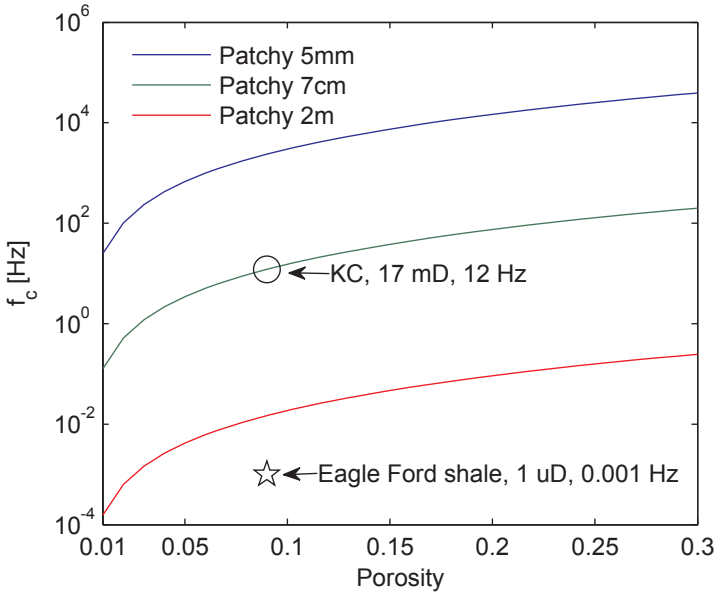

Figure 6.16: Effect of lithology on characteristic frequency. Saturation of 50% and effective pressure of zero are assumed.

tion 6.6 is used to compute the characteristic frequency for different saturation scales. We see that in Figure 6.16, when the porosity is reduced from 30% to 1%, the characteristic frequency decreases substantially by 3 orders of magnitude. For sandstone of large porosity, the millimetre saturation scale results in an attenuation peak in kilohertz range, thus, it is effectively 'homogeneous' scale at seismic frequencies. For tight sands or shales of small intrinsic porosity, the millimetre saturation scale gives rise to a attenuation peak in seismic frequency range. In this case, the millimetre saturation scale will act as 'patchy'. With respect to centimetre and metre saturation scales, the attenuation peaks of the small-porosity rocks (ϕ <5%) locate below seismic frequency. Therefore, seismic frequency band turns into the high frequency regime. In this case, incident waves of seismic frequency results in unrelaxed undrained rock, the attenuation of which becomes negligible whereas the velocity given by Hill theory. Common thinking is that millimetre saturation scale are only responsible for attenuation taking place at high frequencies (e.g., ultrasonic, sonic log and crosswell). However, this is no longer true for rocks with small porosity. This phenomenon has recently been observed in low frequency laboratory measurement of Eagle Ford shale (Mikhaltsevitch et al., 2015). In their work, in presence of fluid patches of 7 centimetres (sample size), no velocity dispersion presents in frequency range from 0.1 Hz to 500 KHz. The porosity of the Eagle Ford shale sample is 9%. Using Kozeny-Carman (KC) relation, it results in a permeability of 17 mD and

f_c of 12 Hz (denoted by circle in Figure 6.16). The measured permeability is 1 μD in the work of Mikhaltsevitch et al. (2015). Apparently Kozeny-Carman relation fails to predict the right permeability for shale in this case. However, if we reduce the characteristic frequency ($f_c \propto \kappa$) by 4 orders of magnitude as the exact overestimation in permeability from KC, we will have a f_c equal to 0.001 Hz. This indicates that the employed frequency range in the experiment resides in the non-dispersive regime (high frequency), which is consistent with the lab observation. Since seismic frequencies become effective 'high' frequency for low-porosity saturated rock, velocity would be close to Hill prediction. Therefore, we may expect less influence of saturation scale variation on 4D signatures.

6.4.5 Effect of in-situ fluid property

The reservoir fluid properties, such as fluid bulk modulus and density can be affected by the changes in composition, pressure and temperature during production (Johnston, 2013). Our concern here is how the changes of the in-situ fluid properties affect the attenuation characteristics. Let us further examine the expression of the characteristic frequency with particular emphasis on fluid properties. Again f_c can be written as

$$f_c = \frac{1}{2\pi}\frac{D}{b^2} = \frac{1}{2\pi}\frac{\kappa}{b^2}\frac{N_w S_w + N_g S_g}{\eta_w S_w + \eta_g S_g}, \tag{6.12}$$

with stiff frame approximation $K_g \gg K_f$, it further reduces to

$$f_c = \frac{1}{2\pi}\frac{\kappa}{\phi b^2}\frac{K_{fw} S_w + K_{fg} S_g}{\eta_w S_w + \eta_g S_g}. \tag{6.13}$$

Because the gas modulus K_{fg} and viscosity η_g are much smaller than those of water, we have

$$f_c = \frac{1}{2\pi}\frac{\kappa}{\phi b^2}\frac{K_{fw}(T,P)}{\eta_w}. \tag{6.14}$$

Therefore, f_c essentially relies on the water properties, or precisely the properties of the stiffer fluid phase. Several important points can be drawn from equation 6.14. We see that in-situ gas properties do not affect the position of the attenuation peak and consequently has no influence on the characteristic of the saturation scale. However, it does affect the amount of attenuation. This is because when the gas modulus increases with increasing depth, the compressibility contrast between gas and water saturated region becomes smaller. Consequently,

the attenuation due to wave-induced pressure diffusion becomes small. On the other hand, f_c is inversely proportional to the fluid viscosity in equation 6.14. Let us assume the reservoir contains heavy oil with high viscosity. In this situation, the attenuation peak (or the characteristic frequency) will shift towards lower frequency and consequently affect the attenuation characteristic of the discussed saturation scale. The effect of fluid viscosity on attenuation has been observed in laboratory by Batzle et al (2006). Same logic with the low porosity rock (last section) can be applied here: with high viscosity fluids, we may expect less influence of saturation scale variation on 4D signatures. Despite the complex causes of in-situ fluid properties, one can always calculate them using equations based on thermodynamic laws or apply empirical relations obtained from laboratory measurement (Johnston, 2013). These reservoir fluid properties will be used in the model and the resulting attenuation characteristics can be analyzed accordingly.

6.4.6 Effect of geological complexity

The homogeneous reservoir model employed in this study is of course a simplification of the realistic reservoir. The natural reservoir and its overburden in sedimentary environment may be fractured (lecture by Liu, 2013) and thinly layered (Gelinsky et al., 1998; MacBeth and Stephen, 2008). Reservoir heterogeneities can lead to frequency-dependent attenuation, which further complicates the interpretation of time-lapse seismic signatures. Thus, it is important to estimate the attenuation caused by these frame heterogeneities and correct them from the observed attenuation or amplitude. The corrected attenuation/amplitude which is due to fluid heterogeneities, may then be interpreted with the patchy saturation model. However, the superposition rule (for attenuation) is not valid for velocity and hence the interpretation of time shift becomes more difficult. Therefore, further refinement of patchy saturation model is recommended to take geological heterogeneities into account. The fluid distribution provided by flow simulation can be used to constrain the development of the saturation model (MacBeth and Stephen, 2008).

6.5 Identification of saturation scale

Last but not the least, the important question yet to be addressed is where do we find the saturation scale? From previous discussion, we see that finding the representative saturation scale for each survey time as input for 4D interpretation

can be crucial. As shown in Figures 6.12 and 6.14, the AVO has the potential to serve as an indicator for the saturation scale. Considering all possible saturations and pressure, the characteristics and value of AVA signatures between homogeneous and patchy saturation are different. This can be used to distinguish the two scenarios. Laboratory rock physicists also try to study the evolution of the fluid distribution with change of saturation from core-flooding experiment. However, the observed fluid distribution is restricted to both the image resolution and size of the sample. Hence, it is still under debate if it can be used as the representative fluid distribution at reservoir scale. The accepted fact is that the realistic fluid distribution and attenuation mechanism are still poorly understood. Nonetheless, as a first order approximation, the best way for obtaining the 'seismic' fluid distribution is perhaps using the patchy saturation model to fit the real data. With the commonly available time-lapse well logs and VSP data (Caspari et al., 2011; Al Hosni et al., 2015), one has the constrained velocity versus saturation relation around the well location. The established velocity -saturation relation can be fitted with the patchy saturation model. The deduced saturation scale or patch size can be seen as the representative fluid distribution at the survey moment. It can be used as a constraint at the well location when applying seismic inversion in combination with the patchy saturation model. With integration of time-dependent saturation scale from well log and VSP into inversion, we may be able to achieve the more robust fluid distribution over time and space, and consequently, more accurate information on the variation of saturation and fluid pressure. Recent studies also indicate that spectral decomposition (Castagna et al., 2003; Rubino et al., 2011) and resistivity -saturation relation (Alemu et al., 2013) can potentially become useful tools for obtaining the fluid distribution information.

6.6 Chapter conclusions

Dynamic fluid injection in operations such as enhanced oil recovery and CO_2 sequestration inevitably leads to the formation of fluid clusters (patches). These fluid clusters continuously change in shape and size. Despite their spatio-temporal variability, these clusters have a characteristic length scale at every instant of time. This saturation scale is a per se unknown variable and induces yet another uncertainty into quantitative seismic interpretation of time-lapse signatures in addition the to the saturation and formation pressure changes usually considered.

In contrast to empirical models (for example, Brie et al. (1995)), the saturation scale is firmly embedded in the random patchy saturation model including its extensions for capillarity and residual saturation. Thus, it can be used to analyse the effect of saturation-scale on time-lapse changes. Both, travel-time shifts and time-lapse attenuation can be addressed.

In this work, three contrastingly different saturation scales (namely millimetre, centimetre and metre sized patches) are used to demonstrate their influence on time-lapse signatures of a simplistic geological model: The reservoir consists of an unconsolidated partially saturated sand – modelled as a poroelastic solid embedded between two shale layers. We find that

- The millimetre saturation scale is associated with dominant attenuation due to wave-induced pressure diffusion (in the reservoir zone) in the kilohertz range; the metre scale is responsible for attenuation in the millihertz band. The centimetre scale leads to significant attenuation at seismic frequencies. This scale leads to the highest attenuation for all saturations and pressures. The attenuation levels off at high effective pressure.
- The saturation scale significantly changes the AVF (amplitude versus-frequency) and AVA (amplitude-versus-angle) responses of the reflected P-wave. For a class III reservoir, the amplitude of the reflected P-wave decreases with increasing saturation scale.
- The reflected P-wave from the base of a centimetre-saturation-scale reservoir possesses the smallest amplitude. The earliest arrival time of the base reflection is associated with the metre saturation scale. The seismic signature of the millimetre saturation scale is the same with elastic modelling result using homogeneous saturation assumption.
- The time shift and amplitude change of a millimetre saturation-scale reservoir is less sensitive to the change of gas saturation compared to the other two scales. In presence of saturation scale increase/decrease, interpreting an observed time shift and amplitude change using Gassmann model or a single scale patchy model will lead to underestimation/overestimation of gas saturation.
- The saturation scale has less impact on the prediction of fluid pressure changes. Nevertheless, interpreting an observed time shift or amplitude

change with the Gassmann model or a single scale patchy model will underestimate/overestimate the fluid pressure if the saturation scale increases/decreases during the gas injection.

- When the time-lapse signal is dominated by either saturation or pressure changes, the associated time-lapse AVA signature is different between uniform and patchy saturation. This indicates that time-lapse AVA can be used to infer the subsurface fluid distribution.

- Including the effects of capillarity and residual saturation into the interpretation can potentially reduce the uncertainty from saturation scale effect. We expect less influence of saturation scale variation on time-lapse seismic signature either when the porosity of rock is low or the viscosity of fluids are high.

Chapter 7

Conclusions and outlook

Capillarity is a crucial petrophysical parameter which is extensively used by petroleum engineer for evaluating the reservoir quality and performance. Though capillarity provides key source of petrophysical information, its role on the modelling of the acoustic signatures has been largely overlooked in rock physics until this thesis. Through the study of this thesis, we have achieved two major objectives: one is to investigate the role of capillarity on the wave characteristics (i.e., velocity, attenuation, reflectivity) in partially saturated porous rocks and another is to address the implications of the new theory on QSI (quantitative seismic interpretation) across the hydrocarbon exploration and production life cycle. The study has been carried out through three primary steps including the development of the rock physics model, the model calibration via laboratory data modelling and the practical implementation of the model into QSI. In this final chapter, I will briefly summarize the obtained results. Based on these results, I will discuss their application potentials and the associated future aspects.

The presence of the capillarity in response to the dynamic wave propagation can be represented by a fluid pressure discontinuity boundary condition. Including this boundary condition in the upscaling procedure of Biot's dynamic equations with respect to a mesoscopic geometry configuration enables the study the combined effects of capillarity and mesoscopic fluid flow. Based on this central idea, the classical White's model for P-wave attenuation in patchy-saturated layered media is generalized to account the capillary pressure. The original White's theory predicts that the low frequency limit of the P-wave velocity is given by the

Gassmann's equation with an effective fluid modulus calculated by the Wood's formula. In contrast, the new theory indicates that such static velocity limit can be further controlled by the capillary pressure. The capillary pressure gives rise to a membrane stiffness which exerts between the contact area of the immiscible fluid phases. As a result, the dispersion and attenuation diminishes. These results lead to an intriguing fact that the Gassmann-Wood theory as well as the original White's model are only valid when the capillarity effect is negligibly small. In other words, it implies that when the reservoir capillarity effect is strong, modelling the velocities obtained from well-log or seismic data with the capillarity-corrected model will give an increased estimation of the gas saturation (see Figure 3.3 for example). In the current framework of the capillarity-extended White's model, the rock frame is required to be homogeneous and isotropic. Given that the resulting analytical expression (i.e., equation 3.24) for the P-wave modulus is simple, one possible extension of the model is to further consider the presence of fractures in the porous host rock. This requires that the generalized White's model would to be parametrized within the framework of linear slip theory (Brajanovski et al., 2005; Kong et al., 2013). This could be a simple recipe for studying the capillarity effect in fractured rocks. Frame heterogeneities such as fractures and permeability fluctuations often lead to an effective anisotropic behaviour of rocks. If the fractures are aligned, the generalized White's model can be further extended to investigate angle-dependence of the attenuation and dispersion using the recipe suggested by Krzikalla and Müller (2011) and Carcione et al. (2013).

The capillary force controls the two-phase flow behaviour and is inherently coupled with the fluid distribution. The fluid distribution again influences the elastic properties of the saturated porous rock via mesoscopic fluid flow. To explore the relationships between the capillarity, fluid distribution and acoustic properties, the concept of membrane stiffness is incorporated into the framework of the 3D random patchy saturation model. It is found that not only the membrane stiffness but also the spatial fluid distribution (i.e., correlation length, specific surface area) can affect the capillarity stiffening. It is interesting to see that the capillarity-extended static P-wave velocity increases with increasing correlation length of the fluid patches. Consequently, the dispersion and attenuation further decreases with increasing correlation length of the fluid patches at seismic frequencies. The developed model can be useful for the seismic reservoir monitoring where the capillarity may play an important role during the dynamic fluid injection. To validate this idea, the model is applied to interpret the ultrasonic data acquired

during a core-flooding experiment where the capillary force dominates the two-phase flow regime. The predicted velocity- and attenuation- saturation relations indeed show consistency with the laboratory data. The model has shown its predictive power at ultrasonic frequencies, however, its applicability at low frequencies still needs to be verified. Therefore, it is recommended as future work to conduct low-frequency experiments on partially saturated rocks (Batzle et al., 2006; Tisato and Quintal, 2013) for a thorough examination of the capillarity phenomenon. The employed frequency of the measurement shall reside in the low-frequency asymptotic regimes of any attenuation mechanisms. Thus, the additional stiffening of the rock (if observed) can be attributed to the capillarity effect. The experiments shall also be combined with X-ray CT imaging. The statistical analysis of these CT images will be helpful for quantifying the effect of the spatial fluid distribution on the capillarity stiffening.

It is shown that the capillary pressure across the mesoscopic fluid heterogeneities has a strong effect on the velocity and attenuation. On the other hand, in a large reservoir, the capillary pressure can present between the gas-water contact and affect the seismic reflectivity. The reflection theory based on Biot's poroelasticity has been extended to investigate the role of the interfacial impedance (i.e., capillarity, interface permeability) on the P-wave reflectivity. It is found that the capillarity effect has a negligible impact on the P-wave reflectivity for a gas-water contact at seismic frequencies. Because the capillarity effect on the mesoscopic fluid flow is much more predominant than the capillarity effect on the P-wave reflectivity, we suggest that the viscoelastic modelling with attenuation estimated from the capillarity-extended patchy saturation model is sufficient to capture the capillarity effect on seismic signatures at reservoir scale. On the other hand, we do find that the capillarity has a substantial effect on the P-wave seismic reflectivity for a fluid/gas-saturated-medium contact. Especially, the contrasting amplitude-versus-angle behaviour resulting from open-pore, capillarity and imperfect hydraulic contact (see Figure 5.3, 5.3) provide a theoretical basis for examining these interface scenarios in the laboratory settings. For example, by comparing the theoretically calculated reflectivity with the measure reflectivity in the lab, one may quantify the value of the membrane stiffness, interface permeability in real rocks. These values can be further used in acoustic models, i.e., extended White's layered model or extended random patchy saturation model to compute the velocity and attenuation of a specific rock. It is therefore recommended as future work to devise a laboratory pulse-transmission

set-up (Johnson et al., 1994; Bouzidi and Schmitt, 2009) for investigating the seismic reflectivity associated with a fluid/gas-saturated-medium contact. Another possible application of the extended theory is to use AVO technique for quantifying the sea-floor properties (Amundsen and Reitan, 1995). Particularly, for a gas-saturated sea-floor whose interface is not perfectly sealed by sediments, the resulting AVO behaviour is expected to be different from the prediction of the elastic theory.

A workflow for the interpretation of the time-lapse seismic signatures has been established based on the developed patchy saturation model. We find that a changing saturation scale can be yet another crucial factor which controls the time-lapse seismic signal. Saturation scales of different orders are associated with contrasting acoustic characteristics of a partially saturated reservoir. A time-dependent saturation scale further complicates the analysis of the associated time-shifts and amplitude changes. As a result, ignoring the potential saturation scale variation over the repeated seismic surveys can result in biased estimation/discrimination of the saturation and fluid pressure from time-lapse seismic data. It is also found that including the effects of capillarity and residual saturation into the time-lapse analysis potentially reduces the uncertainty introduced by the scale effect. The study implies that integrating the saturation scale and capillarity effect into time-lapse AVO analysis (Landrø, 2001) can potentially lead to better discrimination of the saturation and pressure effects. The sub-resolution saturation scale, as an input for this theory, can be deduced from time-lapse well-log or VSP data (Konishi et al., 2009; Caspari et al., 2011; Al Hosni et al., 2015). These data is of high spatial resolution and can provide constraints on the spatial-temporal fluid distribution. A simple analysis such as comparison of the log- or VSP- derived velocity-saturation relations with Gassmann modelling results (i.e.,low saturation scale limit) should determine whether the saturation scale is a first order effect. If the saturation scale variation is evident, then a patchy saturation model is suggested to be applied in the time-lapse AVO analysis (Landrø, 2001) to honour the accompanied attenuation and dispersion effects. Feasibility studies are also required in the future to examine the sensitivity of the seismic amplitudes on the log-derived saturation scales.

List of Figures

List of Tables

Appendix A

Static undrained bulk modulus including capillary action

We consider a representative poroelastic volume defined in terms of a unit cell Ω. The displacement field of the solid and fluid $u_i^{(m)},\ U_i^{(m)}$ can be decomposed into a uniform displacement field $\beta x_i^{(m)}$ and periodic displacement field $\chi_{,i}^{(m)},\ \psi_{,i}^{(m)}$ (Milton, 2002) such that

$$u_i^{(m)} = \beta x_i^{(m)} + \chi_{,i}^{(m)}, \qquad U_i^{(m)} = \beta x_i^{(m)} + \psi_{,i}^{(m)}. \tag{A.1}$$

and their associated strain fields are

$$e_{ij}^{(m)} = \beta x_{i,j}^{(m)} + \chi_{,ij}^{(m)}, \qquad \epsilon^{(m)} = 3\beta + \psi_{,ii}^{(m)}, \tag{A.2}$$

where x_i $(i = 1, 2, 3)$ are cartesian coordinates. Superscript m denotes the mth phase and $\chi,\ \psi$ are periodic scalar potentials. β is a constant which can be regarded as a uniform strain within the unit cell. Substituting equation A.2 into equation 4.6, the total stress field of the respective saturated patch can be written as

$$\tau_{ij}^{(m)} = [(H^{(m)} - \phi C^{(m)} - 2\mu)(3\beta + \chi_{,ii}^{(m)}) + \phi C^{(m)}(3\beta + \psi_{,ii}^{(m)})]\delta_{ij} + 2\mu(\beta x_{i,j}^{(m)} + \chi_{,ij}^{(m)}). \tag{A.3}$$

According to Johnson (2001), the fluid strain $\epsilon^{(m)}$ within each patch can be expressed through the constitutive equations 4.6 and 4.7

$$\epsilon^{(m)} = \frac{1}{3\phi}\left(\frac{1}{K_\mathrm{s}} - \frac{1-\phi}{K_0}\right)\tau_{ii}^{(m)} + \frac{1}{\phi}\left(\frac{1}{K_\mathrm{s}} - \frac{1-\phi}{K_0} - \frac{\phi}{K_\mathrm{f}}\right)p_\mathrm{f}^{(m)}. \tag{A.4}$$

In the static limit, the fluid pressure $p_\mathrm{f}^{(m)}$ as well as $\epsilon^{(m)}$ are piecewise constant within each patch. Therefore $\tau_{ii}^{(m)}$ in equation A.4 has a constant solution. According to equation A.3, the dilatational part of the total stress can be expressed as

$$\tau_{ii}^{(m)} = 3(3\beta H^{(m)} - 6\beta\mu^{(m)}) + (3H^{(m)} - 3\phi C^{(m)} - 4\mu^{(m)})\chi_{,ii}^{(m)} + 3\phi C^{(m)}\psi_{,ii}^{(m)}. \tag{A.5}$$

$\tau_{ii}^{(m)}$ has constant solution requires that the Laplacian terms are constant in equation A.5. That is

$$\chi_{,ii}^{(m)} = a^{(m)}, \qquad \psi_{,ii}^{(m)} = b^{(m)}\,, \tag{A.6}$$

where a and b are some constants. The periodicity of displacement potential contained in equation A.2 implies that the average Laplacian terms $\langle\chi_{,ii}^{(m)}\rangle$, $\langle\psi_{,ii}^{(m)}\rangle$ vanishes within the unit cell. The average solid volumetric strain appearing in equation 4.8 is therefore obtained

$$\Omega\langle\chi_{,ii}^{(m)}\rangle = \langle e_{ii}^{(m)}\rangle - 3\beta = 0. \tag{A.7}$$

Through eqs A.6 and A.7, we obtain the relations for the average dilatational potential

$$\langle\chi_{,ii}^{(m)}\rangle = \langle a^{(m)}\rangle = 0, \qquad \langle\psi_{,ii}^{(m)}\rangle = \langle b^{(m)}\rangle = 0. \tag{A.8}$$

The boundary condition equation 4.1 signifies the marcroscopic pressure discontinuity in presence of membrane stiffness W. It can be integrated over the fluid interfacial area A_f within the unit cell Ω

$$\int_{A_\mathrm{f}} (p_\mathrm{f}^{(1)} - p_\mathrm{f}^{(2)})dA_\mathrm{f} = W\phi\int_{A_\mathrm{f}} (U_n - u_n)dA_\mathrm{f}. \tag{A.9}$$

In the static limit, the fluid pressure on the left hand side of equation A.9 is equilibrated, thus piecewise constant and related via constitutive equation 4.7. We set the outward of the normal displacement component from phase 1 to phase 2. Therefore the volume integration of equation A.9 is taken over phase 1. By

application of divergence theorem we obtain

$$(p_{\mathrm{f}}^{(1)} - p_{\mathrm{f}}^{(2)})A_{\mathrm{f}} = W\phi \int_{\Omega_1} (\epsilon - e)d\Omega_1 = W\phi S_1\Omega(\epsilon^{(1)} - e^{(1)}), \tag{A.10}$$

where $\Omega_1 = S_1\Omega$ is the volume of phase 1, v_m is the volume fraction of phase m. From eqs A.2 and A.6, we have

$$e^{(m)} = 3\beta + a^{(m)}, \qquad \epsilon^{(m)} = 3\beta + b^{(m)}; \tag{A.11}$$

With the substitution of the strains A.11 into equation A.10 we find

$$\sigma_{\mathrm{f}}^{(1)} - \sigma_{\mathrm{f}}^{(2)} = T\phi^2(a^{(1)} - b^{(1)})S_1, \tag{A.12}$$

where the $\sigma_{\mathrm{f}}^{(m)} = -\phi p_{\mathrm{f}}^{(m)}$ denotes the fluid stress of phase m and $T = W\frac{\Omega}{S_{\mathrm{f}}}$ describes the capillarity stiffening effect. The ratio $\frac{\Omega}{S_{\mathrm{f}}}$ is the reciprocal specific surface area. The condition of traction continuity across the fluid interface requires that

$$(\tau_{ij}^{(1)} - \tau_{ij}^{(2)})n_j = 0, \tag{A.13}$$

where n is an outward normal across the patch interface. Combining equation A.13 with eqs A.3, A.6 we obtain

$$\begin{aligned} \{[(H^{(1)} - \phi C^{(1)} - 2\mu)(3\beta + a^{(1)}) + \phi C^{(1)}(3\beta + b^{(1)})] \\ -[(H^{(2)} - \phi C^{(2)} - 2\mu)(3\beta + a^{(2)}) + \phi C^{(2)}(3\beta + b^{(2)})]\}n_i \\ +2\mu(\chi_{,ij}^{(1)} - \chi_{,ij}^{(2)})n_j = 0. \end{aligned} \tag{A.14}$$

According to Hill (1964), the discontinuity in the second derivative of the displacement potential is given by

$$\chi_{,ij}^{(1)} - \chi_{,ij}^{(2)} = (a^{(1)} - a^{(2)})n_i n_j. \tag{A.15}$$

Therefore, the last term of equation A.14 can be replaced by $2\mu(a^{(1)} - a^{(2)})n_i$. The average stress $\langle\tau_{ii}^{(m)}\rangle$ of the undrained solid can be obtained via averaging equation A.3 over the two phases by their saturations: $S_1\tau_{ii}^{(1)} + S_2\tau_{ii}^{(2)}$. Substituting the above averaged stress and averaged strain given by equation A.7 into relation 4.8, the effective static undrained bulk modulus becomes

$$K_{\mathrm{ud}}^{*} = \left\langle (K_{\mathrm{ud}}^{(m)} - \phi C^{(m)})\frac{a^{(m)}}{3\beta} + \phi C^{(m)}\frac{b^{(m)}}{3\beta} + K_{\mathrm{ud}}^{(m)} \right\rangle \tag{A.16}$$

The four unknowns of $\{a^{(m)},\ b^{(m)}\}/\beta$ $(m = 1, 2)$ in the expression can be solved from the four linear conditions of A.8, A.12, A.14, i.e.,

$$\begin{cases} S_1 a^{(1)} + S_2 a^{(2)} = 0 \\ S_1 b^{(1)} + S_2 b^{(2)} = 0 \\ [\phi^2 M^{(1)}(3\beta + b^{(1)}) - \phi(\phi - \alpha^{(1)}) M^{(1)}(3\beta + a^{(1)})] - [\phi^2 M^{(2)}(3\beta + b^{(2)}) \\ -\phi(\phi - \alpha^{(2)}) M^{(2)}(3\beta + a^{(2)})] = \tilde{W}(a^{(1)} - b^{(1)}) S_1 \\ \{[(H^{(1)} - \phi C^{(1)} - 2\mu)(3\beta + a^{(1)}) + \phi C^{(1)}(3\beta + b^{(1)})] - [(H^{(2)} - \phi C^{(2)} \\ -2\mu)(3\beta + a^{(2)}) + \phi C^{(2)}(3\beta + b^{(2)})]\} + 2\mu(a^{(1)} - a^{(2)}) = 0. \end{cases} \tag{A.17}$$

Upon solving the system of equations analytically, the P-wave modulus can be obtained via $H^* = K^*_{\mathrm{ud}} + \frac{4}{3}\mu$, see equation 4.9.

For a finite increment of ΔT, the slope of static modulus (as a function of parameter T) can be written as

$$\frac{H^*(T + \Delta T) - H^*(T)}{\Delta T} = \frac{(\frac{z}{H^{\mathrm{GW}}} - \frac{z}{H^{\mathrm{GH}}})}{(\frac{z}{H^{\mathrm{GW}}} + \frac{T}{H^{\mathrm{GH}}})(\frac{z}{H^{\mathrm{GW}}} + \frac{T + \Delta T}{H^{\mathrm{GH}}})}. \tag{A.18}$$

For immiscible fluid saturation $H^{\mathrm{GW}} < H^{\mathrm{GH}}$, hence $\frac{z}{H^{\mathrm{GW}}} - \frac{z}{H^{\mathrm{GH}}} > 0$ and the slope is always positive. This shows that the static modulus is a monotonically increasing function of the parameter T.

Appendix B

Procedure of constructing saturation maps

In order to exclude the influence of the rock frame and determine only the fluid distribution, we construct water-saturation maps through the raw CT scans. The pixel value of the CT scan for partially saturated rock linearly relates the CT value of each constituent (solid, water, gas) weighted by volume fraction (Toms et al., 2009),

$$\mathrm{CT} = (1-\phi_i)\mathrm{CT_s} + \phi_i S_{\mathrm{w}}^i \mathrm{CT_w} + \phi_i S_{\mathrm{g}}^i \mathrm{CT_g}, \tag{B.1}$$

where ϕ_i is the volume fraction of the local pore space represented by the $i-th$ pixel, S_{w}^i is the water saturation of the local pore space and the gas saturation $S_{\mathrm{g}}^i = 1 - S_{\mathrm{w}}^i$. By subtracting the CT scan of the dry rock,

$$\mathrm{CT_{dry}} = (1-\phi_i)\mathrm{CT_s} + \phi_i \mathrm{CT_g}, \tag{B.2}$$

the high CT value of the rock frame is cancelled and we obtain

$$S_{\mathrm{w}}^i = \frac{\mathrm{CT} - \mathrm{CT_{dry}}}{(\mathrm{CT_w} - \mathrm{CT_g})\phi_i}. \tag{B.3}$$

In equation B.3, $\mathrm{CT_w}$ is zero HU (Hounsfield Unit) and $\mathrm{CT_g} = -1000$ HU. We assume that porosity is uniform within the monitored area and hence we take porosity in equation B.3 to be equal to the measured porosity of the whole sample . The corresponding saturation maps are shown in Figure 4.7.

Appendix C

Extracting statistical properties from saturation maps

From the binary maps, we characterize the morphological structure using spatial correlation functions. The spatial correlation function can be constructed from so-called indicator functions $\mathcal{I}(\mathbf{x})$ (Torquato, 2002). A value of 1 is assigned to $\mathcal{I}(\mathbf{x})$ if position $\mathbf{x}$ resides in the material of the water phase, and 0 if position $\mathbf{x}$ resides in the material of the gas phase. By assuming that the two-phase medium is statistically homogeneous, the spatial correlation function of $\mathcal{S}_1$ and $\mathcal{S}_2$ is defined as

$$\mathcal{S}_1 = \langle \mathcal{I}(\mathbf{x}) \rangle, \tag{C.1}$$

$$\mathcal{S}_2(\mathbf{r}) = \langle \mathcal{I}(\mathbf{x}) \mathcal{I}(\mathbf{x} + \mathbf{r}) \rangle, \tag{C.2}$$

where the angle brackets denote volume averaging. Function $\mathcal{S}_1$ provides an estimate of the volume fraction of phase 1. For a statistically isotropic material, the two-point correlation function (TPCF) $\mathcal{S}_2$ depends only on the distance $|\mathbf{r}|$, and thus we write $\mathcal{S}_2(r)$. The TPCF can be understood as the probability of finding two randomly sampled points residing in the same phase. The statistical sample size decreases as the scalar distance between points increases. This affects the accuracy of the correlation function at larger offsets. In order to eliminate this effect, we apply a random boundary condition (Toms, 2008) to the binary map and reconstruct its statistically equivalent map. We utilize Monte Carlo simulations to extract TPCF from the reconstructed binary map.

We further analyze the quality of the segmentation method. When $r = 0$, the value of the $\mathcal{S}_2$ curve provides information on the volume fraction of the 'water' phase in the filtered image $\mathcal{S}_2(0) = S_{\mathrm{w}}$. The saturation deduced from the binary map deviates from the value obtained from the saturation map. We test the influence of different segmentation techniques on both the volume fraction of the 'water' phase and SSA. We find that when the change of the former is 1%, the change of the latter is only 0.06% which is negligible. Thus, we can assume the segmentation method does not affect the morphological information.

For the continuous random model, spatial information of the variation of the fluid modulus is required. A fluid storage modulus map is constructed from the water saturation map in two steps: First, by assuming that the fluid pressure achieves equilibrium at pixel scale, we compute an effective fluid bulk modulus for each pixel using Wood's mixing law

$$\mathcal{M}_{\mathrm{b}} = \left(\frac{\mathcal{M}_{\mathrm{w}}}{K_{\mathrm{fw}}} + \frac{\mathcal{M}_{\mathrm{g}}}{K_{\mathrm{fg}}} \right)^{-1}, \tag{C.3}$$

where K_{fw} is water bulk modulus, K_{fg} is air bulk modulus and $\mathcal{M}_{\mathrm{g}}$ is the gas-saturation map given by $\mathcal{M}_{\mathrm{g}} = 1 - \mathcal{M}_{\mathrm{w}}$. Secondly, $\mathcal{M}_{\mathrm{b}}$ is converted into a fluid storage modulus map using the equation

$$\mathcal{M}_{_M} = \left[\frac{(\alpha - \phi)}{K_{\mathrm{s}}} + \frac{\phi}{\mathcal{M}_{\mathrm{b}}} \right]^{-1}. \tag{C.4}$$

The fluid storage modulus map $\mathcal{M}_{_M}$ is converted into a binary map $\mathcal{M}^*_{_M}$ by segmentation using the mean distribution value as a threshold. From this map we obtain the autocovariance

$$\chi_{_M}(r) = \frac{\mathcal{S}_2(r) - \mathcal{S}_1^2}{\mathcal{S}_1(1 - \mathcal{S}_1)} \tag{C.5}$$

where $\mathcal{S}_1,\ \mathcal{S}_2$ are the one- and two-point correlation functions.

To estimate the patch-scale fluid storage modulus, we introduce the characteristic length scale of the patch size λ_p, which increases with increasing water saturation (see Figure 4.9). The number of the partitioned patches is

$$m = \left(\frac{h}{\lambda_p} \right)^2, \tag{C.6}$$

where h is the side length of the map (in number of unit cell). Then the map $\mathcal{M}_{\mathrm{b}}$ is partitioned into m effective patches $\bar{K}_j$, $(j = 1, ..., m)$. Each patch $\bar{K}_j$ consists of λ_p unit cells. Assuming pressure equilibration within each rescaled patch, the bulk modulus of the patch $\bar{K}_j$ can be calculated with the bulk modulus K_b of each unit cell via Wood's law

$$\bar{K}_j = \left(\sum_{n=1}^{\lambda_p} \left(\frac{1}{K_b^n} \right) \right)^{-1} \qquad (j = 1, .., m). \tag{C.7}$$

The patch fluid storage modulus M_j relates $\bar{K}_j$ via $M_j = [(\alpha - \phi)/K_{\mathrm{s}} + \phi/\bar{K}_j]^{-1}$, and the normalized variance $\sigma^2_{_{MM}}$ can be computed using the equation

$$\sigma^2_{_{MM}} = \frac{\sum_{j=1}^{m} (M_j - \langle M_j \rangle)^2}{m \langle M_j \rangle^2} \qquad (j = 1, .., m). \tag{C.8}$$

The steps C.6-C.8 are repeated over the eight CT images. The partitioning works as an effective approximation for the unrelaxed mesoscopic fluid patches formed at intermediate saturations.

Appendix D

Viscoelastic reflection coefficient for isotropic media

The P-wave reflection coefficient R_{pp} can be solved from the following linear system (Aki and Richards, 2002; Liu et al., 2011)

$$\begin{bmatrix} \sin\theta_{pu} & \cos\theta_{su} & -\sin\theta_{pl} & \cos\theta_{sl} \\ \cos\theta_{pu} & -\sin\theta_{su} & \cos\theta_{pl} & \sin\theta_{sl} \\ \frac{\rho_1 c_{su}^2}{c_{pu}}\sin 2\theta_{pu} & \rho_1 c_{su}\cos 2\theta_{su} & \frac{\rho_2 c_{sl}^2}{c_{pl}}\sin 2\theta_{pl} & -\rho_2 c_{sl}\cos 2\theta_{sl} \\ \rho_1 c_{pu}\cos 2\theta_{su} & -\rho_1 c_{su}\sin 2\theta_{su} & -\rho_2 c_{pl}\cos 2\theta_{sl} & -\rho_2 c_{sl}\sin 2\theta_{sl} \end{bmatrix} \times \begin{bmatrix} R_{pp} \\ R_{ps} \\ T_{pp} \\ T_{ps} \end{bmatrix} = \begin{bmatrix} -\sin\theta_{pu} \\ \cos\theta_{pu} \\ \frac{\rho_1 c_{su}^2}{c_{pu}}\sin 2\theta_{pu} \\ -\rho_1 c_{pu}\cos 2\theta_{su} \end{bmatrix} \tag{D.1}$$

where the superscripts u, l denote the upper and lower media. The complex velocity c and angles of the converted waves can be calculated via

$$c = \left(\frac{1}{V} - \frac{ia}{\omega}\right) , \quad a = (\sqrt{Q^2+1} - Q)\frac{\omega}{V} , \tag{D.2}$$

$$\theta_k = \arcsin\frac{c_k \sin\theta_{pu}}{c_{pu}} , \quad k = su,\ pl,\ sl. \tag{D.3}$$

The phase velocity V and quality factor Q are provided by the patchy saturation model.

Appendix E

Slow shear waves and the concept of dynamic permeability

E.1 Abstract

Modelling seismic wave propagation in poroelastic media is based on macroscopic equations, such as proposed by Biot. It is clear, however, that some microstructural information must enter into the computation of the macroscopic parameters. One example, is the flow permeability in Biot's theory. Though it is a macroscopic quantity, it is commonplace to find permeability estimates using microstructural descriptors. From a wave-propagation point of view, there is also a temporal upscaling involved. If the wave frequency is high enough then the flow permeability will loose its meaning. This phenomenon is often captured by postulating a generalized Darcy law with a frequency-dependent (so-called dynamic) permeability. Within the viscosity-extended Biot framework the dynamic permeability can be modelled as convserion scattering process from the the Biot slow compressional wave into the slow shear wave. The latter accounts for viscous dissipation through vorticity diffusion in the fluid phase. This stochastic dynamic permeability model accounts for pore-scale heterogeneity through the two-point correlation function. Using digitized images of a limestone sample we extract the correlation function and predict the dynamic permeability.

E.2 Introduction

The physical significance of oscillatory Stokes flow in the context of wave propagation in porous media has been recognized by Biot (Biot, 1956; Biot, 1962). In many of today's poroelastic wave propagation numerical simulations the transition from the viscosity- to inertia dominated regime is captured through the concept of dynamic permeability (Carcione, 2007; Blanc et al, 2013; Wenzlau and Müller, 2009) as introduced by Johnson et al. (1987). For quasi-static fluid flow the dc permeability is a real-valued quantity defined through the macroscopic Darcy law. At very high frequencies the dc permeability looses its meaning as the Darcy law is not any longer valid and inertia dominates. The determination of a dynamic permeability for particular porous media is the scope of many research papers (Carcione, 2007; Boutin and Geindreau, 2008; Dinariev and Mikhailov, 2011).

There is yet another approach to understand the concept of dynamic permeability. As originally envisaged by De la Cruz and Spanos (1985), the volume-averaging theory of dynamic poroelasticity also entails a slow shear wave in addition to the fast compressional and shear modes and the slow compressional wave (Sahay et al., 2001). Sahay (2008) showed that the Biot theory also contains a slow shear mode but the velocity of this mode is zero. This is because the fluid strain-rate term is absent in the constitutive relation. Using the framework of volume-averaging, once the missing fluid strain rate term is incorporated into the Biot constitutive relation, this mode turns out to be, in the inertial regime, a diffusive process akin to a viscous wave in a Newtonian fluid, and in the viscous regime, a process governed by a diffusion equation with a damping term. This extension of the Biot theory we refer to as the viscosity-extended Biot (VEB) framework (Müller and Sahay, 2009; Müller and Sahay, 2011). The existence of this slow shear process has been also predicted using the Lagrangian framework to obtain macroscopic poroelasticity equations (Maximov, 2010).

Within this VEB framework we develop a theory for the dynamic permeability in deformable porous media. The analysis is based on the momentum flux transfer from the slow compressional into the slow shear wave in the presence of random heterogeneities. A first-order statistical smoothing approximation is used to infer a dynamic permeability in the form of an integral over the covariance function modulated by the slow shear wave (Müller and Sahay, 2011). This stochastic

dynamic permeability (SDP) model opens the possibility to link statistical information derived from pore-scale images to the framework of poroelasticity. As an example, we compute the autocovariance function for a digitized limestone rock sample and estimate the corresponding dynamic permeability. This appendix is structured as follows. We briefly review the pertinent equations of the VEB framework. The analysis of the conversion scattering from the slow compressional into the slow shear wave entails a model for the dynamic permeability. By extracting the spatial statistics of a digitized rock sample we show how the SDP model can be applied.

E.3 A stochastic model for dynamic permeability

At high frequencies, say $\omega \approx \omega_c$ (Biot's relaxation frequency, eq. 2.38), the fluid velocity field can be thought of as a superposition of a potential flow field and a boundary layer flow region attached to the pore walls. The potential flow field does not depend on the fluid shear viscosity and is controlled by inertia instead. The flow field within the viscous boundary layer can be interpreted as viscous wave having wave number $\tilde{\mathrm{k}}_v = (1+\mathrm{i})/\delta$ wherein the viscous skin depth is $\delta = \sqrt{2\eta/\rho_f\omega}$. The more the potential flow field is pronounced the less is the flow permeability. Therefore, the frequency-dependent interaction between the potential flow field and the viscous wave in the boundary layer can be used as a proxy for the dynamic permeability behaviour. To quantify this frequency-dependent interaction we identify the two flow fields with wave processes inherent to poroelasticity theory. In poroelastic media for $\omega > \omega_c$ the slow compressional wave of Biot's theory (Biot, 1962) can be understood as an analog for the potential flow field. Correspondingly, in VEB framework the slow shear wave can be interpreted as viscous wave in the boundary layer. Thus a recipe for a dynamic permeability analysis can be based on the momentum flux transfer from the slow compressional wave into the slow shear wave. This momentum flux transfer is modelled as conversion scattering between these two wave fields in the presence of pore-scale heterogeneities. The latter are assumed to vary randomly, but in a statistically isotropic fashion. Then the random field is characterized by the autocovariance function $B(r)$. This conversion scattering approach in a random medium has also been applied in a different context (Müller and Gurevich, 2005). The outlined calculations for the dynamic permeability have been presented in

Müller and Sahay (2011) and the result is

$$\tilde{\kappa}(\omega) = \kappa_0 \frac{\int_0^\infty rB(r)\mathrm{e}^{\mathrm{i}\tilde{\mathrm{k}}_4 r}dr}{\int_0^\infty rB(r)\mathrm{e}^{\mathrm{i}\tilde{\mathrm{k}}_4^0 r}dr}\,, \tag{E.1}$$

where the slow shear wavenumber can be approximated by $\tilde{\mathrm{k}}_4 = \mathrm{k}_- + \mathrm{i}\mathrm{k}_+$ with

$$\mathrm{k}_\mp = \sqrt{\frac{\omega\rho_f}{2d_\mathrm{f}\eta}}\sqrt{\sqrt{(1+d_\mathrm{f}m_\mathrm{f})^2 + \frac{\omega_c^2}{\omega^2}} \mp \frac{\omega_c}{\omega}}\,. \tag{E.2}$$

$d_\mathrm{f} = (S^\infty - m_\mathrm{f})^{-1}$ and m_f is the fluid mass fraction. The slow shear wavenumber at zero frequency is

$$\tilde{\mathrm{k}}_4^0 \equiv \tilde{\mathrm{k}}_4(\omega = 0) = \mathrm{i}\sqrt{\phi/\kappa_0}\,. \tag{E.3}$$

We refer to equation (E.1) as the stochastic dynamic permeability (SDP). If there was no slow shear wave ($\tilde{k}_4 = 0$) then the dynamic permeability would reduce to the dc permeability κ_0. As soon as viscous boundary layers develop (δ is on the order of a typical pore-space length scale), equation (E.1) quantifies the deviation from κ_0. This deviation depends on the spatial variability of the pore-scale heterogeneities as quantified by the autocovariance function $B(r)$. We will now show how the SDP model can applied using information from digitized rock images.

E.4 Dynamic permeability estimation using digitized rock

Figure E.1 shows a X-ray tomographic image of a Savonnières limestone sample. A millimetre-scale sample was imaged at the 2-BM beamline at the Advanced Photon Source, Argonne National Laboratory, Chicago. The dataset consists of a cube of 2048 × 2048 × 2048 pixels with a pixel size of 1.5 micro meters. Such an image can be interpreted as a two-phase medium consisting of grains (light gray) and pores (dark gray).

Pore-scale heterogeneity can be mapped with the pore-space indicator function $\mathcal{I}(\mathbf{r})$ assuming a value of unity if $\mathbf{r}$ is in the pore space and zero otherwise (Torquato, 2002). Upon ensemble averaging, $\langle\mathcal{I}(\mathbf{r})\rangle = \phi$ and the two-point correlation function is

$$S_2(\mathbf{r}) = \langle\mathcal{I}(\mathbf{x})\mathcal{I}(\mathbf{x}+\mathbf{r})\rangle\,. \tag{E.4}$$

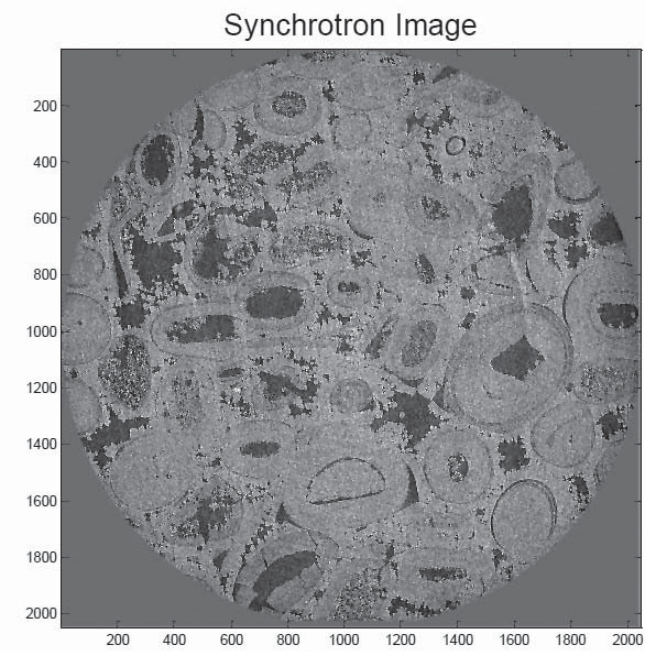

Figure E.1: Synchrotron image of a Savonnières limestone sample (2048 × 2048 pixels with a pixel size of 1.5 micro meters).

In a statistically isotropic medium S_2 only depends on the correlation lag r. For values of correlation lags near 0, a relation between the slope of the two-point correlation function, S_2', and specific surface area (SSA) s_v of the pore-space exists, $S_2'(0) = -s_v/4$. The SSA is defined as the ratio of the total surface area of the pore-grain interface to the total volume of the porous material (Blair et al., 1996).

Here we use a Monte Carlo simulation to extract the two-point correlation function (TPCF). The result is shown in Figure E.2. The TPCF decreases monotonically suggesting that our two-phase porous medium can be interpreted as a Debye random medium in which one phase consists of different sizes and shapes. The S_2 value at zero correlation lag is the porosity and the linear fit at $r \approx 0$ yields the SSA. The results of image-derived porosity and SSA values for 5 different synchrotron images are specified in Table 1.

In order to compare the image-derived porosity and permeability with laboratory measurements for this particular Savonnières limestone sample we use some empirical relations. Walsh and Brace (1984) developed a Kozeny-Carman relation by approximating the flow in a porous rock as flow through a bundle of parallel

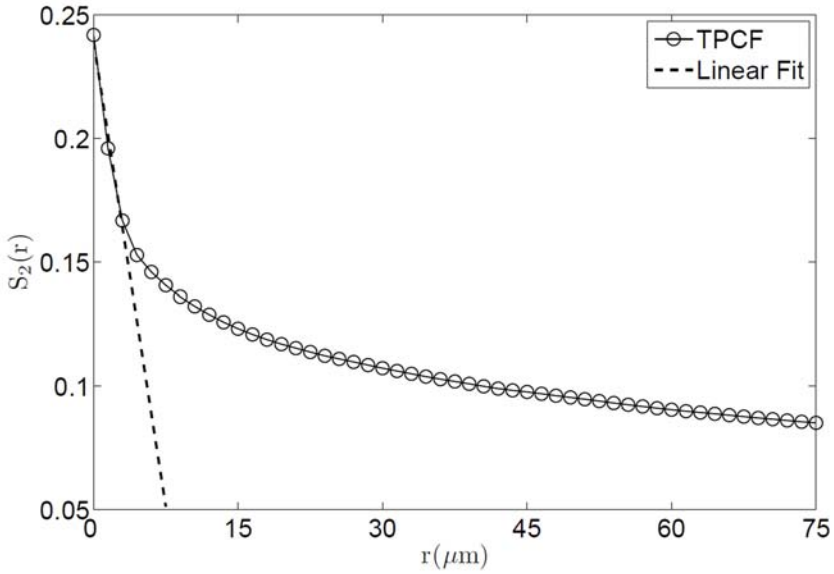

Figure E.2: Two-point correlation function S_2 (symbols) inferred from the synchrotron images by Monte-Carlo simulations.

Table E.1: Image-derived properties

# slice	ϕ	s_v (μm^{-1})	κ_0 (mD)
1	0.17	0.06	124
2	0.18	0.06	126
3	0.19	0.06	182
4	0.19	0.07	155
5	0.24	0.1	170
average	0.194	0.07	151
laboratory	0.265	–	91

circular pipes of arbitrary cross section. Their relation is $\kappa_0 = \phi^2/(cFs_v^2)$, where the constant c depends on the tube cross section and F is the formation factor. Typically, $c = 2$ for circular tubes and $c = 3$ for flat cracks. Here we use the $c = 2$ for limestone because permeability is more likely controlled by pores rather than cracks. Due to lack of measurement, the formation factor F is estimated using Archies law, $F = \phi^{-m}$. Focke and Munn (1987) suggest to use a cementation exponent of $m \approx 2$ for limestone of intergranular type with porosity larger than 5%. Then the Kozeny-Carman relation yields permeability estimates as specified in Table 1. For all of the synchrotron images, taken at different positions, the estimated permeability agrees with the measured permeability within approximately a factor of 2. It appears that the local porosity fluctuations are significant and that the average, image-derived porosity is less than the measured

value (Table 1). The latter observation indicates that either some pore spaces are below the image resolution, or that the X-ray imaged millimetre-scale sample is not fully representative of the centimetre-scale Savonnières limestone core plug. We also note that the porosity and permeability measurements were performed under moderate confining pressure.

The autocovariance function is constructed according to Torquato (2002)

$$B(\mathbf{r}) = \frac{S_2(\mathbf{r}) - \phi^2}{\phi(1-\phi)} \,. \tag{E.5}$$

and is displayed in Figure E.3. The autocovariance function can be well approximated by a superposition of two Debye exponential correlation functions

$$B(r) = b_s e^{-|r/a_s|} + b_l e^{-|r/a_l|} \,. \tag{E.6}$$

where the weighting coefficients satisfy $b_s + b_l = 1$. $B(r)$ entails two correlation lengths, one (a_s) characterizing the size of the smallest heterogeneities and another one (a_l) indicating the presence of longer-range disorder. See also Figure E.3. Though $B(r)$ entails four parameters, it is important to remember that all these parameters can be derived from the image(s) without invoking empirical relations.

Having estimated the autocovariance function we are now in the position to predict the dynamic permeability behaviour when a specific fluid fully saturates the pore space. By substituting equation (E.6) for $B(r)$ into equation (E.1) we obtain explicit analytical formulas for the dynamic permeability. Assuming water as pore fluid (shear viscosity $\eta = 0.001$ Pa $\cdot$ s and density $\rho_\mathrm{f} = 1000$ kg/m^3) and $S^\infty = 2$ the modulus of the dynamic permeability is shown in Figure E.4 (solid line). It is important to understand that all micro-structure related properties in the SDP model have been extracted from the digitized images. The only parameter which needs to be estimated independently is the tortuosity. We verified, however, that different values of S^∞ do not introduce significant changes.

We compare our prediction to the dynamic permeability model of Johnson et al. (1987) that in the explicit form can be written as

$$\tilde{\kappa}_\mathrm{JKD}(\omega) = \kappa_0 \left(\sqrt{1 - 4\mathrm{i}\frac{\omega}{\omega_c}\frac{\eta}{\Lambda^2 \rho_\mathrm{f} \omega_c}} - \mathrm{i}\frac{\omega}{\omega_c} \right)^{-1} \,. \tag{E.7}$$

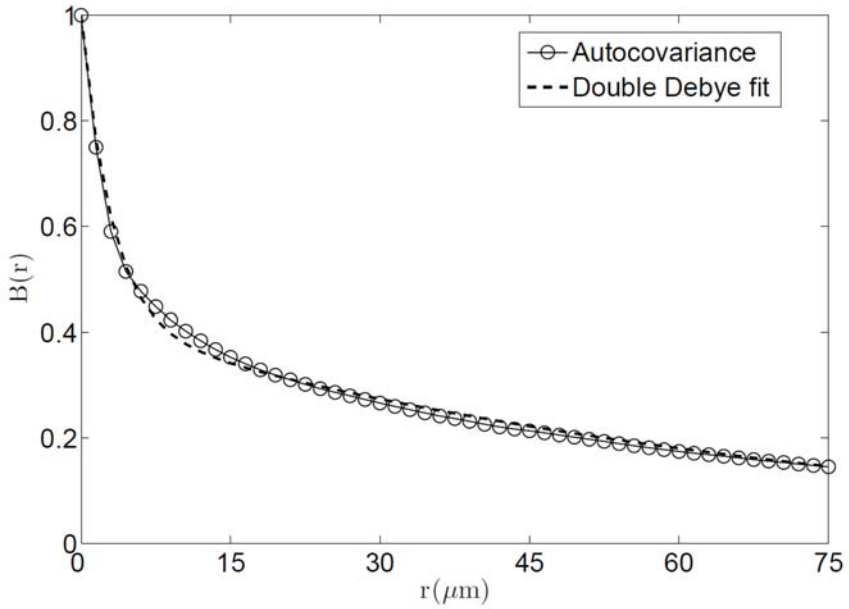

Figure E.3: Extracted auto-covariance function (circles) can be well approximation by a double Debye correlation function (dashed line).

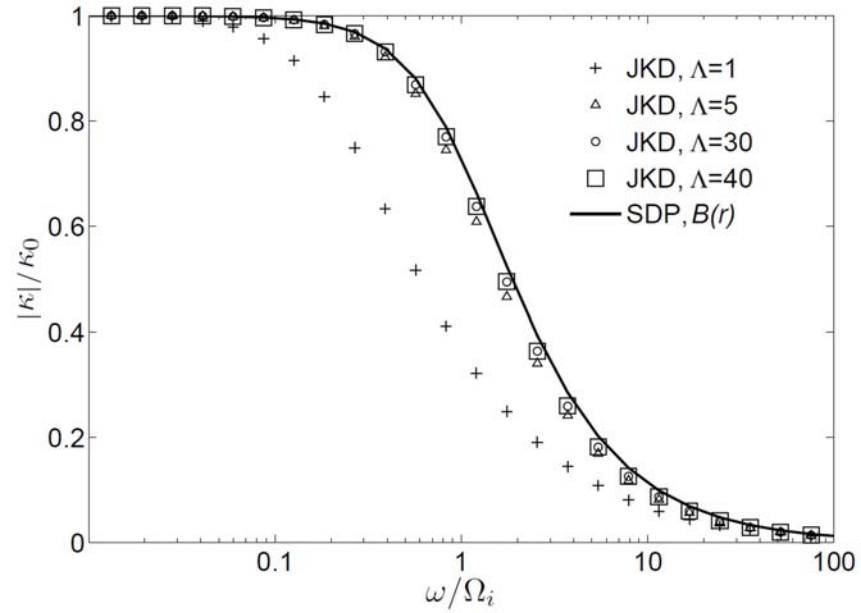

Figure E.4: Normalized modulus of the dynamic permeability versus frequency. The stochastic dynamic permeability model (SDP) uses the auto-covariance function extracted from the digitized images. The JKD model depends on the Λ parameter (given in μm).

Λ is sometimes referred to as the viscous relaxation length as it can be viewed as a characteristic length scale governing the viscous fluid flow in the presence of pore-scale heterogeneities. In Figure E.4 it can be observed that for $\Lambda \approx$

30 μm both predictions coincide. Choosing a larger Λ value introduces no change (squares in Figure E.4). In general, the Λ parameter should be determined from independent measurements. However, estimating Λ by comparison with the SDP model indicates yet another, digitized image-based way of determining Λ.

E.5 Conclusion

The slow shear wave in the viscosity-extended Biot framework has a distinct physical meaning. Its importance becomes most apparent if the transition from the viscosity- to inertia dominated regime is modelled. It is the interplay between the slow compressional and slow shear wave which governs this transition. The conversion scattering from the slow compressional into the slow shear wave is a proxy for the dynamic permeability. An advantage of the stochastic dynamic permeability model is that it connects micro-structural information, as contained in digitized rock images, to the macroscopic poroelasticity framework.

Appendix F

Copyright consent

Print

Permissions

SEG publishes journals, books, and digital works with the primary aim of disseminating research in and theory and applications of applied geophysics. Consistent with this objective, the Society provides mechanisms for those who seek to reuse or republish material from SEG publications while protecting the viability of the SEG publications program. Any further questions about permissions can be sent via email to the SEG publications department at permissions@seg.org.

Fair use
Authors and publishers may present or republish up to two figures or tables per SEG article or per SEG book without seeking written permission from SEG, provided that full acknowledgment of the source is provided in the new work. If SEG has cited a publication for which it is not the publisher, rights should be obtained from that publisher. SEG considers this fair use. There are no fees associated with this permission. Authors who need documentation that SEG is extending this permission are encouraged to print this message and present it to their publishers. Those who require further documentation should contact the SEG publications director. Requests to use any portion of "Seismic Data Analysis: Processing, Inversion, and Interpretation of Seismic Data" should be directed to the SEG publications director.

Permission granting
Those seeking permission to republish more material than described above should contact the SEG publications director. Such requests should include complete citations of works for which permission to republish is sought. If permission for specific figures or tables is sought, please provide figure and table numbers. Requests should include a description of the work in which the SEG material would be republished. Information about the audience and the intended distribution also should be included. The requests should be prepared on institutional letterhead if the requesting party is representing an institution. License fees are assessed only when the request is for a large amount of material or when the proposed usage is commercial in nature or would limit SEG's market. If a license fee is assessed, it must be paid prior to use or the permission is void.

Purchase redistribution rights online
Those seeking to redistribute SEG publications or portions thereof in print, by fax, or online may purchase permission to do so online. SEG publications are registered with the Copyright Clearance Center, and licenses to redistribute SEG articles and portions of books are obtained through this nonprofit agency. Special pricing is available for university professors, including license to distribute SEG material through electronic course packs. Licenses also are available for distribution of journal articles and expanded abstracts via email or posting on Intranets and Extranets for limited time periods.

Authors' right to redistribute
Authors of articles in GEOPHYSICS, INTERPRETATION, THE LEADING EDGE, and the Technical Program *Expanded Abstracts* may post their own articles on their personal Web sites or the Web sites of their institutions without obtaining further permission from SEG. Authors of journal articles and *Expanded Abstracts* retain similar rights for print redistribution. If an author or an author's institution redistributes an author's article online or in print, the original publication venue encompassed in a complete citation and including SEG's status as publisher must be identified. Authors of SEG books, or portions of SEG books, must seek permission from the SEG publications director to redistribute these works in any form. Such permission will not be withheld if SEG's investment in the original publication of the works is not threatened. Questions should be directed to the publications director.

Qiaomu Qi

From: Laura van Kal <lkl@eage.org>
Sent: Thursday, 20 August 2015 5:33 PM
To: Qiaomu Qi
Subject: RE: Copyright permission

Dear Qiaomu Qi,

Hereby EAGE grants permission to use Figure 6 -- Arts, R. J., Andy Chadwick, Ola Eiken, Sylvain Thibeau, and Scott Nooner. "Ten years' experience of monitoring CO2 injection in the Utsira Sand at Sleipner, offshore Norway." From First break 26, no. 1 (2008).
Please provide clear references in the thesis.

Kind regards,

Laura van Kal
Publications Coordinator
European Association of Geoscientists & Engineers (EAGE)
PO Box 59
3990 DB Houten
The Netherlands

Tel: +31 889955055
Fax: +31 30 6343524
Email: lkl@eage.org

From: Qiaomu Qi [mailto:qiaomu.qi1@postgrad.curtin.edu.au]
Sent: dinsdag 18 augustus 2015 20:35
To: Laura van Kal
Subject: Copyright permission

Dear publisher,

I am currently undertaking a PhD at Curtin University, Perth, Western Australia. In my doctoral thesis entitled 'Effect of capillarity on acoustics of partially saturated rocks', I would like to reproduce the figure listed below in the thesis:

Figure 6 -- Arts, R. J., Andy Chadwick, Ola Eiken, Sylvain Thibeau, and Scott Nooner. "Ten years' experience of monitoring CO2 injection in the Utsira Sand at Sleipner, offshore Norway." First break 26, no. 1 (2008).

Once completed, the thesis will be made available in hard-copy form in the Curtin Library and in digital form on the website: http://library.curtin.edu.au/find-books-and-resources/theses.cfm . The material will be provided strictly for educational purposes and on a non-commercial basis.

1

I would be most grateful for your consent to the copying and republishing of the material as proposed. Full acknowledgement of the ownership of the copyright and the source of the material will be provided in the thesis. I would be willing to use a specific form of acknowledgement that you may require and to communicate any conditions related to the use of this material.

If you are not the copyright owner of the referred material, I would be grateful for any information you can provide as to who is likely to hold the copyright. I look forward to hearing from you and thank you in advance for your consideration of my request.

Best regards,

Qiaomu Qi **| PhD Student**
Department Exploration Geophysics | Western Australian School of Mines
Postal Address: GPO Box U1987, Perth, Western Australia, 6845] [Bld 613, Rm 2H15]
Street Address: ARRC/CSIRO Building, H Block, Level 2, 26 Dick Perry Avenue, Kensington 6151, Western Australia]
Tel | +61 8 9266 3521
Mob | +61 4 69 618 549
Fax | +61 8 9266 3407

Email | qiaomu.qi1@postgrad.curtin.edu.au
Web | www.geophysics.curtin.edu.au

Permissions
Author Reuse and Self-Archiving

Author Reuse and Self-Archiving

As an author of an Oxford University Press title, published by our Academic, Trade, Reference, Science and/or Medical books groups, there are certain rights granted to you in the area of Reuse and Self Archiving. This policy sets out the way in which you, as authors of these titles, may reuse pre and post publication versions of your work for your own teaching, publishing and self-archiving purposes, without the need to obtain written permission from OUP.

Scope of the policy

The specific parameters set out in this policy relate to the following Global Academic Business (GAB) book publishing groups in the UK, US, India and Canada **ONLY:**

- **Academic**
- **Trade**
- **Science**
- **Medical**
- **Reference**

This **does not** cover authors of titles published by the following GAB publishing groups:

- **Higher Education**
- **Law**
- **Education - Schools/K-12 (Canada), or**
- **ELT (Canada)**

Requests from these areas will continue to be handled on a case-by-case basis by the book's editor.

If you are unsure about which division or publishing group is responsible for publishing your title, please contact your Commissioning/Acquiring Editor.

Authors wishing to reuse work that they have published with **English Language Teaching (ELT) or Oxford Educational (OE)** divisions must contact the respective rights teams directly in order to request permission.

ELT
OXED

Our Journals publishing group has its own author reuse guidelines which may be found on the homepage of each journal.

Rights Granted

Prior to publication

Prior to publication, you retain the right to make a maximum of one chapter (or article where appropriate) of the original pre-copyedited version of your work available on the following, where necessary:

- your personal website
- the website of your employer and/or
- in pre-print servers (i.e. free public servers of original version articles or other content in your subject area)

This is permitted provided that you acknowledge that the content has been accepted for publication by including an acknowledgement as follows:

This is a draft of a chapter/article that has been accepted for publication by Oxford University Press in the forthcoming book [title] by/edited by (Author/editor) due for publication in [year].

After publication Oxford would also ask that you update this record to ensure that the details

are accurate, and if possible include links to the OUP catalogue and webpage.

After publication

After publication you may reuse the following portions of your content without obtaining formal permission for the activities expressly listed below:

- one chapter or up to 10% of the total of your single author or co-authored book,
- a maximum of one chapter/article from your contribution to an edited book or collection (e.g. Oxford Handbooks),
- a maximum of one chapter/article of your contribution to an online only, or digital original publication, or
- three figures/illustrations/tables of your own original work

OUP is pleased to grant this permission for the following uses:

- posting on the your own personal website or in an institutional or subject based repository after a **12 month** period for **Science and Medical** titles and a **24 month** period for **Academic, Trade and Reference** titles;
- inclusion in scholarly, not-for-profit derivative reuses, (these can include the extension of your contribution to a book-length work, or inclusion in an edited collection of your own work, or any work of which you are an author or editor);
- reproduction within coursepacks or e-coursepacks for your own teaching purposes, (with the proviso that the coursepacks are not sold for more than the cost of reproduction);
- inclusion within your thesis or dissertation.

Permission for these reuses is granted on the following conditions:

- that the material you wish to reuse is your own work and has already been published by OUP;
- that the intended reuse is for scholarly purposes, for publication by a not-for-profit publisher;
- that full acknowledgement is made of the original publication stating the specific material reused [pages, figure numbers, etc.], [Title] by/edited by [Author/editor], [year of publication], reproduced by permission of Oxford University Press [link to OUP catalogue if available, or OUP website];
- In the case of joint-authored works, it is the responsibility of the authors to obtain permission from co-authors for the work to be reuse/republished.
- that reuse on personal websites and institutional or subject based repositories includes a link to the work as published in an OUP online product (e.g. Oxford Scholarship Online), and/or or to the OUP online catalogue entry; and that the material is not distributed under any kind of Open Access style licences (e.g. Creative Commons) which may affect the Licence between yourself and OUP.

This policy does not cover my intended reuse

If this policy does not cover your intended reuse, either because your material is not published by the subject groups listed above, or falls outside the specific parameters set out here, this does not automatically mean that you will be unable to obtain permission. For all uses not described here, permission may be sought by contacting your Commissioning/Acquiring Editor or by filling in a Permissions Request Form.

We will aim to process your request within 7-10 working days.

FAQ for authors:

Why do I need permission to reuse my own writing?

Our publishing agreement with you enables OUP to make many investments in your work, including editorial review, copyediting, typesetting, design, printing, coding for electronic publication, marketing, distribution, and securing copyright against piracy and plagiarism. Reuse permission protects these investments.

Because I am using less than 10% of my chapter or book, I do not need formal written permission. How should I word the credit?

We ask that you include this wording: "This material was originally published in [Title] by / edited by [Author / Editor], and has been reproduced by permission of Oxford University Press [link to book within an OUP online product and/or http://global.oup.com/academic]. For permission to reuse this material, please visit http://global.oup.com/academic/rights."

I am planning to use a portion of my OUP publication in my thesis or dissertation. Will I be given permission to do so?

Yes. We would appreciate you letting your OUP editor know.

I am planning to use a portion of my OUP publication in a future book. Will I be given permission to do so?

Generally speaking, yes, permission will be granted without charge. We ask that you request formal permission here.

References

Achenbach, J., 1984, Wave propagation in elastic solids: Elsevier.

Ajo-Franklin, J., J. Peterson, J. Doetsch, and T. Daley, 2013, High-resolution characterization of a CO_2 plume using crosswell seismic tomography: Cranfield, MS, USA: International Journal of Greenhouse Gas Control, **18**, 497–509.

Aki, K., and P. G. Richards, 2002, Quantitative seismology, Second Edition: University Science Books.

Alemu, B. L., E. Aker, M. Soldal, Ø. Johnsen, and P. Aagaard, 2013, Effect of sub-core scale heterogeneities on acoustic and electrical properties of a reservoir rock: a CO_2 flooding experiment of brine saturated sandstone in a computed tomography scanner: Geophysical Prospecting, **61**, 235–250.

Amalokwu, K., A. I. Best, J. Sothcott, M. Chapman, T. Minshull, and X.-Y. Li, 2014, Water saturation effects on elastic wave attenuation in porous rocks with aligned fractures: Geophysical Journal International, **197**, 943–947.

Amundsen, L., and A. Reitan, 1995, Estimation of sea-floor wave velocities and density from pressure and particle velocity by AVO analysis: Geophysics, **60**, 1575–1578.

Aronsen, H. A., B. Osdal, T. Dahl, O. Eiken, R. Goto, J. Khazanehdari, S. Pickering, and P. Smith, 2004, Time will tell: New insights from time-lapse seismic data: Oilfield Review, **14**, 48–65.

Arts, R., A. Chadwick, O. Eiken, S. Thibeau, and S. Nooner, 2008, Ten years' experience of monitoring CO_2 injection in the Utsira Sand at Sleipner, offshore Norway: First break, **26**.

Averbakh, V., V. Bredikhin, A. Lebedev, and S. Manakov, 2010, Acoustic spectroscopy of fluid saturation effects in carbonate rock: Acoustical Physics, **56**, 794–806.

Avseth, P., T. Mukerji, and G. Mavko, 2005, Quantitative seismic interpretation: Applying rock physics tools to reduce interpretation risk: Cambridge

University Press.

Ba, J., J. Carcione, O. Du, H. Zhao, and T. Müller, 2014, Seismic exploration of hydrocarbons in heterogeneous reservoirs: New theories, methods and applications–Chapter 3: Acoustics of partially saturated rocks: Theory and experiments: Elsevier.

Bacon, M., R. Simm, and T. Redshaw, 2007, 3-D seismic interpretation: Cambridge University Press.

Batzle, M. L., D.-H. Han, and R. Hofmann, 2006, Fluid mobility and frequency-dependent seismic velocity—Direct measurements: Geophysics, **71**, N1–N9.

Bear, J., 1972, Dynamics of fluids in porous media.

Bedford, A., and M. Stern, 1983, A model for wave propagation in gassy sediments: The Journal of the Acoustical Society of America, **73**, 409–417.

Best, A. I., T. Han, and J. Sothcott, 2013, Elastic wave attenuation and electrical formation factor of shaly sandstones: Presented at the Second International Workshop on Rock Physics.

Biot, M. A., 1941, General theory of three-dimensional consolidation: Journal of applied physics, **12**, 155–164.

———, 1956a, Theory of propagation of elastic waves in a fluid-saturated porous solid. i. low-frequency range: the Journal of the Acoustical Society of America, **28**, 168–178.

———, 1956b, Theory of propagation of elastic waves in a fluid-saturated porous solid. ii. higher frequency range: the Journal of the Acoustical Society of America, **28**, 179–191.

———, 1962, Mechanics of deformation and acoustic propagation in porous media: Journal of applied physics, **33**, 1482–1498.

Bjørlykke, K., 2010, Petroleum geoscience: From sedimentary environments to rock physics: Springer Science & Business Media.

Blair, S. C., P. A. Berge, and J. G. Berryman, 1996, Using two-point correlation functions to characterize microgeometry and estimate permeabilities of sandstones and porous glass: Journal of Geophysical Research, **101**, 20359–20.

Blanc, E., G. Chiavassa, and B. Lombard, 2013, Biot-JKD model: simulation of 1D transient poroelastic waves with fractional derivatives: Journal of Computational Physics, **237**, 1–20.

Blanchard, T. D., and P. Delommot, 2015, An example of the measurement and practical applications of time-lapse seismic attenuation: Geophysics, **80**, WA25–WA34.

Bourbié, T., O. Coussy, and B. Zinszner, 1987, Acoustics of porous media: Editions technip.

Bourbié, T., and A. Gonzalez-Serrano, 1983, Synthetic seismograms in attenuating media: Geophysics, **48**, 1575–1587.

Boutin, C., and C. Geindreau, 2008, Estimates and bounds of dynamic permeability of granular media: The Journal of the Acoustical Society of America, **124**, 3576–3593.

Bouzidi, Y., and D. R. Schmitt, 2009, Measurement of the speed and attenuation of the Biot slow wave using a large ultrasonic transmitter: Journal of Geophysical Research: Solid Earth (1978–2012), **114**.

Brajanovski, M., B. Gurevich, and M. Schoenberg, 2005, A model for P-wave attenuation and dispersion in a porous medium permeated by aligned fractures: Geophysical Journal International, **163**, 372–384.

Brie, A., F. Pampuri, A. Marsala, O. Meazza, et al., 1995, Shear sonic interpretation in gas-bearing sands: Presented at the SPE Annual Technical Conference and Exhibition, Society of Petroleum Engineers.

Brooks, R. H., and A. T. Corey, 1964, Hydraulic properties of porous media and their relation to drainage design: Transactions of the ASAE, **7**, 26–0028.

Cadoret, T., D. Marion, and B. Zinszner, 1995, Influence of frequency and fluid distribution on elastic wave velocities in partially saturated limestones: Journal of Geophysical Research, **100**, 9789–9803.

Calvert, R., 2005, Insights and methods for 4D reservoir monitoring and characterization: SEG/EAGE Distinguished Instructor Short Course, **8**.

Carcione, J. J. M., 2007, Wave fields in real media: Elsevier Science.

Carcione, J. M., 1998, Viscoelastic effective rheologies for modelling wave propagation in porous media: Geophysical prospecting, **46**, 249–270.

Carcione, J. M., B. Gurevich, J. E. Santos, and S. Picotti, 2013, Angular and frequency-dependent wave velocity and attenuation in fractured porous media: Pure and Applied Geophysics, **170**, 1673–1683.

Carcione, J. M., H. B. Helle, and N. H. Pham, 2003, White's model for wave propagation in partially saturated rocks: Comparison with poroelastic numerical experiments: Geophysics, **68**, 1389–1398.

Carcione, J. M., and S. Picotti, 2006, P-wave seismic attenuation by slow-wave diffusion: Effects of inhomogeneous rock properties: Geophysics, **71**, O1–O8.

Carcione, J. M., S. Picotti, D. Gei, and G. Rossi, 2006, Physics and seismic modeling for monitoring CO_2 storage: Pure and Applied Geophysics, **163**,

175–207.

Caspari, E., T. Müller, and B. Gurevich, 2011, Time-lapse sonic logs reveal patchy CO_2 saturation in-situ: Geophysical Research Letters, **38**.

Castagna, J. P., and M. Backus, 1993, AVO analysis–tutorial and review: Offset-dependent reflectivity: theory and practice of AVO analysis, 3–36.

Castagna, J. P., S. Sun, and R. W. Siegfried, 2003, Instantaneous spectral analysis: Detection of low-frequency shadows associated with hydrocarbons: The Leading Edge, **22**, 120–127.

Chandler, R. N., and D. L. Johnson, 1981, The equivalence of quasistatic flow in fluid-saturated porous media and Biot's slow wave in the limit of zero frequency: Journal of Applied Physics, **52**, 3391–3395.

Chapman, M., 2003, Frequency-dependent anisotropy due to meso-scale fractures in the presence of equant porosity: Geophysical Prospecting, **51**, 369–379.

Chapman, M., E. Liu, and X.-Y. Li, 2006, The influence of fluid sensitive dispersion and attenuation on AVO analysis: Geophysical Journal International, **167**, 89–105.

Chapman, M., S. V. Zatsepin, and S. Crampin, 2002, Derivation of a microstructural poroelastic model: Geophysical Journal International, **151**, 427–451.

Cheng, H., and S. Torquato, 1997, Effective conductivity of periodic arrays of spheres with interfacial resistance: Proceedings of the Royal Society of London. Series A: Mathematical, Physical and Engineering Sciences, **453**, 145–161.

Chilingar, G. V., R. W. Mannon, and H. Rieke III, 1972, Oil and gas production from carbonate rocks.

Cole, S., D. Lumley, M. Meadows, A. Tura, et al., 2002, Pressure and saturation inversion of 4D seismic data by rock physics forward modeling: Presented at the 2002 SEG Annual Meeting, Society of Exploration Geophysicists.

Cooper Jr, H. F., 1967, Reflection and transmission of oblique plane waves at a plane interface between viscoelastic media: The Journal of the Acoustical Society of America, **42**, 1064–1069.

Davolio, A., C. Maschio, D. J. Schiozer, et al., 2011, Incorporating 4D seismic attributes into history matching process through an inversion scheme: Presented at the SPE EUROPEC/EAGE Annual Conference and Exhibition, Society of Petroleum Engineers.

De la Cruz, V., and T. Spanos, 1985, Seismic wave propagation in a porous

medium: Geophysics, **50**, 1556–1565.

De la Cruz, V., T. Spanos, and D. Yang, 1995, Macroscopic capillary pressure: Transport in porous media, **19**, 67–77.

Debye, P., and A. Bueche, 1949, Scattering by an inhomogeneous solid: Journal of Applied Physics, **20**, 518–525.

Denneman, A. I., G. G. Drijkoningen, D. M. Smeulders, and K. Wapenaar, 2002, Reflection and transmission of waves at a fluid/porous-medium interface: Geophysics, **67**, 282–291.

Deresiewicz, H., and J. Rice, 1964, The effect of boundaries on wave propagation in a liquid-filled porous solid: V. transmission across a plane interface: Bulletin of the Seismological Society of America, **54**, 409–416.

Deresiewicz, H., and R. Skalak, 1963, On uniqueness in dynamic poroelasticity: Bulletin of the Seismological Society of America, **53**, 783–788.

Dinariev, O. Y., and D. Mikhailov, 2011, Simulation of the dynamic (frequency-dependent) permeability and electrical conductivity in porous materials based on the concept of an ensemble of pores: Journal of applied mechanics and technical physics, **52**, 82–95.

Dutta, N., and H. Odé, 1979, Attenuation and dispersion of compressional waves in fluid-filled porous rocks with partial gas saturation (White model)-Part I: Biot theory: Geophysics, **44**, 1777–1788.

———, 1983, Seismic reflections from a gas-water contact: Geophysics, **48**, 148–162.

Dutta, N., and A. Seriff, 1979, On White's model of attenuation in rocks with partial gas saturation: Geophysics, **44**, 1806–1812.

Dvorkin, J. P., and G. Mavko, 2006, Modeling attenuation in reservoir and nonreservoir rock: The Leading Edge, **25**, 194–197.

Eberhart-Phillips, D., D.-H. Han, and M. D. Zoback, 1989, Empirical relationships among seismic velocity, effective pressure, porosity, and clay content in sandstone: Geophysics, **54**, 82–89.

Feng, S., and D. L. Johnson, 1983, High-frequency acoustic properties of a fluid/porous solid interface. I. New surface mode: The Journal of the Acoustical Society of America, **74**, 906–914.

Focke, J., and D. Munn, 1987, Cementation exponents in middle eastern carbonate reservoirs: SPE Formation Evaluation, **2**, 155–167.

Gassmann, F., 1951, Über die elastizität poröser medien: Vierteljahrss-chrift der naturforschenden gesellschaft in zurich 96, 1-23: Paper translation at http://sepwww. stanford. edu/sep/berryman/PS/gassmann. pdf.

Geertsma, J., and D. Smit, 1961, Some aspects of elastic wave propagation in fluid-saturated porous solids: Geophysics, **26**, 169–181.

Gelinsky, S., S. Shapiro, T. Müller, and B. Gurevich, 1998, Dynamic poroelasticity of thinly layered structures: International Journal of Solids and Structures, **35**, 4739–4751.

Gelinsky, S., and S. A. Shapiro, 1997, Poroelastic Backus averaging for anisotropic layered fluid-and gas-saturated sediments: Geophysics, **62**, 1867–1878.

Gerner, A., E. H. Saenger, and S. A. Shapiro, 2007, Attenuation of P-waves due to interlayer fluid flow in hydrate-bearing sediments: Journal of Geophysics and Engineering, **4**, 394.

Gist, G. A., 1994, Interpreting laboratory velocity measurements in partially gas-saturated rocks: Geophysics, **59**, 1100–1109.

Goloshubin, G., E. Chabyshova, et al., 2012, A possible explanation of low frequency shadows beneath gas reservoirs: Presented at the 2012 SEG Annual Meeting, Society of Exploration Geophysicists.

Goloshubin, G., C. Van Schuyver, V. Korneev, D. Silin, and V. Vingalov, 2006, Reservoir imaging using low frequencies of seismic reflections: The Leading Edge, **25**, 527–531.

Granli, J. R., B. Arntsen, A. Sollid, and E. Hilde, 1999, Imaging through gas-filled sediments using marine shear-wave data: Geophysics, **64**, 668–677.

Gurevich, B., 1996, On:wave propagation in heterogeneous, porous media: A velocity-stress, finite difference method, by N. Dai, A. Vafidis, and ER Kanasewich (March-April 1995 Geophysics, p. 327-340): Geophysics, **61**, 1230–1231.

Gurevich, B., R. Ciz, and A. I. Denneman, 2004, Simple expressions for normal-incidence reflection coefficients from an interface between fluid-saturated porous materials: Geophysics, **69**, 1372–1377.

Gurevich, B., and S. Lopatnikov, 1995, Velocity and attenuation of elastic waves in finely layered porous rocks: Geophysical Journal International, **121**, 933–947.

Gurevich, B., D. Makarynska, O. B. de Paula, and M. Pervukhina, 2010, A simple model for squirt-flow dispersion and attenuation in fluid-saturated granular rocks: Geophysics, **75**, N109–N120.

Gurevich, B., and R. Pevzner, 2015, How frequency dependency of q affects spectral ratio estimates: Geophysics, **80**, A39–A44.

Gurevich, B., and M. Schoenberg, 1999, Interface conditions for biots equations

of poroelasticity: The Journal of the Acoustical Society of America, **105**, 2585–2589.

Hill, R., 1964, Theory of mechanical properties of fibre-strengthened materials: I. elastic behaviour: Journal of the Mechanics and Physics of Solids, **12**, 199–212.

Hilterman, F. J., 2001, Seismic amplitude interpretation: 2001 Distinguished Instructor Short Course: SEG Books.

Homsy, G. M., 1987, Viscous fingering in porous media: Annual review of fluid mechanics, **19**, 271–311.

Hudson, J., E. Liu, and S. Crampin, 1996, The mechanical properties of materials with interconnected cracks and pores: Geophysical Journal International, **124**, 105–112.

Hudson, J., T. Pointer, and E. Liu, 2001, Effective-medium theories for fluid-saturated materials with aligned cracks: Geophysical Prospecting, **49**, 509–522.

Johnson, D. L., 2001, Theory of frequency dependent acoustics in patchy-saturated porous media: The Journal of the Acoustical Society of America, **110**, 682.

Johnson, D. L., D. L. Hemmick, and H. Kojima, 1994, Probing porous media with first and second sound. I. Dynamic permeability: Journal of Applied Physics, **76**, 104–114.

Johnson, D. L., J. Koplik, and R. Dashen, 1987, Theory of dynamic permeability and tortuosity in fluid-saturated porous media: Journal of fluid mechanics, **176**, 379–402.

Johnston, D. H., 2013, Practical applications of time-lapse seismic data: Distinguished Instructor Series, Society of Exploration Geophysicists.

Johnston, D. H., M. Toksöz, and A. Timur, 1979, Attenuation of seismic waves in dry and saturated rocks: Ii. mechanisms: Geophysics, **44**, 691–711.

Karal Jr, F. C., and J. B. Keller, 1964, Elastic, electromagnetic, and other waves in a random medium: Journal of Mathematical Physics, **5**, 537–547.

Kjartansson, E., 1979, Constant Q-wave propagation and attenuation: J. geophys. Res, **84**, 4737–4748.

Knight, R., J. Dvorkin, and A. Nur, 1998, Acoustic signatures of partial saturation: Geophysics, **63**, 132–138.

Knight, R., and R. Nolen-Hoeksema, 1990, A laboratory study of the dependence of elastic wave velocities on pore scale fluid distribution: Geophysical Research Letters, **17**, 1529–1532.

Kong, L., B. Gurevich, T. M. Müller, Y. Wang, and H. Yang, 2013, Effect of fracture fill on seismic attenuation and dispersion in fractured porous rocks: Geophysical Journal International, **195**, 1679–1688.

Konishi, C., H. Azuma, D. Nobuoka, Z. Xue, and J. Watanabe, 2009, CO_2 saturation estimation from P-wave velocity changes by considering patchy saturation: Presented at the SEG Summer Research Workshop.

Korneev, V. A., G. M. Goloshubin, T. M. Daley, and D. B. Silin, 2004, Seismic low-frequency effects in monitoring fluid-saturated reservoirs: Geophysics, **69**, 522–532.

Krzikalla, F., and T. M. Müller, 2011, Anisotropic P-SV-wave dispersion and attenuation due to inter-layer flow in thinly layered porous rocks: Geophysics, **76**, WA135–WA145.

Kudarova, A., K. Karel van Dalen, G. Guy Drijkoningen, et al., 2014, Seismic wave propagation in porous media with spherical inclusions: Extension of whites model: Presented at the 2014 SEG Annual Meeting, Society of Exploration Geophysicists.

Kudarova, A. M., K. N. van Dalen, and G. G. Drijkoningen, 2013, Effective poroelastic model for one-dimensional wave propagation in periodically layered media: Geophysical Journal International, **195**, 1337–1350.

Lebedev, M., J. Toms-Stewart, B. Clennell, M. Pervukhina, V. Shulakova, L. Paterson, T. M. Müller, B. Gurevich, and F. Wenzlau, 2009, Direct laboratory observation of patchy saturation and its effects on ultrasonic velocities: The Leading Edge, **28**, 24–27.

Lei, X., and Z. Xue, 2009, Ultrasonic velocity and attenuation during CO_2 injection into water-saturated porous sandstone: Measurements using difference seismic tomography: Physics of the Earth and Planetary Interiors, **176**, 224–234.

Lenormand, R., 1990, Liquids in porous media: Journal of Physics: Condensed Matter, **2**, SA79.

Liner, C. L., 2012, Elements of seismic dispersion: A somewhat practical guide to frequency-dependent phenomena: Society of Exploration Geophysicists.

Liu, E., and A. Martinez, 2013, Seismic fracture characterization: Concepts and practical applications: EET Course, EAGE.

Liu, H.-L., and D. L. Johnson, 1997, Effects of an elastic membrane on tube waves in permeable formations: The Journal of the Acoustical Society of America, **101**, 3322–3329.

Liu, L., S. Cao, and L. Wang, 2011, Poroelastic analysis of frequency-dependent

amplitude-versus-offset variations: Geophysics, **76**, C31–C40.

Lo, W.-C., and G. Sposito, 2013, Acoustic waves in unsaturated soils: Water Resources Research, **49**, 5674–5684.

Lo, W.-C., G. Sposito, and E. Majer, 2005, Wave propagation through elastic porous media containing two immiscible fluids: Water Resources Research, **41**.

Lopatnikov, S., and P. Y. Gorbachev, 1987, Propagation and attenuation of longitudinal-waves in a partially gas-saturated porous-medium.

Lopes, S., and M. Lebedev, 2012, Research note: Laboratory study of the influence of changing the injection rate on the geometry of the fluid front and on P-wave ultrasonic velocities in sandstone: Geophysical Prospecting, **60**, 572–580.

Lopes, S., M. Lebedev, T. M. Müller, M. B. Clennell, and B. Gurevich, 2014, Forced imbibition into a limestone: measuring P-wave velocity and water saturation dependence on injection rate: Geophysical Prospecting, **62**, 1126–1142.

Love, A. E. H., 1944, A treatise on the mathematical theory of elasticity: Courier Corporation.

MacBeth, C., and K. Stephen, 2008, Seismic scale saturation relations in turbidite reservoirs undergoing waterflood: Geophysical Prospecting, **56**, 693–714.

Markov, M., 2009, Reflection of elastic waves at an interfaces between two porous half-spaces filled with different fluids: Izvestiya, Physics of the Solid Earth, **45**, 769–776.

Markov, M., and V. Levin, 2007, The role of surface tension in elastic wave scattering in an inhomogeneous poroelastic medium: Waves in Random and Complex Media, **17**, 615–626.

Markov, M., and A. Y. Yumatov, 1988, Acoustic properties of a porous laminated medium: Journal of Applied Mechanics and Technical Physics, **29**, 107–111.

Masson, Y. J., and S. R. Pride, 2007, Poroelastic finite difference modeling of seismic attenuation and dispersion due to mesoscopic-scale heterogeneity: Journal of Geophysical Research: Solid Earth (1978–2012), **112**.

Mavko, G., and T. Mukerji, 1998, Bounds on low-frequency seismic velocities in partially saturated rocks: Geophysics, **63**, 918–924.

Mavko, G., T. Mukerji, and J. Dvorkin, 2009, The rock physics handbook: Tools for seismic analysis of porous media: Cambridge University Press.

Mavko, G., and R. Nolen-Hoeksema, 1994, Estimating seismic velocities at ultrasonic frequencies in partially saturated rocks: Geophysics, **59**, 252–258.

Maximov, G., 2010, Generalization of Biot's equations with allowance for shear relaxation of a fluid: Acoustical Physics, **56**, 493–500.

Mikhaltsevitch, V., M. Lebedev, and B. Gurevich, 2015, A laboratory study of the elastic and anelastic properties of the eagle ford shale: 3rd International Workshop on Rock Physics, Extended Abstract.

Milton, G. W., 2002, The theory of composites: Cambridge University Press.

Moerig, R., W. Waite, O. Boyd, I. Getting, and H. Spetzler, 1996, Seismic attenuation in artificial glass cracks: Physical and physicochemical effects of fluids: Geophysical research letters, **23**, 2053–2056.

Monsen, K., and S. Johnstad, 2005, Improved understanding of velocity–saturation relationships using 4D computer-tomography acoustic measurements: Geophysical Prospecting, **53**, 173–181.

Morgan, E. C., M. Vanneste, I. Lecomte, L. G. Baise, O. Longva, and B. McAdoo, 2012, Estimation of free gas saturation from seismic reflection surveys by the genetic algorithm inversion of a P-wave attenuation model: Geophysics, **77**, R175–R187.

Müller, T., Q. Qi, C. D. Piane, and P. Sahay, 2013, Slow shear waves in poroelasticity and the concept of dynamic permeability: Poromechanics V, Fifth Biot Conference on Poromechanics, ASCE, 316–325.

Müller, T., and P. Sahay, 2009, Compressional wave attenuation and dispersion due to conversion scattering into slow shear wave: Poro-Mechanics, IV, 673–678.

Müller, T. M., and B. Gurevich, 2004, One-dimensional random patchy saturation model for velocity and attenuation in porous rocks: Geophysics, **69**, 1166–1172.

———, 2005, A first-order statistical smoothing approximation for the coherent wave field in random porous media: The Journal of the Acoustical Society of America, **117**, 1796–1805.

Müller, T. M., B. Gurevich, and M. Lebedev, 2010, Seismic wave attenuation and dispersion resulting from wave-induced flow in porous rocksa review: Geophysics, **75**, 75A147–75A164.

Müller, T. M., G. Lambert, and B. Gurevich, 2007, Dynamic permeability of porous rocks and its seismic signatures: Geophysics, **72**, E149–E158.

Müller, T. M., and P. N. Sahay, 2011a, Fast compressional wave attenuation

and dispersion due to conversion scattering into slow shear waves in randomly heterogeneous porous media: The Journal of the Acoustical Society of America, **129**, 2785.

———, 2011b, Stochastic theory of dynamic permeability in poroelastic media: Physical Review E, **84**, 026329.

Müller, T. M., J. Toms-Stewart, and F. Wenzlau, 2008, Velocity-saturation relation for partially saturated rocks with fractal pore fluid distribution: Geophysical Research Letters, **35**, L09306.

Murphy, W. F., 1984, Acoustic measures of partial gas saturation in tight sandstones: Journal of Geophysical Research: Solid Earth (1978–2012), **89**, 11549–11559.

Murphy III, W. F., K. W. Winkler, and R. L. Kleinberg, 1986, Acoustic relaxation in sedimentary rocks: Dependence on grain contacts and fluid saturation: Geophysics, **51**, 757–766.

Nagy, P. B., 1992, Observation of a new surface mode on a fluid-saturated permeable solid: Applied physics letters, **60**, 2735–2737.

Nagy, P. B., and G. Blaho, 1994, Experimental measurements of surface stiffness on water-saturated porous solids: The Journal of the Acoustical Society of America, **95**, 828–835.

Nagy, P. B., and A. H. Nayfeh, 1995, Generalized formula for the surface stiffness of fluid-saturated porous media containing parallel pore channels: Applied physics letters, **67**, 1827–1829.

Nakagawa, S., T. J. Kneafsey, T. M. Daley, B. M. Freifeld, and E. V. Rees, 2013, Laboratory seismic monitoring of supercritical CO_2 flooding in sandstone cores using the split hopkinson resonant bar technique with concurrent x-ray computed tomography imaging: Geophysical Prospecting, **61**, 254–269.

Norris, A. N., 1993, Low-frequency dispersion and attenuation in partially saturated rocks: The Journal of the Acoustical Society of America, **94**, 359–370.

Nur, A., and J. Byerlee, 1971, An exact effective stress law for elastic deformation of rock with fluids: Journal of Geophysical Research, **76**, 6414–6419.

Ostrander, W., 1984, Plane-wave reflection coefficients for gas sands at nonnormal angles of incidence: Geophysics, **49**, 1637–1648.

Picotti, S., J. M. Carcione, J. G. Rubino, J. E. Santos, and F. Cavallini, 2010, A viscoelastic representation of wave attenuation in porous media: Computers & Geosciences, **36**, 44–53.

Plona, T. J., 1980, Observation of a second bulk compressional wave in a porous

medium at ultrasonic frequencies: Applied Physics Letters, **36**, 259–261.

Pride, S. R., J. G. Berryman, and J. M. Harris, 2004, Seismic attenuation due to wave-induced flow: Journal of Geophysical Research: Solid Earth (1978–2012), **109**.

Priest, J. A., A. I. Best, and C. R. Clayton, 2006, Attenuation of seismic waves in methane gas hydrate-bearing sand: Geophysical Journal International, **164**, 149–159.

Purcell, W., et al., 1949, Capillary pressures-their measurement using mercury and the calculation of permeability therefrom: Journal of Petroleum Technology, **1**, 39–48.

Qi, Q., T. M. Müller, B. Gurevich, S. Lopes, M. Lebedev, and E. Caspari, 2014a, Quantifying the effect of capillarity on attenuation and dispersion in patchy-saturated rocks: Geophysics, **79**, WB35–WB50.

Qi, Q., T. M. Müller, and J. G. Rubino, 2014b, Seismic attenuation: effects of interfacial impedance on wave-induced pressure diffusion: Geophysical Journal International, **199**, 1677–1681.

Quintal, B., S. M. Schmalholz, and Y. Y. Podladchikov, 2009, Low-frequency reflections from a thin layer with high attenuation caused by interlayer flow: Geophysics, **74**, N15–N23.

Ren, H., G. Goloshubin, and F. J. Hilterman, 2009, Poroelastic analysis of amplitude-versus-frequency variations: Geophysics, **74**, N41–N48.

Riaz, A., G.-Q. Tang, H. A. Tchelepi, and A. R. Kovscek, 2007, Forced imbibition in natural porous media: Comparison between experiments and continuum models: Physical Review E, **75**, 036305.

Rosenbaum, J., 1974, Synthetic microseismograms: logging in porous formations: Geophysics, **39**, 14–32.

Rubino, J., and K. Holliger, 2012, Seismic attenuation and velocity dispersion in heterogeneous partially saturated porous rocks: Geophysical Journal International, **188**, 1088–1102.

———, 2013, Research note: Seismic attenuation due to wave-induced fluid flow at microscopic and mesoscopic scales: Geophysical Prospecting, **61**, 882–889.

Rubino, J., D. R. Velis, and M. D. Sacchi, 2011, Numerical analysis of wave-induced fluid flow effects on seismic data: Application to monitoring of CO_2 storage at the sleipner field: Journal of Geophysical Research: Solid Earth (1978–2012), **116**.

Rutherford, S. R., and R. H. Williams, 1989, Amplitude-versus-offset variations

in gas sands: Geophysics, **54**, 680–688.

Sahay, P. N., 2008, On the Biot slow S-wave: Geophysics, **73**, N19–N33.

———, 2012, Poroelastic seismic boundary conditions: 9th Biennial International Conference and Exposition on Petroleum Geophysics.

Sahay, P. N., T. T. Spanos, and V. De la Cruz, 2001, Seismic wave propagation in inhomogeneous and anisotropic porous media: Geophysical Journal International, **145**, 209–222.

Sams, M., J. Neep, M. Worthington, and M. King, 1997, The measurement of velocity dispersion and frequency-dependent intrinsic attenuation in sedimentary rocks: Geophysics, **62**, 1456–1464.

Santos, J. E., J. Douglas Jr, J. Corberó, and O. M. Lovera, 1990, A model for wave propagation in a porous medium saturated by a two-phase fluid: The Journal of the Acoustical Society of America, **87**, 1439–1448.

Schmidt, H., 2004, Oases version 3.1 user guide and reference manual: Department of Ocean Engineering, Massachusetts Institute of Technology.

Sengupta, M., and G. Mavko, 2003, Impact of flow-simulation parameters on saturation scales and seismic velocity: Geophysics, **68**, 1267–1280.

Shapiro, S. A., and T. M. Müller, 1999, Seismic signatures of permeability in heterogeneous porous media: Geophysics, **64**, 99–103.

Shi, J.-Q., Z. Xue, and S. Durucan, 2007, Seismic monitoring and modelling of supercritical CO_2 injection into a water-saturated sandstone: Interpretation of P-wave velocity data: International Journal of Greenhouse Gas Control, **1**, 473–480.

Smeulders, D., and M. Van Dongen, 1997, Wave propagation in porous media containing a dilute gas–liquid mixture: theory and experiments: Journal of Fluid mechanics, **343**, 351–373.

Spencer, J. W., 1981, Stress relaxations at low frequencies in fluid-saturated rocks: Attenuation and modulus dispersion: Journal of Geophysical Research: Solid Earth (1978–2012), **86**, 1803–1812.

Tisato, N., and B. Quintal, 2013, Measurements of seismic attenuation and transient fluid pressure in partially saturated Berea sandstone: evidence of fluid flow on the mesoscopic scale: Geophysical Journal International, **195**, 342–351.

Toms, J., 2008, Effect of fluid distribution on compressional wave propagation in partially saturated rocks: PhD thesis, Curtin University of Technology.

Toms, J., B. Gurevich, T. Mueller, and D. Johnson, 2007a, Acoustics of random patchy saturation: Presented at the 69th EAGE Conference & Exhibition.

Toms, J., T. M. Müller, and B. Gurevich, 2007b, Seismic attenuation in porous rocks with random patchy saturation: Geophysical Prospecting, **55**, 671–678.

Toms, J., T. M. Müller, B. Gurevich, and L. Paterson, 2009, Statistical characterization of gas-patch distributions in partially saturated rocks: Geophysics, **74**, WA51–WA64.

Torquato, S., 2002, Random heterogeneous materials: microstructure and macroscopic properties: Springer, **16**.

Tserkovnyak, Y., and D. L. Johnson, 2002, Can one hear the shape of a saturation patch?: Geophysical Research Letters, **29**, 12–1.

———, 2003, Capillary forces in the acoustics of patchy-saturated porous media: The Journal of the Acoustical Society of America, **114**, 2596.

Tuncay, K., and M. Corapcioglu, 1997, Wave propagation in poroelastic media saturated by two fluids: Journal of applied mechanics, **64**, 313–320.

Tura, A., and D. Lumley, 1999, Estimating pressure and saturation changes from time-lapse AVO data, SEG 69th Annual Meeting: Expanded Abstracts, SRC, **4**.

Vogelaar, B., and D. Smeulders, 2007, Extension of White's layered model to the full frequency range: Geophysical prospecting, **55**, 685–695.

Vogelaar, B., D. Smeulders, and J. Harris, 2010, Exact expression for the effective acoustics of patchy-saturated rocks: Geophysics, **75**, N87–N96.

Walsh, J., and W. Brace, 1984, The effect of pressure on porosity and the transport properties of rock: Journal of Geophysical Research: Solid Earth (1978–2012), **89**, 9425–9431.

Wang, H. F., 2000, Theory of linear poroelasticity: Princeton Series in Geophysics, Princeton University Press, Princeton, NJ.

Wenzlau, F., and T. M. Müller, 2009, Finite-difference modeling of wave propagation and diffusion in poroelastic media: Geophysics, **74**, T55–T66.

White, J., 1975, Computed seismic speeds and attenuation in rocks with partial gas saturation: Geophysics, **40**, 224–232.

White, J. E., N. Mikhaylova, and F. Lyakhovitskiy, 1975, Low-frequency seismic waves in fluid-saturated layered rocks: Physics of the Solid Earth, **11**, 654–659.

Winkler, K. W., 1985, Dispersion analysis of velocity and attenuation in Berea sandstone: Journal of Geophysical Research: Solid Earth (1978–2012), **90**, 6793–6800.

Zener, C., 1948, Elasticity and anelasticity of metals: University of Chicago

press.

Zhang, Y., O. Nishizawa, T. Kiyama, S. Chiyonobu, and Z. Xue, 2014, Flow behaviour of supercritical CO2 and brine in Berea sandstone during drainage and imbibition revealed by medical X-ray CT images: Geophysical Journal International, **197**, 1789–1807.

Zhao, L., D.-h. Han, Q. Yao, R. Zhou, and F. Yan, 2015, Seismic reflection dispersion due to wave-induced fluid flow in heterogeneous reservoir rocks: Geophysics, **80**, D221–D235.

Zhubayev, A., and R. Ghose, 2012, Contrasting behavior between dispersive seismic velocity and attenuation: Advantages in subsoil characterization: The Journal of the Acoustical Society of America, **131**, EL170–EL176.